UNIVERSITY OF UDINE

POLYTECHNIC DEPARTMENT OF
ENGINEERING AND ARCHITECTURE

XXIX Cycle Ph.D. Course
Environmental and energy engineering science

Energy recovery systems based on high temperature phase change materials

Ph.D. Candidate
Mr. Fabio Dal Magro

Supervisor
Assoc. Prof. Stefano Savino

Co-supervisors
Prof. Gioacchino Nardin
Assoc. Prof. Antonella Meneghetti

March 2017

To my parents, for always trusting in me
and supporting my aspirations

To Francesca, whose love gave me the strength to
overcome all the obstacles faced during these years

SUMMARY

Energy recovery from the waste heat released by industrial processes represents one of the greatest opportunity to reduce the consumption of primary energy and the related emission of greenhouse gases. Nevertheless, the fluctuating and/or intermittent nature of many energy-intensive processes (e.g. electric arc furnace in steel industry) hinders the deployment of current energy recovery systems. Thus, the development of technologies able to minimize the thermal power fluctuations released by such processes is required to enable the deployment of affordable energy recovery systems.

With the aim of developing such type of technology, this thesis explores the potential of latent heat storage systems based on phase change materials (PCMs) to minimize the thermal power fluctuations of high-temperature waste heat sources. In particular, three significant areas of investigation characterised by different types of thermal power fluctuations are investigated: electric arc furnace, billet reheating furnace and waste-to-energy plant. An interdisciplinary approach is adopted to face the crucial issues of developing a PCM-based technology (e.g. thermo-mechanical stresses, transient heat transfer).

Chapter 1 includes the background, the motivation, the aim, the methodology and the structure of thesis. In chapter 2, a general overview on the thermal energy storage systems with a particular focus on latent heat storage systems based on PCMs is provided. Chapter 3 addresses the issues related to the energy recovery from the electric arc furnace and proposes three different configurations of a PCM-based device to increase the efficiency and the capacity factor of the downstream energy recovery system. In Chapter 4 an existing waste heat recovery system of a steel billet preheating furnace is retrofitted by adding a PCM-based device. In Chapter 5 a refractory brick technology based on PCMs is proposed for the protection of the radiant superheaters against high temperature corrosion and temperature fluctuations.

At the end of each chapter a series of conclusions are reported, concerning the performed investigations and the obtained results.

ACKNOWLEDGEMENTS

I would like to thank all the people who contributed to the research work presented in this thesis. A special thank goes to my enthusiastic supervisor prof. Gioacchino Nardin, who first encouraged me to strongly pursuit my passion for the engineering research and taught me to believe in my own ideas.

I am also grateful to my supervisors prof. Stefano Savino, for the continuous support of my research, and prof. Antonella Meneghetti, for her precious guidance.

My sincere thanks also go to prof. Denis Benasciutti, for his cooperation and insightful advices, and prof. Alessandro Romagnoli, who gave me the opportunity to join his team and work in an international environment.

TABLE OF CONTENTS

LIST OF FIGURES

LIST OF TABLES

Chapter 1

INTRODUCTION

1.1 Background and motivation

According to the International Energy Agency (IEA) [1], energy efficiency should be at the centre of the energy policy of any country since it is far from fulfilling its potential. In addition to this, IEA states that any credible and realistic energy development strategy must be led by energy efficiency; for this reason, IEA calls energy efficiency the "first fuel" in the context of decarbonization.

In the Paris Agreement achieved at the 21st Conference Of the Parties (known as COP21) in December 2015, 189 countries submitted 162 Nationally Determined Contributions, which set out high-level intentions, goals, targets and prescriptive actions to reduce Greenhouse Gas (GHG) emissions. The output of several climate mitigation scenarios showed that energy efficiency is one of the most economical options to reduce GHG emissions.

An analysis on the costs of climate mitigation by 2030 carried out by the Fraunhofer Institute for Systems and Innovation Research [2], demonstrated that a scenario in which the deployment of significant measures on energy efficiency is considered, would be at least 2.5 trillion US dollars less costly than those considering more energy-intensive

mitigation scenarios; this paves the way in the political agenda of governments as they work towards achieving the target set in the Paris Agreement.

The implementation of measures in favour of energy efficiency can help to reduce energy consumption whilst still maintaining a constant level of energy-use services. Moreover, improving energy efficiency enables a higher level of services from the same energy input; this is a very important aspect to consider since in the coming decades the industrial activity is expected to increase in both developing countries and emerging economies.

Nevertheless, energy efficiency measures are more complex to implement than other measures (e.g. renewable energy production, nuclear power or carbon capture and storage systems) because of the involvement of several players and relatively small impact of each individual measure. Furthermore, the complexity of the energy efficiency measures and their dependence on additional factors, such as energy prices and energy demand, make difficult to estimate their cost; the difference in payback times and lifetime of technologies also play an important role. Moreover, the contribution of energy efficiency measures has been questioned because of rebound effects that may reduce their effectiveness in lowering energy demand.

Among the energy efficiency measures, energy recovery from the waste heat released by industrial processes represents one of the greatest opportunity to reduce the consumption of primary energy and the related emission of greenhouse gases. Energy recovery positively impacts the efficiency of production processes by reducing operating costs, increasing the plant productivity and reducing the emission of pollutant. The benefits (i.e. operational, energy, economic, environmental and social) related with energy recovery are fundamental nowadays, indeed energy recovery has now become a common practice when easy to implement.

Sources of waste heat include hot combustion gases discharged to the atmosphere, heated products from industrial processes and heat transfer from hot equipment surfaces. The exact quantity of industrial waste heat is poorly quantified, but various studies have estimated that as much as 20 to 50% of industrial energy consumption is ultimately discharged as waste heat [3]. While some heat losses from industrial processes are inevitable, facilities can reduce these losses by installing waste heat recovery

technologies. These technologies include heat exchangers (e.g. waste heat boilers, deep economizers, water preheating, etc.), thermal energy storage systems (e.g. hot water tanks, steam accumulators) and energy conversion technologies.

The recovered waste heat can be reused directly for heating purposes or for power production. Even though the most efficient usage of the recovered heat is to directly employ it for heating purposes, its direct utilization is constrained by several factors such as temperature matching, distance between the waste heat source and the thermal user as well as lack of a thermal user. When these constraints hinder the direct use of the recovered heat, power production should be considered since its outcome is a high exergy product that can be easily transported and used for other processes [4].

Several energy recovery technologies for power production (e.g. steam and organic Rankine cycles) are already well developed and technically proven; however, there are several applications where such technologies are not applied due to a combination of market and technical barriers. The most important technical and economical barrier that limits the implementation of energy recovery systems for power production is the fluctuating and/or intermittent nature of the waste heat source. Typically, in an industrial process the main parameters that fluctuate - thus causing the variability in the thermal power of the waste heat source - are temperature and mass flow rate.

Current energy recovery systems are designed for a nominal operating point (i.e. design point) which can either be the upper boundary [5–7] or the average value of the fluctuation range [8,9]. Such a design approach leads the energy recovery system to operate for most of the time at part load (i.e. off-design conditions), thus severely reducing its efficiency and capacity factor; this means that the power production capacity of the energy recovery system is not fully exploited and, from the economical point of view, an inefficient and sub-optimal energy recovery system leads to high payback periods, thus reducing its actual implementation.

Therefore, by keeping in mind the limitations of the current energy recovery systems for power production mentioned earlier, the development of technologies able to minimize the exergy losses and the thermal power fluctuations is required to enhance the deployment of affordable energy recovery systems. In fact, it is worth remarking that the

minimization of the exergy losses corresponds with the maximization of the efficiency of the energy conversion technology, while the reduction of the thermal power fluctuations corresponds to an increased capacity factor. The combined effect of these factors allows increasing the power production (i.e. revenues), while reducing the size of the energy recovery system (i.e. capital expenditure), thus leading to shorter payback periods.

1.2 Aims of the research

Energy efficiency is one of the most cost-effective options to reduce GHG emissions. Among energy efficiency measures, energy recovery from waste heat released by industrial processes represents one of the greatest opportunity to reduce the consumption of primary energy and the related GHG emissions. Nevertheless, its implementation is often hindered by the fluctuating and/or intermittent nature of the waste heat source. Thus, to enhance the deployment of affordable energy recovery systems, the development of technologies able to minimize the exergy losses and the thermal power fluctuations is required.

With the aim of developing such type of technology, this thesis explores the potential of latent heat storage systems based on phase change materials (PCMs) to minimize the thermal power fluctuations of high-temperature (i.e. temperature higher than 300°C) waste heat sources. More in particular, the use of metallic PCMs (e.g. aluminium and its alloys) is investigated because of their high thermal conductivity and latent heat of fusion.

Latent heat storage systems based on PCMs exploit the large value of the latent heat of phase change of specific materials (i.e. phase change materials) to store and release thermal energy at a constant temperature [10]. As underlined in [11–14], latent heat storage is one of the most efficient ways of storing thermal energy: unlike sensible heat storage, latent heat storage provides much higher storage density, with a smaller temperature difference between storing and releasing heat.

Nevertheless, a paper on the recent research trend on latent heat storage systems [15] highlighted that the use of PCMs for recovering high-temperature waste heat has not been given great attention despite its large potential. Thus, this thesis also aims to enhance the knowledge on the use of phase change materials for recovering high temperature waste heat.

1.3 Methodology

Given the many technical challenges involved (e.g. thermo-mechanical stresses in the PCM container, heat transfer under transient conditions, part-load behavior of the energy recovery system), this thesis adopts an interdisciplinary approach to face the crucial issues of developing a PCM-based technology:

- *Structural analysis*, which is used to develop the PCM encapsulation technology and to select the encapsulation material;
- *Thermo-fluid dynamic analysis*, which is used to study and optimise the thermal performances of the PCM-based technology and to select the most proper heat transfer fluid to be employed for the system integration with an energy conversion technology (e.g. steam turbine);
- *System design and integration*, which is used to analyse the impact of the introduction of the PCM-based technology on the performance of energy recovery system; it is also used for studying the potential configurations that integrate the PCM-based technology with the existing energy recovery technology.

1.4 Areas of investigation

The development of the PCM-based technology is then based on three significant areas of investigation characterised by different types of thermal power fluctuations:

1. *Electric arc furnace*: characterised by temperature fluctuations with an average temperature close to the melting point of the PCM and a near-constant mass flow rate;
2. *Billet reheating furnace*: characterised by mass flow rate fluctuations and a near-constant temperature above the PCM melting point;
3. *Waste-to-energy plant*: characterised by temperature fluctuations with an average temperature above the PCM melting point and a near-constant mass flow rate.

The electric arc furnace and the billet reheating furnace are two important energy-intensive processes used in the steel industry, which is one of the major consumer of primary energy. In fact, in 2012, the steel industry consumed about 5 % of the overall primary energy produced worldwide contributing to 7 % of all global CO2 emissions [16]. Moreover, it has to be considered that the world steel production increased from 28

million tons in 1950 to nearly 1.6 billion tons in 2015 [17]. Although recently significant improvements in the energy efficiency have been achieved, this sector still has the potential to further reduce by 20% energy consumption and GHG emission.

In particular, waste heat recovery in steel industry represents one of the greatest opportunity to reduce the consumption of primary energy (i.e. reduction of CO_2 emissions) while increasing the sustainability of the steelmaking process [18–21].

The electric arc furnace, which is one of the two modern ways of making steel and accounts for the 28% of the worldwide steel production [22], releases as waste heat from 15% to 35% of the total energy provided to the process [23]. While the billet reheating furnace, which is used to heat steel slabs above the recrystallization temperature of the steel for the subsequent hot rolling process (i.e. metal forming process), consumes 15÷20% of the total energy consumption of a steel plant [24] and releases as waste heat 16% of the total energy provided to the process[25].

The third area of investigation considers the energy recovery from waste incineration, which efficiency is limited by high temperature corrosion occurring on the surface of steam superheater and temperature fluctuations, because they represent an important opportunity to reduce the greenhouse gases emitted by the landfills. In fact, it has been estimated that the fugitive emissions of methane in landfill gas contributes for the 4% of the anthropogenic GHG emissions [26].

1.5 Main contents of the thesis

Below, an overview of the main contents of the thesis is detailed according to the thesis structure.

Overview on phase change material (Chapter 2). The second chapter provides a general overview on the thermal energy storage systems with a particular focus on latent heat storage systems based on PCMs. After introducing the role of thermal energy storage systems in improving the efficiency of energy recovery systems in Section 2.1, the thermal energy storage technologies are discussed in Section 2.2. A detailed discussion on PCMs is carried out in Section 2.3; the required properties and the selection criteria of the PCMs as well as their classification is first discussed. Then, potential PCM candidates

for high temperature applications are analysed and compared; pure aluminium and its eutectic alloys was found to have superior properties among the high temperature PCMs. The technologies (e.g. macro-, micro- and nano-encapsulation), the materials for the containment of high temperature PCMs (e.g. metals, ceramics) as well as the technology limitation (e.g. corrosion) are discussed in the final part of Section 2.3. Concluding remarks are reported in Section 2.4.

Energy recovery from electric arc furnace (Chapter 3). In the third chapter, the problem of temperature fluctuations of the waste gas released by the electric arc furnace is addressed. In particular, a PCM-based device is developed to reduce the temperature fluctuation in order to increase the efficiency and the capacity factor of the downstream energy recovery system. The proposed device is composed by a set of cylindrical PCM containers, which are in direct contact with the surrounding waste gas in such a way that the PCM absorbs heat from the waste gas, when the waste gas temperature is greater than the phase change temperature, and releases heat to the waste gas, when the waste gas temperature is lower than the phase change temperature. The combination of these two effects leads to a reduction of the temperature fluctuation of the waste gas, which tends to stabilise at the phase change temperature. The chapter starts by introducing the issues that affect the energy recovery from the electric arc furnace and the content of the chapter in Section 3.1. Then, the energy balance and the energy recovery potential from the steelmaking process based on electric arc furnace are evaluated in Section 3.2. Then, the state of the art of the waste heat recovery system from electric arc furnace is reviewed in Section 3.3; advantages and disadvantages of each energy recovery technology are highlighted.

Passive configuration of the PCM-based device. The development of the PCM-based device starts in Section 3.4, where the simplest configuration is developed and analysed for a EAF process operating with discontinuous scrap charging. In this configuration, the heat exchange between the waste gas and the PCM occurs without any direct control, thus the device operates in a passive way; for this reason, this configuration is named “Passive PCM-based device for temperature smoothing”. Since the temperature-smoothing effect becomes as more effective as the average temperature of the waste gas (about 600°C) is closer to the phase change temperature, pure aluminium (melting point 660°C) is

employed as PCM. The performances of the device are analysed and optimized by means of computational thermo-fluid dynamic simulations. In addition to the development of the PCM-based device, a new waste heat boiler configuration equipped with cyclones is proposed to overcome also the problem of high dust content of the waste gas. The high recovery efficiencies, the low investment and operation costs and non-invasive plant modifications induced by the introduction of the PCM-based device, make the proposed configuration a feasible solution to reduce energy supply costs and emissions in the steel industry. Referring to the Italian context, it is estimated that adoption of the proposed system could lead to a potential energy saving of more than 1,065 GWh_e/year for a percentage equal to 12.9%. This, in turn, is equal to 0.34% of the whole Italian electricity consumption, with related benefits on national GHG emissions targets. Section 3.4 is part of the research paper "PCM-based energy recovery from electric arc furnaces. G. Nardin, A. Meneghetti, F. Dal Magro, N. Benedetti. *Applied Energy* (2014), Vol.136, pag. 947–955".

Thermo-mechanical analysis of PCM container. Section 3.5 develops an analytical and numerical approach to evaluate thermal stress in the cylindrical PCM container used in the PCM-based device of Section 3.4. The thermal analysis shows that temperature distribution in the PCM system can be considered uniform in the whole domain (i.e. PCM and container) at any time instant according to the lumped capacitance method; the thermal behaviour of the PCM system is thus simulated as a sequence of steady state analyses. The mechanical analysis adopts an axialsymmetric plane analytical model to compare elastic thermal stress distribution for different stainless steels; AISI 316 is identified as the most suitable material for the PCM container. A simple two-bars model and a stress index are also used to allow a physical understanding and a satisfactory interpretation of the PCM system response. The mechanical analysis shows that thermal stresses exceed the yield point of both stainless steels used in the container. A finite element elastic-plastic model is then developed to estimate the extension of the plastic zone. Finally, an alternative geometry based on concentric pipes is designed to keep the maximum stresses in the PCM container below the yielding point. A sensitivity analysis shows that the most relevant design parameters of the alternative geometry are the diameter of inner pipe and thickness of the external pipe. Section 3.5 is based on the publication "Thermal stress analysis of PCM containers for temperature smoothing of

waste gas. F. Dal Magro, D. Benasciutti, G. Nardin. *Applied Thermal Engineering* (2016), Vol.106, pag. 1010–1022".

Active configuration of the PCM-based device. In Section 3.6, the PCM-based device developed in Section 3.4 is extended to a EAF process with continuous charge and scrap preheating. In addition to this, a heat transfer fluid flowing through PCM containers is introduced and selected by means of an *ad-hoc* code based on an analytical thermal model. The developed code identifies carbon dioxide as the best heat transfer fluid among the considered gases. The introduction of the heat transfer fluid allows the active control of the PCM temperature to overcome overheating issues; because of this feature, the improved configuration is named "Active PCM-based device for temperature smoothing". Besides the temperature control, the introduction of the heat transfer fluid enables the adoption of smaller pipe diameters, which in turn allows the active PCM-based device to be more compact and efficient than the passive PCM-based device. Likewise Section 3.4, the performance of the improved device is analysed and optimized by means of computational thermo-fluid dynamic simulations; a comparison with the passive device is also carried out. The simulations show that maximum off-gas temperature is lowered and the resulting maximum thermal power is reduced by 25.4% with respect to a traditional plant with no smoothing device. Furthermore, the minimum load factor of the steam turbine can be enhanced from 23% of the traditional plant to 65% for the proposed system during the whole Tap-to-Tap cycle; the resulting turbine capacity factor, which affects electrical energy revenues, is increased from 60% to 82%. The content of Section 3.6 is based on the research paper "Enhancing energy recovery in the steel industry: Matching continuous charge with off-gas variability smoothing. F. Dal Magro, A. Meneghetti, G. Nardin, S. Savino. *Energy Conversion and Management* (2015), Vol. 104, pag.78–89".

Integrated configuration of the PCM-based device. In Section 3.7 the PCM-based device is fully integrated with the steam-based waste heat recovery boiler; the resulting configuration is named "PCM-coupled steam generator". The aim of this technology is to further increase the efficiency of the energy recovery systems developed in Sections 3.4 and 3.6 by providing superheated steam with low thermal variability, but also with higher temperature to a steam turbine for power production. Such a waste heat recovery

boiler is obtained by introducing an auxiliary section between the PCM Section and the steam generation one, which provides the auxiliary heat needed to level the thermal content of off gas. The auxiliary heat is extracted from the PCM by a heat transfer fluid flowing across the inner tube of each PCM container. Different models to properly size and simulate the operations of the proposed energy recovery system have been developed and integrated. Results show how the size of the steam generator and the turbine can be reduced of about 41% with respect to traditional solutions, while increasing electric power production by 22% thanks to the reduced fluctuation in steam parameters at the turbine inlet, which leads to a greater overall efficiency. The content of Section 3.7 is part of the conference paper "Coupling waste heat extraction based on phase change material with steam generation: evidence from steel industry. F. Dal Magro, S. Savino, A. Meneghetti, G. Nardin. *Proceedings of the 11th Conference on Sustainable Development of Energy, Water and Environmental Systems*, Lisbon, September 2016".

Finally, Section 3.8 summarises the results obtained in the previous sections highlighting the most important findings and the topics that need further investigations.

Energy recovery from billet reheating furnace (Chapter 4). In the fourth chapter an existing waste heat recovery system of a steel billet preheating furnace is retrofitted by adding a PCM-based device using the eutectic alloys Al-12%Si (in mass %) as high temperature PCM. The analysis of the performance of the plant with the proposed modifications is done by means of a plant-level dynamic model developed in the *Modelica* language and simulated in the simulation environment *Dymola*. The chapter starts by describing the existing waste heat recovery system as well as the issues related to the variability of the thermal energy load. Afterwards, the components of PCM-based device, their layout and the integration with the existing system are described in Section 4.3. Then the methodology used to model the existing and proposed new layout of the waste heat recovery system is reported in Section 4.4 0, while the results of the simulations and the advantage of the proposed modifications together with the economic assessment are presented in Section 4.5. The final remarks are discussed in Section 4.6.

Energy recovery from waste incineration (Chapter 5). The fifth chapter proposes the application of high temperature PCMs for increasing the energy efficiency of Waste-to-Energy plants. In particular, an innovative refractory brick technology based on PCMs

(named *"PCM-based refractory brick"*) is proposed for the protection of the radiant superheaters against high temperature corrosion and temperature fluctuations. The proposed technology enables the installation of radiant superheater in the hottest zone of the WtE plants, meaning that higher steam temperature and efficiency can be achieved. The proposed technology considers aluminium and its eutectic alloys as PCMs since they offer good thermal properties (i.e. high thermal conductivity, high latent heat of fusion and high melting temperature) amongst high temperature PCMs. Several commercial ceramics are instead considered as containment material since they offer high resistance to high temperature corrosion. The design challenge is given by the remarkable difference in the coefficient of thermal expansion between the selected PCMs and ceramics. In Section 5.1, the current state of the art of Waste-to-Energy plants is briefly explained and the main issues that limit their efficiency, which are the corrosion at high temperature and the fluctuation of temperature, are analysed. Then, the working principle of the PCM-based refractory brick and its installation within Waste-to-Energy plants is reported in Section 5.2. The thermomechanical model, which has been used to demonstrate the technological feasibility of the proposed technology, and the thermo-fluid dynamic model, which has been used to compare the performance of the traditional refractory brick technology with that of the proposed technology, are shown in Section 5.3. The results of the simulations are discussed in Section 5.4, while final remarks are given in Section 5.5. The content of Chapter 5 is part of the conference paper "Application of high temperature Phase Change Materials for improved efficiency in waste-to-energy plants. F. Dal Magro, A. Romagnoli, H. Xu, G. Nardin. *Proceedings of the 6th International Symposium on Energy from Biomass and Waste*, Venice, November 2016".

Chapter 2

OVERVIEW ON HIGH TEMPERATURE PHASE CHANGE MATERIALS

2.1 Introduction

Thermal energy storage (TES) systems have the potential of increasing the effective use of thermal energy equipment and of facilitating large-scale switching, thus they are of great importance to many fields of energy engineering. Thermal energy storage systems are normally useful for correcting the mismatch between the supply and demand of energy. For instance, in industrial processes where great amount of waste heat could be reused by means of a waste heat recovery system, but the heat availability period differs from its usage period, not having a storage system means that the waste heat is unrecoverable. Thermal energy storage systems can help to reduce backup equipment required to secure power supply in hospitals, data centres, and all those places where a reliable supply is vital [27]; furthermore, thermal energy storage can be used to provide thermal comfort in many types of buildings with heavy heating and air conditioning needs and thereby achieve a reduction in electric rates [28].

The development of energy saving technologies is very actual issue of present day. Heat storage technologies, which can effectively store intermittent heat from sources such as solar heat and exhaust heat, are very important in the field of thermal energy conversion.

Recently, accelerated development has been taking place of advanced heat storage systems with high-heat storage capacity and high-thermal responsivity to overcome the poor performance of conventional sensible heat storage (SHS) systems using ceramics, bricks, and liquid molten salts. Under these circumstances, latent heat storage (LHS) technology has attracted considerable attention. Latent heat storage is based on the storage or release of latent heat when a phase change material (PCM) undergoes phase transition from solid to liquid or vice versa. According to [29], latent heat storage has three advantages:

1. High-heat storage capacity when compared to sensible heat storage;
2. Constant heat source at the phase change temperature during the phase transition;
3. Reversible phase-changing process allows for repeated use [30].

These advantages allow latent heat storage to be used as an advanced thermal energy storage system. There are many studies related to latent heat storage covering the fundamentals and application research of materials, heat transfer and system analysis. As underlined in [11], latent heat storage is one of the most efficient ways of storing thermal energy: unlike sensible heat storage, latent heat storage provides much higher storage density, with a smaller temperature difference between storing and releasing heat. Latent heat storage has been widely investigated for a variety of applications, such as space conditioning and domestic hot water to meet the need for a sustainable energy use in urban context (see [31] for a recent review). PCM-based peak load control in commercial buildings, in particular, can lead to peak load reduction ranging from 10% to 57%, significant overall cost savings and improved thermal comfort [32]. PCMs have been incorporated in heat spreaders for electronics cooling, in order to maintain the temperature of microprocessors within acceptable limits [33]. In solar water heating application, which strongly relies on efficient thermal storage, PCMs show great potential due to their high energy density [34]. PCM is a desirable component in solar thermal power plants based on steam cycles to provide heat for evaporation at nearly constant temperature [35]; the overall exergy efficiency can be increased up to 30% [36]. Industrial waste heat recovery at low temperature can also be enabled by adopting PCM-based technologies [37]. In the steel industry, in particular, the PCM engine system uses volume expansion

of a paraffin mixture during phase change to produce electricity from available heat below 230 °C [38].

Latent heat storage technologies for recovery of high-temperature waste heat have not been given great attention despite their large potential [12]. A main issue to be faced is the development of a proper encapsulation system for PCM [15].

2.2 Thermal energy storage technologies

The thermal energy storage (TES) technologies can be classified into six types [39]:

1. Utilization of sensible heat;
2. Utilization of latent heat;
3. Utilization of chemical reaction heat;
4. Thermoelectric conversion;
5. Utilization of different concentration;
6. Utilization of photochemistry reaction.

The first thermal energy storage technologies are the most widely used in thermal energy storage systems. In particular, the sensible heat storage is the most conventional technology and latent heat storage is the second most used. In Table 2.1 an overview on the six thermal energy storage technologies is reported; Table 2.1 reports the difficulty of use when the technology is commercially available or the technology readiness level when it is not commercially available.

Gil et al. [40] reported that several facts should be considered when deciding on the type and the design of any thermal storage system. In particular, the authors reported that a key issue in the design of a thermal energy storage system is its thermal capacity as well as the selection of the appropriate type, which depends on many cost-benefit considerations, technical criteria and environmental criteria. The cost of a thermal energy storage system mainly depends on the following items: the storage material itself, the heat exchanger for charging and discharging the system and the cost of the space and/or enclosure for the thermal energy storage system. According to [40], the most important technical requirements are:

- high energy density in the storage material (storage capacity);

- good heat transfer between heat transfer fluid (HTF) and storage medium (efficiency);
- mechanical and chemical stability of storage material (must support several charging/discharging cycles);
- compatibility between HTF, heat exchanger and/or storage medium (safety);
- complete reversibility of several charging/discharging cycles (lifetime);
- low thermal losses;
- ease of control.

while the most important design criteria from the technological point of view are:

- operation strategy;
- maximum load;
- nominal temperature and specific enthalpy drop in load;
- integration into the energy conversion plant (e.g. waste heat recovery plant).

Table 2.1 Overview on thermal energy storage technologies. Source: [16]

Heat storage technology	Note
Utilization of sensible heat (easiest to use)	Utilization of temperature difference of solid or liquid. As an example, heating a brick by blast furnace gas is well known.
Utilization of latent heat - PCM (quite easy to use)	The production of ice as cold storage at night-time for a reasonable cost of electric power is practical. The energy can be successfully stored during the melting of the solid. Paraffin, organic material and molten salts can be phase change materials (PCMs)
Utilization of chemical reaction heat (under development)	A) Utilization of reversible reaction: $Ca(OH)_2 \leftrightarrow CaO+H_2O$ Hydrogen storage alloys, composition and decomposition of methanol, etc. have carried out B) Irreversible reaction: direct heat storage by endothermic reactions such as: $C+H_2O \rightarrow CO + H_2$ $CaCO_3 \rightarrow CaO +CO_2$ are under development from co-production
Thermoelectric conversion (Under development)	Thermoelectric couple, BiTe, SiGe, Mg_2Si can be used
Utilization of different concentrations (difficult)	The concentration-dilution of sulfuric acid solution is one example
Utilization of photochemistry (most difficult)	The photochemistry of anthracene is promising

The following overview is mainly focused on latent heat storage with a transition from solid to liquid phase for reasons explained further on.

2.2.1 Sensible heat storage

Sensible heat storage involves heating a material, without causing a phase change in it. Thermal energy is accumulated because of increasing the temperature of the storage medium. The amount of energy stored depends on the specific heat capacity, the temperature change and the amount of material [27] and may be represented by the following expression:

$$Q = \int_{T_i}^{T_f} mc_p dT = m \cdot c_p \cdot (T_f - T_i) \tag{2.1}$$

where Q is the amount of stored heat, m is the mass of the storage medium, c_p is the specific heat capacity of the storage medium, assumed constant in this case, T_f and T_i are the final and initial temperature of the storage medium, respectively.

Sensible heat storage systems can be classified on the used storage material, which can be a liquid material (such as water, oil, molten salt, etc.) or a solid material (such as rocks and metals).

2.2.2 Latent heat storage

Latent heat storage involves heating a material until it experiences a phase change, which can be from solid to liquid or from liquid to gas. When the material reaches its phase change temperature it absorbs a large amount of heat to carry out the transformation, known as the latent heat of fusion or vaporization depending on the case.

The graph in Figure 2.1 further explains the storage mechanism. When a solid material is heated, its temperature begins to increase in direct proportion to the received energy until it reaches its melting temperature. Beyond this point, the energy delivered to the material ceases to raise the temperature and is used instead to perform the transition from solid to liquid (latent heat), meaning that the material stores isothermally the thermal energy received. Once the melting process is complete and the material is wholly in the liquid state, the temperature begins to increase again as it receives a heat input until it reaches the vaporization point where what occurred in the first phase change is repeated. The

heating process works the same way for cooling, which means that it is possible to extract the stored energy as latent heat at a constant temperature (see Figure 2.1).

As can be seen, it is impossible to exclusively store latent heat, as to reach the phase change point the material had to undergo a temperature increase which represents storage of sensible heat. The storage capacity of a latent heat storage system can be represented by the following expression [27]:

$$Q = \int_{T_i}^{T_m} mc_{p,s}dT + ma_m\Delta h_m + \int_{T_m}^{T_f} mc_{p,l}dT \tag{2.2}$$

$$Q = m\left[c_{p,s}(T_m - T_i) + a_m\Delta h_m + c_{p,l}(T_f - T_m)\right] \tag{2.3}$$

where m is the mass of the storage medium, $c_{p,s}$ and $c_{p,l}$ are the specific heat capacity of the solid and liquid phase, respectively, which are assumed to be constant; T_m is the melting point, a_m is the fraction of the material that has experienced a phase transformation and Δh_m is the latent heat.

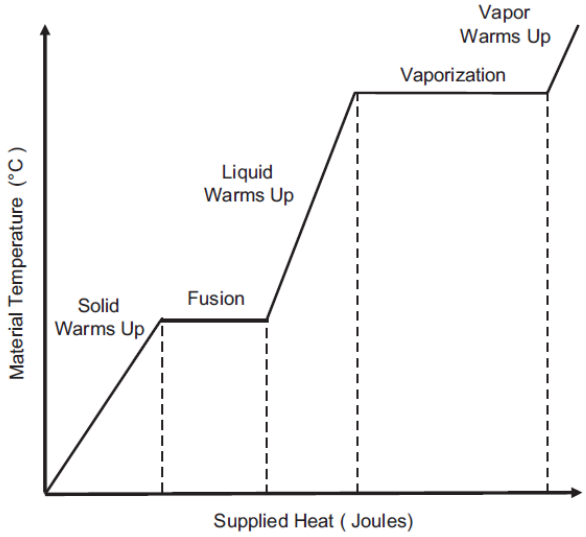

Figure 2.1 Temperature increase profile in respect of supplied heat Source: [41]

Figure 2.2 shows the difference of cumulative heat storage capacity of latent heat storage using solid–liquid phase transition and sensible heat storage. It can be observed that the heat storage capacity given by the latent heat of fusion is much greater than the heat

storage capacity given by the sensible heat, which is related to the specific heat capacity of the storage medium.

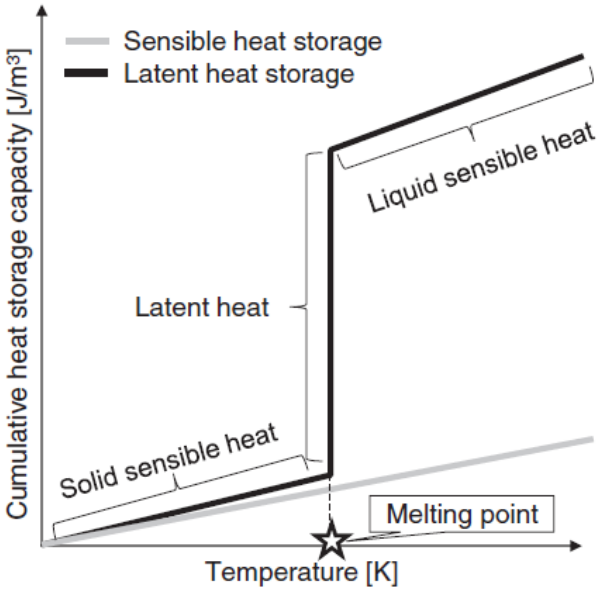

Figure 2.2 Difference of cumulative heat storage capacity of latent heat storage using solid–liquid phase transition and sensible heat storage. Source: [42]

Materials used for latent heat thermal energy storage are known as phase change materials (PCMs). The PCM may undergo solid–solid, solid–liquid and liquid–gas phase transformations.

2.2.2.1 Solid-solid latent heat storage

Generally, LHS systems use the latent heat between solid and liquid phases of the storage medium, whereby the PCM is required to be contained or encapsulated within a container to prevent the liquid from leaking. However, the capsules decrease the energy density of the system and increase the cost of production. To overcome these problems the use of the solid–solid phase change of certain materials has been proposed as an alternative. Relatively few solid–solid phase change materials (SSPCM) with suitable transition temperatures and latent heats for thermal storage applications have been identified.

Solid–solid phase change is quite simple and provides advantages such as easy handling and cost effectiveness because the lack of liquid material eliminates the risk of leakage and hence there is no need for encapsulation. There has been work focused on developing steel alloy based SSPCM for high temperature waste heat recovery [15].

Despite the advantages that SSPCM offer, their latent heat of transition is about one order of magnitude smaller than that of the solid–liquid PCM, which is a major drawback that should be addressed to achieve a greater introduction of this technology. SSPCM based on metal alloys are expected to be used in the future in stationary systems, as structural materials with a heat storage function, because they have a small latent heat per mass unit, but a rather large per volume unit. This means that they are suitable for energy storage on site but unsuitable for energy transport.

2.2.2.2 Liquid–gas latent heat storage

Transformations from liquid to gas have the highest latent heat of phase change. Nevertheless, the enormous changes in the volume of the storage material associated with the evaporation make the storage complex and highly impractical. Thus, the possible use for thermal energy storage systems is discarded, the reason why the gaseous state information of many materials is quite limited.

2.2.2.3 Solid-liquid latent heat storage

The change from solid to liquid phase is the transformation that has been most widely studied and used in latent heat storage applications. despite having a smaller latent heat compared with the liquid- gas phase change it does not present such a serious problem regarding volumetric expansion, which is generally in the order of an increase of 10% or less relative to the original volume [43].

During fusion, the heat is transferred to the PCM in the first instance by conduction and by natural convection afterwards; this is because the solid region moves away from the heat transfer surface and the liquid region thickness increases near the heat transfer surface. Since the liquid PCM thermal conductivity is often much lower than that of the solid PCM, the conductive heat transfer becomes almost negligible as the melting process continues due to the density gradient that exists in the liquid PCM. Contrary to the melt, solidification is dominated by conduction. During solidification natural convection exists only in the beginning of the process and as time passes the effect is negligible compared to the conduction effect [44].

Using solid–liquid transition PCMs has several technical complications; one of the biggest problems that hindered the widespread use of LHS is the unacceptably low

thermal conductivity of most PCMs. Besides that, there are other problems such as the complexity of the container, phase segregation and subcooling, which can be very severe and completely impede the extraction of the stored energy[11]. To avoid these problems, various techniques for improving the heat transfer in fusion LHS systems have been proposed, such as fins and extended surfaces, PCM embedded porous matrices, dispersion of highly conductive particles within the PCM [41].

The distinctive feature and main advantage of LHS systems is the isothermal operation at the phase change temperature of the material (i.e. it can deliver the stored energy at a nearly constant temperature). Another advantage offered by this type of storage is its compactness; due to that in most materials the latent heat of fusion is much greater than the specific heat. Given its characteristics, the phase change materials are chosen over sensible heat materials primarily for applications where volume and weight are restrictions and therefore a high-energy density is required or when there is a load whose power input must be at constant temperature.

Typically, PCMs are placed in long slender tubes tightly packed within a container. During a storage cycle in a solar application, for example, the heat collected by the unit is transported by a heat transfer fluid (HTF) through the narrow spaces between the tubes, melting the PCM. During the extraction cycle or heat recovery, the circulation of low temperature HTF collects the energy stored in the PCM and transports it to the thermal load.

Any LHS system must possess at least the three following basic components:

1. a substance or energy storage medium, which undergoes a solid to liquid phase change at the required temperature range where most of the added heat is stored as latent heat;
2. a container for containing the storage medium;
3. a heat exchange surface to transfer the energy from the heat source to the PCM and from the PCM to the load [28].

Nomura and Akiyama [45] classified the heat exchangers that can be used in the latent heat storage systems using PCM based on solid–liquid transformation as follows: 1) packed-bed, 2) shell and tube, 3)fluidized-bed and 4) direct-contact types; Figure 2.3 reports the classification of heat exchangers for latent heat storage reported in [45].

The packed-bed and shell and tube types are classified as indirect-passive heat exchangers, where heat exchange proceeds through a heat transfer wall between the PCM and the heat transfer fluid (HTF). A packed-bed heat exchanger using PCM capsules has advantages such as quick thermal response and high-heat storage density [46].

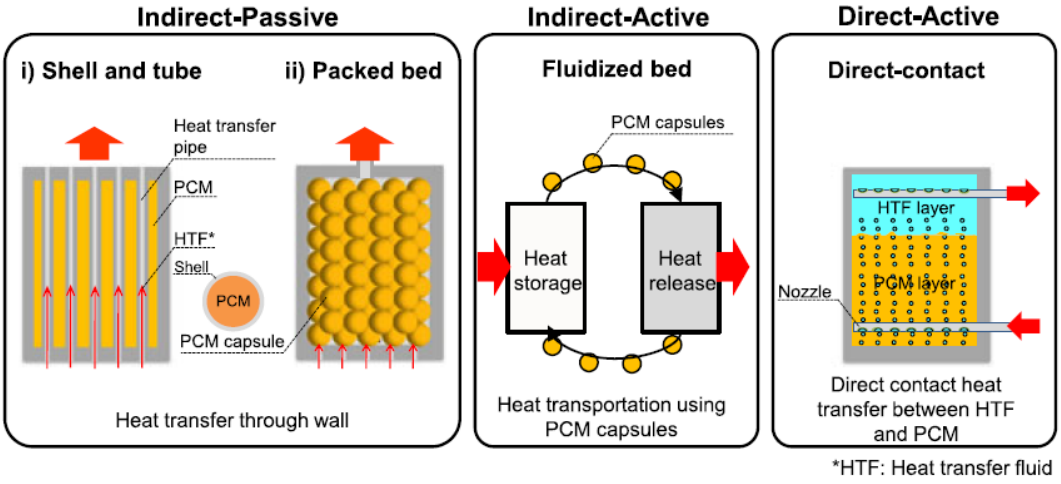

Figure 2.3 Classification of heat exchangers for latent heat storage. Source: [45]

The advantages of the shell and tube type are that high-pressure steam can be used as the HTF, by only considering the high pressure design of the heat transfer tubes [46]. Fluidized bed designs are classified as indirect-active heat exchangers where heat is exchanged through a heat transfer wall between the PCM and the HTF. Here, not only the HTF but also the PCM is circulated in the heat storage system. The fluidized-bed type can transport dense thermal energy from one process to another. Both liquid [47] and gases [48,49] have been proposed as HTF.

The other type is a direct-contact heat exchanger [30,50–53] where the heat exchange proceeds between the PCM and the HTF without any heat transfer wall. Here, the PCM is required to be insoluble in the heat transfer medium, and the density of the PCM is required to be high enough to ensure that a phase separation is possible. The direct-contact heat exchanger has a very simple light structure and a high-thermal storage density. This is because only inlet and outlet nozzles are required for the HTF, and a heat transfer pipe and capsule are not required. Therefore, this process can be employed not only to provide a stationary system, but also a heat transport system [52,54].

2.2.3 Thermochemical heat storage

There is a third method of thermal energy storage which consists in the use of reversible endothermic chemical reactions. The chemical heat is the heat necessary to dissociate or break joints in a chemical compound; almost all of this energy will be retrieved later when a synthesis reaction takes place. This type of storage offers very attractive advantages. Nevertheless, the development of reversible thermochemical reactions is at a very early stage [55].

2.3 Phase change materials (PCMs)

Phase change materials (PCM) are substances with a high latent heat of fusion that absorb and release thermal energy at a constant temperature during the process of melting and solidification, respectively. When a PCM solidifies, it releases a large amount of energy in the form of latent heat at a relatively constant temperature. Conversely, when such material melts, it absorbs a large amount of heat from the surrounding environment.

2.3.1 Required material properties and material selection

The basic requirements of a phase change material have been formulated in [11,27] and in [56–61]; the properties of the phase change material can be classified in four categories: thermal properties, physical properties, chemical properties and economic factors. The desirable properties that a PCM should possess are listed and classified in Table 2.2.

The selection of the PCM to be used in a LHS as the storage media is directed by the desirable properties listed above. When selecting a PCM for a particular application, the phase change temperature of the material must be equal or very similar to the operating temperature. The latent heat should be as high as possible, especially on a volumetric basis to minimize the size of the storage unit. In addition to that, a high specific heat is desired for providing additional sensible storage capacity.

A high thermal conductivity, in both states, solid and liquid, is desirable to improve the energy storage and extraction processes, and to obtain a more uniform temperature distribution within the heat storage unit. A high density, small volume changes between solid and liquid phases and low vapor pressure at the operating temperature are sought to maintain a small size storage unit and a simple design of container. The PCM must exhibit

congruent melting, otherwise there will be irreversible component segregation and the storage capacity will be gradually lost with work cycles.

An important aspect of the material is to have null or insignificant subcooling and a sufficient crystallization rate; this has been one of the most problematic aspects of PCM development. A subcooling of more than a few degrees will interfere with heat extraction and may completely impede it. It is important that the selected PCM is chemically stable to provide a reasonable lifetime of the storage unit, given that during operation it may undergo oxidative degradation, chemical decom position or incompatibility with the container materials. Also, for safety reasons, the PCM should not be toxic, flammable and explosive. Finally, it is important to consider the economic aspect; the PCM must be abundant and commercially available, and have a reasonable cost for the application that allows development to be feasible.

Table 2.2 Desirable properties of phase change materials

Category	Property
Thermal properties	▪ Suitable phase change temperature ▪ Large latent heat ▪ Large thermal conductivity in both solid and liquid phases ▪ Rapid heat transfer
Physical properties	▪ Large density ▪ Small volume change during phase change ▪ Low vapor pressure ▪ No subcooling ▪ Sufficient crystallization rate ▪ Favourable phase equilibrium
Chemical properties	▪ Long term chemical stability ▪ Compatibility with construction and container material ▪ Completely reversible freeze/melt cycle ▪ No chemical decomposition ▪ Non-toxic ▪ Non-flammable ▪ Non-explosive
Economic factors	▪ Abundant ▪ Available ▪ Cost effective

The phases of development and production of a new commercial latent heat storage technology (i.e. PCM and its container) are rather time-consuming and long-term

processes, which require the contribution of experts of different disciplines. Figure 2.4 presents the basic stages of works, which should be solved to bring to the market a new heat storage unit based on phase change materials.

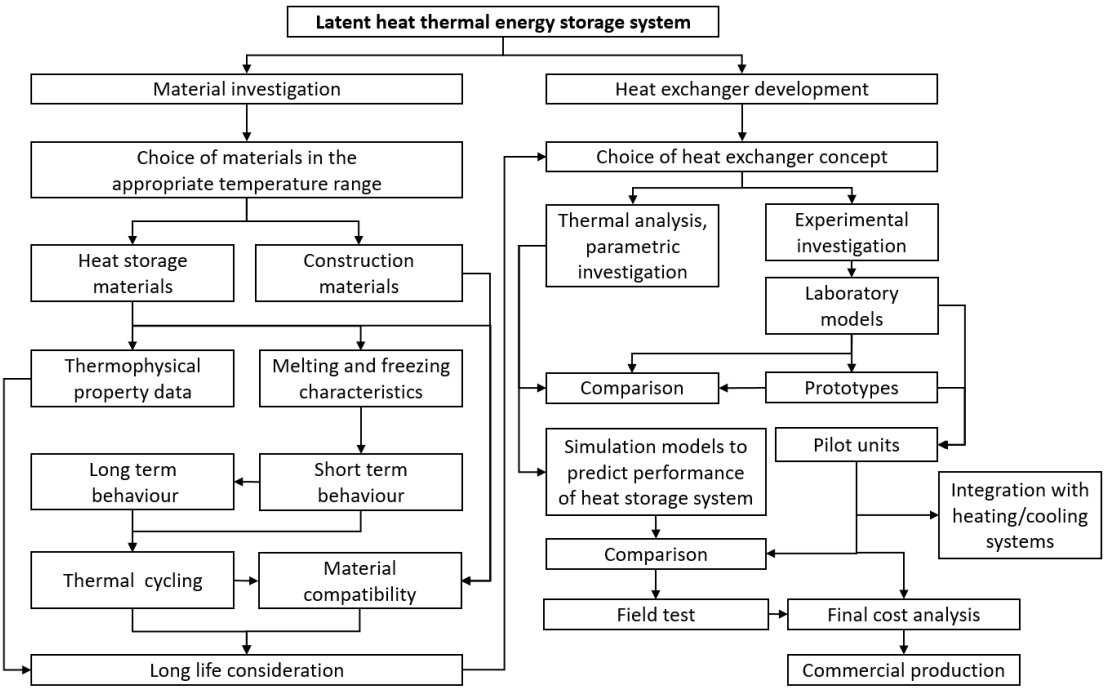

Figure 2.4 Flowchart for the development of a latent heat storage system. Source: [58]

2.3.2 Classification of the phase change materials

Many phase change materials are available for a wide range of operating temperatures. In 1983, Abhat presented a classification of the potential materials that can be used in latent heat thermal energy storage technologies [58], which is still used today by various researchers. Figure 2.5 reports the classification diagram of the PCMs, providing some example of the PCM candidates and their melting points. As it can be seen in the classification diagram of Figure 2.5, there are organic and inorganic materials which can be used as latent heat storage media. Organic materials include paraffins and non-paraffins such as fatty acids, while inorganic materials comprise salt hydrates, saline composites and metallic alloys. In general, inorganic compounds have near twice the energy storage capacity per volume unit than organic compounds and they possess much higher operating temperatures.

Despite the large amount of materials identified as suitable PCMs from a melting point and latent heat standpoint, it is impossible to find a PCM that satisfies all required criteria

for being a suitable storage medium; therefore engineers and developers must compensate poor physical properties with an appropriate system design; for example, metallic fins can be employed to increase the thermal conductivity of the PCM and subcooling can be suppressed by adding nucleating agents into the storage media.

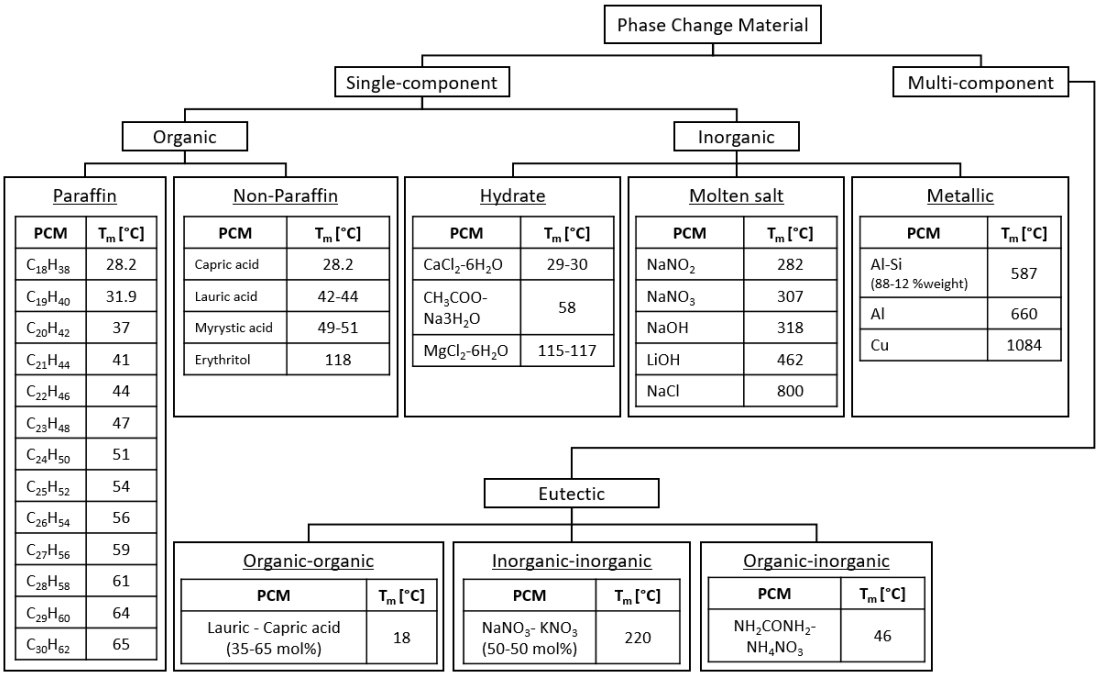

Figure 2.5 Classification of PCM. Source: [15]

2.3.3 High temperature phase change materials

In this section, the high temperature PCMs with melting temperatures above 300 °C, which for their melting point and storage capabilities have the potential for being used as storage media in industrial waste heat recovery systems, are reviewed. This high temperature group includes:

- Inorganic salts and salt eutectic compounds;
- Metals and metal alloys;

Materials in the range of 300÷550 °C are compatible with the currently available heat transfer technology in solar plants; however alternative heat transfer fluids such as supercritical CO_2 and other molten salts are under investigation by research teams worldwide; therefore, higher operation temperatures are going to be achievable and higher storage temperatures (above 550 °C) will be required [62]. From the literature it

appears that molten salts have been more widely researched for heat storage applications than molten metals and alloys [63]. Molten metals and eutectic alloys currently find applications as heat transfer fluids in nuclear power plants [64], and the performance of these materials as PCMs has also been evaluated for high temperature energy storage [32,65–69]. Molten metals show better heat transfer performance over molten salts due to their high thermal conductivity. In [66], zinc and tin have been evaluated as PCMs for high temperature applications (>450 °C) and it has been found that they have superior thermal performance compared to molten salts. In experimental study reported in [65], a zinc–tin alloy (70% Zn – 30% Sn, % in weight) has been investigated as PCM in a reflux heat transfer storage concept for steam generation at about 400°C. This alloy showed better thermal storage performance than molten salts, having superior thermal conductivity (50 W/mK) in liquid state, and the capability to deliver stable steam temperature. The thermo physical properties of a near eutectic aluminium-silicon alloy (88% Al – 12% Si, % in weight) has been studied in [69] for use as thermal energy storage. The compatibility of a ternary eutectic alloy of aluminium, magnesium and zinc (60%%Mg–%6Zn, % in weight) with encapsulating materials made from stainless steel AISI 304L and carbon steel C20 grades has been investigated [70]; the stainless steel AISI 304L was found to be suitable for handling the metallic alloy.

2.3.3.1 Inorganic salts and saline compounds

In the considered temperature range, above 300 °C, inorganic salts are of great interest. Table 2.3 reports the thermophysical properties of some inorganic salts that have been investigated by several researchers for their potential for being used as PCM in high temperature applications; thermophysical properties such as melting temperature, latent heat of fusion and density in solid state and in some cases in both, solid and liquid states are included. High heat of fusion of chlorides and fluorides, and the low cost of the former have encouraged further studies of salt compositions on their basis. Besides fluorides and chlorides, inorganic salt based on hydroxides, nitrates, carbonates are of considerable interest.

The use of inorganic salts as PCMs presents three main drawbacks:

- low-thermal conductivity: for a typical molten salt PCMs is under 1W/mK;

- high-volume expansion ratio during phase transition: it makes difficult to design the PCM container because of the thermal stress generated by the volume expansion;
- high level of chemical corrosion of metallic shell materials.

Current research efforts are focusing on molten salt with melting temperature above 500 °C such as chloride, sulphate and carbonate.

Table 2.3 Thermophysical properties of some inorganic salts with PCM potential. Source: [41]

Material	Melting temperature (°C)	Heat of fusion (kJ/kg)	Density (g/cm^3) Solid	Liquid
$NaNO_3$	306	182	2.26	1.908
KOH	380	149.7	2.044	1.47
SrI_2	527	57	4.55	4.085
LiBr	550	203	3.46	2.528
LiCl	610	441	2.07	1.502
CsBr	638	105	4.44	3.133
CsCl	645	121	3.7808	2.79
RbI	646	104	3.55	2.904
$SrBr_2$	650	41	4.175	3.7
LiH	688	2678	0.82	0.58

2.3.3.2 Metals and metal alloys

According to [15], the use of metals and metals alloys as high temperature PCMs has been underestimated by the researcher, probably because their elevated weight [41]. Zalba et al. [27] noted that the thermophysical properties of metallic PCMs have not been studied enough yet to have clear recommendations for the design of a commercial LHS unit and, so far, there is no comprehensive database of thermophysical properties which facilitates the selection of materials. In fact, practically all experiments for properties determination of possible PCMs have been limited only to temperature and latent heat of fusion measurements and except very few cases there are no measurements done to establish the temperature dependence of certain parameters such as thermal conductivity, heat capacity and density [71].

The use of metals and metal alloys as high-temperature PCMs presents many pros; in particular, when they are compared to inorganic salts, the main advantages of metals and metal alloys are:

- comparable heat storage capacity;
- larger latent heat per volume (i.e. more compact LHS systems);
- much higher thermal conductivity (e.g. thermal conductivity of Al is 400 times greater than that of $NaNO_3$);
- lower expansion ratio during phase transition (i.e. design of the LHS easier): for example, the volume expansion of Al is equal to 0.07 and it is much lower than that of inorganic salts.

Table 2.4 lists some of metal alloys with melting temperatures above 300°C proposed and studied by various researchers as possible high temperature PCMs.

Table 2.4 Thermophysical properties of some metal alloys with PCM potential. Source: [41]

Alloy	Composition (wt %)	Melting temperature (°C)	Heat of fusion (kJ/kg)	Density (kg/m^3)
Zn/Mg	53.7/46.3	340	185	4600
Zn/Al	96/4	381	138	6630
Al/Mg/Zn	59/33/6	443	310	2380
Mg/Cu/Zn	60/25/15	452	254	2800
Mg/Cu/Ca	52/25/23	453	184	2000
Al/Mg	65.35/34.65	497	285	2155
Al/Cu/Mg	60.8/33.2/6	506	365	3050
Al/Cu/Si/Mg	64.6/28/5.2/2.2	507	374	4400
Al/Cu/Mg/Zn	54/22/18/6	520	305	3140
Al/Cu/Si	68.5/26.5/5	525	364	2938
Al/Cu/Sb	64.3/34/1.7	545	331	4000
Al/Cu	66.92/33.08	548	372	3600
Al/Si/Mg	83.14/11.7/5.16	555	485	2500
Al/Si	87.76/12.24	557	498	2540
Al/Si/Sb	86.4/9.6/4.2	575	471	2700
Si/Al	86/12	576	560	2700
Cu/Zn/P	69/17/14	720	368	7000
Cu/Zn/Si	74/19/7	765	125	7170
Cu/Si/Mg	56/27/17	770	420	4150
Cu/Si	80/20	803	197	6600
Si/Mg/Ca	49/30/21	865	305	2250
Si/Mg	56/44	946	757	1900

In addition to the above mentioned advantages, metallic PCMs offer also high charging and discharging rates with minimal material modification [72]. The main drawback is that liquid metal alloys generally exhibit high-chemical corrosion of metallic shell materials. This is the most serious problem regarding the use of metallic PCMs. To facilitate their

use, ceramics must be applied over the structural materials used to build the heat storage units and shells of capsules.

2.3.3.3 Material comparison and selection

Khare et al. [73] demonstrated the use of a software for materials selection based on a multi- objective optimisation methodology to identify potential PCM media for high temperature thermal energy storage. In addition to this, an environmental audit function of the software has been used to evaluate the environmental credentials of PCMs. The methodology for selection of PCMs for high temperature energy storage used in [73] is based on the desirable properties of PCM reported in Table 2.2; from an initial screening, metals/alloys and composites were identified as promising family classes for a detailed study. Figure 2.6 has been produced in [73] by using a materials selection software package based on CES package; it shows a materials properties chart with energy density against melting point of numerous materials from the metals/alloys and composites families. Different metals and alloys show high energy density within the melting range. Metal alloys such as 88Al–12Si (melting point 576 °C) and 60Al–34Mg–6Zn (melting point 454°C) are for example at the top right of the graph, whereas tin and lead alloys towards the bottom left are less suitable. Pure metals such as Al and Zn have high melting points with high energy density as well as high volumetric heat of fusion.

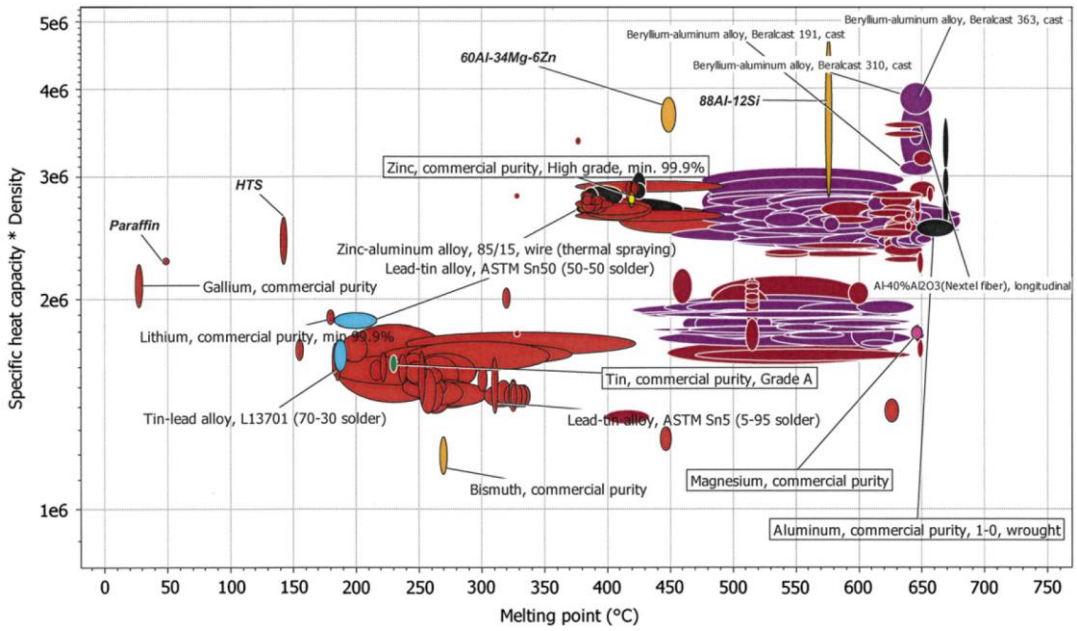

Figure 2.6 Energy density Vs melting point. Source: [73]

Figure 2.7 shows a comparison of the material property for volumetric heat of fusion against melting point. The basic four metals Al, Zn, Mg and Sn are shown in rectangles in relation to the position of their alloys and associated properties. The envelopes in these figures represent ranges of material properties recorded with various measurement precisions and variability in material properties, and rom different composition and test conditions. Elongation in the vertical direction reflects a range of values for specific heat capacity. The common heat storage materials such as paraffin and heat transfer salt (HTS-HiTech) are also included for comparison with the metals and alloys. Metals show high thermal conductivities (100 W/mK) over salts (<1 W/mK) as shown in Figure 2.8.

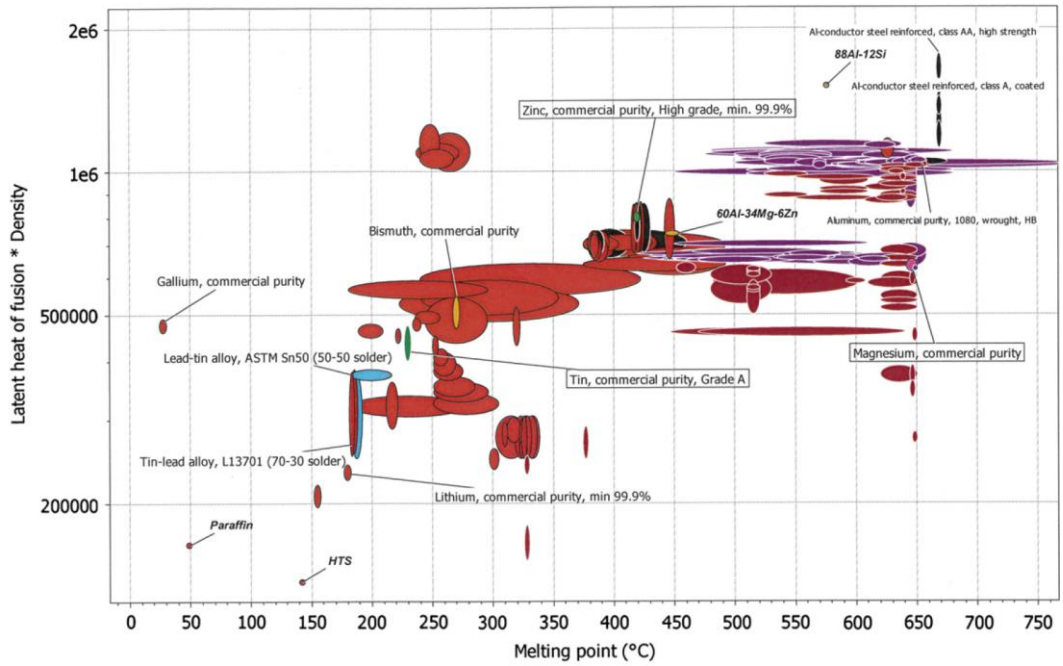

Figure 2.7 Volumetric heat of fusion Vs melting point. Source: [73]

The X-axis in Figure 2.9 shows a ranking of materials in terms of mass required to store a unit amount of energy. For a given temperature interval, the mass per unit of energy stored is the inverse of heat capacity with no other independent variables. On Y-axis, the cost is optimised by minimising the cost of material per unit energy stored. For a fixed temperature rise, the cost per unit of thermal energy stored is dependent on cost per unit of material and heat capacity of material with no other independent variables. The dotted line represents a trade-off curve. Materials which are closer to the curve, such as magnesium and aluminium metals and their alloys have the lowest cost per unit of thermal energy stored.

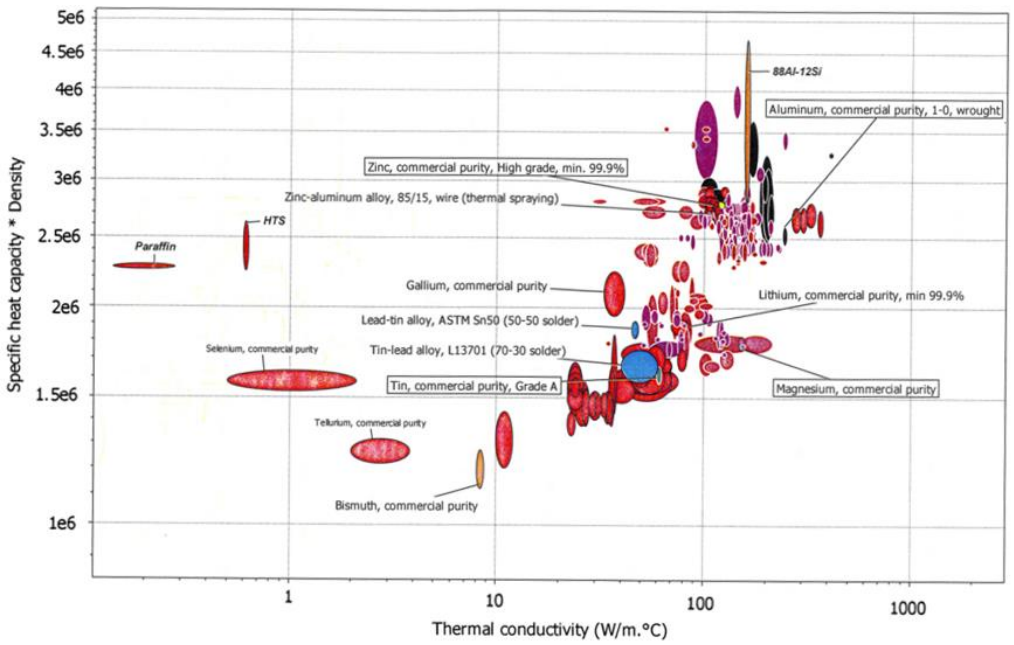

Figure 2.8 Energy density (J/m^3 °C) vs. thermal conductivity (W/m °C). Source: [73]

It should also be noted, however, that other considerations for the choice of a material as a PCM include engineering issues such as corrosion or reactivity of materials used, linear and volumetric expansion, balancing charging and discharging of heat to the working fluid such as steam or CO_2.

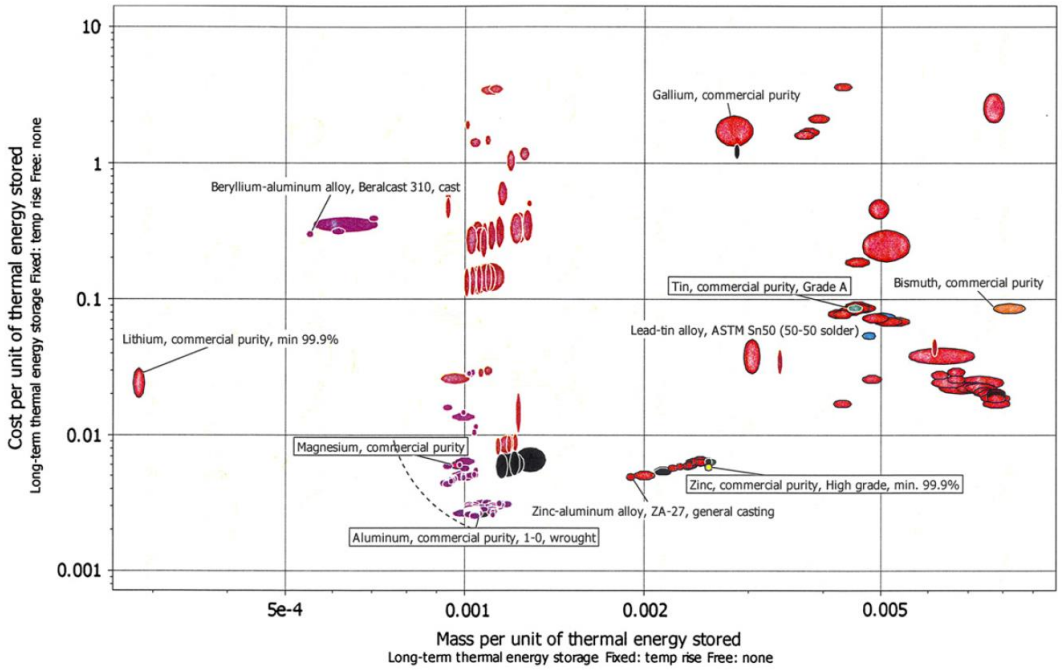

Figure 2.9 Cost per unit of energy stored Vs mass per unit of energy stored. Source: [73]

2.3.4 Encapsulation of phase change materials

Encapsulation is the process of covering a PCM with a suitable coating or shell material; the primary purpose of encapsulation is holding both the liquid and solid phase of the PCM and keeping it isolated from the surrounding. This ensures correct composition of the PCM that would have otherwise changed due to mixing of the PCM with the surrounding fluid. Other advantages of encapsulation involve reduction in reaction of PCM with the surrounding, flexibility in frequent phase change processes, an increase in heat transfer rate and enhancement in thermal and mechanical stability of the PCM. It can also improve the compatibility of hazardous PCMs that cannot be directly used or immersed in certain applications such as blood transport, food storage, building cooling/ heating, etc.

2.3.4.1 Container geometry

Based on the size, PCM encapsulation can be classified as follows:

- macro-encapsulation: size above 1 mm;
- micro-encapsulation: size 1÷1000 μm;
- nano-encapsulation: size 1÷1000 nm.

Macro-encapsulation is a common way of encapsulating the PCM for thermal energy storage applications. The container shape may be spherical, tubular, cylindrical or rectangular. Metallic encapsulant is preferred if high heat transfer is the criteria, otherwise, plastic containers are most widely used for low temperature applications. However, compatibility of both metallic and plastic encapsulants with the PCM needs to be checked.

PCMs are typically encapsulated in long thin heat pipes [74], cylindrical containers [75,76] or rectangular containers [77,78]. A survey of previously published papers dealing with LHS systems reveals that two geometries commonly employed as PCM containers are the rectangular and cylindrical containers. The most intensely analysed LHS system is the shell and tube system, accounting for more than 70%. This is probably due to the fact that most engineering systems employ cylindrical pipes and also heat loss from the shell and tube system is minimal. Figure 2.10 gives the schematics of the cylindrical and rectangular containers.

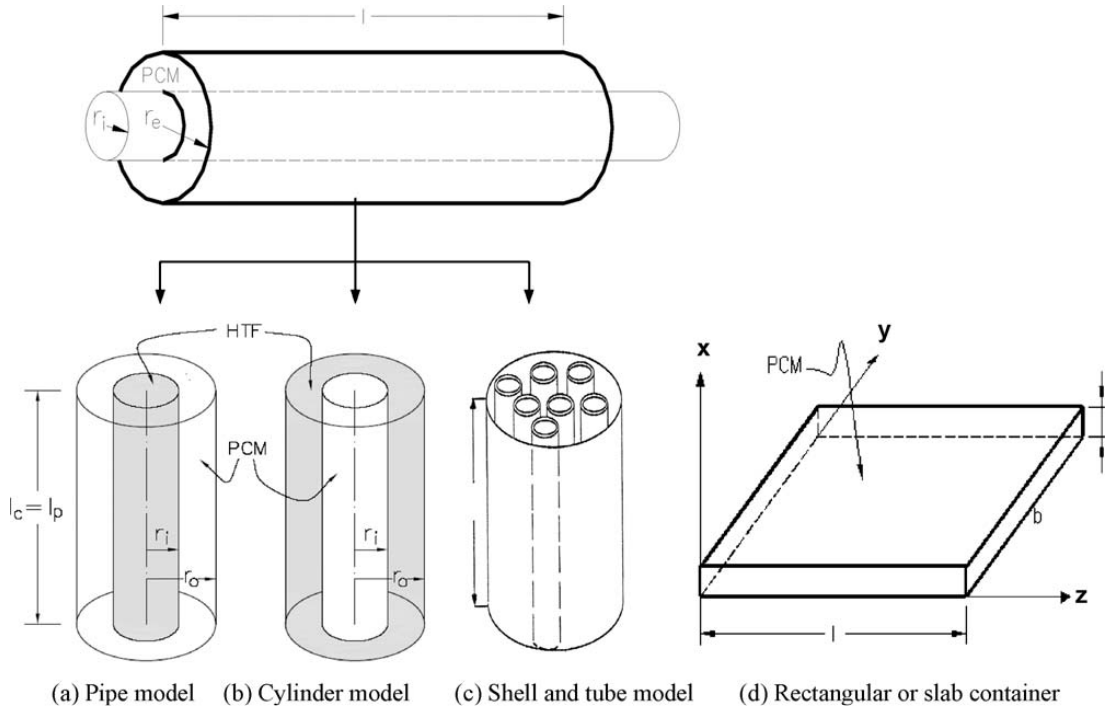

Figure 2.10 Classification of commonly used PCM containers in terms of the geometry and configuration. Source: [10]

Three modes of cylindrical PCM container configurations are distinguished. The first is where the PCM fills the shell and the heat transfer fluid flows through a single tube (Figure 2.10a) [10,75,79] designated the pipe model. In the second model the PCM fills the tube and the HTF flows parallel to the tube (Figure 2.10b) [80–82]. The third cylinder model is the shell and tube system [79,83] commonly used to improve heat transfer in PCMs.

Figure 2.11a shows the macro-encapsulation of metallic PCM (Al-Si_{12}) in stainless steel cylinders used in a high-temperature thermocline-type thermal energy storage designed by Zanganeh et al. [84] for the application in concentrated solar power plants.

The manufacturing of microencapsulated PCM is more complex than macro-encapsulated PCM as its size falls below 1 mm (see Figure 2.11b). However, microencapsulation result in a higher heat transfer rates as compared to that of macro-encapsulation [85,86]. This is attributed to a substantially higher surface area to volume ratio, ability to withstand the change in volume during phase change process and less chemical reactivity of PCM with the shell material.

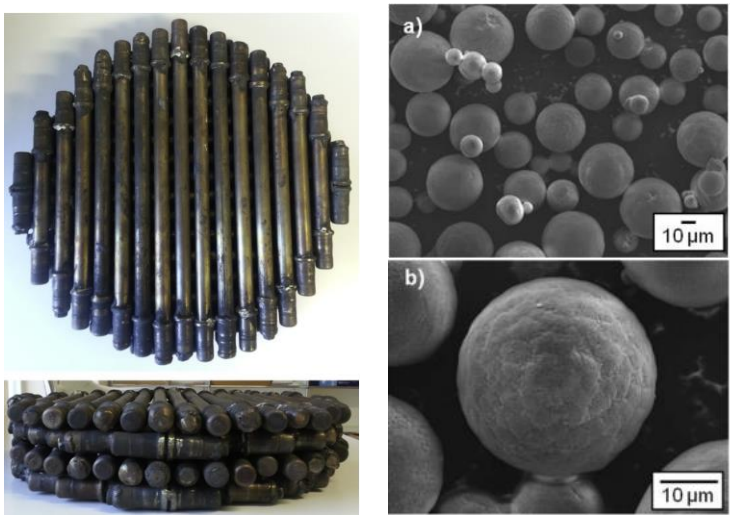

(a) (b)

Figure 2.11 Encapsulation of Al-Si alloys as PCM: a) Macro-encapsulation in steel cylinders [84]**; b) micro-encapsulation in alumina shell** [87]**.**

Higher heat transfer rate results in rapid melting and solidification of the micro-encapsulated PCM. For macro-capsules, the large capsule size results in temperature differential at the PCM core and boundary. The edge remains solid, whereas, core part may still remain in the liquid form, thus preventing the effective heat transfer [88]. Sari et al. [89] demonstrated that micro-encapsulated PCMs are thermally more reliable and chemically more stable than that of macro-encapsulated PCMs. The only problem with microencapsulated PCM is the possibility of increase in subcooling [90]. Due to subcooling, PCM retains its liquid phase even below its freezing point; the subcooling can be prevented by incorporating nucleating agents [91].

There are also studies on the nano-encapsulated PCM for thermal energy storage [92–94]. The advanced technological developments have made it possible to encapsulate the PCM at the nano-scale. Nano-capsules are structurally more stable as compared to macro and micro-capsules and there is a great potential in the use of nano-capsules for thermal energy storage applications. However, the research on nano-capsule is still at the laboratory level. More investigations are required to bring nano-capsules into the commercial applications. The macro and micro-capsules have been successfully commercialized in the market for the applications in LHS systems.

2.3.4.2 Encapsulation material

The encapsulation material is an important factor to consider when designing a latent heat storage system as the encapsulation material plays a key part in the efficient heat transfer from the heat transfer fluid (HTF) to the PCM. The encapsulation material must also be compatible with the PCM and the storage materials and be durable as it must provide a barrier to the outside environment as well as it must prevent liquid PCM leakage. Thus, it is important to ensure that the encapsulation (or containment) material:

- meet the requirements of strength, flexibility, corrosion resistance and thermal stability;
- act as a barrier to protect the PCM from harmful interaction with the environment;
- provide sufficient surface for heat transfer, when the PCM has a low thermal conductivity;
- provide structural stability and easy handling [60].

Concerning high temperature applications, Jacob and Bruno [95] reported that the majority of high-temperature macro-encapsulated PCMs are fabricated using a steel-based metallic shell.

Nevertheless, serious corrosion problem arises when metal alloys are used as high temperature PCMs. According to Sun et al. [70], stainless steels containing alloying elements of Cr, Ni and Ti (e.g. AISI 304L), may be considered suitable as a container material for Al–34%Mg–6%Zn when used as PCM. However, other authors [96,97] claimed that stainless steel is not suitable for the encapsulation of molten aluminium and its alloy since they easily react with the iron and nickel contained in the steel. In addition, the same authors reported that, among metals, only miscibility gap alloys [98,99] present a good resistance to molten aluminium corrosion.

To overcome the corrosion issue, the use of ceramics as a shell material for a LHS system using metallic PCMs has been proposed in [96,97]. In [96], the corrosion characteristics of four Al–Si alloys with Si contents between 0 and 25 wt% with engineering ceramics (namely Al_2O_3, AlN, Si_3N_4, SiC, and SiO_2) have been studied. The corrosion tests revealed that Al_2O_3, AlN and Si_3N_4 have high corrosion resistance to molten Al-Si alloys

and, thus, they are suitable materials for encapsulation of high temperature PCM based on Al-Si alloys.

Based on the results of [96], Fukahori et al. [97] proposed the use of alumina ceramic containers for macro-encapsulation of metallic PCMs (see Figure 2.12); the authors employed a cylindrical container composed by a cap and a cup and, in addition, they developed a sealing method to endure the thermal stress from volume expansion during the phase change. The resulting PCM capsule have shown excellent corrosive resistance and cycling performance.

It is worth remarking that the use of ceramics in industrial application may be limited by their brittleness and high cost, and alternative solution needs to be investigated. A suitable alternative could be using steel as container material and coating its surfaces in contact with the metallic PCM with a thin film of Al_2O_3, which can be obtained by means of an aluminizing and oxidation treatment [100]; however, such a solution has not been studied yet for the application of PCM encapsulation and needs to be studied experimentally.

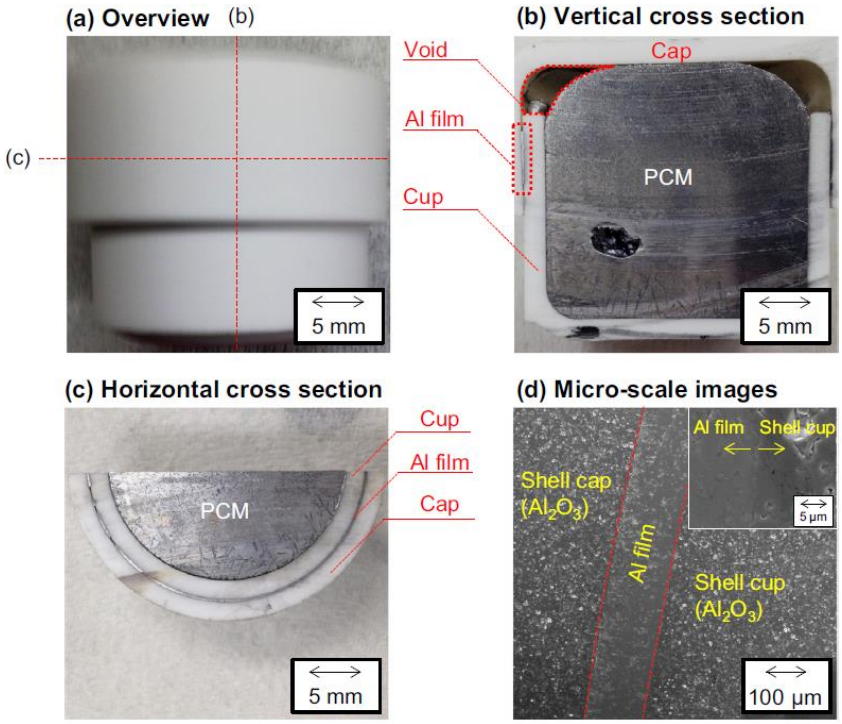

Figure 2.12 Macro-encapsulation of metallic PCM (Al–25 wt%Si) based on alumina ceramic; a) overall view, b) vertical cross section, c) horizontal cross section, and d) micro-scale images. Source: [75]

2.4 Conclusions

In this chapter, information available in the literature about thermal energy storage systems have been reviewed with a special focus on high temperature latent heat storage systems based on solid-liquid phase change materials. A general overview on the required properties of the phase change material as well as the classification of the phase change materials have been reported. Materials with potential to be high temperature PCMs have been considered and compared. The use of metals and metal alloys has been found of particular interest for waste heat recovery application. In particular, pure aluminium and its eutectic alloys, such as Al–12%Si and Al–34%Mg–6%Zn have been identified to have superior properties among high temperature PCMs. Finally, considerations on the geometry and the materials to be employed for the encapsulation of high temperature PCMs have been reported.

Chapter 3

ENERGY RECOVERY FROM ELECTRIC ARC FURNACE

3.1 Introduction

In 2012, the steel industry consumed about 5 % of all primary energy produced worldwide contributing to 7 % of all global CO2 emissions due to a high share of coal in the industry fuel mix [16]. World steel production increased from 28 million tons in 1950 to nearly 1.6 billion tons in 2015 [17]. Although recently significant improvements have been achieved, this sector has the potential to further reduce of 20% both energy consumption and greenhouse gas emission.

Since both current and future energy-related scenarios (growth of energy demand, production costs and pollution) claim for more rational use of energy in order to foster sustainable development, waste heat recovery in steel industry represents one of the greatest opportunity to reduce the consumption of primary energy (i.e. reduction of CO_2 emissions) while increasing the sustainability of the steelmaking process [18–21].

One of the most important and challenging source of waste heat in the steel industry is the waste gas (usually called off gas) emitted by the Electric Arc Furnace (EAF)

steelmaking process, which accounts for the 28% of the worldwide steel production [22]. The thermal energy wasted through these off gases varies from 15% to 35% of the total energy provided to the EAF steelmaking process [23].

The most common heat recovery system from EAF waste gas involves pre-heating of metal scrap; however, its diffusion is mainly limited by problems related to dioxins formation [101]. In the last years, new approaches of heat recovery based on steam production (e.g. in [102,103]) have been developed to overcome the environmental issues caused by scrap pre-heating. The efficiency of heat recovery by steam production is limited, however, by the high variability of temperature and flow rate of the waste gas [15,104]. During the steelmaking process, the waste gas temperature at settling chamber inlet generally shows a fluctuation within a wide range (e.g. from 100°C to 1000°C in tens of minutes).

These operative conditions make difficult to size a direct contact heat exchanger, even by taking into account oversizing and appropriate control systems. In addition to the high variability of temperatures, the high concentration of dust makes the adoption of current energy recovery solutions quite difficult, both from the technological and the economical perspective.

In this chapter, the problem of temperature fluctuations in energy recovery from the electric arc furnace is addressed. In particular, a series of systems exploiting aluminium and its alloys as high temperature phase change materials (PCMs) are developed in order to reduce the temperature fluctuation of the off-gas and increase the overall efficiency of the energy recovery system.

The chapter starts by evaluating the energy balance and the energy recovery potential from the EAF steelmaking process in Section 3.2. Then, the state of the art of the waste heat recovery system from electric arc furnace is reviewed in Section 3.3; advantages and disadvantages of each energy recovery technology are highlighted.

The development of the PCM-based device starts in Section 3.4, where the simplest configuration of the proposed technology is developed and analysed for a EAF process operating with discontinuous scrap charging. Since this first configuration of the PCM-

based device operates in a passive way (i.e. no control systems are employed) and its main feature is to smooth the temperature fluctuation of the off gas, it is named "*Passive PCM-based device for temperature smoothing*". In this configuration, pure aluminium is employed as high temperature PCM; its performances are analysed and optimized by means of computational thermo-fluid dynamic simulations. In addition to the development of the PCM-based device, a new configuration of the steam-based waste heat boiler equipped with cyclones is proposed to overcome also the problem of high concentration of dust in the off-gas. The high recovery efficiencies, the low investment and operation costs and non-invasive plant modifications induced by the smoothing system, make the proposed PCM-based recovery system a feasible solution to reduce energy supply costs and emissions in the steel industry. In particular, it is estimated that the adoption of the proposed system has a potential energy saving of more than 1,065 GWh_e/year for a percentage equal to 12.9%. This in turn is equal to 0.34% of the whole Italian electricity consumption, with related benefits on national GHG emissions targets.

Section 3.5 develops an analytical and numerical approach to evaluate thermal stress in the cylindrical PCM container used in the PCM-based device of Section 3.4. Thermal analysis shows that temperature distribution in the PCM system can be considered as uniform at any time instant according to the lumped capacitance method; the thermal behaviour of PCM system is thus simulated as a sequence of steady state analyses. Mechanical analysis adopts an axialsymmetric plane analytical model to compare elastic thermal stress distribution for different stainless steels and to identify AISI 316 as the most suitable material for the PCM container. A simple two-bars model and a stress index are also used to allow a physical understanding and a satisfactory interpretation of the PCM system response. Mechanical analysis shows that thermal stresses exceed the yield point of both stainless steels used in the container. A finite element elastic-plastic model is then developed to estimate the extension of the plastic zone. Finally, an alternative geometry based on concentric pipes is designed to keep the maximum stresses in the PCM container below the yielding point. A sensitivity analysis shows that the most relevant design parameters of the alternative geometry are the diameter of inner pipe and thickness of the external pipe.

In Section 3.6, the PCM-based device developed in Section 3.4 is extended to a EAF process with continuous charge and scrap preheating. In addition to this, a heat transfer fluid flowing through PCM containers is introduced and selected by means of an ad hoc code based on an analytical thermal model. The developed code identifies carbon dioxide as the best heat transfer fluid among the considered gases. The introduction of the heat transfer fluid allows the active control of the PCM temperature; because of this feature, the improved configuration is named "*Active PCM-based device for temperature smoothing*". Besides the temperature control, the introduction of the heat transfer fluid enables the adoption of smaller pipe diameters, which in turn allows the active PCM-based device to be more compact and efficient than the passive PCM-based device. As in Section 3.4, the performances of the improved device are analysed and optimized by means of computational thermo-fluid dynamic simulations; a comparison with the passive device is also carried out. The simulations show that maximum off-gas temperature is lowered and the resulting maximum thermal power is reduced by 25.4% with respect to a traditional plant with no smoothing device. Furthermore, the minimum load factor of the steam turbine can be enhanced from 23% in the traditional plant to 65% for the proposed system during the whole Tap-to-Tap cycle. The resulting turbine utilization factor, which affects electrical energy revenues, is increased from 60% to 82%.

In Section 3.7 the PCM-based device is fully integrated with the steam-based waste heat recovery boiler; the resulting technology is named "*PCM-coupled steam generator*". The aim of this technology is to further increase the efficiency of the energy recovery systems developed in Sections 3.4 and 3.6 by providing superheated steam with low thermal variability, but also with higher temperature to a steam turbine for power production. Such a waste heat recovery boiler is obtained by introducing an auxiliary section between the PCM Section and the steam generation one, which provides the auxiliary heat needed to level the thermal content of off gas. The auxiliary heat is extracted from the PCM by a heat transfer fluid flowing across the inner tube of each PCM container. Different models to properly size and simulate the operations of the proposed energy recovery system have been developed and integrated. Results show how the size of the steam generator and the turbine can be reduced of about 41% with respect to traditional solutions, while increasing electric power production by 22% thanks to the reduced fluctuation in steam parameters at the turbine inlet, which leads to a greater overall efficiency.

Finally, Section 3.8 summarises the results obtained in the previous sections highlighting the most important findings and the topics that need further investigations.

3.2 Energy balance and energy recovery potential from the electric arc furnace

A first evaluation of the flue gas enthalpy content can be made by analysing the energy balance that characterizes the smelting process of the steel occurring in an electric arc furnace. In [23] the energy balance of 70 electric arc furnaces has been carried out; in Table 3.1 some of this energy balances are reported.

Table 3.1 Energy balance of several electric arc furnaces. Adapted from [23]

Furnace		Energy Input [kWh/t]					Energy Output [kWh/t]				
Number	Capacity [t]	Electric energy	Exothermic reaction	Gaseous fuel	Scrap preheat	Total	Steel	Slag	Off-gas	Cooling	Total
1	100	541	234	23		798	423	80	168	127	798
2	55	571	155			726	415	59	100	152	726
3	60	408	204	20	51	683	367	68	109	139	683
4	80	560	118			678	382	50	81	165	678
5	100	577	155			732	415	59	33	225	732
6	150	450	199			649	385	35	102	127	649
7		390	170	60	12	632	345	50	170	67	632
8	100	557	233	21		810	427	83	158	142	810
9	115	487	217			704	397	46	127	134	704
10	125	462	94	34	70	660	401	70	48	140	660
11	100	459	295			754	354	62	138	199	754
12	100	413	378			791	354	62	140	235	791
13	100	401	397			798	354	62	141	241	798
14	100	445	341			786	355	47	141	243	786
15	100	423	325	61		809	355	47	141	266	809
16	100	91	249	182	106	628	385	50	68	125	628
17	80	380	195	15		590	388	52	85	65	590
18	100	365	222	33		625	5	431	110	84	625
19	100	287	223	33		606	63	431	97	78	606
20	75	459	230	7		696	362	49	90	195	696
21	75	422	237			659	362	40	105	152	659
22	70	477	187			664	392	62	96	114	664
23	150	312	278	88		678	320	47	229	83	678
24	150	300	377	97		775	355	53	232	135	775
25	55	347	399	86		832	407	26	317	82	832
26		368	348	38		754	380	32	155	187	754
27		482	170	25		677	360	31	160	126	677
28	60	465	215	36		715	408	72	150	86	715
29	60	429	215	21	50	715	408	72	150	86	715
30		450	130	90		670	395	35	122	118	670

The total energy required by an electric arc furnace process typically ranges from 510 kWh/t to 880 kWh/t [23]; the minimum energy required to melt the scrap and to superheat the melt and basic slag to 1600°C is approximately 444 kWh/t [105]. Energy consists for 40%-65% of electrical energy, and for 22%-60% of thermal and chemical energy generated from oxidation reactions during refining. Only the 50%-70% of the output energy is represented by steel and slag enthalpies, while the remaining part is dissipated by the water cooling systems of the furnace (10%-20%) and by the off-gas (15-35%) [23]. This means that potentially a portion of about 25%-55% of the input energy could be exploited by energy recovery. Figure 3.1 reports a typical energy balance of an electric arc furnace producing special steels.

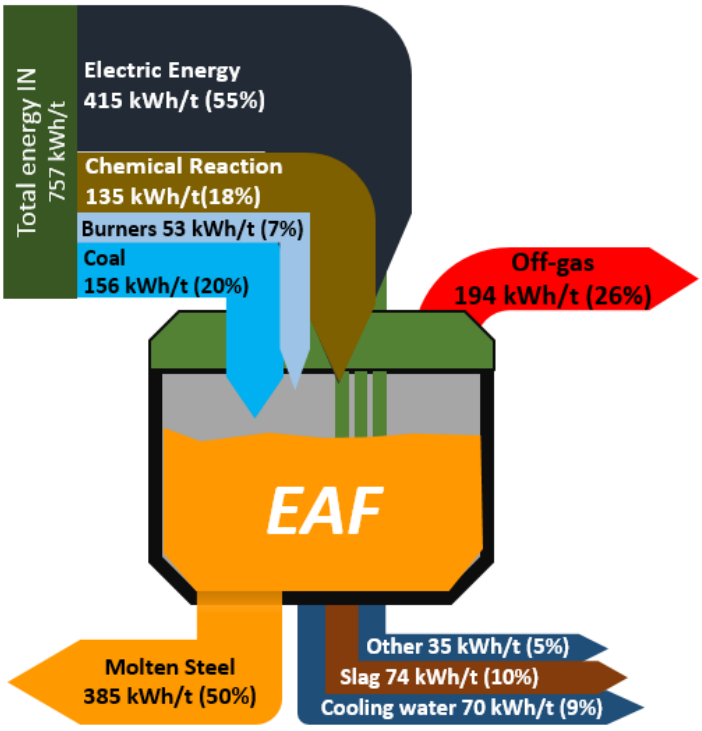

Figure 3.1 Energy balance of an electric arc furnace. Source: [106]

From Figure 3.1, it can be observed that the most of the energy input entering the electric arc furnace is high quality energy (i.e. chemical and electric energy), while the output energy exiting the furnace is low quality energy (i.e. thermal energy). Thus, the problem must be addressed through an analysis of the second law (i.e. exergy analysis) that allows evaluating the energy balance from a qualitative point of view and not just from a quantitative point of view.

Table 3.2 shows the comparison between the energy and exergy balance in EAF process with scrap preheating; it can be noted that the energy of the off-gas represents the 21% of the total energy output, while the exergy content of the off-gas represents the 15% of exergy output (due to the high off-gas temperature), which demonstrate the high potential of the energy recovery.

Table 3.2 Energy and exergy balances comparison in a EAF process. Adapted from: [107]

Input			Output		
Source	**Energy (%)**	**Exergy (%)**	**Product**	**Energy (%)**	**Exergy (%)**
Electrical energy	60	60	Liquid steel	57	41.9
Scrap	7	2.16	Off-gas	21	15.3
Oxy-fuel burner	3	3	Slag	10	7.6
Chemical reaction	30	30	Cooling	12	0.3
			Exergy destruction		30.06

For what concerns the efficiency of the EAF process, it can be defined as:

$$\eta_{EAF} = \frac{\Delta h_{steel}}{E_{input}} \tag{3.1}$$

where Δh_{steel} is the increase of enthalpy in the steel during the process and E_{input} is the energy absorbed by the process. The energy loss E_{loss} is instead expressed as:

$$E_{loss} = E_{input} - \Delta h_{steel} \tag{3.2}$$

The efficiency η_{EAF} provides an estimation of the melting process quality; the maximum efficiency is achieved when all the absorbed energy E_{input} contributes to increase the steel enthalpy Δh_{steel} (i.e. the energy loss E_{loss} is zero and the efficiency η_{EAF} is equal to 1). According to [23], the current efficiency η_{EAF} ranges from 40 to 75%.

One way to increase the efficiency of an EAF is to decrease the absorbed energy E_{input} by reintroducing into the process the energy recovered by means of a bespoke energy recovery system. To quantify the amount of useful recoverable energy from the off-gas of an EAF, the technological and energy limits should be considered. In the following paragraphs, an estimation of the recoverable energy from the EAF off-gas is carried out.

A total input energy entering the EAF process per tonne of produced steel of 750 kWh/t is considered. As described in the previous paragraphs, only 45÷60% of the total energy supplied is absorbed by the fusion of the steel. Fruehan et al. [105] reported that the minimum theoretical enthalpy of a tonne of steel at the tapping temperature of 1600°C is equal to 361 kWh/t. The rest of the energy is dissipated through the slag, the cooling water and the off-gas.

For what concerns the slag, it is not considered in the following thermodynamic considerations since its contribution is minimal. It should also be noted that a part of the energy of the flow is inevitably lost. In fact, it is assumed that the off-gas temperature at the outlet of the energy recovery system cannot be lower than 200°C in order to avoid acid condensation at the chimney and to ensure the integrity of the filters; the enthalpy of the flue gas referred to 200°C is of about 110 kWh/t.

Table 3.3 Assumptions for the estimation of the recoverable energy from the EAF off-gas

	Energy (kWh/t)	**Share (%)**
Total energy to the EAF process	750	100
Minimum steel enthalpy (at 1600 °C)	361	48
Off-gas enthalpy exiting the energy recovery (at 200 °C)	110	15
Off-gas enthalpy + Cooling water	279	37

Table 3.3 summarises the assumptions made for the estimation of the recoverable energy from the EAF off-gas; it can be noted that the maximum recoverable energy (i.e. off-gas enthalpy and cooling water) account for the 37% of the total energy. Figure 3.2 reports the distribution of the energy exiting the EAF; it can be observed that the theoretical limit is given by the minimum steel enthalpy, while the technical limit is due to the limit on the off-gas temperature exiting the energy recovery system (i.e. 200°C). The field of intervention is then identified by the remaining energy, which is represented by the off-gas enthalpy (at temperatures higher than 200°C) and the cooling water.

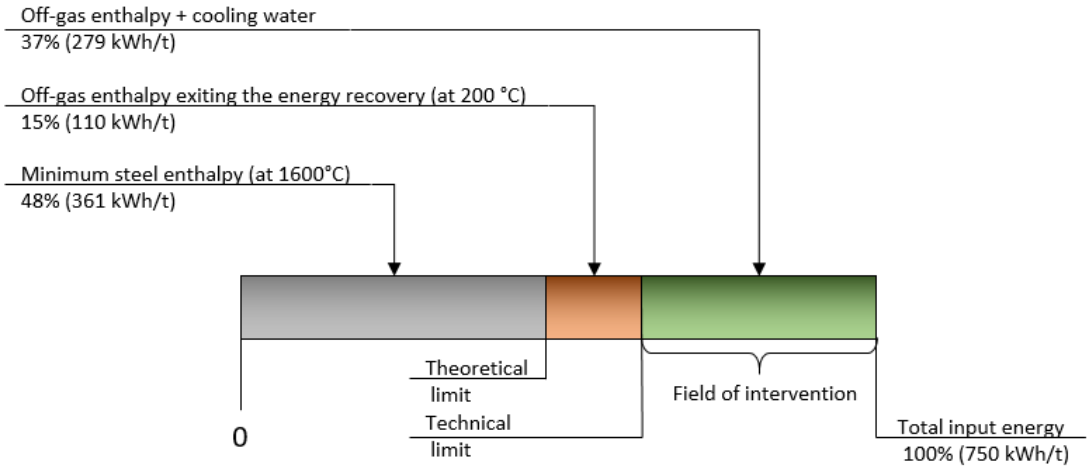

Figure 3.2 Distribution of the energy exiting the EAF: field of intervention, theoretical and technical limits of waste heat recovery

A real energy recovery system can recover only a portion of the maximum recoverable energy (i.e. field of intervention). The analyses carried out in the sections 3.4 and 3.6, which are based on real data plant, show that energy recovery systems based on phase change materials can achieve a power production higher than 50 kWh/t. Nevertheless, current energy recovery systems achieve lower performance (i.e. power production lower than 45 kWh/t).

Figure 3.3 represents the recoverable electric energy with current energy recovery technologies; it can be observed that the recoverable electric energy represents the 6% of the total energy used in the EAF process.

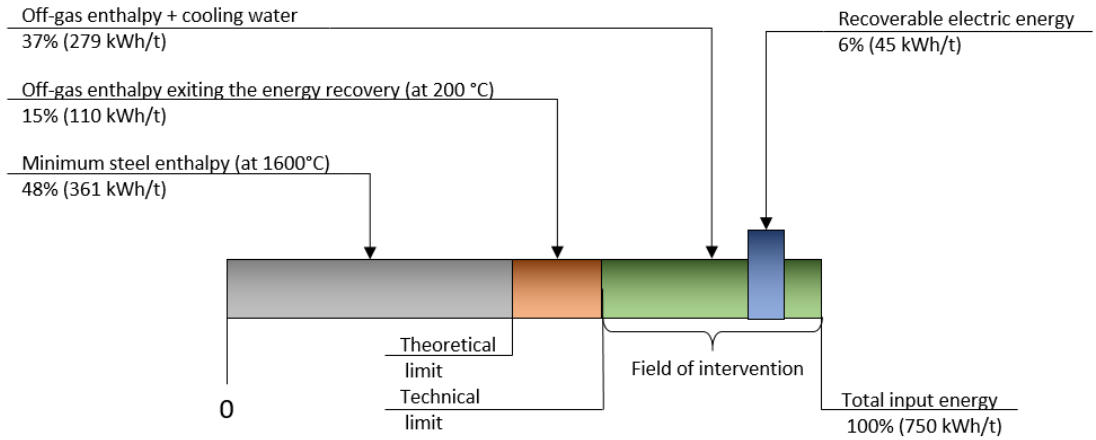

Figure 3.3 Recoverable electric energy with current energy recovery technologies

3.3 State of the art of waste heat recovery from EAF

Current available technologies for energy recovery from off gas of the EAF steelmaking process can be classified depending on the final use of recovered heat (see Table 3.4). In direct recovery, off-gas thermal energy is recuperated without the introduction of a heat transfer fluid (HTF) and directly used to preheat the scrap before its charging into the furnace. As shown in Table 3.4, related technologies can be further classified into two groups based on the type of scrap charging, which can be continuous or discontinuous. Direct recovery in discontinuous charging is mainly carried out by means of two technologies: shaft furnace and twin-shell. In spite of significant advantages [108], such as the reduction of the tap-to-tap (TTT) cycle time, the decrease of power requirements, and the reduction of CO2 emissions [109], these techniques present problems that have hindered their effective development and use. Most difficulties concern plant complexity, as well as surface oxidation of the charge, its partial melting, and high emission factors for dioxins [101].

Table 3.4 Current technologies for energy recovery from EAF off-gas.

Energy Recovery	Charge	Technology	Reference
Direct (scrap preheating)	Discontinuous	Shaft furnaces	[110]
		Twin-Shell	[111]
	Continuous	Consteel	[112,113]
		Ecoarc	[114]
		EPC System	[115]
Indirect (using steam, molten salt or superheated water)	N/A	SMS Siemag AG	[116]
		iRecovery (Lv. 1)	[102]
		iRecovery (Lv.2)	[117,118]
		Simetal EAF Quantum	[119]
		Danieli CHR	[120]

In indirect recovery, off-gas thermal energy is carried out by a HTF, such as steam, molten salt or superheated water. Systems based on steam flowing through the cooling pipes of the off-gas ducts are SMS Siemag AG [116] and iRecovery Level 1 [102]; iRecovery Level 2 technology [118] adds a waste heat boiler located downstream the off-gas ducts. To the author knowledge, the only system using superheated water to feed an ORC turbine has been implemented by Danieli Spa in an Italian steel industry [120]. For what concerns the use of molten salt, a pilot project installed in a Simetal EAF Quantum employs molten

salts as heat transfer and storage media [119]. There are several applications where the recovered heat by the HTF can be used downstream, such as district heating, vacuum degasser, and power production [118]. However, as underlined in [104], due to off-gas variability, thermal energy storage (TES) is necessary to provide the downstream systems with a constant supply of thermal energy.

As highlighted in [121], the most modern installations in the EU steel industry are close to the limits of what current technologies can do, and the steel industry will struggle to achieve further energy efficiency improvement without the introduction of breakthrough technologies.

3.3.1 Direct recovery: scrap preheating

The preheating of scrap has become a technique commonly used in the last 30 years. Conventional scrap preheating involves the use of hot gases to heat scrap in the bucket prior to charging the scrap into the EAF. The source of the hot gases can be either off-gases from the off-gases from the EAF or gases produced by burning natural gas which will be discussed later.

The scrap can be preheated at both low temperature (around 300÷400°C using continuous charging systems) and high temperature (around 800÷1000 ° C using discontinuous charging systems). The main objective is the reduction of energy required for the steel melting. Thus, this technique contributes to the optimization of the EAF process by increasing its efficiency and productivity. The advantages associated with this technique are listed below:

- Reduced energy consumption during a Tap-to-Tap (TTT) cycle;
- Increased furnace productivity;
- Reduced electrodes consumption and breakage;
- Reduced consumption of the furnace refractories;
- Reduced moisture in the scrap (i.e. prevention of possible explosions in the furnace);
- Reduced oxygen consumption;
- Reduced greenhouse gases emission and dust concentration;
- Reduced furnace maintenance;
- Reduced process costs.

The main problem of the scrap preheating is related to scrap composition. In fact, the scrap may contain organic substances, such as oils and plastics, whose incomplete combustion leads to the formation of toxic substances, such as dioxins. Referring to dioxin concentration, continuous charging systems coupled with rapid off-gas cooling systems, such as quenching tower, seem to ensure compliance with the regulatory limits (usually 0.1 ng I-TEQ / Nm^3). However, in at least two plants using this technology higher values of dioxin concentration have been recorded. Furthermore, in a conventional preheating system (shaft furnace) a value of 9.2 ng I-TEQ / Nm^3 has been measured [101].

The use of fuel burners in addition to quenching towers can prevent the process of De Novo Synthesis (i.e. mechanism of dioxin formation in the temperature range of 250÷450°C), but it reduces the efficiency of the process because of the energy employed by the fuel burners.

3.3.1.1 Conventional technology: scrap preheating in the charging bucket

Conventional scrap preheating can be accomplished by delivering the hot furnace gases to the scrap charging bucket by piping the off-gases from the fourth hole in the EAF to a special hood over the charging bucket. A schematic of a typical conventional scrap preheating system is shown in Figure 3.4. Typically, the gases leave the EAF at about 1200°C, enter the bucket at 815°C, and leave at around 200°C. The amount of preheating depends on the heat transfer to the scrap which is a function of scrap size and time at temperature.

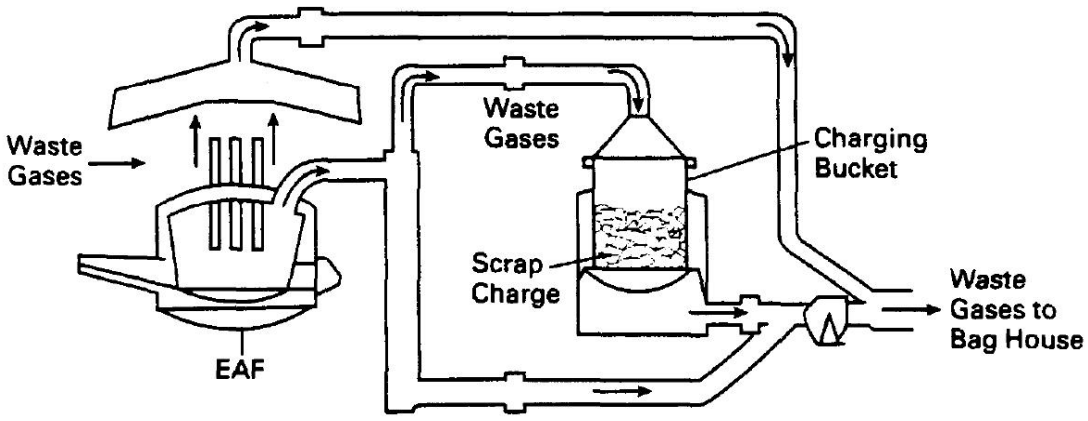

Figure 3.4 Schematic Diagram of Scrap Preheating in a Charging Bucket. Source: [110]

Usually, the scrap is preheated to a range of 315÷ 450°C. In some cases, higher temperatures have been reported. This amount of preheating usually reduces energy consumption by 40 to 60 kWh/t, electrode consumption by 0.3 to 0.36 kg/m, refractory consumption 0.9 to 1.4 kg/m, and tap-to-tap time by 5 to 8 minutes.

Some of the disadvantages to conventional scrap preheating include:

- Inconvenient to operate such as scrap sticking to bucket and short bucket life;
- Poor controllability of preheating due to cycling of the off-gas temperature and flowrate through various EAF operating phases;
- For tap-to-tap times less than 70 minutes, the logistics of conventional scrap preheating lead to minimal energy savings that cannot justify the capital expense of a preheating system.

3.3.1.2 Shaft technology

For what concerns shaft furnace technologies, two main arrangements can be considered: single shaft and double shaft. The single shaft furnace is a batch-type preheater. The system can be used with either DC or AC furnaces. The shaft furnace is situated on top of the EAF as shown in Figure 3.5a. The shaft is water cooled, charging about 1/3 of the scrap to the EAF. The balance of the furnace charge is added by scrap bucket through the furnace shaft, normally one or two additional bucket charges. In the shaft, scrap is preheated by low-velocity off-gases and then dropped into the EAF. It has been reported that the system can reduce electric consumption up to 18%, and increase production by 17 to 20%. With the system providing a more stable operation, flicker and harmonics are reduced. In addition, some of the furnace dust is trapped by the scrap and returned to the furnace thus reducing EAF dust generation and disposal.

The same advantages reported for the single shaft furnace are obtained with the double shaft, which consists of two EAF furnaces, each with a shaft and one common electrode mast and set of electrodes to serve both furnaces (see Figure 3.5b).

The dual furnace operation begins with charging scrap to furnace A and its shaft. During initial meltdown in furnace A, furnace B and its shaft are charged with scrap. When furnace A is in the refining mode, the hot off-gases from this furnace are directed to pass

through ductwork to heat the scrap in furnace B and in its shaft. When vessel A is ready to tap, the electrodes are moved to furnace B and the meltdown procedure begins in this furnace and the process is reversed.

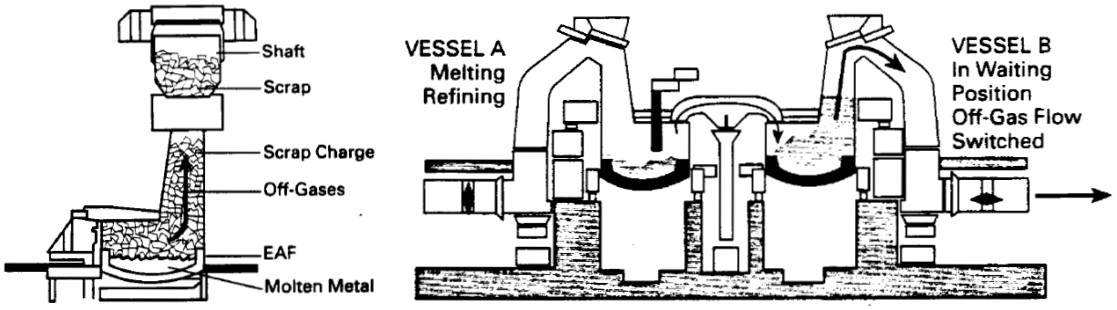

(a) (b)

Figure 3.5 (a) Single and (b) double shaft furnace system. Source: [110]

Tap-to-tap cycles have been reported to be as low as 40 minutes. In order to achieve the full benefits of the double shaft system, it is important to manage the material flow on time. Scrap management should be carefully planned since power-on times for the furnace are generally around 32 to 34 minutes. The idle furnace should be charged not later than 15 minutes after tapping to achieve the full benefits of scrap preheating. Compared to single shaft furnace, the productivity is further increased and the electric usage is lower. Similar to the double shaft technology, twin-shell technology includes two EAF vessels with a common arc and power supply system [111].

3.3.1.3 Consteel technology

Consteel is a patented continuous feeding, preheating, and melting steelmaking process developed by lntersteel Technology Inc. A schematic of the process is shown in Figure 3.6. In the process scrap is placed on a conveyor and passes through a seal into the preheating section.

Off-gases coming from the EAF flow through the preheater (countercurrent to the scrap charge direction) and into the ductwork leading to the bag house. After moving through the preheating section, the scrap is discharged onto a connecting conveyor car which enters the side of the furnace and drops the scrap into the molten steel bath, see cross section of furnace in Figure 3.6. Reportedly, scrap has been heated to 316°C by the off-gases. A continuous hot metal heal is always kept in the furnace to melt the incomings

crap. The arc primarily is used only to keep the bath molten. In this way, the furnace maintains a constant flat bath condition, which makes possible to continuously refine the bath while scrap is being melted.

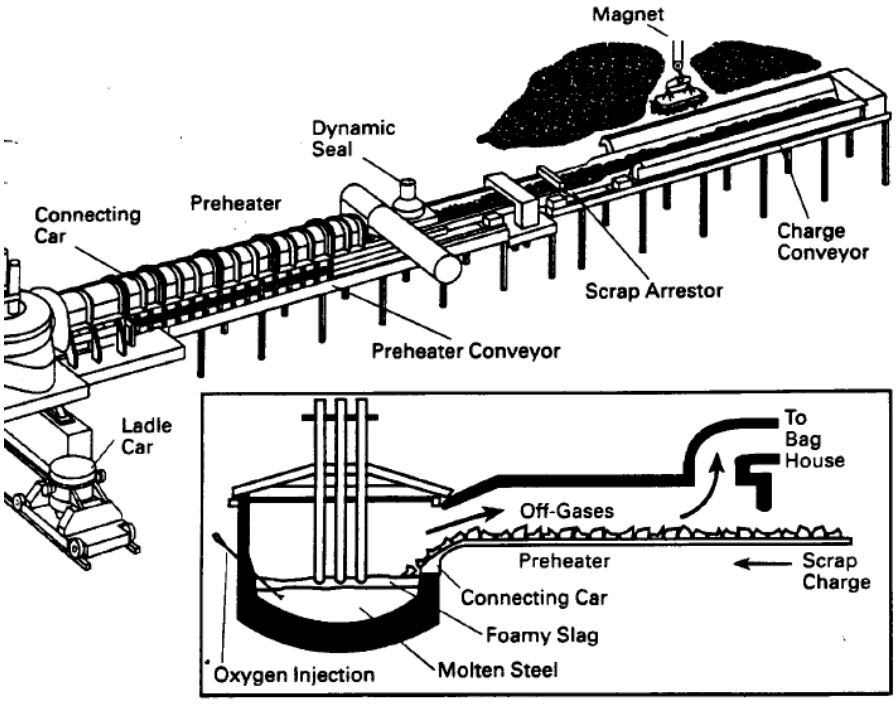

Figure 3.6 Consteel preheating system. Source: [110]

Advantages of the Consteel process are:

- Low electricity usage, about 360 kWh/t;
- Tap-to-tap times under 50 minutes;
- Low electrode consumption (about 1.5 kg/m);
- Reduced harmonic and flicker problems;
- A reduction in dust generation of about 30%;
- Reduced shop noise.

The evolution of the Consteel process (see Figure 3.18) consists of wider conveyors to increase the exchange surface, a different tunnel profile to improve the convective heat exchange, and a new tunnel section equipped with burners, to boost chemical energy input [113].

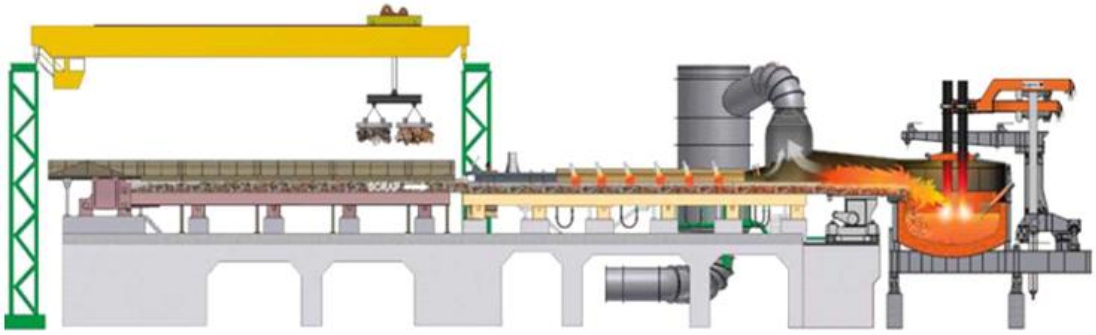

Figure 3.7 Consteel evolution preheating system. Source: [113]

3.3.1.4 BBC-Brusa technology

This Italian process consists of a rotary kiln inclined 12° to the horizontal and positioned such that the scrap exiting the kiln drops into the furnace through the roof of the EAF. The off-gases flow counter current to the scrap and reportedly can heat the scrap to 450°C. Benefits for the process include decreased energy, electrode, and refractory consumption. Also natural gas burners can be used to supplement the off-gases to heat the scrap to as high as 982°C. A scheme of the BBC-Brusa technology is shown in Figure 3.8.

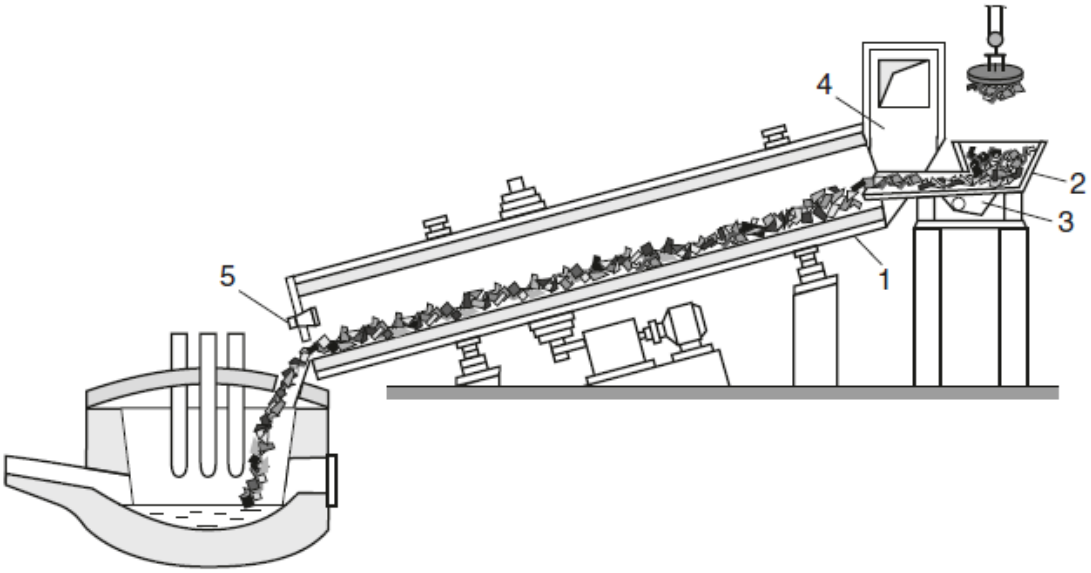

Figure 3.8 BBC Brusa technology. Source: [122]

Gas burners (5) are located at the lower end of the rotary furnace. According to [122], the scrap passes through the furnace for 6–10 min. During this time the scrap is heated up to medium mass temperature of about 1000 °C. This temperature was reached not quite due

to off-gas heat but mostly due to the burners which account approximately 73 % of all heat coming into the rotary furnace. Rotation of the furnace prevents welding of the scrap lumps despite their high temperature and assures that heat from the refractory lining is being used for scrap heating. This enhances the advantages of countercurrent system of gas and scrap motion which makes gases exit the furnace at low temperature. The thermal efficiency of the rotary furnace calculated for the total heat input reached approximately 45%. Performance of the BBC-Brusa unit equipped with transformer power of 7.2 MW for 3 years of service shows great potentialities and principle energy advantages of high-temperature scrap heating. With natural gas consumption of 30 m^3/t, electric energy consumption was cut by 220 kWh/t. Furnace productivity increased up to 100,000 ton per year which at that time was equal to the productivity of a furnace with the same capacity, but equipped with high-power transformer. Continuous charge of scrap assured very quiet arcing and low noise level (less than 80 Db). Durability of the refractory lining of the rotary furnace was 1500 heats. Despite the advantages attributed to the high-temperature scrap heating, such units had quite limited use and only for a short period of time.

This can be explained by the fact that for the modern high-productivity EAF the dimensions of a rotary furnace required call for really too big size and height of the buildings for EAF's shops. Besides, rotary furnaces can operate only using properly prepared fragmentized scrap. This narrows raw material supply base and increases cost. The units with rotary furnaces also have other significant drawbacks which prevent them from being used. Nevertheless, the impressive results obtained on BBC-Brusa units promoted a search for new options of high-temperature heating a scrap in combination with continuous charging it into the bath. This has resulted in development of modern shaft and conveyor EAFs.

3.3.1.5 COSS technology

The Continuous Optimized Shaft System, COSS, is a next-generation technology, developed by Fuchs Technology AG which combines the benefits of the Shaft systems (pre-heating at high temperatures) with those of Consteel process (continuous scrap charging). Scrap can be charged into the shaft without interrupting the power input. The furnace can operate with or without the shaft which is connected by means of a removable car. The scrap is loaded into the vat without interrupting the administration of energy.

The lower maintenance costs, less power-off time, the high energy content of the flat bath operations and higher preheat temperatures than the other two technologies (i.e. Shaft and Consteel technologies) ensure low conversion costs and high productivity [123].

3.3.1.6 EPC technology

EPC technology, which has been developed by the Company KR Tec GmbH (Germany), aims to avoid the of gas-dust emissions when charging scrap into the shaft [124]. The EPC technology consists of two main components, the preheating chamber with its telescopic feeder, and the charging deck where a hopper operates; the preheating chamber is installed beside the EAF upper shell and the preheated scrap is charged continuously by the telescopic feeder system into EAF for melting [115]. The operating principle of the EPC technology is following explained with the support of Figure 3.9.

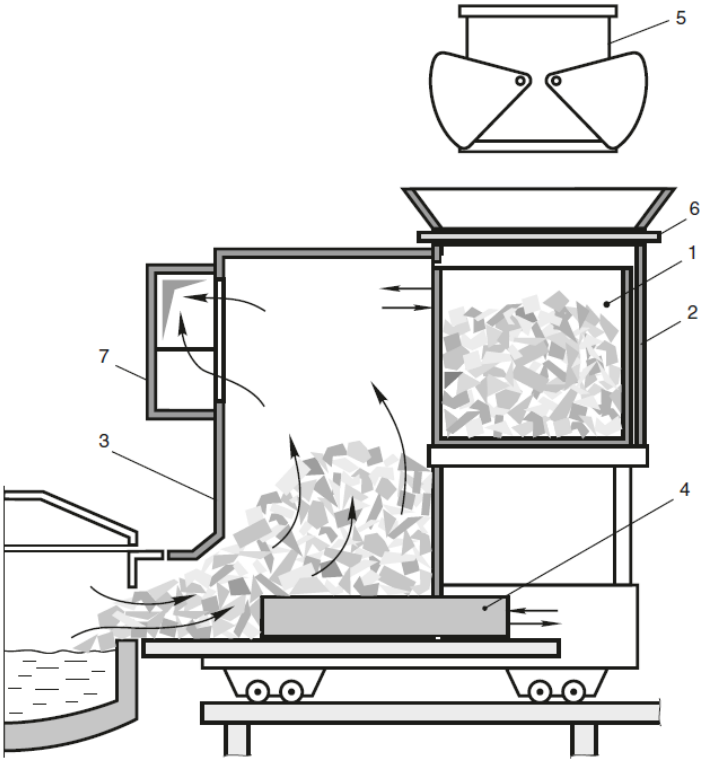

Figure 3.9 EPC Technology. Source: [122]

The main component of the EPC system is a movable hopper (1) with an opening bottom placed in a bunker (2) adjacent to the shaft (3). By means of hydraulic cylinders of the bunker the hopper can be moved into the shaft through an aperture in its sidewall. When

the hopper is placed in the bunker its front wall is closing the aperture. When the hopper is positioned in the shaft the aperture is closed with the hopper back wall. At this position the bottom of the hoper is opened and the scrap falls smoothly into the shaft. In the course of feeding of the scrap into the bath by means of a pusher (4) the scrap caves in inside the shaft and the hopper can be moved backward to the bunker. The hopper is charged there again with the help of a scrap basket (5). A slide gate (6) is opened for a while to charge the hopper only. Thus, during the heat the scrap can be charged into the shaft by separate batches without loss of airtight of the system. Therefore, gas-dust emissions from the shaft into the shop atmosphere are almost completely eliminated. Melting of the scrap starts when the scrap batch preheated in the shaft during the prior heat is feeding into the hot heel.

The system allows realizing different variations of furnaces operation. During the heat one or several of scrap batches can be charged into the shaft depend on a furnace capacity, shaft and hopper dimensions. This requires the certain number of hopper movements and charging of the hopper with baskets. Figure 3.9 shows a stage of the heat preceding the next charging of the scrap from the hopper into the shaft. Off-gases passing through the scrap layer heat it and are evacuated via a gas duct (7).

3.3.1.7 Ecoarc technology

In the Ecoarc technology, scrap is continuously fed into the preheating shaft and is in constant contact with the molten steel in the melting chamber; during the melting phase the furnace including the shaft is tilted backwards [114]. The off gas from Ecoarc includes a large volume of combustible ingredients, which minimizes the necessary amount of fuel for post combustion. The off gas volume itself is also minimized by the use of a semi-airtight furnace and off gas ducts. The following advantages are reported:

- Lower power consumption: 200 kWh/t at 40Nm^3/t oxygen
- Lower electrode consumption: 0.8-1.0 kg/t
- Lower cost for flexibility of scrap mixing
- Lower dioxin emission level
- Lower dust emission level
- Low flicker and harmonics

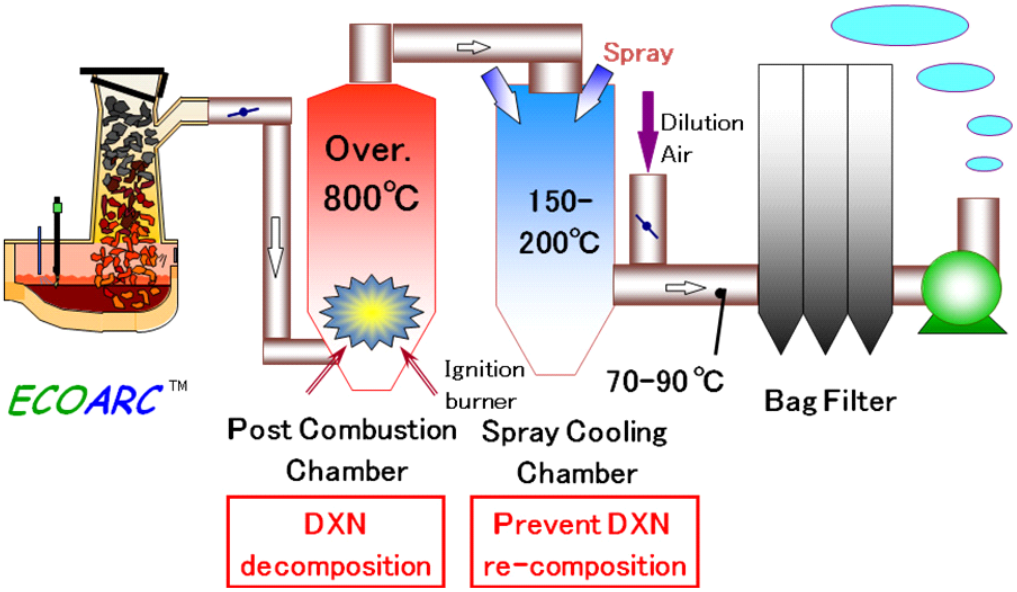

Figure 3.10 Ecorarc Technology. Source: [114]

3.3.2 Indirect recovery: waste heat utilization

In contrast to integrated iron and steel plants, electric steel plants have only a limited demand for steam (e.g. steam ejectors for VOD). Due to the low steam demand, electric steel plants often ask for a waste heat recovery system with power production. However, the installation of a power block (ORC or steam turbine) requires an additional investment, which has a significant influence on the return on invest of the system. In the following, the most important applications for waste heat utilization are discussed.

3.3.2.1 Hot water production for heating purpose

The most efficient way to use the recovered energy is to use the heat directly for heating purposes. Hot water for heating can be either supplied to external consumers, such as district heating networks, or can be used internally for heating purposes. The system should operate in a separate cycle, where the heat is provided via a plate heat exchanger. Since downstream consumers require constant heat supply, a storage tank should be used to equalize furnace fluctuations. The hot water coming from the plate heat exchanger is fed in the upper part of the tank, while the cold return water, coming from the district heat exchanger is fed in the bottom of the tank.

From the tank, hot water is fed continuously to another plate heat exchanger, where heat is provided to the district heating network. The system should be operated at a certain temperature, depending on the required water parameter of the downstream consumer. For normal district heating networks (e.g. 90°C) the existing water cooled duct can be used for hot water production.

3.3.2.2 Steam production

The recovered heat can also be used for generation of steam. Due to the cyclic fluctuating off-gas emissions from the steelmaking process, a storage system should be foreseen. Storage system can be from type of Ruth's steam accumulator or hot water storage tank. Two approaches for steam generation can be used:

a. Steam generation with flash evaporation: the water-cooled parts of the off gas system are cooled with hot water. The hot water can be stored in a tank in order to continuously feed a flash evaporator for the production of saturated steam. During high off gas duties, the tank is charged with hot water coming from the hot gas duct, while during idle times the hot water is discharged by the continuous flow to the flash evaporator.
b. Heat recovery steam generator: in this case, the off gas duct of the furnace is evaporative cooled. Water coming from the steam drum is fed to the off gas duct at saturated temperature. The water is partly evaporated in the tubes of the off gas duct. Water-steam mixture is fed back to the steam drum, where water and steam is separated. The saturated steam is fed to the consumer, whereas a Ruth's steam accumulator can be used to buffer the steam and to compensate fluctuating off gas emissions from the steelmaking process.

Even though this concept allows economic recovery of waste heat, it is only applicable if the produced steam can be used directly for certain consumers, such as:

- Steam ejectors for creating vacuum in VD/VOD plants
- Steam for process heating (e.g. steel pickling bath, sea water desalination, paper industry, etc.)
- Air separation
- Pickling lines

One of the existing system of heat recovery by steam production is the iRecovery® system (see Figure 3.11), which is available for two levels: the level 1 [102] is based on steam flowing through the cooling pipes of the off-gas ducts, while the level 2 [118] adds a waste heat boiler located downstream the off-gas ducts. In the level 1, the off-gas is cooled down to 600°C, while in the level 2 the off-gas is cooled down to 200°C. The iRecovery® duct is made up of tubes of the same look and the same working principle as a conventional off-gas duct with cold-water cooling circuit. The main difference is the pressure and temperature level inside; while cold water cooling circuits typically operate within a temperature range from 20 to 50°C, an iRecovery® system operates with water of approximately 180 to 250°C towards the ducting and decouples the off-gas energy by means of evaporation. This mixture of steam and water is guided into a steam drum where the steam and water are separated. While the steam is taken out (and replaced by condensate/fresh water), the water returns to the circuit.

It is worth mentioning that the key advantage of heat recovery is not obtained at the cost of operational disadvantages. In fact, iRecovery® brings additional advantages:

- no dew point problems (inner surface of the pipes is always above dew point of sulphuric acid);
- no inner corrosion (self-passivation of tubes by the Schikorr reaction);
- less thermal stress (constant temperature of the evaporation process allow all elements to maintain a constant temperature during all operation phases);
- lower water consumption (it is a closed-loop system, cooling towers consume 3 – 8% of water during every loop);
- lower water volume flow due to higher heat transfer resulting in smaller pumps, smaller piping and lower maintenance cost;
- higher safety in different emergency situations by different redundant backup levels.

A heat recovery system like the iRecovery® has been proposed by SMS SIEMAG AG in 2009 (i.e. cooling the ducts of primary off-gases with steam instead of water). In this solution, the use of a steam accumulator has been considered [116].

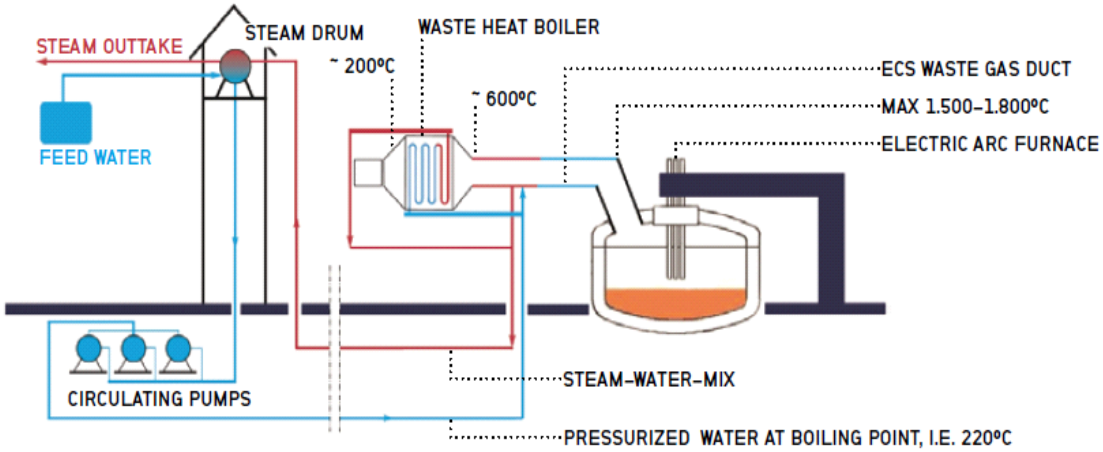

Figure 3.11 Simplified scheme of an iRecovery® Level 2 system. Source: [118]

Another similar study has been proposed by JP Steel Plantech (see Figure 3.12); in this case the considered EAF uses Direct Reduced Iron (DRI) and the steam generation is assumed to be used for the supply internal steelworks processes or for the production of energy. The cooling duct of the EAF off-gas is directly used as a steam generation boiler, and the sensible heat from the exhaust gas of approximately 1100°C is recovered. The steam intermittently generated by the batch operation of the electric arc furnace is smoothed by the steam accumulator and then supplied to the internal user. For the power generation, a steam superheater or a boiler with auxiliary burner can be additionally installed downstream to manage combined operational control.

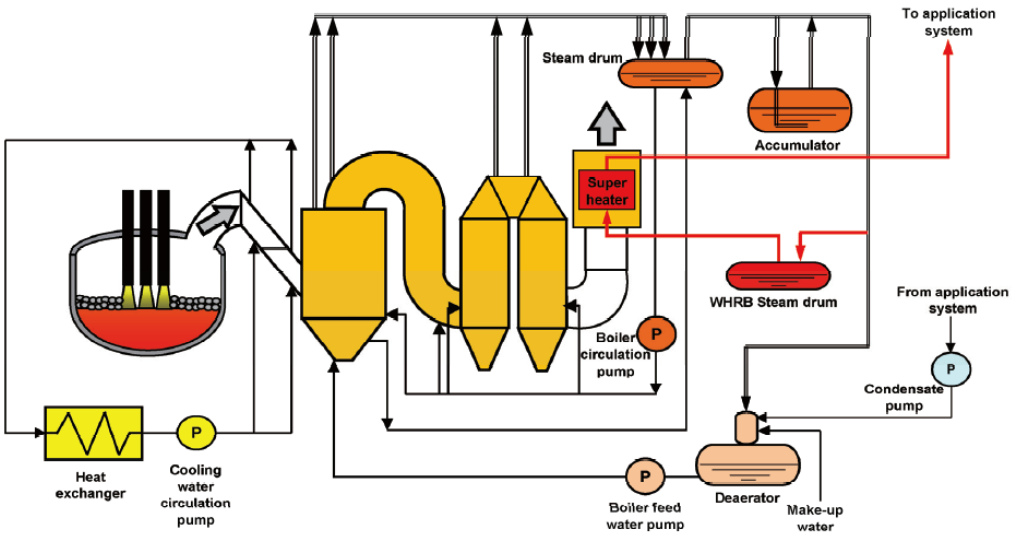

Figure 3.12 Scheme of the heat recovery system proposed by JP Steel Plantech. Source: [103]

3.3.2.3 Chilled water production

Usually, chilled water production for comfort and process cooling applications is done by compression type chillers, driven by electrical motors. An alternative technology for producing chilled water is thermal driven chillers. A widely spread and proven technology for such thermal chillers are absorption type heat pumps. The main difference between this technology and the compressor-type technology is the main operating energy source – in this case thermal power in form of hot water or steam from a waste heat source. So this creates the opportunity for utilization of a low temperature waste heat recovery source for producing chilled water.

3.3.2.4 Power generation

In addition to the applications described in the previous paragraphs (i.e. heating, steam generation, chilled water production), the recovered energy can be used to generate electric energy. There are two technologies for power production:

1. Steam turbines;
2. Organic Rankine cycle turbines.

Many existing Waste Heat to Power (WHTP) systems used in energy intensive industries with continuous high temperature processes use steam turbines to convert heat to power. Waste heat recovery boilers capture the valuable energy of the hot exhaust gases generated by the primary process to evaporate water and produce saturated or superheated steam. Steam is then expanded in a steam turbine and eventually condensed back to water. This is the classical Rankine cycle, employed, for instance, in the chemical industry, nonferrous metal making and for the production of ferroalloys. These traditional water-steam systems are typically employed in industry for plants over 10 MW and extending up to 50 MW and above. In these cases, and where the primary calcining or metallurgical process generates a steady flow of high temperature exhaust gas, superheated steam cycles are employed to maximize efficiency in converting heat to power.

Superheated steam systems require costly equipment (high temperature and pressure demand more sophisticated equipment and materials) and high O&M costs (i.e. operators must be certified steam engineers, water quality requires special care etc.). Due to the capital and running costs, superheated steam cycles are seldom convenient for WHTP

plants below 15-20 MW. At smaller capacities, less costly non-superheated (saturated) steam Rankine cycle systems have been employed; also in these cases, local regulations typically require the continuous presence of certified steam engineers, increasing operating personnel costs to unacceptable levels. In addition, when the process heat source is discontinuous or highly variable, steam turbines running on saturated steam cannot be easily employed.

Due to all these factors, all the existing energy recovery systems from EAF off-gas for power generation adopt ORC turbines. In fact, the ORC technology, widely employed in hundreds of renewable energy plants in Europe and North America (mostly in biomass based generation and in geothermal applications) was successfully proven also in various WHTP installations in the industrial environment [117,125]. The only concern about the ORC technology regards the use of thermal oil as heat carrier between the primary heat source (EAF off-gas ducting) and the ORC. Even though thermal oil is widely employed in the Oil & Gas or Marine Industry, EAF plant operators prefer to avoid the presence of thermal oil near the EAF because of the fire risk. Thus, other heat carriers, such as saturated steam and superheated water, have been used in the existing WHTP plants. For what concerns the use of saturated steam as heat carrier, the study reported in [126] showed that saturated steam at about 20 bar is a good heat carrier for an ORC system.

The first waste heat to power system based on ORC has been started up on December 2013, in the plant of Feralpi Group (Riesa – Germany) [127]. The waste heat recovery system and the ORC were specifically developed for this application in the framework of the EU funded HREII demo (Heat Recovery in Energy Intensive Industry) project [128]. A simplified scheme of the solution adopted is shown in Figure 3.13. The use of steam, instead of the more usual thermal oil as heat carrier, required several changes to the “hot” heat exchangers (i.e. preheater and evaporator) of the ORC. The system uses saturated steam at a pressure of 26 bar, which gives a saturation temperature of 226 °C. Considering that a traditional ORC system fed with thermal oil operates in the range 280÷310°C, the reduction in ORC efficiency is quite small.

It is worth noting that the saturated steam conveying heat to the ORC does not expand like in a traditional steam turbine. In this case, the saturated steam just transfers heat to the ORC working fluid through surface heat exchangers, then it cools down and

condenses with a small pressure drop, returning as condensate to the off-gas ducts, where it is heated up to vaporise.

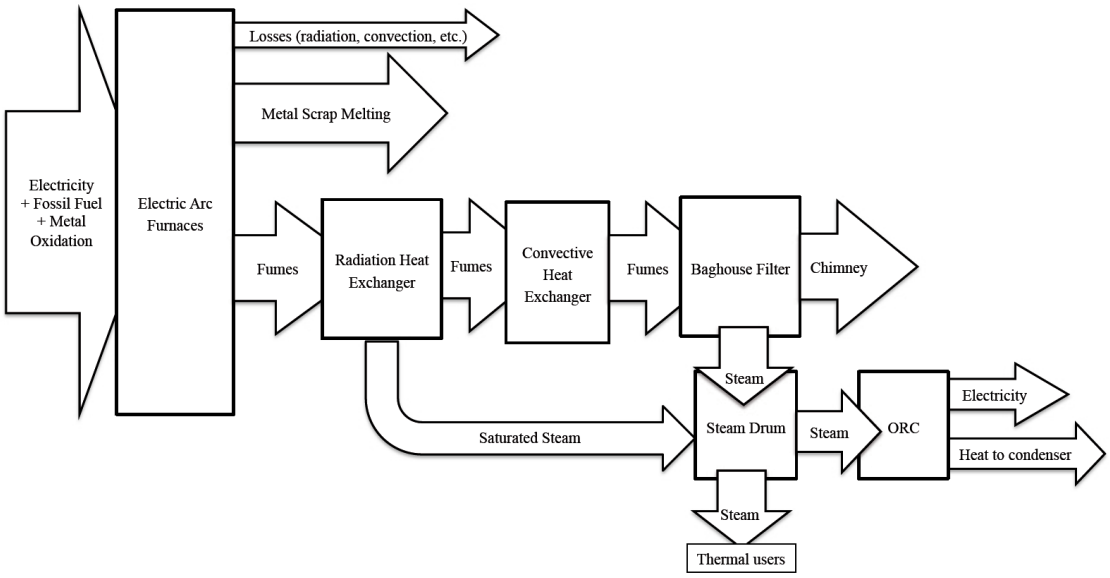

Figure 3.13 Scheme of the solution adopted in the Feralpi Group plant. Source: [129]

An alternative solution to the use of saturated steam as heat carrier is the superheated water. A waste heat to power system employing superheated water has been implemented by Danieli Spa (known as Clean Heat Recovery® system) in the ABS steel plant, Italy [106,120]. Figure 3.14 reports the scheme and energy balance of the Clean Heat Recovery® system. When compared to a traditional off-gas line, the cooling components (i.e. water cooled panels and the air cooler) have been substituted by the following heat recovery components:

- Hot Water Cooled Panels (HWCPs): usually, cooling water enters the water-cooled panels (WCPs) at a temperature of 30°C and it exits at about 50°C; such temperatures are not suitable for power production. The traditional pipe-to-pipe design of WCP is adapted to resist to the higher pressure needed to obtain superheated water. In addition to the heat recovery function, the use of hot water increase the lifetime of the ducts by reducing corrosion issues and thermal stresses, such as in the evaporative cooling ducts (e.g. iRecovery® system).
- Heat exchanger: it has been designed for the heavy-duty conditions due to the high concentration of dust in the off-gas; it allows recovering the remaining heat that cannot be not directly recovered by the HWCP.

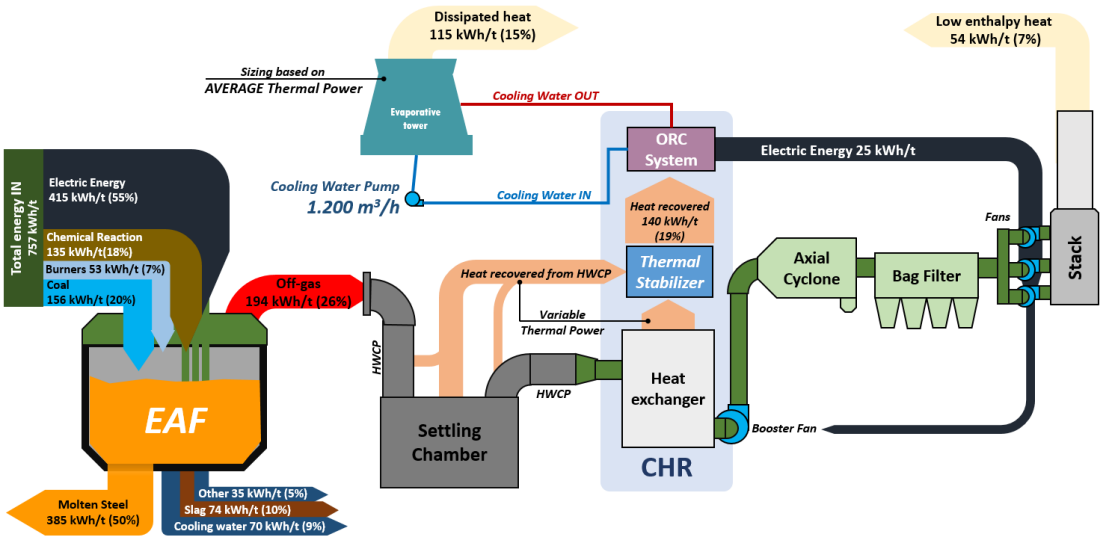

Figure 3.14 Scheme and energy balance of the Clean Heat Recovery® system. Source: [120]

The recovered heat is then converted into power by using an ORC turbine. However, the introduction of heat recovery components is not enough to feed the energy conversion system (i.e. ORC System) in an efficient way. In fact, the heat recovered by the HWCP and the heat exchanger is characterized by a fluctuating thermal power, which affects the efficiency of the downstream ORC System. Thus, an innovative equipment able to smooth the thermal power variability has been developed. To this end, Danieli Spa in collaboration with the University of Udine [130], has developed the Thermal Stabilizer Unit (TSU); currently, this technology is under patenting process.

The Thermal Stabilizer Unit is an innovative tank of superheated water that acts as both heat storage system and system for smoothing thermal power fluctuations. The design of the thermal stabilizer unit is based on multiple water inlets and outlets, which are specifically positioned to maximize the smoothing effect. Figure 3.15 shows an example of the Thermal Stabilizer Unit performance; red line represents the water temperature entering the Thermal Stabilizer Unit, while gold line represents the water temperature exiting the Thermal Stabilizer Unit. From Figure 3.15, it is possible to observe that the maximum temperature difference of 50°C at the inlet is reduced to 10°C at outlet of the TSU.

The Thermal Stabilizer Unit works in synergy with the ORC system by means of a control system that evaluates the energy required by the ORC and the energy entering the TSU.

The introduction of a heat recovery system affects also the water requirement of the evaporative tower. In fact, the sizing of the evaporative tower and its components is no longer based on the peak thermal power, but it is based on the average thermal power. This change in the design principle leads to a reduction of about 40% of the water consumption of the evaporative tower. Thus, a further reduction of the operative costs is added.

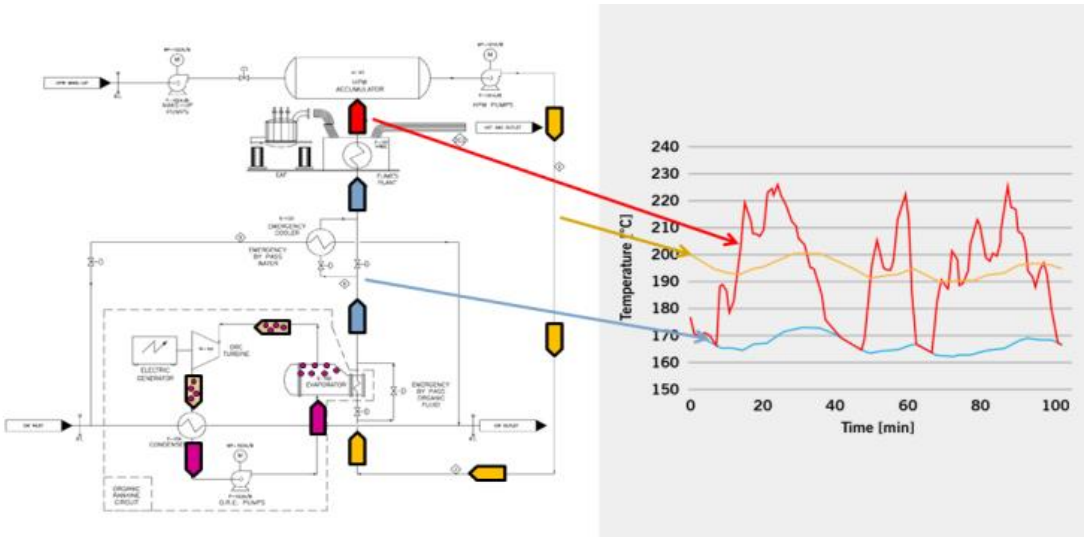

Figure 3.15 Performance of the Thermal Stabilizer Unit. Source: [120]

It is worth mentioning that in Europe the theoretical potential power production by means of ORC has been estimated to be over 400 MW_{el}; the estimation was made according the methodology presented in [131] which is based on the results of 3 energy audits on EAF and considering that there are almost 200 EAF [132] in Europe. Nevertheless, the use of steam turbine for power production is still considered.

In particular, the use of molten salt as heat transfer fluid and storage media for constant production of superheated steam generation has been proposed and studied in [119]; a testing plant has been installed inside the existing off-gas system of a German mini mill in order to evaluate tube materials and to measure the influence of hot corrosion and dust settlement. When molten salts are used as heat transfer fluid, the heat recovery system needs to be designed for fast draining of the liquid and for freezing prevention. In [119] the heat exchanger was designed as self-draining if the pumps stop and an up-down constructions for the tubing were chosen.

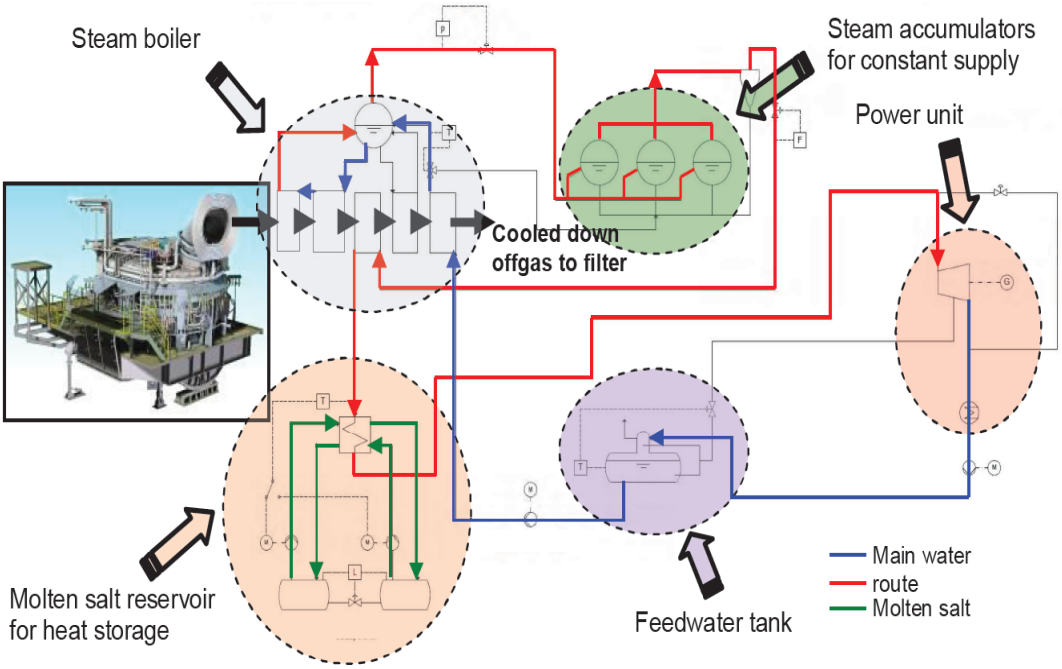

Figure 3.16 Process flow diagram of the molten salt off-gas energy recovery system. Source: [104]

One of the major goals of the testing plant was to investigate material properties of several heat exchanger grades in respect to high temperature chlorine corrosion as well as the impact of EAF dust and off-gas composition on wear and heat transfer. The test rig consisted basically of a molten salt storage tank, a molten salt off-gas heat exchanger, a molten salt air cooler and various control and measurement instruments; the tests have been performed during one year.

The experiment showed that the dust load and the dynamic oscillation of off-gas side temperatures leads to high material stress both in terms of corrosion and erosion. Further investigation needs to be carried out to better assess the economic feasibility of the proposed technology.

3.4 Passive PCM-based device for temperature smoothing

The problem of energy recovery from the electric arc furnace process of steel industry is addressed. During a tap to tap cycle, a significant part of the energy required for steel production is dissipated by the off-gas. The high variability of temperatures and flows, and the high concentration of dust, which characterize the production process, make the adoption of current energy recovery solutions quite difficult, both from the technological and the economical perspective.

A new system is proposed exploiting aluminium as phase change material (PCM) to reduce the variability of off-gas temperatures and thermal powers, in order to allow an efficient energy recovery. The smoothing device is analysed by thermo-fluid dynamic simulations to optimize its performance. A new boiler configuration equipped with cyclones is proposed to overcome also the problem of high dust content of the off-gas. The high recovery efficiencies, the low investment and operation costs and non-invasive plant modifications induced by the smoothing system, make the proposed PCM-based recovery system a feasible solution to reduce energy supply costs and emissions in the steel industry.

3.4.1 The PCM-based smoothing system concept

In this section, a system based on phase change materials (PCM) is proposed, which, by accumulating and releasing large amounts of energy, acts as a “thermal flywheel”, thus allowing to smooth off-gas temperatures. Temperature smoothing is achieved by directly operating on off-gas unlike the other current technologies and it is separated from the downstream energy conversion system, based on a traditional Rankine cycle but with an innovative boiler structure. This allows a non-invasive intervention on the system with minimum plant modifications. The simple structure, the low cost of operation, and the high recovery efficiency can make this just patented [133] recovery system a feasible solution to increase energy efficiency in steel industry.

The design of the energy recovery system refers to a typical EAF steel plant with 120 tons per TTT cycle capacity and 68 min TTT cycle time, whose off-gas cleaning section is shown in Figure 3.17. After passing the settling chamber and the cooler, off-gas of the primary line joins the secondary line one, which was captured during the furnace roof

opening phase, and proceeds to the cyclonic separator and the filter. The analysis of the new recovery system is based on the experimental data provided by an Italian firm and measured at the inlet section of the settling chamber during several castings (see Table 3.5 for average values of off-gas properties and Figure 3.18 for temperature pattern). Similar variability in off-gas flow and temperature was obtained in [134].

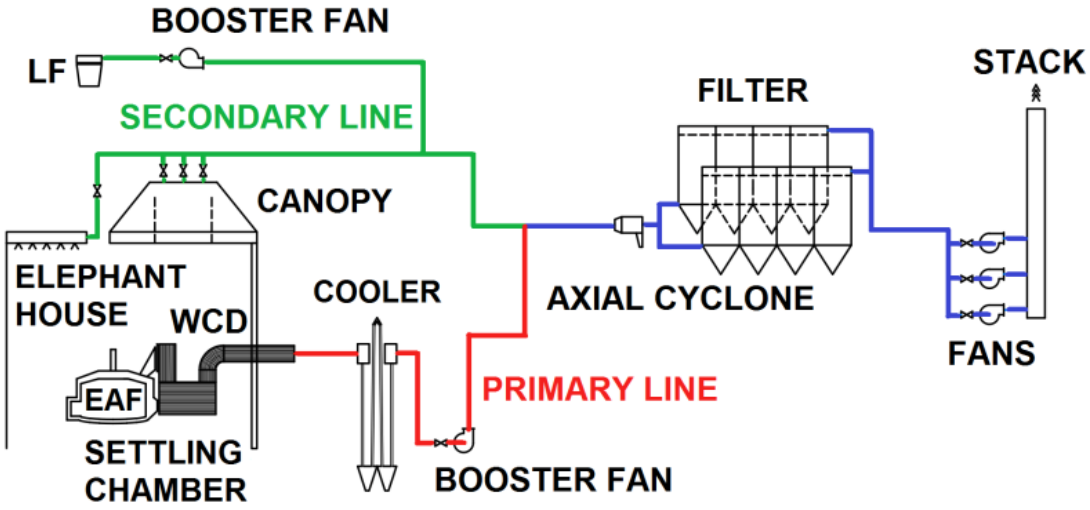

Figure 3.17 Off-gas cleaning section of the reference EAF steel plant

The characteristics phases of a melting cycle can be clearly recognized in the temperature profile in Figure 3.18. The two temperature increases (from 220 °C to 950 °C and from 485 °C to 885 °C) correspond to the melting of the first and second bucket, respectively. The two decreases (from 950 °C to 485 °C and from 885 °C to 230 °C) correspond to the charging and to the tapping phase, respectively. The small drops around 570 °C and 655 °C are related to burners opening.

To achieve an efficient energy recovery from EAF off-gas, its temperature variability range should be properly reduced. This thesis proposes the adoption of a PCM-based device located in the settling chamber, which captures thermal energy from off-gas and return it to off-gas later, acting as a heat accumulator. During the phases at high temperature, off-gas raises the temperature of the PCM above its melting temperature, causing the transition from the solid state to the liquid one with accumulation of the latent heat of fusion. During the phases at low temperature, off-gas causes the PCM transition

from liquid to solid state with release of the latent heat of solidification (see [10] for a review on PCM properties and issues for latent heat storage).

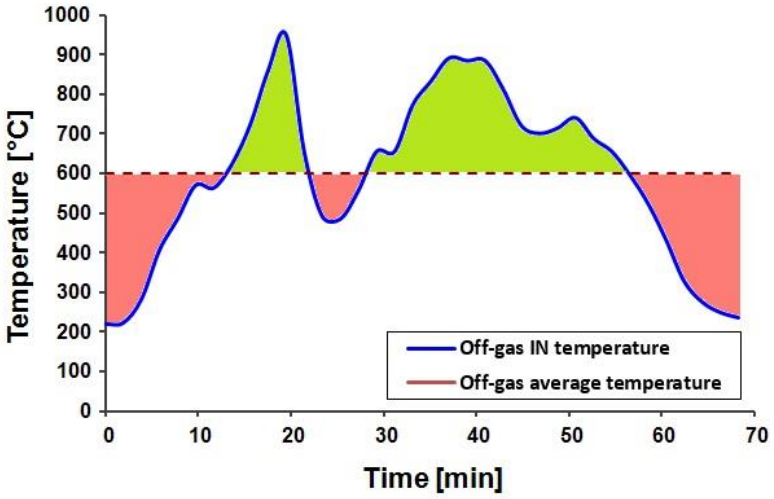

Figure 3.18 Off-gas temperature profile at the chamber inlet in the reference TTT cycle; in green energy potentially accumulated by the PCM, in red energy released by the PCM.

Off-gas energy is approximately proportional to the area under the temperature curve. In particular, the portion above the average off-gas temperature, supposed to be near the PCM melting value (green area in Figure 3.18), can be considered as representative of the energy that can be subtracted from off-gas and accumulated by the PCM. The portion below the average temperature (red area in Figure 3.18), instead, describes the latent heat of solidification that can be released to off-gas by the PCM, whenever its temperature profile decreases below its melting point.

To obtain a good reduction of the variability of the off-gas temperature, the PCM should have a melting temperature close to the average temperature of the off-gas (dotted line in Figure 3.18), while the boiling temperature should be greater than the maximum value reached by the off-gas to preserve the system integrity and safety.

Table 3.5 Off-gas properties.

Average temperature [°C]	600
Rate flow [Nm^3/h]	166700
Normalized density [kg/Nm^3]	1.3
Specific heat capacity [$J/(Nm^3K)$]	1330
Thermal conductivity [W/(mK)]	0.051

In [38] the PCM engine system for the exploitation of low temperature excess heat generated in the iron and steel industry (e.g. heat from hot material, cooling water of low temperatures) is analysed and compared with the ORC and the thermoelectric generator (TEG) technologies. Several studies have also been conducted on the use of PCMs in thermal energy storage systems for domestic water and space heating, and for the exploitation of solar energy [31]. Both the PCM engine and the latent heat storage systems employ PCMs that are appropriate for low temperatures application, as for example the paraffin. A lower number of studies were instead carried out on PCMs for high temperature applications such as the energy recovery from the EAF off-gas.

This thesis considers different PCMs suitable for the reported range of off-gas temperatures. As underlined in [12], the use of phase change metals for heat storage at high temperatures has been underestimated by researchers, though they are deprived of many lacks which are characteristic for salts, such as low heat conductivity, corrosion activity, the big change in volume at melting, considerable subcooling and high cost of some salts. Some metals have been analysed for the smoothing module such as aluminium, lead and tin. Their physical characteristics such as density, thermal conductivity, thermal capacity, thermal diffusivity, specific heat, and latent heat, as well as the current cost per unit of weight, of volume, and of latent heat are well known, as reported in Figure 3.18. As concerns metal alloys, there is a lack of reliable data on their properties and their degradation over operation time in literature [70], so it has been preferred to base the analysis on pure metals.

The aluminium was recognized as the preferable choice due to its favourable melting temperature, which is very close to the average off-gas one, and its high values of thermal conductivity, thermal diffusivity, thermal capacity, and latent heat of fusion. It also presents low values of density and costs. Moreover, no particular system safety problems arise when managing solid/liquid aluminium. The main disadvantage in the adoption of this material is represented by the relatively high value of the coefficient of linear expansion that should be managed by a proper storage equipment.

The location of the PCM smoothing module has been evaluated according to several factors, such as the temperature reached in the different sections of the off-gas cleaning line and the installation complexity.

Table 3.6 Properties of the considered metals to be used as PCM

	Aluminium	Lead	Tin
Melting temp. [°C]	660	327.4	231.9
Boiling/critical* temp. [°C]	2057	1620	2602
Density [kg/m^3]			
- Solid phase	2550	11340	7280
- Liquid phase	2380	10660	6980
Fusion latent heat [kJ/kg]	396	23.8	59.9
Thermal conductivity [W/(mK)]			
- Solid phase	215	33	67
- Liquid phase	90	16	35
Thermal capacity [J/(dm^{3}K)]			
- Solid phase	2530	1474	1733
- Liquid phase	2806	1567	1773
Thermal diffusivity [10^{-5} m^2/s]			
- Solid phase	8.49	2.23	3.86
- Liquid phase	3.20	1.02	1.97
Linear expansion coefficient [10^{-6}K^{-1}]	24	28	23.4
Vol. expansion coefficient [%]	6.9	3.8	2.4
Cost per weight [€/kg]	1.86	1.62	20.01
Cost per volume [€/m^3]	4751	18388	145673
Cost per latent heat [c€/kJ]	0.47	6.81	33.41

The final choice was to insert the device into the settling chamber, as shown in Figure 3.19a, since here the off-gas is still very hot and therefore a great amount of energy can be recovered.

The settling chamber also allows an easy insertion of the recovery device without any special modifications to the existing structure of the plant. Moreover, the increased flow resistance in the settling chamber provided by the PCM module can enforce the dust removal effect, similarly to an impact separator.

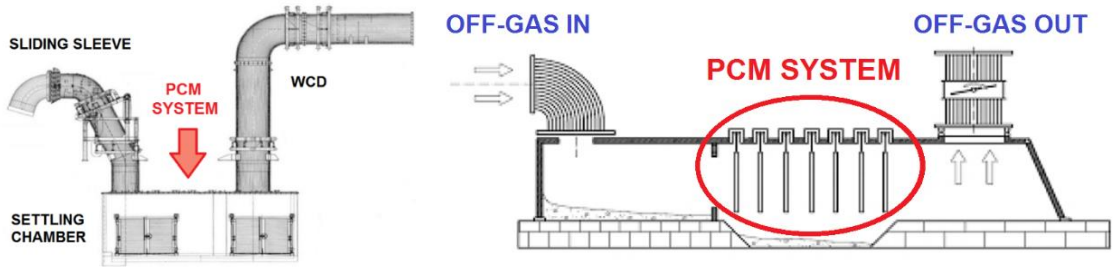

(a) (b)

Figure 3.19 The PCM smoothing module: a) position, b) PCM containment system.

Additional dust removal equipment is not needed, since dust intercepted by the module simply joins what normally collected in the settling chamber.

3.4.2 Preliminary analysis

The high temperatures could alter the properties of PCM containers causing the leakage of molten material, and fouling might clog the device reducing its dampening effect. Thus, the material used to contain the PCM should be characterized by high thermal resistance, high thermal conductivity, low chemical reactivity with the PCM, and should present the most stable chemical-physical characteristics during the process. Moreover, the enveloping material should have a melting temperature greater than the maximum temperature reached by the off-gas and enable transitions to solid and liquid PCM states without interfering with them. The final choice lied on the stainless steel, which has proven to have good resistance to corrosion and good mechanical characteristics at high temperatures over long operation periods [70].

The PCM should be contained in hollow cylinders properly spaced to ensure the integrity of the thermal system and to properly dampen the temperatures (see Figure 3.19b). As reported in [10], several systems employ cylindrical pipes; it should be underlined, however, that such applications consider a heat transfer fluid, which is introduced into the tube. In our system, instead, PCM containers are externally crossed by the off-gas flow and directly exchange heat with it to increase or decrease its temperature.

The cylindrical geometry allows to increase heat exchange surfaces thereby optimizing the process both from the point of view of recovery efficiency and of cost. The cylindrical geometry also doesn't present neither sharp edges, common causes of breakage and crack formation, nor creeks and concavities where materials can accumulate. Cylinders are hung so that they can oscillate when off-gas passes through, in order to assure structural flexibility and prevent cracks and strains. Furthermore, dust is easily removed and dropped down.

Considering a typical settling chamber (10 m length, 4 m width, and 5.5 m height) the space available for installation of the PCM-based device is about 16 m^2. The height of cylinders cannot exceed 3.5 m in order to allow dust extraction. Cylinders should also be sized in order to allow volume expansion of aluminium inside.

3.4.3 Sizing criteria of the PCM smoothing device

Based on the concept of the PCM smoothing device, the sizing criteria are determined by the latent heat of fusion H_{PCM} of the chosen PCM and the off-gas thermal energy E_{OG} at temperatures higher than PCM melting point T_{melt}. The thermal energy that the off-gas can potentially release to the PCM is estimated as in equation (3.3):

$$E_{OG} = \Delta\tau \sum_{i:T_i>T_{melt}} \dot{m}_i [c_i T_i - c_{melt} T_{melt}] \tag{3.3}$$

where $\Delta\tau$ is the length of time spans in which the TTT cycle time is discretized, equal to the temperature data sampling interval at settling chamber inlet. For each time interval *i*, the off-gas temperature T_i and the mass flow $\dot{m}_i$ are derived from measured data, while the off-gas specific heat c_i is calculated as function of T_i, as well c_{melt} is the off-gas specific heat at T_{melt}.

The total PCM mass m_{PCM} can be calculated as:

$$m_{PCM} = \frac{E_{OG}}{H_{PCM}} \tag{3.4}$$

The net volume of PCM container together with PCM density will determine the PCM mass per cylinder; from equation (3.4) the number of cylinders needed to assure the desired smoothing effect can be eventually derived.

3.4.4 Computational fluid dynamics simulations

Computational fluid dynamics simulations were performed by ANSYS FLUENT associated with the pre-processor GAMBIT to investigate the performance of the PCM-based smoothing system. The speed of off-gas was considered constant over time. Moreover, only average values of material properties near the melting temperature were considered; the k-epsilon model was adopted to simulate the turbulent flow. The simulations are related to two different layouts of cylinders: in the first layout (see Figure 3.20a) cylinders are perfectly aligned, while in the second one (Figure 3.20b) they are staggered.

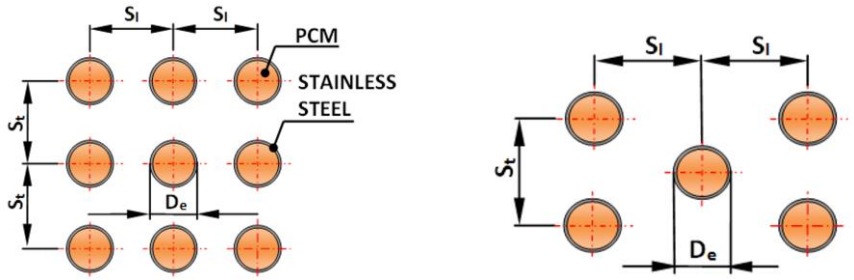

(a) (b)

Figure 3.20 PCM containers layout: a) aligned cylinders; b) staggered cylinders.

Stainless steel tubes with commercial diameters of 2", 1" and 3/4" were initially considered as PCM containers. This allowed to study the effect of the ratio of the container surface and the aluminium mass on temperature smoothing. Specifications for the aligned layout of PCM cylinders are reported in Table 3.7, while off-gas temperature profiles for the analysed diameters are shown in Figure 3.21.

Table 3.7 Smoothing system specifications for different cylinder commercial diameters and layout

Layout	**Aligned**			**Staggered**
Commercial diameter [inch]	**2"**	**1"**	**¾"**	**1"**
External diameter, D_e [mm]	60.3	33.4	26.7	33.4
Thickness [mm]	4.0	2.5	2.0	2.5
Longitudinal pitch, S_l [mm]	121.2	66.7	53.3	66.7
Transversal pitch, S_t [mm]	121.2	66.7	53.3	66.7
Al mass per cylinder meter [kg/m]	5.5	1.6	1	1.6
Steel mass per cylinder meter [kg/m]	5.6	1.9	1.2	1.9
Number of cylinders	1089	3600	5625	3540
Total Al mass [t/m]	5.96	5.81	5.8	5.72
Total steel mass [t/m]	6.15	6.97	6.96	6.86
Total system mass [t/m]	12.11	12.78	12.76	12.57
Heat exchange surface/Al mass [mm^2/kg]	34.6	65.0	81.3	65.0

The temperature profiles highlight a reduction of over 230 °C of the off-gas maximum temperature and an increase of the minimum temperature of about 218 °C for all the analysed configurations. The smoothing effect is significant, as measured by both standard deviation of temperatures and by the difference between the maximum and minimum temperature of off-gas, as shown in Table 3.8.

Analysing off-gas temperature profiles in Figure 3.21, the high temperature phases can be hardly distinguished in the smoothed profile of the ¾" cylinders in comparison to the 2" one. The peak of temperature during the first TTT phase is, in fact, totally dampened.

Table 3.8 Simulation results for both layouts.

	INPUT	OUTPUT			
Layout		Aligned			Staggered
Commercial diameter [inch]		2"	1"	¾"	1"
Max off-gas temperature [°C]	950.8	719.8	681.0	679.2	674.2
Min off-gas temperature [°C]	223.0	447.2	455.9	441.3	439.2
ΔT max [°C]	727.9	272.7	225.1	237.9	235.0
Standard deviation [°C]	203.7	80.3	71.5	77.5	77.6
Pressure drop [Pa]	-	257	459	592	973

This means that an increase of the ratio between the surface of cylinders and the PCM mass leads to an increase of the device reactivity. However, in the ¾" configuration the aluminium overheats above the fusion point in most tubes (see Figure 3.22a), thus affecting the structural resistance of cylinders. Moreover, pressure drop (see Table 3.8) are more significant than those for greater diameters.

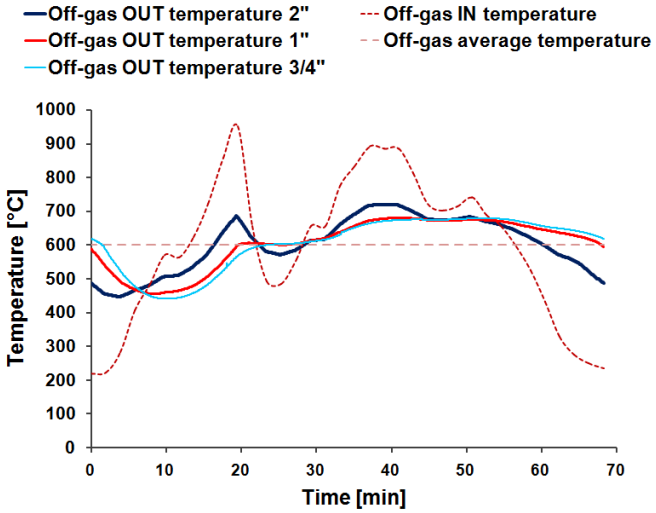

Figure 3.21 Off-gas temperature profiles for the aligned layout: the dotted lines refer to temperatures at the chamber inlet.

Analysing Figure 3.22b, it can be seen how a good heat exchange is provided also in the last row of cylinders, where temperature variability of off-gas is lower due to the smoothing effect of the previous rows. Considering the second layout (staggered cylinders, see Figure 3.20b), a temperature profile similar to the aligned layout was obtained, even if slightly more uniform (see Figure 3.23a for 1" cylinders and the last column in Table 3.7 for related specifications). However, it presents increased pressure drop, as can be seen by comparing results in Table 3.8, which discourage its adoption.

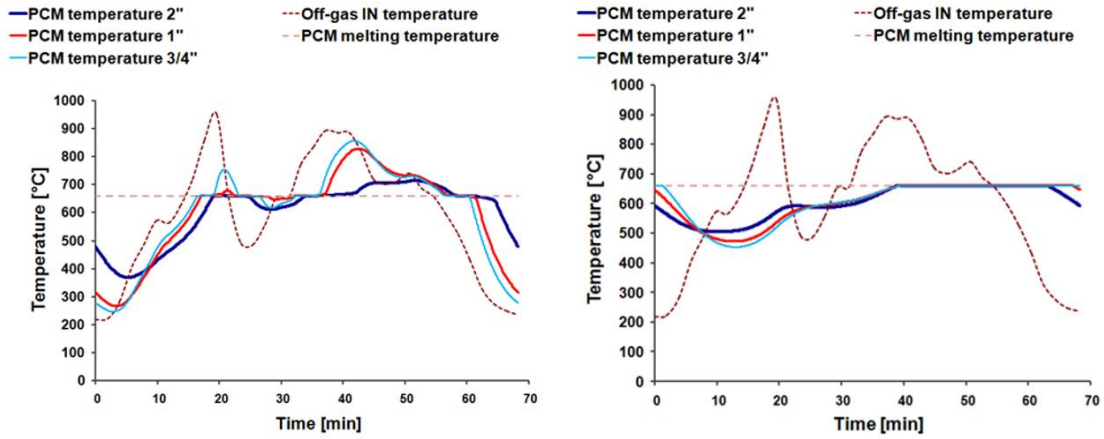

Figure 3.22 PCM temperature profiles: a) first row of cylinders and b) last row of cylinders; the dotted lines refer to temperatures at the chamber inlet.

Given the high dust content of off-gas, the influence of fouling was also analysed by simulation, considering a 10 mm layer of fouling on the surfaces of all cylinders and only of the first 10 rows.

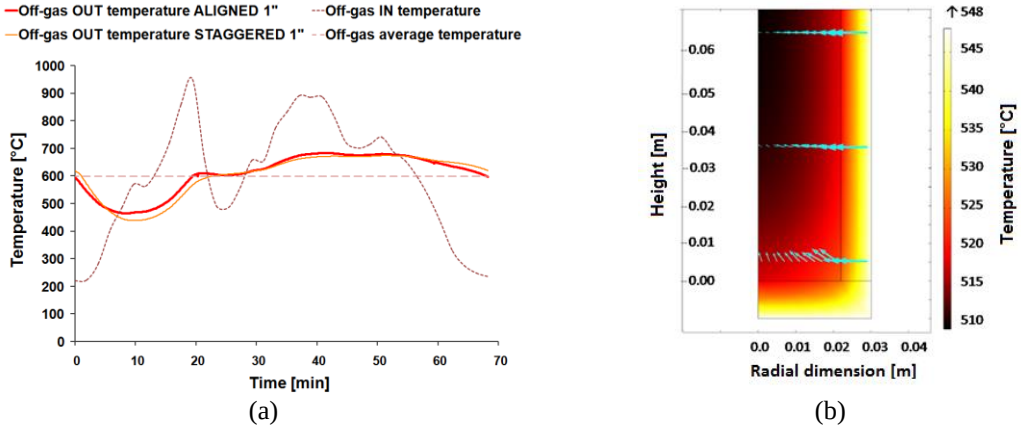

Figure 3.23 a) Comparison of off-gas temperature profiles for 1" cylinders with aligned and staggered layout; b) Temperature field in the bottom part of a 2" cylinder

In both the simulations a minor impact on performance of the smoothing system was obtained. The containers should be provided with an insulation layer on the bottom to prevent overheating, as resulting from simulations (see Figure 3.23b for the temperature field of an insulated cylinder).

3.4.4.1 Final configuration of the PCM-based smoothing system

From the application point of view, the best configuration should be characterized by the lowest number of cylinders with the simplest arrangement.

This leads to select the aligned layout with the 2" cylinders, which prevents overheating of the aluminium, while still providing an efficient heat exchange between off-gas and the PCM, as suggested by simulations. Furthermore, if on one hand the larger pitch between cylinders (see Table 3.7) quite penalizes the dampening effect, on the other hand it reduces dust accumulation on cylinders surfaces and obstruction of off-gas passage, with related pressure drop. From the economic point of view, the cost of the device can be reduced due to the lower overall steel requirement and the lower number of heat exchange elements.

However, the strong difference between the linear thermal expansion of aluminium and of stainless steel can lead to structural stress with potential break of the container. In order to address this problem, a container configuration different from the preliminary analysis one has been analysed. The detailed thermo-mechanical analysis is reported in Section 3.5. The concentric pipe configuration (see Figure 3.24a) replaces the hollow cylinder one.

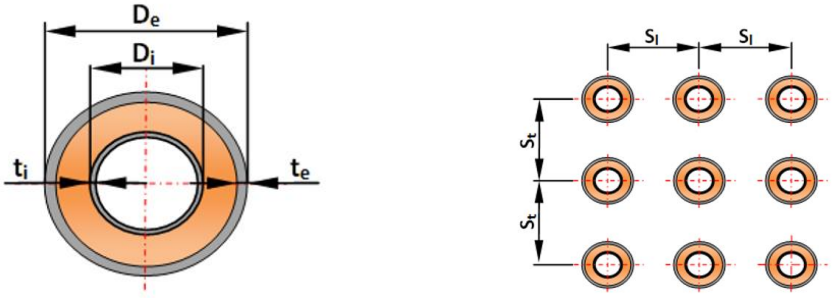

(a) (b)

Figure 3.24 Concentric pipe configuration of the PCM containers a) and final layout b).

By reducing the radial development of the PCM in the cross section, in facts, the stresses on the external pipe due to thermal expansion of the aluminium are expected to be lower than in the hollow cylinder, thus complying with the linear elastic range of the selected AISI 316 stainless steel.

Each container is designed in such a way that its external diameter is as similar as possible to the 2" configuration of the preliminary analysis, while maintaining the total mass of PCM inside the whole smoothing device to gain the same dampening effect. The final dimensions of containers are reported in Table 3.9, while the final layout is shown in

Figure 3.24b. The smoothing effect of the new configuration in comparison to the 2" aligned layout of the preliminary analysis is reported in Figure 3.25.

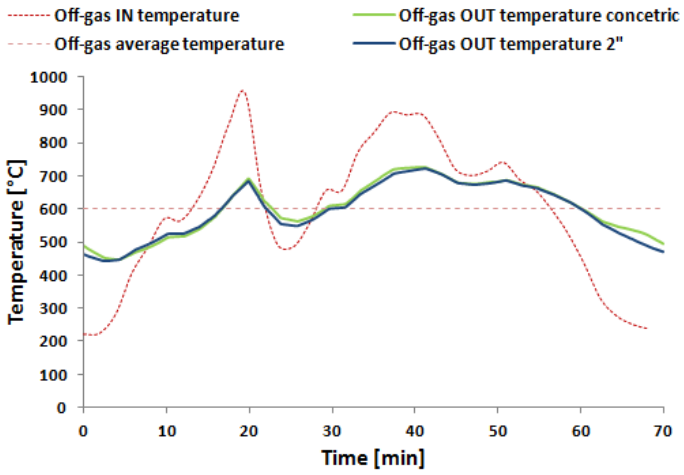

Figure 3.25 Comparison of the off-gas temperature profiles of 2" hollow cylinders and concentric pipe containers.

The temperature profiles of the off-gas are very similar, so we can conclude that the final configuration of concentric containers preserves the smoothing performance, while providing the proper resistance to structural stress.

Table 3.9 Final smoothing system specifications with concentric pipes in comparison with the 2" cylinders

	Concentric pipes	**Cylinders 2"**
External diameter, D_e [mm]	76.1	60.3
External thickness, t_e [mm]	4.0	4.0
Internal diameter, D_i[mm]	42.4	-
Internal thickness, t_i [mm]	2.0	-
Longitudinal pitch, S_l [mm]	137	121.2
Transversal pitch, S_t [mm]	137	121.2
Specific steel mass per cylinder [kg/m]	9.3	5.6
Number of cylinders	841	1089
Total steel mass [t/m]	7.78	6.15
Al mass per cylinder [kg/m]	5.7	5.5
Total Al mass [t/m]	4.78	5.96
Total system mass [t/m]	12.56	12.11
Heat exchange surface/Al mass [mm^2/kg]	42.1	34.6

Moreover, the smoothing device can affect the dioxins generation process. According to [135] three main mechanisms of dioxins formation should be considered: 1) high temperature pyrosynthesis, 2) low temperature de novo synthesis from macromolecular carbon and organic or inorganic chlorine present in the fly ash matrix, and 3) formation from organic precursors.

The high temperature pyrosynthesis occurs during combustion and post-combustion reactions, when the range of temperature is 500°C÷800°C. For temperature higher than 800°C and a proper residence time (1-2 s), the dioxins are thermo-destroyed. Since the smoothing device is placed in the final part of the settling chamber, it is possible to consider that the post-combustion reactions are fully developed when the off-gas reaches the device inlet; therefore, this particular mechanism of dioxins formation cannot be affected by the smoothing process.

Mechanisms 2) and 3) are considered to cause about the 70% of the total dioxins generated [136]. The range of temperature in which mechanisms 2) and 3) take place is 200-400°C. The maximum dioxins formation occurs around 300-325°C; generally small amounts can be detected for temperature under 250°C and over 450°C [137]. Referring to Figure 3.25, it is possible to note how the PCM smoothing device increases the outlet off-gas temperature to values greater than 450°C, therefore out of the typical temperature range for dioxins formation. In the absence of the smoothing device, instead, the off-gas remains under 450 ° C for about 15% of the TTT time, and therefore they are subjected to low temperature mechanisms of dioxins formation. Thus, it is reasonable to conclude that the inclusion of the PCM smoothing device leads to a reduction in the formation of PCDD/PCDF with related benefits on environmental performance.

3.4.5 The energy recovery system

According to actual measures and specifications of the reference plant, the insertion of the recovery system into the off-gas cleaning section can be analysed. We suppose to provide the settling chamber with water jackets; then a boiler and a steam turbine are taken into account for energy recovery and properly sized.

The boiler has a maximum steam flow rate of 49 t/h, an average steam temperature of 400 °C, and a pressure of 40 bar at turbine inlet; a 0.08 bar pressure is recorded at the condenser. The boiler represents the second step to affect off-gas properties; after smoothing the temperature profile, in fact, it is possible to affect also off-gas speed and fouling factor. The first boiler section (see Figure 3.26), characterized by a low off-gas speed (8-10 m/s) and a high fouling factor, includes the screen superheater (very rarefied tubes), two superheaters, and the evaporator at high temperature. Downstream, two

parallel cyclones drastically reduce the dust content of the off-gas with an overall efficiency of 75% and allow a speed increase around 12-14 m/s. Therefore, the second section of the boiler can involve a low temperature evaporator and an economizer with very densely distributed tubes and consequently high thermal performance with reduced space requirements.

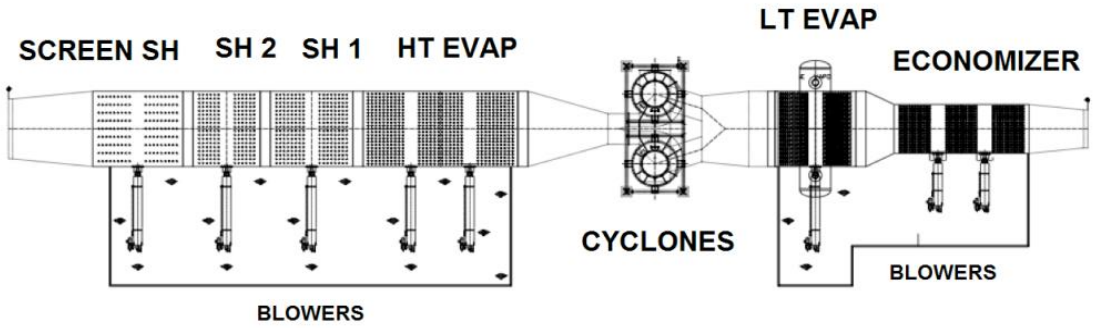

Figure 3.26 The boiler structure. SH (superheater); HT (high temperature); LT (low temperature); EVAP (evaporator)

When the off-gas enters the boiler with the maximum temperature allowed by the smoothing system (~720 °C, as shown in Figure 3.25), its outlet temperature is reduced to 199 °C, while water/steam temperature is increased from 105 °C at the economizer inlet to 420 °C at the superheater outlet (see Figure 3.27a). When off-gas, instead, enters the recovery system at its lowest smoothed temperature (~447 °C, see Figure 3.25), its outlet temperature is reduced to 216 °C; steam exits at 385 °C from the superheater (see Figure 3.27b). In both situations, the steam produced allows the turbine to work near nominal conditions.

To ensure a proper heat exchange, the off-gas temperature should be higher than the temperature of the superheated steam along the whole TTT cycle. While this is assured when the smoothing system is installed, in a traditional system a heat backflow from the working fluid to the off-gas occurs during charging and stand-by phases, when off-gas temperature decreases below the working fluid one. This leads to a decrease of thermodynamics properties of the produced steam, with a negative impact on turbine electrical efficiency.

The total energy released during a TTT cycle (68 min in our case) by the off-gas exiting the boiler at near 200 °C is approximately 33 MWht, for an average thermal power of

about 29 MWt (see power duration curves in Figure 3.28). This value can be considered reasonably equal in both conditions, i.e. when the plant is provided with the smoothing module and when it is not, since the PCM-based module affects thermal power profile, not the energy content of off-gas significantly. However, the off-gas thermal power profile plays a major role when the steam turbine is sized, since the latter should be able to convert the maximum thermal power.

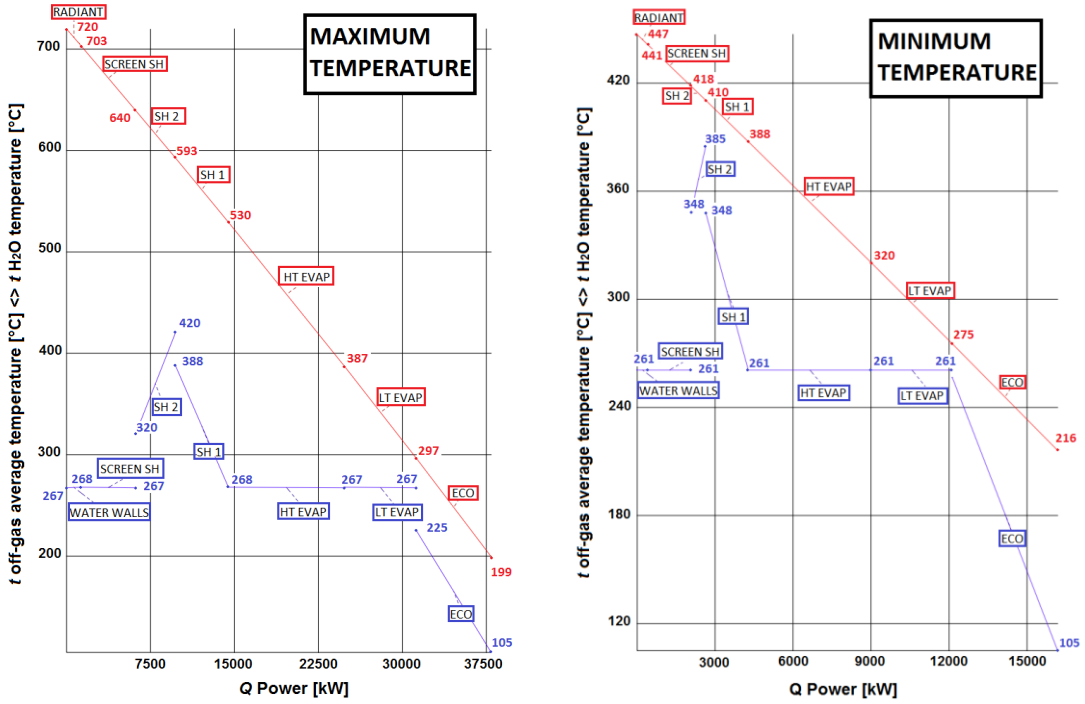

(a) (b)

Figure 3.27 Off-gas and water/steam temperatures when smoothed off-gas is at its a) maximum and b) minimum input temperature.

In our case, the thermal power released by the off-gas at the boiler when exiting the smoothing module at the maximum temperature of 720 °C is 35.5MWt, while it grows to 52.8MWt for off-gas at 950 °C when the smoothing system is not installed. By considering a full-load turbine efficiency of 0.3, these values lead to select a turbine of 10.65MWe for the plant with the smoothing system and of 15.85 MWe for the traditional plant, to convert quite the same amount of thermal energy.

If the actual thermal power released by off-gas for a given thermal power profile is divided by the maximum potential power that off-gas would release if it could persist at its highest temperature for the whole TTT cycle (e.g. 35.5 MWt for 720 °C), we can obtain

a measure of the energy loss due to off-gas temperature variability, in comparison to the nominal power of the turbine. In our case, this measure is equal to 0.55 for the traditional system and to 0.81 for a plant with the PCM-based smoothing system.

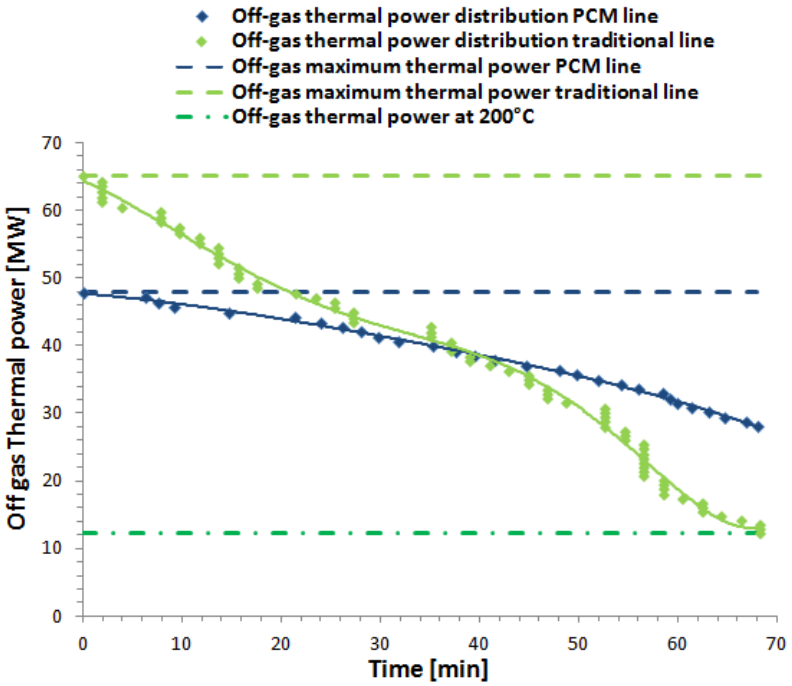

Figure 3.28 Off-gas thermal power duration curves.

Therefore, an actual power of 8.6MWecan be supposed to be generated by the turbine in both systems, but with very different turbine sizes and investment costs. It should be noticed, however, that in a traditional plant several technological issues related to the strong temperature variability of the off-gas should be addressed to effectively recover its energy. Furthermore, given the reduced variability of steam properties at the turbine inlet in the case of the smoothing system plus the proposed boiler installation, a greater electrical efficiency of the turbine can also be expected, thus increasing the benefits on final energy recovery. Taking into account efficiency loss due to turbine partial load operations, fouling of exchange surfaces, and auxiliary equipment requirements, we can estimate to generate a net electrical power of about 6MWe, if the smoothing module plus the described recovery system are installed.

Referring to steel production, a final amount of 57 kWhe/ton can therefore be recovered. Given an electrical energy consumption of 396 kWhe/ton for the EAF of our reference case, 14.4% saving on electrical energy supply can be gained.

3.4.6 Economic analysis

By inserting the proposed PCM-based smoothing system and energy recovery equipment, the investment and operation costs reported in Table 3.10 should be faced. The estimated total cost of the smoothing system, including installation, is about € 430,000, as provided by a local manufacturer. For an energy recovery of 48,000 MWhe/year and a power supply cost equal to 80 €/MWhe, as reported by local steel plants, the cost savings are about 3,840,000 €/year. To this amount, possible incentives for energy efficiency (white certificates or EEC) should be added whenever available. Current Italian value of white certificates is about 103 €/TOE [138], equivalent to 19.26 €/MWhe on the basis of the Italian conversion factor for EEC calculation. This leads to about 924,500 €/year revenue for the first 5 years. The simple pay-back period is therefore 3.97years.

If the smoothing system is not installed, the investment cost for the increasing boiler and turbine size required to exploit maximum temperatures has been estimated by local suppliers to be € 16,500,000. Thus, an increase of about € 2,700,000 should be faced in comparison to the same plant equipped with the PCM-based system, whose cost is only € 430,000.

Table 3.10 Cash flows of the smoothing module plus energy recovery system.

INVESTMENT COSTS	
PCM-based smoothing system [€]	430,000
Boiler and steam turbine group [€]	13,800,000
Other costs (design, safety, etc.) [€]	1,070,000
OPERATIONAL COSTS	
Maintenance cost [€/yr]	758,500
Personnel cost [€/yr]	150,000
INCOMES	
Electrical energy savings [€/yr]	3,840,000
Energy efficiency certificates [€/yr]	924,528

Other investment costs should also be added for heat storage and/or other equipment required to manage temperature variability in the absence of the proposed smoothing module. Furthermore, due to lower turbine efficiency, energy savings should be reduced accordingly.

3.4.7 Conclusions

The off-gas temperature variability typical of EAFs in the steel industry can be drastically reduced by exploiting the characteristics of PCMs for high temperatures such as metals. The proposed smoothing system is made by concentric pipes containers filled with aluminium and positioned in the settling chamber; the location of the device and its simple structure allow a non-invasive intervention on the off-gas cleaning section with minimum plant modification and costs. The performed simulations show that, by a proper configuration of the PCM containers, structural stress as well as aluminium overheating can be controlled.

The profile of off-gas is significantly smoothed, allowing the adoption of a downstream recovery system based on a traditional Rankine cycle. The particular boiler structure with insertion of cyclones for dust abatement allows high thermal exchange efficiency with reduced space requirements. More favourable conditions of steam at turbine inlet are also granted, thus increasing the turbine efficiency due to reduced partial load operations. Furthermore, excessive oversizing of the turbine to face high steam temperatures can be avoided, with benefits on investment costs. With reference to 2011, Italian steel production by EAFs was 18.8 Mt/year [139], for an estimated energy consumption of quite 8270 GWhe/year. The adoption of the proposed system has a potential energy saving of more than 1065 GWhe/year for a percentage equal to 12.9%. This in turn is equal to 0.34% of the whole Italian electricity consumption, with related benefits on national GHG emissions targets.

3.5 Thermo-mechanical analysis of PCM container

In this section, an analytical and numerical approach to evaluate thermal stress in the cylindrical PCM container used for temperature smoothing of waste gas of Electric Arc Furnace (see Section 3.4) is developed. Thermal analysis shows that temperature distribution in the PCM system can be considered as uniform at any time instant according to the lumped capacitance method; the thermal behaviour of PCM system is thus simulated as a sequence of steady state analyses. Mechanical analysis adopts an axialsymmetric plane analytical model to compare elastic thermal stress distribution for different stainless steels and to identify AISI 316 as the most suitable material for the PCM container. A simple two-bars model and a stress index are also used to allow a physical understanding and a satisfactory interpretation of the PCM system response. Mechanical analysis shows that thermal stresses exceed the yield point of both stainless steels used in the container. A finite element elastic-plastic model is then developed to estimate the extension of the plastic zone. Finally, an alternative geometry based on concentric pipes is designed to keep the maximum stresses in the PCM container below the yielding point. A sensitivity analysis shows that the most relevant design parameters of the alternative geometry are the diameter of inner pipe and thickness of the external pipe.

3.5.1 Introduction

The PCM device designed in section 3.4 is formed by a set of PCM systems, in which aluminium is encapsulated in a steel cylinder in direct contact with the surrounding waste gas. The PCM systems are vertically aligned and hung to the rooftop of the settling chamber by an appropriate hooking system (see Figure 3.29a). The outer surface of each PCM system is then subjected to a corrosive environment and to a thermal load, which is mainly due to convection from waste gas. The PCM system is then exposed to thermal loads that vary during the steelmaking process. The thermal expansion coefficient of the contained aluminium is higher than that of the containment material; this mismatch then gives rise to thermal stresses in the PCM container, which can affect its structural integrity.

To the author’s knowledge, design procedures and regulations specifically dedicated to high-temperature applications of this kind of components (cylindrical geometry and PCM

expansion in solid phase) are not available in the literature. Some examples available in literature analyse expansion of PCM in liquid phase usually in spherical containers [140,141] and rarely in cylindrical container [142]. This section then aims to propose a simplified methodology for the thermo-mechanical analysis of a PCM system when in solid state, which would also allow identifying the most relevant design parameters for subsequent experimental validation.

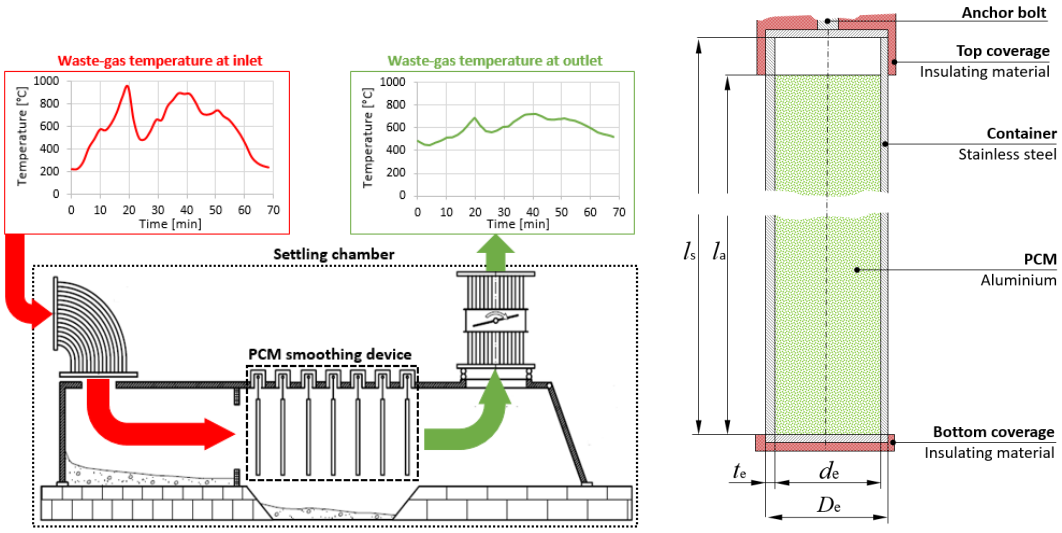

Figure 3.29 a) PCM-smoothing device and b) geometry of the PCM system.

The thermo-structural behaviour of the PCM container is then investigated by a simple analytical thermo-elastic model, followed by an elasto-plastic finite element approach. A simple two-bars model and a stress index are also derived, to allow a physical understanding and a satisfactory interpretation of the PCM system response. This simplified methodology has been privileged over a more complex modelling approach, as it allows the obtained results to be directly used in the design.

After a short description of the PCM system, the section describes the analytical and numerical model used to study its thermo-mechanical behaviour. Finally, an alternative design that improves the structural thermo-mechanical behaviour is proposed.

3.5.2 The PCM system

The PCM smoothing device is based on the phase change phenomenon, which for pure materials and eutectic alloys occurs with a heat exchange at constant temperature (i.e. the

phase change temperature). When the waste gas temperature is greater than the phase change temperature, the PCM absorbs heat from waste gas, whose temperature then decreases. At the opposite, waste gas temperature increases when it is lower than phase change temperature (the PCM then releases heat). The combination of these two effects leads to a smoothing of waste gas temperature, which tends to stabilise at the phase change temperature. The temperature-smoothing effect becomes as more effective as the average temperature of the waste gas (about 600°C) is closer to the phase change temperature, which then becomes one criterion to choose the PCM.

Other thermo-physical properties of PCM (e.g. latent heat of fusion and thermal conductivity) have also to be considered as choice criteria. A high latent heat of fusion is desirable to increase the energy storage capacity of the PCM system, while a high thermal conductivity assures a fast response to waste gas temperature variation.

To summarise, the best PCM should have a high latent heat, high thermal conductivity and a melting point close to waste gas temperature. These criteria identify the aluminium as the best candidate for PCM, as it has the melting point ($T_{m,a}$ = 660 °C) close to the average waste gas temperature ($T_{av,g}$ = 600°C), a high latent heat of fusion (H_a = 396 kJ/kg) and a high thermal conductivity (λ_a = 211 W/m K).

In the PCM system, the PCM material is encapsulated by a steel container (see Figure 3.29b). A PCM device is composed by a set of PCM systems vertically aligned and hung to the rooftop of the settling chamber by an appropriate hooking system, as shown in Figure 3.29a. The hooking system allows the containers to oscillate in order to prevent accumulation of dust, which could hamper the waste gas flow. Table 3.11 reports the main characteristics of the component shown in Figure 3.29b.

Table 3.11 Geometric parameters of the PCM system

Outer diameter, D_e (mm)	60.3
Inner diameter, d_e (mm)	52.3
Thickness, t_e (mm)	4.0
Container length, l_s (m)	3.2
PCM length, l_a (m)	3.0

In the PCM device, all PCM systems are in direct contact with the surrounding waste gas; thus, they are subjected to thermal loads, corrosion (due to combination of high

temperature and high concentration of chlorine compounds) and erosion (due to the high concentration of dust). In order to prevent overheating, the top and the bottom of the PCM container are protected by a coverage of insulating material, as sketched in Figure 3.29b. As reported in section 3.4, the bottom coverage hampers the generation of a thermal bridge between the external wall and the bottom of the container. The presence of corrosive compounds in the settling chamber and the high temperature of the waste gas suggest the use of stainless steel as the most suitable material for the PCM container.

Among available steel grades, two candidates have been identified: austenitic (AISI 316) and ferritic (AISI410S) stainless steel. Their temperature-dependent mechanical properties can be found in Eurocode 3 [143] and are listed in Table 3.13. Such stainless steels have differences in elastic modulus E and coefficient of thermal expansion α, which affect in a different way the thermal stresses generated in the PCM system. The stainless steel that is most suitable as PCM container will be identified by the analytical model developed in section 3.5.4. The typical duty cycle of the PCM system is characterised by a start-up phase where the PCM temperature increases, a running phase where phase change occurs, followed by a switch-off phase where the PCM system is brought back to room temperature.

During the start-up phase, the PCM system is heated from room temperature up to the melting point of the contained aluminium. During this phase, the aluminium always remains at solid state. Since the coefficient of thermal expansion of the steel container is lower than that of the PCM (Table 3.13), it is expected that the maximum stresses in the PCM container will be generated during the start-up phase, which will be then investigated in the next Sections.

During the running phase, instead, the PCM is subjected to phase change (melting or solidification); the coexistence of both liquid and solid states leads to a drastic reduction of PCM mechanical properties (in fact, the PCM in liquid state has almost null mechanical properties). Therefore, the mechanical stresses in the steel container are very small, as they are only due to gravity effects (i.e. the weight of PCM and steel container) and metallostatic pressure. Finally, the mechanical response of the PCM system during the switch-off phase, when the PCM system comes back to solid state, is almost similar to the start-up phase.

Table 3.12 Thermo-physical properties of PCM system and waste gas

PCM – Aluminium	
Thermal conductivity (Solid State), λ_a (W/mK)	211
Melting temperature, $T_{m,a}$ (°C)	660
Latent heat of fusion, H_a (kJ/kg)	396
Density, ρ_a (kg/m^3)	2750
Container – Stainless Steel	
Thermal conductivity, λ_s (W/mK)	17
Density, ρ_s (kg/m^3)	7810
Waste gas	
Reference temperature, T_{ref} (°C)	20
Average temperature, $T_{av,g}$ (°C)	600
Convective heat transfer coefficient, h_{conv} (W/m^{2}K)	50÷100

The real temperature trends in Figure 3.29a, which lead to melting of PCM, suggest that the thermo-mechanical response of the PCM system should be studied by a transient analysis with phase change. From one hand, this modelling would greatly increase the complexity of the analysis, at the expense of high computational cost, which both are not very suitable to industrial needs. Furthermore, a complex modelling approach might also hinder the understanding of the basic mechanisms that govern the system thermo-mechanical response, as well as the identification of the relevant design parameters. It is then desirable to find out a simplified modelling approach, which matches high accuracy and low computational cost.

On the other hand, the results of Appendix A, which will be discussed later in the section, will clearly show how a transient analysis with phase change is actually not necessary in the computation of thermal stresses, as the highest stresses occur only at the start-up phase, when the PCM is solid, whereas much lower stresses occur when the PCM is liquid. In addition, the thermal analysis presented in the next Section will further confirm how a sequence of steady-state analyses with uniform temperature in the PCM system is a quite good approximation of a transient thermal analysis. This conclusion thus fully justifies the thermo-mechanical analysis developed in the next Sections, which considers the PCM container at different temperatures limited to the range of the start-up phase, where the PCM is solid.

3.5.3 Thermal analysis

In the start-up and switch-off phases, the thermal response of the system can be modelled as a problem of transient conduction. According to [144], the simplest and most

convenient method that can be used to solve transient heating and cooling problems is the lumped capacitance method, which assumes that the temperature of a solid body is spatially uniform at any instant during a transient process.

In order to check the conditions that guarantee a reasonable accuracy of this method, it is necessary to estimate the Biot number Bi of the PCM system, defined as the ratio of internal thermal resistance R_{int} and external thermal resistance R_{ext} (see Figure 3.30a):

$$\text{Bi} = \frac{R_{\text{int}}}{R_{\text{ext}}} \tag{3.5}$$

If Bi<0.1, the error associated by using the lumped capacitance method is small and the assumption of uniform temperature within the PCM system can be made with a negligible error. It has to be considered that the PCM system at the back receives less heat as compared to that at the front area of the arrangement of Figure 3.29a. Therefore, each PCM system is characterized by a different Biot number. According to the lumped capacitance method, the smaller the Biot number, the more accurate is the assumption of uniform temperature in the body at any time instant. Therefore, only the PCM system with the highest Biot number has to be checked.

The highest Biot number occurs when the internal thermal resistance is maximum R_{int} (i.e. thermal conductivity of the materials is minimum) and the external thermal resistance R_{ext} is minimum (i.e. heat transfer coefficients of the waste gas are maximum).

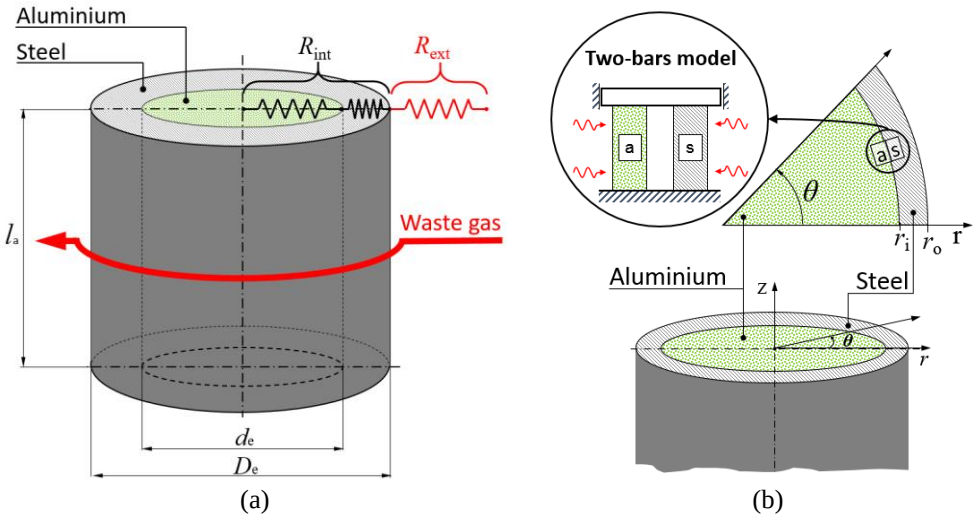

(a) (b)

Figure 3.30 a) Thermal model and b) structural model of the PCM system

The internal thermal resistance R_{int} depends on the resistance to conduction within the materials and the contact resistance at their interface, as expressed in equation (3.6).

$$R_{\mathrm{int}} = \frac{L_{\mathrm{a}}}{\lambda_{\mathrm{a}}} + \frac{L_{\mathrm{s}}}{\lambda_{\mathrm{s}}} + \frac{1}{h_{if}} \tag{3.6}$$

where L is a characteristic length associated with the length scale corresponding to the maximum spatial temperature difference, which for the aluminium part is $L_a = d_e/2$ and for the steel part is $L_s = (D_e\text{-}d_e)/2$. Symbols λ_a and λ_s represent the thermal conductivity of aluminium and steel, respectively, while h_{if} represents the interfacial heat transfer coefficient at aluminium/steel interface. In [145], interfacial heat transfer coefficients have been measured for several metal castings in cylindrical steel moulds. In [145], the interfacial heat transfer coefficients have been measured in several metal castings, where melting and solidification occurred in a cylindrical steel mould, exactly as the melting and solidification in the PCM system. Thus, a good estimation of the maximum contact resistance at the aluminium/steel interface in the PCM system can be obtained considering the minimum h_{if} measured in [145], which reports a minimum value of h_{if} =5000 W/m^{2}K for an almost pure aluminium casting in a vertical cylindrical steel mould. The maximum value of R_{int}=5.59E-04 m^{2}K/W results by using the data in Table 3.12, in which the thermal conductivity of the austenitic stainless steel AISI 316 is used because it is the lowest one among selected steels. According to equation (3.7), the external thermal resistance R_{ext} depends on heat transfer coefficients of convection h_{conv} and radiation h_{rad}, which are related to the PCM system arrangement.

$$R_{\mathrm{ext}} = (\, h_{\mathrm{conv}} + \, h_{\mathrm{rad}})^{-1} \tag{3.7}$$

The thermal analysis considers the PCM system where the heat transfer coefficients are maximum. Estimations carried out in section 3.4 showed that the maximum convection heat transfer coefficient h_{conv} of about 100 W/m^{2}K is achieved in the first row of the PCM system arrangement. As reported in [146], radiation heat transfer coefficient h_{rad} of EAF off-gas can be estimated as:

$$h_{\mathrm{rad}} = k e_{\mathrm{g}} e_{\mathrm{e}} \chi \frac{T_{\mathrm{g}}^4 - T_{\mathrm{e}}^4}{T_{\mathrm{g}} - T_{\mathrm{e}}} \tag{3.8}$$

where k is the Stefan-Boltzmann constant, e_g is the emissivity of the waste gas, e_e is the emissivity of the external surface of the PCM system, T_g is the waste gas temperature and T_e is the temperature of the external surface of the PCM system. The dampening factor χ takes into account the influence of dust load; in order to guarantee a conservative calculation, it can be set to 1. Radiation heat transfer is strongly tied to the emission coefficient of the waste gas e_g, which depends on several factors (temperature, chemical composition, total pressure, partial pressure of gas species and domain geometry). In particular, chemical composition is the most important factor that affects e_g. In fact, only absorbing/emitting gases (e.g. water vapour and carbon dioxide) contribute significantly to the radiation heat transfer, while the contribution of nonabsorbing/emitting gases (e.g. nitrogen) is negligible. Waste gas at settling chamber inlet is usually composed by three components: CO_2 (30%), H_2O (20%) and N_2 (50%) [146]. Thus, according to [147], the emission factor of waste gas can be calculated as:

$$e_g = e_{CO_2} + e_{H_2O} - \Delta e \tag{3.9}$$

where Δe is a correction factor, which takes into account the overlap of the individual emission bands of the gases involved. For what concerns the emission factor e_e of the external surface of the PCM system, it can be considered very close to 1. Based on the data provided in section 3.4, the maximum heat transfer coefficient of waste gas radiation h_{rad} results equal to 26 W/m^{2}K and, according to equation (3.7), the minimum external resistance results R_{ext} = 7.94E-03 m^{2}K/W.

The estimated maximum R_{int} and minimum R_{ext} give a maximum Biot number of the PCM system equal to 0.07, which is lower than 0.1. Thus, the internal thermal resistance R_{int} can be neglected and each PCM system can be assumed, with a negligible error, to be at uniform temperature. Since the PCM system has a very small Biot number, the system temperature can be considered almost uniform at any time instant of start-up and switch-off phases. In such phases, the thermal behaviour of PCM system can thus be simulated as a sequence of steady state analyses. The hypothesis of steady-state thermal analysis and uniform temperature distribution in the PCM system, which is used in the thermo-mechanical analysis of the following Sections, has been further justified by the transient numerical simulation presented in Appendix A.

3.5.4 Analytical model

Before facing an elastic-plastic analysis, which will be described in section 0, it is useful to preliminary evaluate the thermo-mechanical response of the PCM system by a simple linear elastic analysis. An analytical model is then employed to estimate the thermal stress distribution in the PCM system and to identify the most suitable stainless steel for the PCM container.

According to the conclusions of the thermal analysis in section 3.5.3, the PCM system is at almost uniform temperature at any time instant. No thermal gradient then occurs along the axial direction. This allows the thermo-mechanical behaviour of the system to be studied by a plane model, as shown in Figure 3.30b. In addition, the axial symmetry of both geometry and thermal loads (i.e. temperature is symmetrical about the centre) allows using the "axialsymmetric plane model" of Timoshenko [148]. This plane model derives the analytical expressions for the radial σ_r and tangential (or hoop) σ_θ stresses. The axial stress σ_z, instead, can range from plane stress $\sigma_z=0$ (free axial thermal expansion) to plain strain condition $\sigma_z\neq0$ (totally constrained axial thermal expansion), depending on the axial boundary condition applied to the PCM system. The plane stress and plain strain conditions are called the "plane circular disk" and "long circular cylinder" in [148].

In the PCM system, however, the axial stress σ_z is also influenced by the mismatch in the axial thermal expansion of aluminium and steel parts, which also gives rise to a shear stress τ_{rz} at the aluminium/steel interface (note, instead, that $\tau_{\theta z}= \tau_{\theta r}=0$ for symmetry). This shear stress τ_{rz} tends to prevent the free sliding, and thus the free axial thermal expansion, of the aluminium part over the steel container (in fact, the aluminium expands more than steel under the same temperature change). The shear stress is, then, also directly influenced by the value of friction coefficient at the aluminium/steel interface.

Table 3.13 Structural properties of the materials [143,149]

	Elastic Modulus, *E* [GPa]							Thermal expansion, α [10^{-5}/K]	Poisson ratio, ν
Temperature [°C]	*20*	*100*	*200*	*300*	*400*	*500*	*550*	-	-
Aluminium	70	68	60	48	28	14	0	2.3	0.34
AISI 316 - Austenitic	200	192	184	176	168	160	154	1.7	0.3
AISI 410S - Ferritic	220	211	202	194	185	176	172	1.0	0.3

This complex situation makes difficult to identify which axial boundary condition (plane stress or plane strain), and thus which axial stress σ_z, can reasonably be assumed in the analytical model of the PCM system. An answer is then given by a preliminary numerical study that has been performed by the plane axisymmetric finite element model described in Appendix B. The obtained results, shown in Figure B.1 (Appendix B), confirmed that the plane stress hypothesis, where the axial stress σ_z=0, is a reasonable assumption for the analytical model of the PCM system.

In the "axialsymmetric plane model", the general expressions of radial σ_r and tangential σ_θ stresses, as well as radial displacement u, are:

$$\sigma_r(r) = -\alpha E \frac{1}{r^2}\int_a^r \Delta T r dr + \frac{E}{1-\nu^2}\left[C_1(1+\nu) - C_2(1-\nu)\frac{1}{r^2}\right] \tag{3.10}$$

$$\sigma_\theta(r) = \alpha E \frac{1}{r^2}\int_a^r \Delta T r dr - \alpha E \Delta T + \frac{E}{1-\nu^2}\left[C_1(1+\nu) + C_2(1-\nu)\frac{1}{r^2}\right] \tag{3.11}$$

$$u(r) = (1+\nu)\alpha \frac{1}{r}\int_a^r \Delta T r dr + C_1 r + \frac{C_2}{r} \tag{3.12}$$

where r is the radial coordinate, a is the inner radius, E is the elastic modulus, ν the Poisson coefficient and α the coefficient of thermal expansion. The temperature increment is $\Delta T = T(r) - T_{ref}$, where $T(r)$ is the temperature distribution in the body and T_{ref} a reference temperature. In the above equations, symbols C_1, C_2 are unknown parameters that depend on the applied boundary conditions.

Section 3.5.3 emphasised that, at each time instant in start-up and switch-off phases, the PCM system can be considered at a uniform temperature, which means that $T(r) = T_\Gamma$ = const. is the system temperature at time instant Γ. The temperature increment is also constant, $\Delta T = T_\Gamma - T_{ref}$.

For the system in Figure 3.30b, which is formed by two different materials, two sets of three equations must be defined: one set for aluminium, one set for steel. For the part of domain filled with aluminium, it is $a = 0$ (solid disk); the surrounding domain related to the container (steel), it is $a = r_i$. According to [148], for a solid disk $C_2 = 0$, in order that the displacement $u_a(r)$ is zero at the centre $r = 0$. Thus, this gives the following expressions:

$$\begin{cases} \sigma_{r_a}(r) = -\alpha_a E_a \dfrac{\Delta T}{2} + \dfrac{E_a}{1-\nu_a^2}\left[C_{1,a}(1+\nu_a)\right] \\ \sigma_{\theta_a}(r) = -\alpha_a E_a \dfrac{\Delta T}{2} + \dfrac{E_a}{1-\nu_a^2}\left[C_{1,a}(1+\nu_a)\right] \\ u_a(r) = (1+\nu_a)\alpha_a \dfrac{\Delta T}{2} r + C_{1,a} r \end{cases} \tag{3.13}$$

$$\begin{cases} \sigma_{r_s}(r) = -\alpha_s E_s \dfrac{\Delta T}{2}\left(1-\dfrac{r_i^2}{r^2}\right) + \dfrac{E_s}{1-\nu_s^2}\left[C_{1,s}(1+\nu_s) - C_{2,s}(1-\nu_s)\dfrac{1}{r^2}\right] \\ \sigma_{\theta_s}(r) = -\alpha_s E_s \dfrac{\Delta T}{2}\left(1+\dfrac{r_i^2}{r^2}\right) + \dfrac{E_s}{1-\nu_s^2}\left[C_{1,s}(1+\nu_s) - C_{2,s}(1-\nu_s)\dfrac{1}{r^2}\right] \\ u_s(r) = (1+\nu_s)\alpha_s \dfrac{\Delta T}{2}\dfrac{r^2-r_i^2}{r} + C_{1,s} r + \dfrac{C_{2,s}}{r} \end{cases} \tag{3.14}$$

Equation (3.11) shows that, in the aluminium domain, the state of stress is plane hydrostatic, as the radial and hoop stresses are equal and also constant in the whole domain. The remaining three unknown parameters $C_{1,a}$, $C_{1,s}$, $C_{2,s}$ can be determined by imposing the appropriate boundary conditions:

$$\sigma_{r,s}(r_o) = 0 \tag{3.15}$$
$$\sigma_{r,a}(r_i) = \sigma_{r,s}(r_i) \tag{3.16}$$
$$u_a(r_i) = u_s(r_i) \tag{3.17}$$

The above expressions represent zero radial stress (3.15) at outer stress-free surface of the domain, the continuity of radial stresses (3.16) and the continuity of radial displacement (3.17) at the interface $r = r_i$.

The conditions in equations (3.15)-(3.17), combined with the expressions in equations (3.13)-(3.14), allow one to calculate closed-form analytical equations for the parameters $C_{1,a}$, $C_{1,s}$, $C_{2,s}$:

$$C_{1,a} = \frac{\Delta T(1-\nu_a)\alpha_a\{r_i^2(1-\nu_s) + r_o^2(1+\nu_s) + [2\psi\xi - \xi(1+\nu_a)](r_o^2 - r_i^2)\}}{2[r_i^2(1-\nu_s) + r_o^2(1+\nu_s)] + \xi(1-\nu_a)(r_o^2 - r_i^2)} \tag{3.18}$$

$$C_{1,s} = \frac{\Delta T(1-\nu_s)\alpha_a[\psi\xi(1-\nu_a)(r_o^2 - r_i^2) + \psi(1+\nu_s)(r_o^2 - r_i^2) + 2r_i^2]}{2[r_i^2(1-\nu_s) + r_o^2(1+\nu_s)] + \xi(1-\nu_a)(r_o^2 - r_i^2)} \tag{3.19}$$

$$C_{2,s} = \frac{\Delta T r_i^2(1+\nu_s)\alpha_a\{[\psi\xi(1-\nu_a) - \psi(1-\nu_s)](r_o^2 - r_i^2) + 2r_o^2\}}{2[r_i^2(1-\nu_s) + r_o^2(1+\nu_s)] + \xi(1-\nu_a)(r_o^2 - r_i^2)} \tag{3.20}$$

where $\psi = \alpha_s/\alpha_a$ and $\xi = E_s/E_a$ are dimensionless coefficients, which account for the difference in material properties between aluminium and steel. Note that in the hypothesis of same material in the whole PCM system, it is $\psi = \alpha_s/\alpha_a$ and $\xi = E_s/E_a$. Accordingly, the expressions (3.13)-(3.14) give a stress $\sigma_{r,a} = \sigma_{\theta,a} = 0$ and $\sigma_{r,s} = \sigma_{\theta,s} = 0$ in the whole

domain, which coincides with the results given in [148] for the case of solid cylinder and then confirms the correctness of the previous equations.

The distribution of tangential σ_θ and radial σ_r stress in aluminium and steel container can be computed by expressions (3.13)-(3.14) with the coefficients in (3.18)-(3.20). The temperature increment $\Delta T = T_\Gamma - T_{ref}$ is calculated by considering the temperature T_Γ at time instant Γ in the start-up or switch-off phase; in this study, the reference temperature is $T_{ref} = 20$ °C. The axial stress is found, instead, by a simple equilibrium condition along the axial direction. In fact, as previously said, the PCM system is free to expand along its axis, thus the axial stress σ_z in the container is only generated by the total weight of the system. Considering the parameters in Table 3.11, the axial stress is $\sigma_z = 0.5$ MPa and it can be neglected for practical purposes.

Figure 3.31a reports an example of stress distribution in the PCM system at temperature $T_\Gamma = 200$ °C. The stress distribution in the steel container is similar to that in a cylindrical vessel under internal pressure. The radial stress σ_r is compressive within the whole PCM system; it is constant in the aluminium, continuous at the aluminium/steel interface, while it decreases to zero at the outer radius of the container. The tangential stress σ_θ is also compressive in the aluminium (where it overlaps to radial stress), while it becomes tensile in the steel container (i.e. a discontinuity occurs at aluminium/steel interface). The compressive stresses inside the aluminium are then balanced by the tensile tangential stresses in the steel container. The axial stress σ_z is almost zero in the whole domain.

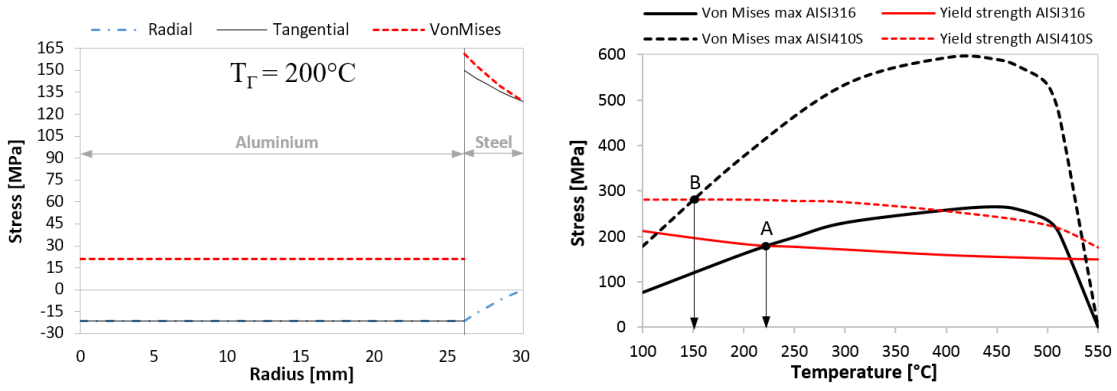

(a) (b)

Figure 3.31 a) Example of stress distribution in PCM system at temperature TΓ =200 °C, steel is AISI 316; b) yield strength and maximum Von Mises stress at inner radius, as a function of temperature TΓ, for the two considered stainless steels

The stress distribution in Figure 3.31a, which occurs in start-up and switch-off phases, can be explained by the mismatch in mechanical properties of aluminium and steel (e.g. coefficient of thermal expansion and elastic modulus). The aluminium has a coefficient of thermal expansion greater than that of steel, which leads aluminium to expand more than the container. This thermal expansion, however, is hindered by the steel container, because of its much higher elastic modulus at any temperature (see Table 3.12). The stress distribution then depends on the mechanical properties of the steel grade used for the container. Figure 3.31a also plots the distribution of the equivalent Von Mises stress:

$$\sigma_{\mathrm{vm}} = \sqrt{\sigma_{\mathrm{r}}^2 + \sigma_{\theta}^2 - \sigma_{\mathrm{r}}\sigma_{\theta}} \tag{3.21}$$

in which the axial stress σ_z has been neglected. The maximum Von Mises stress is located at the inner radius of the steel container, where plastic strain is then expected to occur. This is the most critical point in the PCM system, which has to be monitored in the design. Similarly to the overall stress distribution, also the maximum Von Mises stress depends on the steel type, as shown in Figure 3.31b.

To understand the mechanical behaviour of PCM system during the start-up and switch-off phases, it is of interest to plot the maximum Von Mises stress $\sigma_{\mathrm{vm,max}}$ at each temperature T_Γ reached in such phases (T_Γ = 100÷660 °C).

Figure 3.31b shows that Von Mises stress has a nearly parabolic profile, with a peak around 450°C, where the combination of thermal expansion and mechanical constraint reaches its maximum effect.

The analysis also highlights how the Von Mises stress in AISI410S steel is more than double to that generated into AISI316 steel. This stress difference can be explained by considering that AISI410 steel has a lower coefficient of thermal expansion and a higher elastic modulus than those of AISI 316 steel (see Table 3.12). Figure 3.31b also compares the maximum Von Mises stress to the yield stress σ_y of each steel type considered as container material; it can be observed that, at any temperature, the AISI 316 steel has a yield stress lower than that of AISI410S steel. Yielding occurs at the temperature T_y where the maximum Von Mises stress $\sigma_{\mathrm{vm,max}}$ reaches the yield stress $\sigma_y(T)$. Figure 3.31b shows that yielding occurs at T_y = 150°C for the AISI410S (point B) and at T_y = 225°C for the

AISI316 (point A). For temperatures $T > T_y$ plastic strain begins and, of course, the Von Mises stress calculated by the elastic model is no longer representative of the state of stress in the container. Therefore, the most suitable stainless steel for the container is AISI 316, because its lower stress levels allow the container to behave elastically over a temperature range wider than that of AISI410S.

The mechanism that generates thermal stresses in PCM system can be interpreted and further explained by using the simple two-bars model in Figure 3.30b, which has been suggested by Manson [150]. This mechanical model exemplifies the tangential (hoop) displacements of two small elementary elements of aluminium and steel, located at the interface between aluminium and steel in the PCM system. The two bars, connected at both ends, expand under a temperature increase ΔT.

In the model, the total strain is $\varepsilon_{tot} = \varepsilon_{th} + \varepsilon_{mec}$, where $\varepsilon_{th} = \alpha \Delta T$ is the thermal strain for a temperature variation $\Delta T = T_\Gamma - T_{ref}$ and ε_{mec} is the mechanical strain, which is responsible for the stress $\sigma = E \varepsilon_{mec}$.

In the simplified two-bars model, the amount of thermal strain $\varepsilon_{th} = \alpha \Delta T$ is proportional to the temperature change ΔT and to the coefficient of thermal expansion of the material α. The thermal strain induces a thermal expansion of the system, which, however, can be limited partially, depending on the imposed amount of mechanical constraint.

A free thermal expansion occurs when no mechanical constraint is imposed, which in turn gives no mechanical strain and stress in the system. The amount of mechanical constraint imposed on thermal strain depends, of course, on the mechanical stiffness of the system (e.g. elastic modulus and geometry).

It is then clear that the mechanical strain ε_{mec} (which generates the stress) depends on the relative contribution of thermal expansion and imposed mechanical constraint. Two limiting cases exist: i) free thermal expansion with no mechanical constraint (which gives a stress-free situation) and ii) totally constrained thermal expansion (which gives rise to the maximum stress). In the case of no mechanical constraint on thermal expansion, the total strain equals the thermal strain $\varepsilon_{tot} = \varepsilon_{th}$ and the mechanical strain is zero $\varepsilon_{mec} = 0$, with no stress on the system; this situation describes the free thermal expansion without

any mechanical stress. Conversely, in the case of totally constrained thermal expansion, the total strain is zero $\varepsilon_{tot} = 0$ and all the thermal strain is converted into mechanical strain $\varepsilon_{mec} = -\varepsilon_{th} = -\alpha\Delta T$, which then becomes directly proportional to the temperature variation (the higher the temperature, the higher the stress).

In the PCM system, both aluminium and steel container tend to expand for an imposed temperature variation. The constraint on the free thermal expansion of the aluminium is imposed by the surrounding steel container; this constraint, however, is partially relaxed by the thermal expansion of the steel container itself. On the other hand, the imposed constraint also depends on the stiffness (i.e. elastic modulus) of both materials, which in turn decreases with temperature. A result, the PCM system is in a halfway condition between the two limit cases explained above and the amount of thermal stress depends on several parameters of the PCM system, as well as on temperature.

The governing equations of the two-bars model and the resulting thermal stresses are derived in Appendix C. Based on the stress equations (C.4) and (C.5), all the relevant parameters that control the amount of thermal stress in the steel container can be conveniently summarised in the following stress index:

$$i = \frac{(\alpha_a - \alpha_s)\Delta T}{1 + \xi} \tag{3.22}$$

which is obtained from the expression (C.5) by assuming an equal area ($A_a = A_s$) for the two bars. In expression (3.22), $\Delta T = T_\Gamma - T_{ref}$ is the imposed temperature variation, α_a, E_a and α_s, E_s are, respectively, the coefficient of thermal expansion and elastic modulus for aluminium and steel, evaluated at temperature T_Γ. The assumption of equal area is justified by considering that the two-bars model represents two small elementary elements (see Figure 3.30b) of same geometry: this allows the index i to evaluate the effect of material properties on the coupling at the interface, regardless of the particular geometry of the PCM system.

The stress index i can provide a simple, although approximate, estimate of the severity of thermal stresses that could develop in the PCM steel container, depending on the materials used. The higher the index i, the higher the thermal stresses expected in the system. An index $i = 0$ means that no thermal stress would develop in the steel container.

Quite intuitively, the stress index i is proportional to the difference $(\alpha_a - \alpha_s)$ in thermal expansion coefficients, to quantify that thermal stress is proportional to the mismatch in thermal strain that occurs in different materials subjected to the same temperature change ΔT. The higher the difference $(\alpha_a - \alpha_s)$ is, the higher the thermal strain mismatch and thus the resulting thermal stresses. If both materials had identical thermal strains (which occurs when $\alpha_a = \alpha_s$), the stress index would be $i = 0$ and no stress would virtually develop in the system, irrespective of the values of the elastic moduli E_a, E_s of both materials. The stress index i also depends on the ratio $\xi = E_s/E_a$, to quantify that thermal stress depends on the mechanical constraint imposed on thermal strain.

The ratio ξ is also a function of temperature. For example, when aluminium approaches its melting temperature $T_{m,a}$, its elastic modulus E_a becomes so small compared to E_s, that the ratio ξ diverges to infinity and the stress index $i \rightarrow 0$, with no stress in the steel container (see Figure 3.32). Conversely, at lower temperature the ratio ξ is higher, which means that steel container is so stiff to prevent the thermal expansion of the contained aluminium, and a higher thermal stress develop, see Figure 3.32. Owing to its simple expression, the stress index i can be very useful for a sensitivity analysis on materials properties, which allows a preliminary comparison among different materials in the choice of the best material for the PCM container.

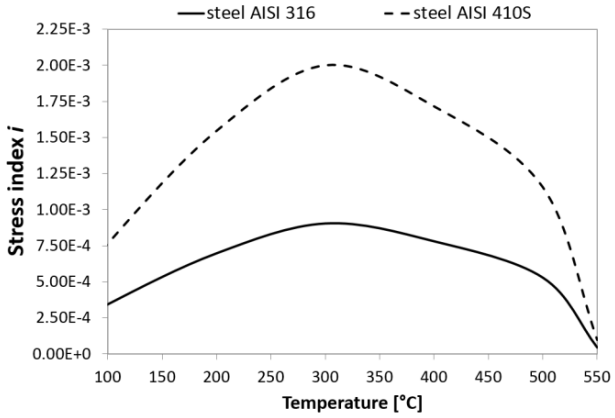

Figure 3.32 Comparison of the stress index i for the steels AISI 316 and AISI 410S.

As an example, Figure 3.32 shows the comparison of the stress index i calculated for the AISI316 and AISI 410S steels, with the materials properties in Table 3.13. The similarly of the trends in Figure 3.32 with the results in Figure 3.31b is evident, which confirms the validity of the two-bars model.

3.5.5 Elastic-plastic model

The results in the previous section have shown that the stresses in the container exceed the yield point of the considered steels for temperature higher than 120°C for the AISI410S and higher than 200°C for AISI316, respectively. An elastic-plastic model of the container is then required to study the behaviour of the component during the whole start-up phase and to estimate the extension of the plastic zone.

The finite element method is used to analyse the thermo-mechanical elastic-plastic behaviour of the thin circular disk model. The results of the elastic model identified the AISI 316 steel as the most suitable containment material among the considered steels and justified the hypothesis of plane stress, which can thus be employed also in the elastic-plastic model.

The one quarter finite element model, shown in Figure 3.33a, adopts 4-nodes isoparametric linear elements to discretise both aluminium and steel parts. A mapped mesh is used for the container domain and the aluminium close to the interface, a free mesh is used elsewhere. The thermal analysis is first carried out to compute the temperature in each node; the calculated nodal temperatures are then input as thermal loads in the next mechanical analysis.

A numerical uncertainty analysis has initially been performed to assess the approximation errors of the finite element solution. In particular, a convergence analysis on the element size has been carried out to identify at which element size the solution of the finite model in Figure 3.33a becomes grid independent. On the other hand, it has to be noted that the model has a very simple geometry (without notches or geometrical discontinuities), that a refined mesh is not necessary. Subsequently, the correctness of the finite element solution has also been verified by comparison with the results of the theoretical model of section 3.5.4 (an error of less than 1% was observed, which is fully acceptable). Unfortunately, a comparison with experimental data is not possible, as to our knowledge experimental data for this type of PCM configuration are not available.

As evidenced in section 3.5.3, it is possible to consider the system at uniform (steady state) temperature at any given time instant. This consideration allows simulating the thermo-mechanic behaviour of the component by a sequence of steady state analyses. In

the thermal analysis, the applied thermal load is simply a uniform temperature on the whole finite element model. In the mechanical analysis, symmetry boundary conditions are applied as shown in Figure 3.33a; the hypothesis of plane stress is considered. An elastic-perfectly plastic material model has been used for aluminium and steel. A small positive value of the hardening modulus has been set to obtain convergence of the numerical solution. All thermal and mechanical properties are considered to be temperature dependent, as in Table 3.13.

Figure 3.34a reports the profile of the Von Mises stress distribution of Figure 3.33b along a radial direction; the distribution of radial, tangential and axial stresses are also shown. The trends in Figure 3.34a are actually similar to those in Figure 3.31a. In the elastic-plastic results, however, a lower tangential stress σ_θ is observed at the inner radius, where the maximum Von Mises stress is equal to the yield stress.

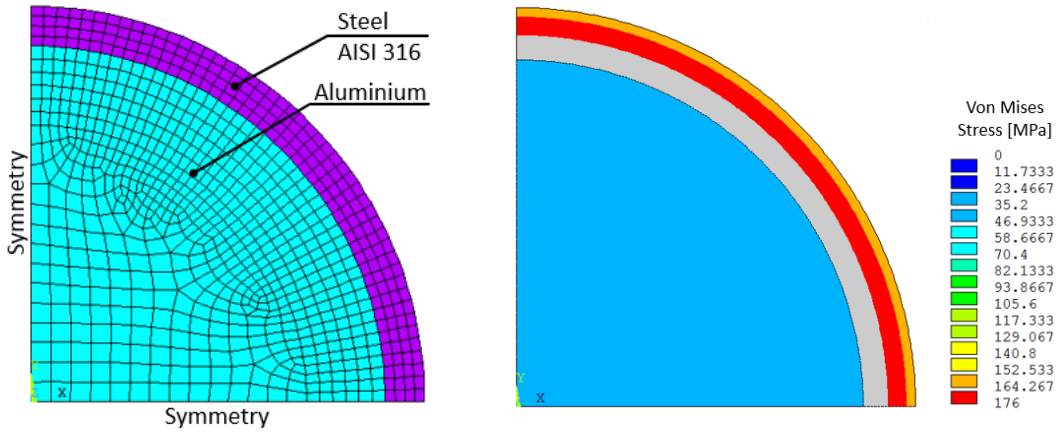

Figure 3.33 a) Finite element model and b) plastic strain (grey colour) of the container at 250 °C

The comparison between the Von stress calculated by the FEM model and the elastic analytical model is reported in Figure 3.34b. In particular, the maximum Von Mises stress at the inner radius r_i and the Von Mises stress at the outer radius r_o of the container are reported in Figure 3.34b; the yield stress of the stainless steel AISI 316 is also shown.

Figure 3.34b shows that the plastic deformation of the container starts at 225 °C (point A) from the inner radius and it expands along radial direction as the temperature increases; the complete plastic deformation of the whole thickness is reached at 275°C (point A').

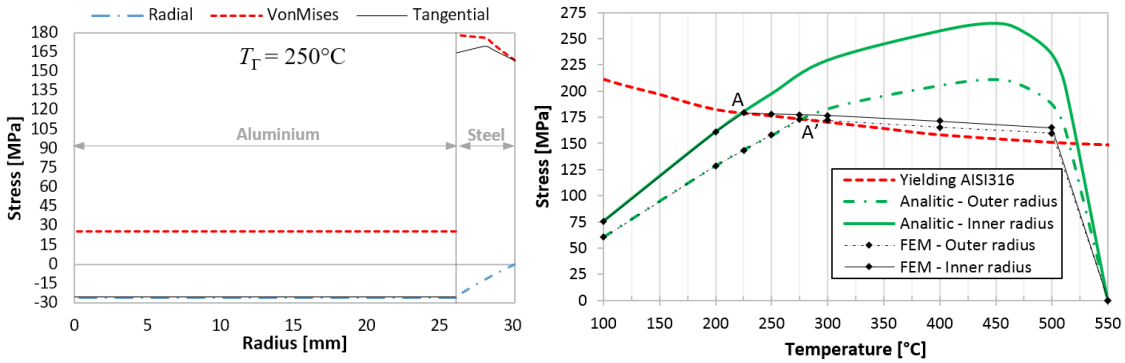

(a) (b)

Figure 3.34 a) Stress distribution as radius function and b) comparison between Von Mises stress distribution of the elastic analytical model and the elastic-plastic FEM model

In the elastic-plastic model, a preliminary evaluation of component structural integrity can be performed by comparing the maximum elastic-plastic strain to the material fracture strain. The graph in Figure 3.34b allows considering that at a temperature of about 500 °C the maximum elasto-plastic strain is 1.79e-3, which is far below the fracture strain ε_f = 0.4 of AISI316 at 500 °C [143]. It can be concluded that the component can resist to a single phase of start-up.

3.5.6 Alternative design of PCM container

The previous analysis highlighted that the proposed PCM container geometry, sketched in Figure 3.29b, leads to plastic deformation of the considered steel. However, it is desirable to individuate a PCM container geometry that allows the steel to work within the elastic field. The design of the alternative configuration has also to be as simple as possible to guarantee a low manufacturing cost.

The proposed alternative configuration (Figure 3.35a) consists of two concentric cylindrical containers (pipes) in stainless steel AISI316, where the hollow cavity is filled by PCM.

For a sake of comparison, the diameter of the external pipe is maintained equal to the diameter D_e= 60.3 mm of the initial configuration. The internal pipe is named as *reduction pipe*, as its purpose is to reduce the volume available to PCM, and it can be used to hang the container to the settling chamber roof. The dimensions of the reduction pipe (outer diameter and thickness) are design parameters that are investigated by a sensitivity analysis. The new geometrical configuration is studied by exploiting the elastic-plastic

finite element model developed in section 3.5.5. A mapped mesh is now used in the whole domain (see Figure 3.35b).

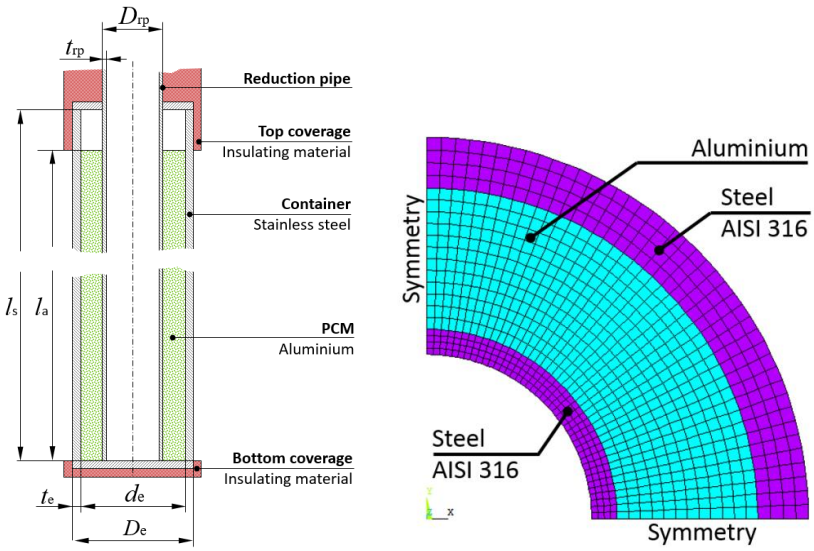

Figure 3.35 a) Alternative configuration with concentric pipes and b) its finite element model

First, a sensitivity analysis by varying the diameter of the reduction pipe, in the range D_{rp} = 20÷40 mm, has been carried out, to find that diameter that allows the steel of the external pipe to work within the elastic field. In the sensitivity analysis, the reduction pipe has a thickness t_{rp} = 2 mm, while the external pipe maintains the same thickness t_e = 4 mm of the initial configuration of Figure 3.29b.

Figure 3.36a shows the maximum Von Mises stress as a function of temperature, for different values of diameter D_{rp} of the reduction pipe; the yield stress of AISI 316 is also reported. For diameters D_{rp} < 30 mm, plastic deformation still occurs in steel of the external pipe; for diameters D_{rp} > 30 mm, instead, yielding does not occur at any temperature and the steel of the external pipe works in the elastic field. For each diameter D_{rp} > 30 mm, Figure 3.36a allows individuating the temperature at which the maximum Von Mises stress is reached in the elastic domain; this temperature is defined as "critical temperature" T_{crit} and, for all diameters, it is equal to 400 °C.

Figure 3.36a shows an example of sensitivity analysis for the configuration with diameter D_{rp} = 35 mm of the reduction pipe. The plot shows that the thermal stress is mainly

influenced by the thickness t_e of the external pipe, while the effect of the thickness t_{rp} of reduction pipe is actually negligible.

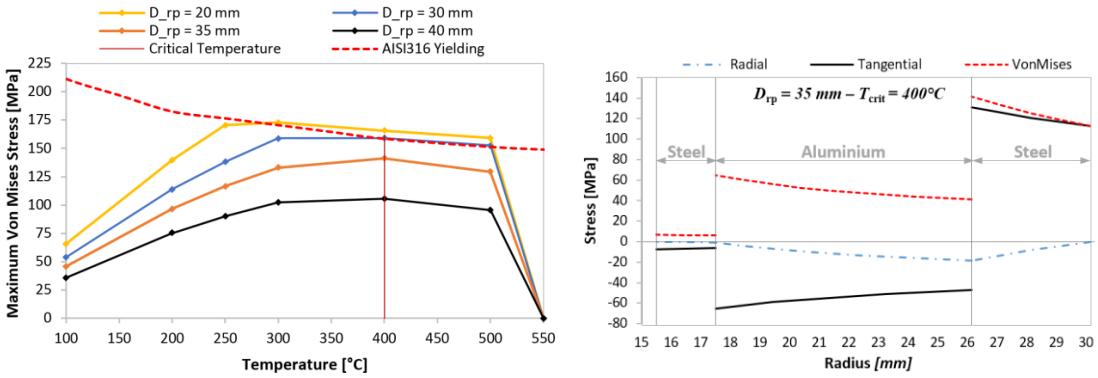

(a) (b)

Figure 3.36 a) Maximum Von Mises stress at different temperature and reduction diameter D_{rp}; b) stress distribution as a function of radius, for D_{rp} =35 mm and T_{crit} = 400 °C

The smallest thickness t_{rp} = 1 mm of the reduction pipe is chosen as it gives the lighter weight of the structure while assuring low stresses (axial stress due to the component weight σ_z< 0.5 MPa and stress generated by the aluminium expansion $\sigma_{vm,max}$ < 10 MPa). The thickness of 1 mm has then been used as a reference value to define the "allowable configurations", which are all the geometrical configurations where the container works in the elastic field. The design of the whole PCM system is first based on thermo-physical parameters, mainly represented by the ratio of external surface of heat exchange A_{est} to the aluminium mass m_{Al}. Figure 3.36b shows an example of allowable configurations for the external thickness t_e = 4 mm in terms of diameter ratio D_{rp} /D_e and as a function of the ratio A_{est}/m_{Al}. Figure 3.36b shows a typical design chart to identify the allowable configurations; in particular, the figure reports the diameter ratio D_{rp} /D_e as a function of A_{est}/m_{Al} for a given external thickness t_e=4 mm and for different external diameters D_e.

3.5.7 Conclusions

This section presented an analytical and numerical approach to evaluate thermal stress in a phase change material (PCM) system, used for temperature smoothing of waste gas of Electric Arc Furnace. Thermal analysis showed that the Biot number of the PCM system is less than 0.1 and therefore the PCM system can be assumed, with a negligible error, to be at uniform temperature at any time instant. This isothermal condition allowed

the thermo-mechanical behaviour of the system to be simulated by a sequence of steady-state analyses.

The mechanical analysis based on axialsymmetric plane analytical model allowed to compare elastic thermal stress distribution for AISI410S and AISI316 stainless steels and to identify the latter as the most suitable material for the PCM container. The simple two-bars model and a stress index are used to explain the thermal stress distribution in the PCM system and the nearly-parabolic profile of Von Mises stress over temperature. Mechanical analysis showed that thermal stresses exceed the yield point of both stainless steels used in the container. Therefore, a FEM analysis has been carried out to evaluate the elastic-plastic behaviour of the component. The results showed that a total plastic deformation of the container can occur even during a single start-up phase, where the PCM system is heated from room temperature up to the melting point of PCM. An alternative geometrical configuration with concentric cylindrical containers (pipes) has finally been designed to avoid plastic deformation in the steel container. A sensitivity analysis on some design parameters allowed identifying diameter of the reduction pipe D_{rp} and thickness of the external pipe as the main design parameters that control the amount of thermal stress in the PCM system.

3.6 Active PCM-based device for temperature smoothing

In this section, the concept developed in section 3.4 is extended to a continuous charge EAF process with scrap preheating. In addition to this, a heat transfer fluid flowing through containers is introduced and selected by developing an analytical model. The introduction of the heat transfer fluid enables the adoption of smaller pipe diameters while overcoming overheating issues.

The performance of the improved smoothing system is analysed by thermo-fluid dynamic simulations. The reduced maximum temperature of off-gas allows the reduction of the size and investment cost of the downstream energy recovery system, while the increased minimum temperature enhances the steam turbine load factor, thus increasing its utilization. Benefits on environmental issues due to dioxins generation are also gained.

3.6.1 Process description and methodology

After preheating the scrap charge as in direct recovery, off-gas enters the PCM smoothing device which reduces its temperature variability, so that downstream indirect recovery by steam generation and power production is enabled.

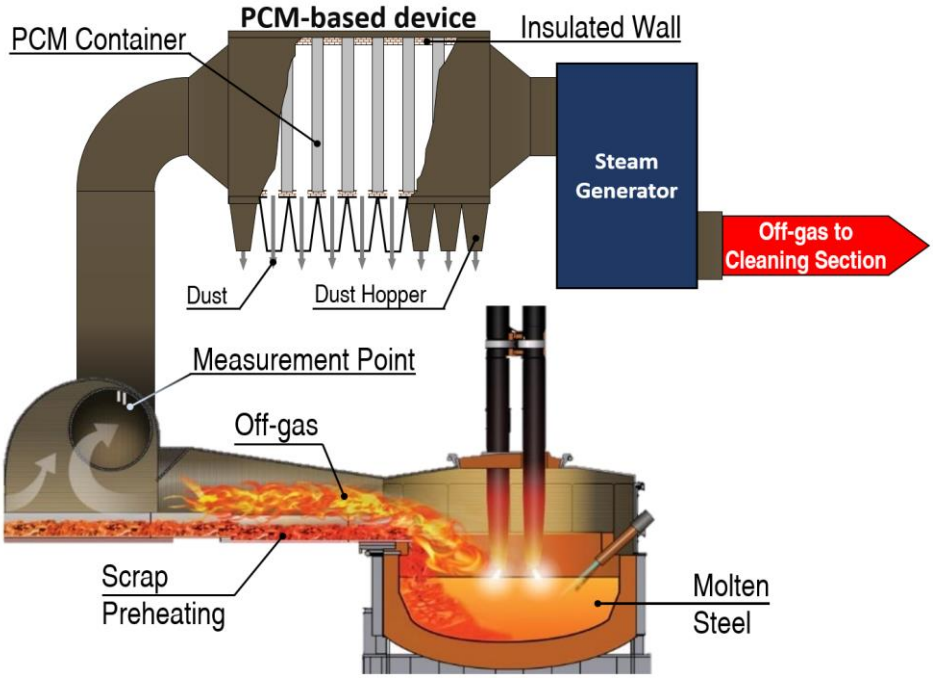

Figure 3.37 Continuous charge EAF with scrap preheating and the PCM-based smoothing system

A continuous charge EAF process is considered: before reaching the furnace, the scrap metal enters a preheating section moving counter to off-gas exiting the EAF (see Figure 3.37) as in Consteel system. According to [151], controlling the carbon content in the bath by feeding hot metal continuously and with an automated pouring/tilting device seems to be the most efficient way to achieve the maximum benefits in terms of operational safety, chemical control, and foamy slag practice, with effects on energy and refractory consumption.

Comparing to the discontinuous charge system analysed in section 3.4, the TTT cycle time is reduced from about 60 min to 40 min. The continuous charge with scrap preheating, in fact, keeps the steel bath in the EAF constantly liquid and the scrap entering the furnace is melted by immersion; since it is not working on solid scrap such as in batch charges, the arc is stable and a faster process can be achieved [151].

Furthermore, the off-gas temperature profile is modified, with a higher average temperature, a lower maximum ΔT, and a slightly reduced variance with respect to section 3.4. This can be ascribed to both the different EAF process induced by continuous charging as described above, and to scrap preheating. The off-gas, in fact, enters the PCM smoothing device not immediately downstream the furnace, but after crossing the scrap preheating section (see Figure 3.37), where it releases a portion of its thermal energy.

Another difference to be accounted for lies on the significant reduced dust content of off-gas: a 30-40% decrease compared to batch charged furnaces can be recognized accordingly to [151]. Heavy particle matter is, in fact, intercepted by the scrap bed in the preheating section, thus reducing downstream slagging and fouling issues. The proposed PCM-based smoothing system is located at the end of the preheating line within a dedicated chamber with insulated walls, as represented in Figure 3.37.

The deployment of the methodology adopted to develop the PCM-based energy recovery system is shown in Figure 3.38, involving a preliminary analysis followed by system improvement. In the first stage, the process characterisation in terms of temperatures and flow rate of the off-gas exiting the preheating line is carried out and the reference TTT cycle is identified. Based on this profile, the preliminary system sizing and layout can be

performed, introducing typical space and technology constraints of steel plants. System performances are then analysed by creating suitable models for CFD simulations.

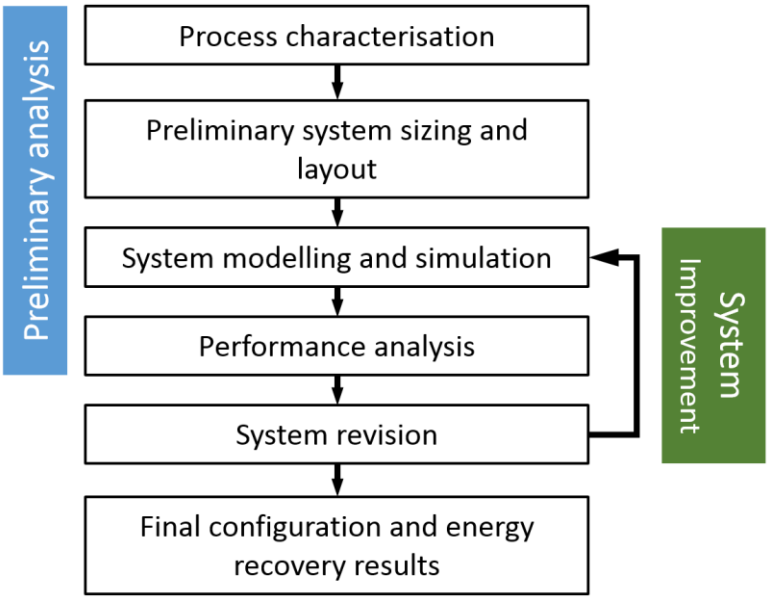

Figure 3.38 Deployment of the PCM-based energy recovery system development

Based on current results, system improvements are identified and introduced by developing new analytical and CFD models, in order to evaluate the revised system configuration. The iterative procedure is repeated until a satisfactory final configuration of the system is achieved; energy recovery results can be derived and the feasibility of the proposed system can be assessed.

3.6.2 Preliminary analysis

3.6.2.1 Process characterization

The characterization of the process should be based on off-gas temperature and flow rate profiles, which can be derived from literature or actual data on the field. In the case of a measurement campaign in real steel plants, the measurement point should be located after the preheating line as represented in Figure 3.37. Data collection should be addressed in order to identify the most representative working day of the month, in terms of specific recoverable energy per tons of "good billet" (steel that satisfies a minimum level of quality).

Figure 3.39 shows the typical temperature and flow rate profiles measured after the preheating line of a continuous charge EAF with a production capacity of 80-90 tons per TTT cycle.

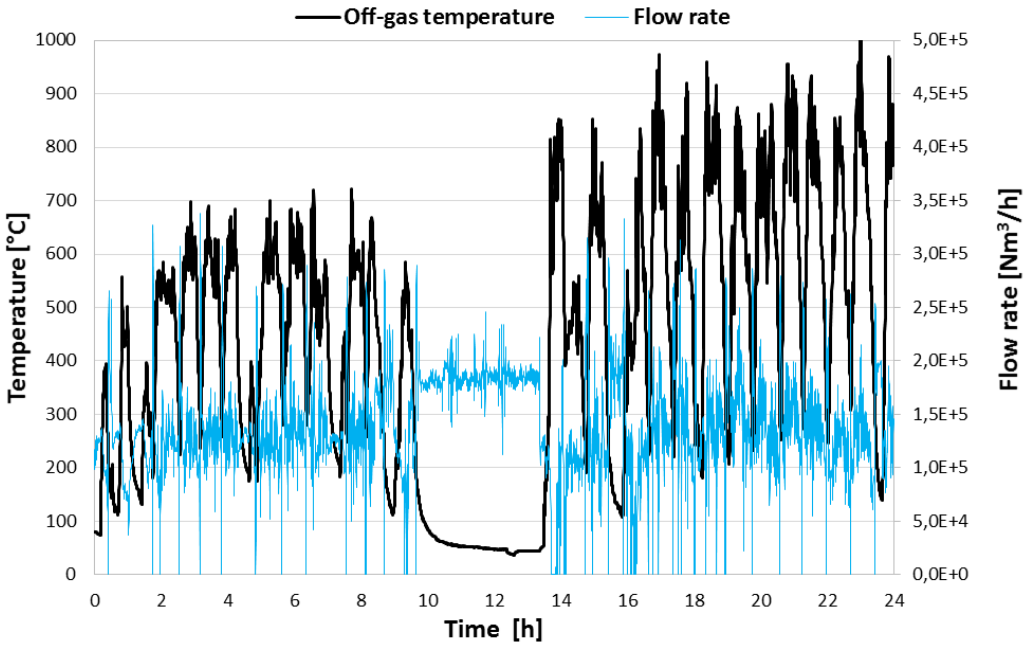

Figure 3.39 Typical off-gas temperature and flow rate profile in a continuous charge EAF process with scrap preheating during a representative working day

Departing from process profiles, the most energy intensive cycle (see Figure 3.40) should be identified as the reference cycle for the preliminary configuration of the PCM system.

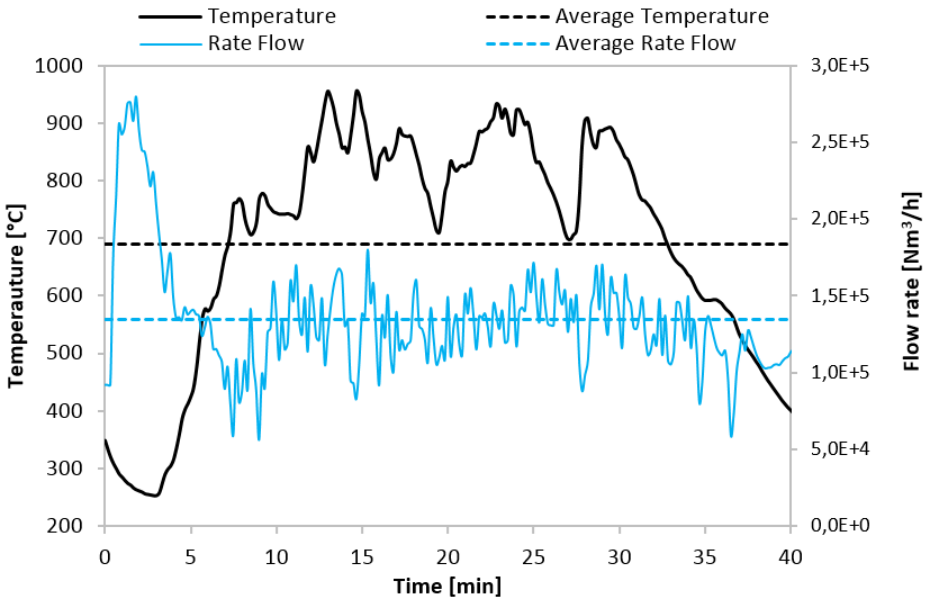

Figure 3.40 The reference cycle

3.6.2.2 Preliminary system sizing and layout

Based on the identified reference cycle (Figure 3.40), the preliminary sizing is carried out considering the average values of off-gas flow rate and temperature. With the purpose of limiting the erosion effect due to the even high dust content in the off-gas, the average inlet speed of 8 m/s has been set as design specification to calculate the flow section of the smoothing device. Finally, a maximum height of the system due to common installation space issues in steel plants has been identified. The final specifications adopted in this study are reported in Table 3.14.

Table 3.14 Design specifications and flow section size

Design specifications	Average flow rate [Nm^3/h]	134,639
	Average temperature [°C]	690
	Average inlet speed [m/s]	8.0
	Maximum height [m]	3.5
Flow section size	Width [m]	4.7
	Area [m^2]	16.5

The longitudinal size of the PCM based device depends on the PCM mass, the geometrical configuration of a PCM container, and the layout of PCM containers. Based on the reference cycle, the maximum required mass of PCM can be calculated by dividing the off-gas thermal energy potentially released to PCM (i.e. thermal energy at temperatures higher than PCM melting point) by the PCM latent heat of fusion (refer to section 3.4 for in-depth description). Aluminium has been selected as PCM since it is characterized by a favourable melting temperature, which is very close to the average off-gas one, and by high values of thermal conductivity, thermal diffusivity, thermal capacity, and latent heat of fusion. It also presents low values of density and costs, while no particular system safety problems arise when managing solid/liquid aluminium.

As concerns the geometrical configuration, the PCM container is composed by two coaxial pipes of stainless steel. Accordingly to [70]**,** stainless steel has been selected as container material due to its high resistance to both off-gas and PCM corrosion. The cylindrical geometry has been chosen because it allows to increase heat exchange surfaces, thereby optimizing the process from the point of view of both recovery efficiency and cost (see section 3.4). Moreover, the geometrical configuration of the

container takes into account the thermo-structural stresses generated by the difference between the thermal linear expansion coefficient of steel and of aluminium. This leads to the choice of stainless steel AISI 316 as container material for the external pipe, since it has the highest coefficient of thermal linear expansion, while for the internal pipe a cheaper stainless steel, such as AISI 304, can be employed. Based on previous results reported in section 3.4, the aligned layout is chosen in order to minimize load losses. The geometry of the PCM containers and their layout are shown in Figure 3.41.

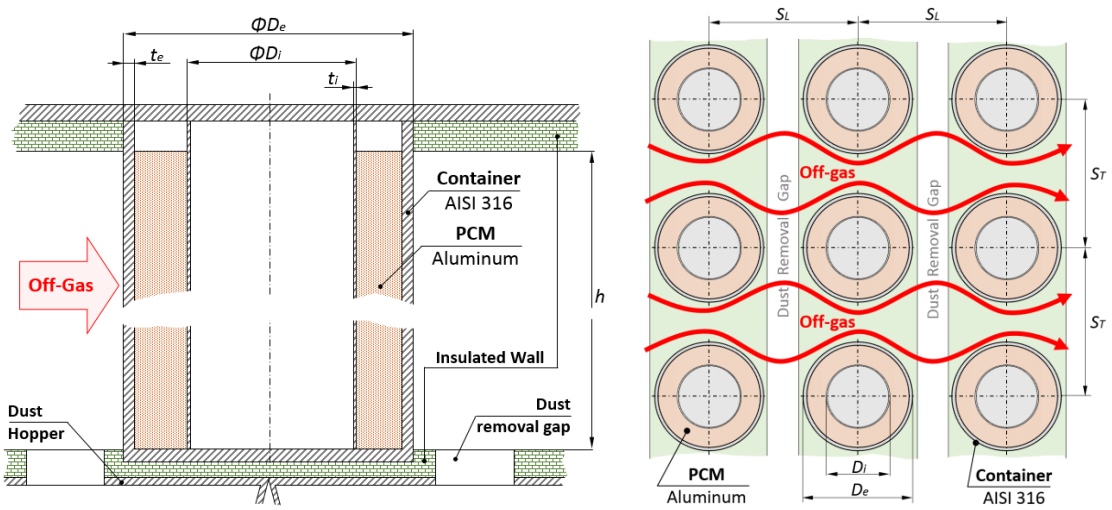

Figure 3.41 Geometry of the PCM containers: a) lateral view and b) bottom view

3.6.2.3 System modelling

In order to identify the parameters which more deeply affect system performance, three different configurations of the system (see Table 3.15) have been evaluated by thermo-fluid dynamic simulations.

A reference configuration has been defined (configuration R40) basing on the results obtained in section 3.4, from which the other two configurations are derived. In particular, given the total PCM mass, configuration R23 keeps the layout parameters (S_T/D_e, S_L/D_e in Table 3.15) unchanged while increasing the size of PCM containers. Configuration R53, instead, maintains the geometrical sizes of containers, while modifying their location, i.e. layout parameters.

A generalized cycle has been developed basing on the features of the reference cycle in Figure 3.40. The generalization aims at simplifying the temperature profile, while

maintaining the same highest temperature, total energy, and the critical temperature gradient of the reference cycle (see Figure 3.42).

Table 3.15 Alternative system configurations

	R23	***R40***	***R53***
D_e external diameter [mm]	141.3	88.9	88.9
t_e external thickness [mm]	6.55	5.5	5.5
D_i internal diameter [mm]	85	52	52
t_i internal thickness [mm]	2	2	2
Number of containers	529	1400	1378
PCM mass per container [kg]	64.6	23.6	23.6
Total heat exchange surface [m^2]	822	1369	1347
S_T Transverse pitch [mm]	212	133	177.8
S_L Longitudinal pitch [mm]	212	133	177.8
S_F Flow pitch [mm]	71	44	89
S_T/D_e	1.5	1.5	2
S_L/D_e	1.5	1.5	2
Transversal Containers	23	35	26
Longitudinal Containers	23	40	53
h chamber height [m]	3.5	3.5	3.5
Minimum chamber length [m]	4.9	5.3	9.4

Transient numerical analyses of the three system alternatives reported in Table 3.15 have been carried out using the commercial finite-volume-based code ANSYS Fluent 15.0. The ANSYS Fluent enthalpy-porosity formulation, which is one of the most applied methods due to the advantage of the implicit treatment of the conditions on the phase change boundary [152], was adopted to model PCM solidification and melting. Since the solidification/melting model can be used only with the pressure-based solver, the Semi-Implicit Method for Pressure-Linked Equations (SIMPLE) has been employed. To simulate turbulent conditions, the widely used k-epsilon model, in conjunction with the enhanced wall treatment approach for the near-wall regions, has been employed.

For what concerns the spatial discretization, the following upwind schemes has been chosen in order to overcome the trade-off between accuracy and computational efforts:

- second order upwind scheme for the discretization of turbulent kinetic energy and dissipation rate equations;
- third order Monotone Upstream-Centered Schemes for Conservation Laws (MUSCL) to discretize energy equations;

- QUICK-type scheme, which is based on a weighted average of second-order-upwind and central interpolations of the variable, has been employed for the discretization of momentum equations.

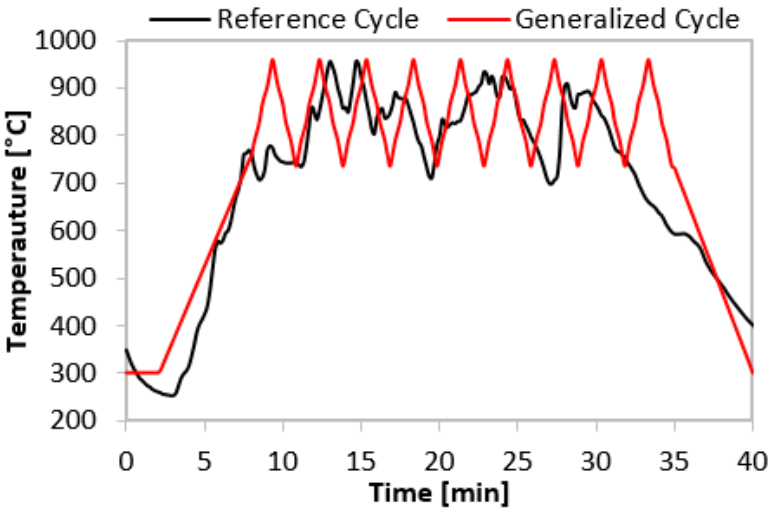

Figure 3.42 Generalized profile of off-gas temperatures in a TTT cycle

Due to the low ratio diameter/height of the PCM containers, 2D simulations were performed. Furthermore, computational domains have been reduced taking into account existing symmetries, in order to reduce computational effort as much as possible. Grid sizes and time steps adopted in the final simulations ensure that numerical results are almost independent of these parameters. Hybrid mesh, consisting of both triangular and quadrilateral elements, was adopted to discretize the boundary layer regions, while triangular elements were adopted for the rest of the fluid domain (off-gas); the hybrid mesh was refined towards the tube walls to comply the values of the dimensionless wall distances y^+ required for the wall enhancement treatment. Mapped mesh was employed for the solid domains (PCM and containers). Before the final runs, the independence of the results from grid and time-step was established on the basis of calculations in which the distance between grid points and the time step were progressively reduced from one simulation to another. When further reductions in grid size, or in time steps, led to changes in the outlet temperature values smaller than 1 percent, the results were considered to be independent of the grid or of the time step, respectively.

The final computational grids consisted of 327,879 cells and the final time step was equal to 0.01 s. All solutions were obtained with normalized residuals less than 10^{-6}. Average values of material properties near the melting temperature were considered.

The PCM melting point temperature was assumed equal to 660 °C, while on the entire domain a temperature of 300°C was set as the initial condition, in order to reproduce the operative state after an ordinary stop (e.g. electrode change) of the steelmaking process. Moreover, the simplified inlet profile of Figure 3.42 has been used to simulate a series of three TTT cycles, in order to evaluate the time required by the system to reach the steady operative conditions (i.e. all the PCM is in phase change).

Performance analysis

Off-gas outlet temperature profiles for the three configurations (and the temperature inlet profile) have been obtained by CFD simulations (see Figure 3.43), as described in the previous subsection.

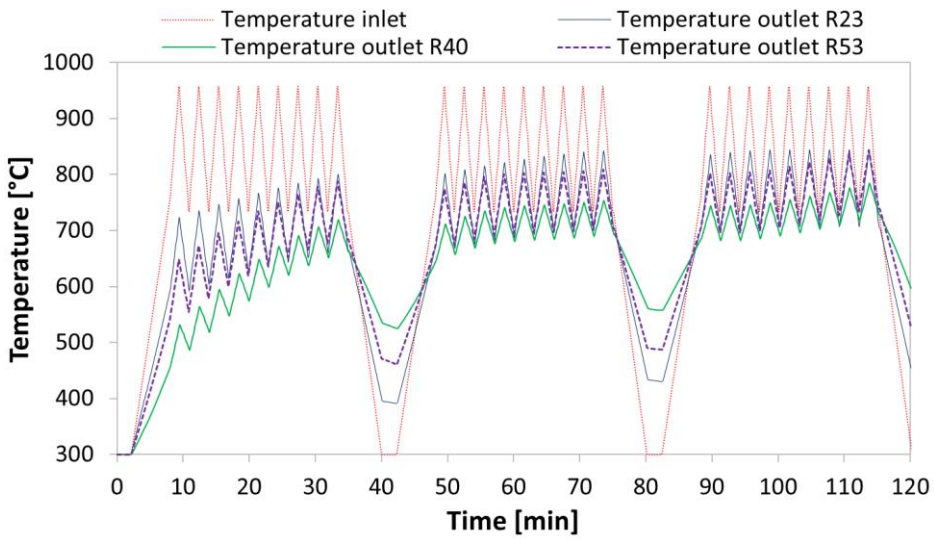

Figure 3.43 Off-gas temperature profile for different system configurations

The off-gas temperature profiles show an important reduction of the smoothing performance of the configuration R23 and R53 in comparison with the reference configuration R40. The performance reduction of the configuration R23, corresponding to an increased size of PCM containers, is due to the reduced available heat exchange surface in comparison to the reference configuration. For the configuration R53, related

to a greater flow pitch among containers, the reduction can be mainly ascribed, instead, to the resulting convection coefficient, which is lower than the R40 one.

In Figure 3.44 the PCM temperature profiles for the first row of containers in the three configurations are also represented. The configurations with lower diameters of PCM containers (R40, R53) show a better response time. On the other hand, the configuration R23, which is characterized by greater diameters, presents a higher resistance to overheating than the other configurations.

Therefore, the reference configuration R40 should be preferred in terms of smoothing potential and response time, but it leads to serious overheating issues which cannot be ignored. For this reason, with reference to the best performing configuration R40, in the next section the introduction of a heat transfer fluid to control PCM overheating is analysed.

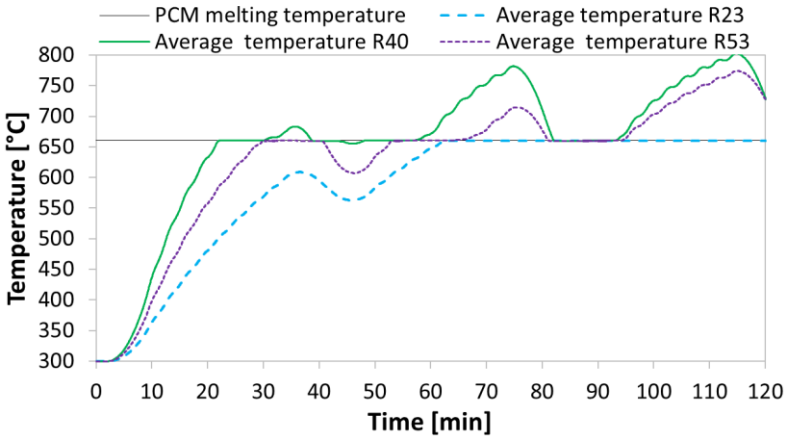

Figure 3.44 PCM temperature profiles for the first row of containers

3.6.3 System revision: introducing a heat transfer fluid through PCM containers

To overcome overheating issues, a proper heat transfer fluid (HTF) can be introduced in the revised system to actively control the PCM temperature. As shown in Figure 3.45, each PCM container is composed by two coaxial pipes: the gap between the internal pipe and the external one is filled with the phase change material, while the HTF flows through the internal tube, i.e. through a duct of circular cross-section. As can be seen in Figure 3.45a, D_i and d_i are the inner and the outer diameters of the internal pipe, respectively, while t_i is the internal pipe thickness.

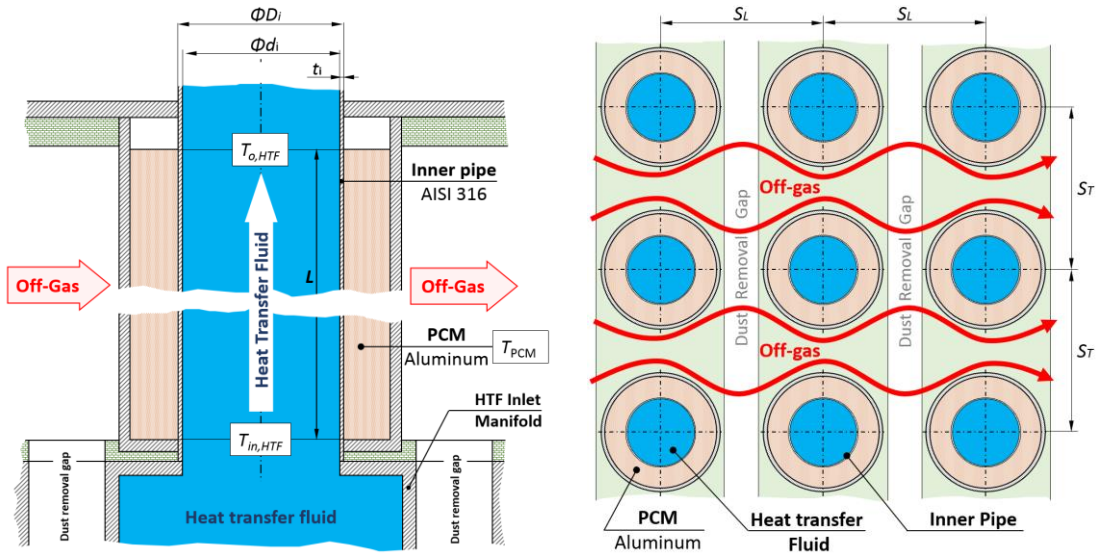

Figure 3.45 a) Lateral view of the HTF inside a PCM container and b) top view of the container layout and the relative HTF

System modelling and simulation

In the revised system, both the off-gas and the heat transfer fluid thermal performance have to be evaluated. Since during normal operating conditions the PCM is kept in phase change at its melting temperature, off-gas and HTF thermal analyses can be conveniently decoupled, being the heat transfer rate q exchanged between off-gases and HTF through the PCM the only connection parameter. For this reason, the heat transfer rate q is first calculated from CFD simulations of the off-gas/PCM system, then its value is exploited by an analytical model for the selection of the HTF.

From the off-gas point of view, the introduction of the heat transfer fluid can be taken into account in the CFD models described in subsection 0 by applying a proper Neumann boundary condition, i.e. a negative heat flux q'' on the inner surface of the internal pipe. A PCM temperature control strategy, aimed to avoid overheating, has been implemented in the numerical model by a user-defined function (UDF) coded in C, which can be dynamically loaded within the ANSYS Fluent solver to enhance its standard features. When the PCM temperature overcomes the melting point and reaches a temperature of 661 °C, the function applies a negative thermal flux on the internal containers wall until the PCM temperature returns to the melting point. Known parameters are the HTF inlet temperature $T_{\mathrm{in,H}}$, the PCM melting temperature T_{P},the operating HTF pressure p_{H}, the

internal tube geometry, i.e. the geometry of the channel through which the HTF flows, and the heat flux q'' that should be extracted from the PCM. The unknowns are the HTF outlet temperature $T_{\mathrm{out,H}}$ and the HTF average velocity v_{H}.

From the HTF point of view, the desired temperature control, obtained by imposing in the CFD simulations the negative heat flux q'', can be conveniently exploited to select a proper heat transfer fluid. To this purpose, an analytical model has been developed and implemented in Fortran 90, as reported in Figure 3.46.

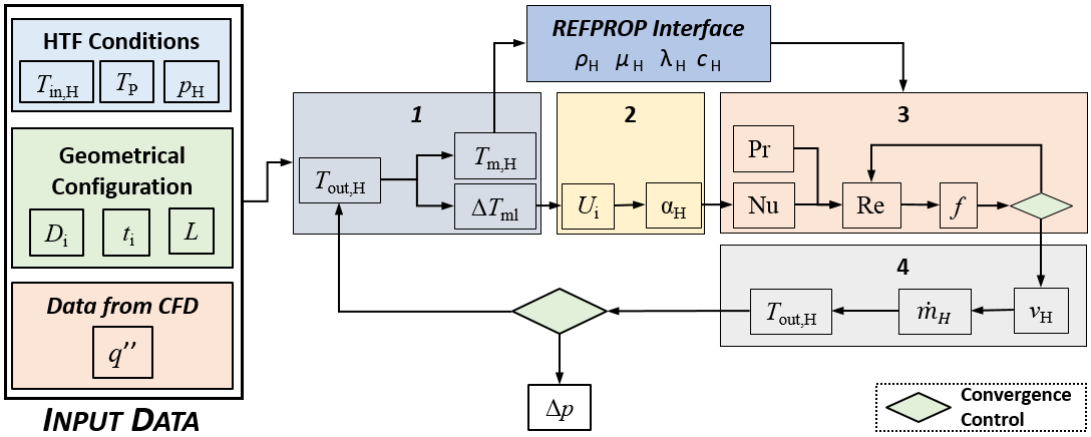

Figure 3.46 Deployment of the analytical model employed for HTF selection

The basic idea of the proposed procedure is that the overheating control system operates such as either the PCM is kept in phase change, thus behaving as a body of infinite specific heat capacity, or its temperature is kept as close as possible to its phase change temperature. Therefore, both the PCM and the cylindrical outer surface of the internal tube of diameter D_{i} can be assumed as isothermal at the PCM melting temperature T_{P}. Accordingly, the problem can be dealt with as a forced convection analysis in a tube with constant temperature on the tube outer surface and the heat transfer rate q between PCM and HTF can be calculated as [144]:

$$q = q''(\pi d_{\mathrm{i}} L) = U_{\mathrm{i}}(\pi d_{\mathrm{i}} L)\Delta T_{\mathrm{ml}} \tag{3.23}$$

where U_{i} is the overall heat transfer coefficient between the phase change material and the heat transfer fluid, defined in terms of the inner surface area of the tube $(\pi d_{\mathrm{i}} L)$, L is the length of heat exchange between PCM and HTF in each tube (see Figure 3.45) and ΔT_{ml} is the log mean temperature difference.

All the thermo-physical properties of the HTF in the following equations have been evaluated at the mean heat transfer fluid temperature $T_{\mathrm{m,H}}$ and at the operating heat transfer fluid pressure p_{H} using the software REFPROP (version 8.0), that has been conveniently interfaced with the Fortran code.

The following iterative procedure, schematized in Figure 3.46 for the sake of clarity, has been adopted to solve the problem.

1. First, a tentative HTF outlet temperature $T_{\mathrm{out,H}}$ is estimated in order to calculate the log mean temperature difference ΔT_{ml}

$$\Delta T_{\mathrm{ml}} = \frac{\left(T_{\mathrm{P}} - T_{\mathrm{in,H}}\right) - \left(T_{\mathrm{P}} - T_{\mathrm{out,H}}\right)}{ln\ \frac{T_{\mathrm{P}} - T_{\mathrm{in,H}}}{T_{\mathrm{P}} - T_{\mathrm{out,H}}}} \tag{3.24}$$

2. Then, the value of the overall heat transfer coefficient U_{i} is inferred from equation (3.25). Assuming the value $\lambda_{\mathrm{w}} = 23\ \mathrm{W/m\ K}$ for the thermal conductivity of the tube wall material, corresponding to the AISI 316 stainless steel at T_{P} [143], the HTF convection heat transfer coefficient α_{H} can be obtained from the definition of U_{i}:

$$U_{\mathrm{i}} = \frac{1}{\alpha_{\mathrm{H}}} + \frac{d_{\mathrm{i}}/2}{\lambda_{\mathrm{w}}} \ln\frac{D_{\mathrm{i}}}{d_{\mathrm{i}}} \tag{3.25}$$

   In equation (3.25) the overall heat transfer coefficient U_{i} includes both the contribution due to convection at the tube inner surface and the contribution due to conduction across the cylindrical tube wall. In the present case, the thin-walled tube has a large thermal conductivity and, therefore, the contribution due to conduction in expression (3.25) is very small.

3. Once the value of α_{H} has been obtained, the Nusselt number is calculated from its definition $\mathrm{Nu} = \alpha_{\mathrm{H}}\, d_{\mathrm{i}}/\lambda_{\mathrm{H}}$, where λ_{H} is the HTF thermal conductivity. At this point, the value of the Reynolds Number Re is calculated by means the widely known Gnielinski formula [153]:

$$\mathrm{Nu} = \frac{\left(\frac{f}{8}\right)(\mathrm{Re} - 1000)\mathrm{Pr}}{1 + 12.7\left(\frac{f}{8}\right)^{1/2}(\mathrm{Pr}^{2/3} - 1)} \tag{3.26}$$

where $\mathrm{Pr} = \mu_\mathrm{H}\, c_\mathrm{H}/\lambda_\mathrm{H}$ is the Prandtl number and c_H is the HTF specific heat at constant pressure. The Gnielinski correlation is valid over large Reynolds and Prandtl number ranges ($3000 \leq \mathrm{Re} \leq 5 \times 10^6$ and $0.5 \leq \mathrm{Pr} \leq 2000$). In equation (3.27) the friction factor f is calculated under the hypothesis of smooth tubes via the Petukhov correlation [154], valid over the same Reynolds number range of equation (3.26):

$$f = (0{,}790\ \ln \mathrm{Re} - 1{,}64)^{-2} \tag{3.27}$$

It should be noted that, since in equation (3.27) the value of the Reynolds number is not known a priori, a further iterative calculation is needed in this step of the procedure. The correlations adopted here are considered to be very accurate for turbulent convection heat transfer in circular tubes and, in the ranges of Reynolds and Prandtl numbers of interest for this work, their accuracy is within 10%.

4. Finally, the average HTF velocity v_H is inferred from the Reynolds number definition and the HTF mass flow rate $\dot{m}_\mathrm{H} = \rho_\mathrm{H} v_\mathrm{H} (\pi d_\mathrm{i}^2/4)$ is exploited in the heat balance for the duct:

$$q = \dot{m}_\mathrm{H} c_\mathrm{H} \left(T_{\mathrm{out,H}} - T_{\mathrm{in,H}}\right) \tag{3.28}$$

in order to provide an updated value of the outlet temperature $T_{\mathrm{out,H}}$.

In all the analyses carried out in this section, convergence has been reached in less than 20 iterations.

3.6.3.1 Performance analysis for heat transfer fluid selection

The desired control performance to overcome PCM overheating issues was achieved, after several trials, by applying in the CFD simulations a negative thermal flux q'' on the inner surface of the internal pipe equal to 15 kW/m^2. The resulting PCM temperature profiles are reported in Figure 3.47 together with those without HTF.

It can be clearly seen how for the first row of PCM containers, which faces the most critical off-gas condition, the introduction of the HTF leads to completely smooth the temperature profile of the PCM, while avoiding the overheating periods.

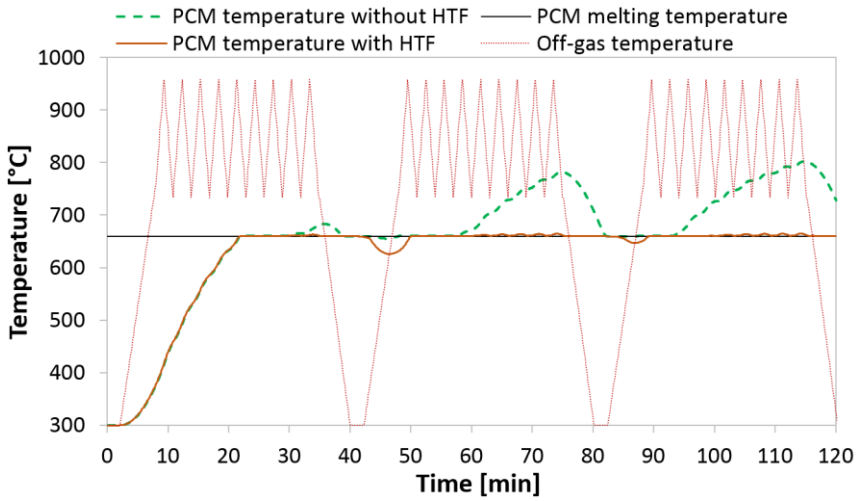

Figure 3.47 Comparison of first row PCM temperature for configuration R40 with and without HTF

The effect of the introduction of HTF on off-gas smoothing performance of the reference configuration is highlighted in Table 3.16 and also in Figure 3.48.

Table 3.16 Performance of the configuration R40 with HTF

	Inlet	**Outlet**
Max temperature [°C]	958	744
Min temperature [°C]	300	542
ΔT max [°C]	658	203
Standard deviation [°C]	196	61
Maximum thermal power [MW]	55.4	41.3
Maximum thermal power reduction [%]	-	25.4

The value of the heat flux q'' that should be extracted from the PCM, calculated by CFD simulations, together with the analytical model described in the previous subsection, have been used to calculate the operative conditions of possible HTFs. Three different fluids, namely air for the low cost and its availability, and the inert gases carbon dioxide, which provides a high specific thermal capacity, and argon, commonly used in steel industry, have been investigated for different values of the operating pressure p_{H} in the range between 0.1 and 1 MPa.

The hypothesis is that the HTF circulates in a close-loop circuit and enters the tubes at a temperature $T_{\mathrm{in,H}} = 260°C$. The inlet temperature has been chosen in order to extract heat from the PCM at a medium-high temperature level, with the aim, for example, to reinforce

steam production. For all the fluids investigated and almost independently of the operating pressure, the outlet temperature $T_{\mathrm{out,H}}$ was very close to $500°C$.

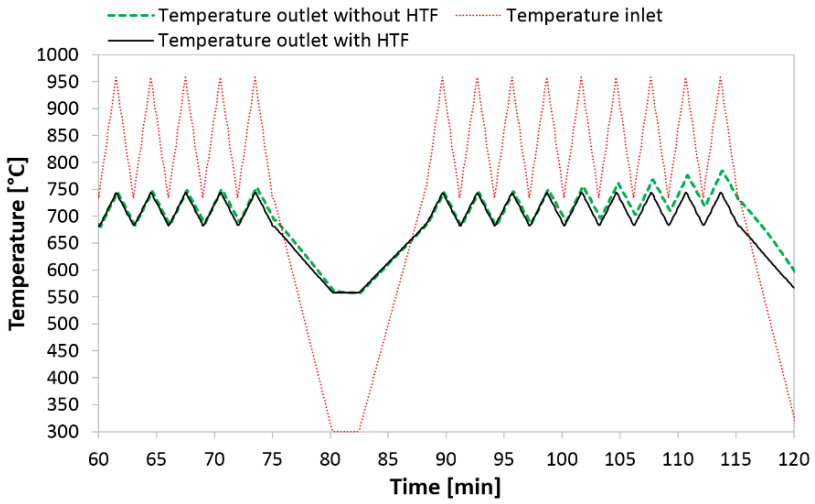

Figure 3.48 Off-gas temperature profiles for configuration R40 with HTF (black line) and without HTF (dotted green line)

In Figure 3.49 (a) and (b), respectively, the HTF average velocity v_{H} and its rate versus pressure $dv_{\mathrm{H}}/dp_{\mathrm{H}}$ for the analysed HTFs are represented as a function of the fluid pressure p_{H}. It can be clearly seen how small variations of HTF velocity, and of pressure drops consequently, are gained by increasing operative pressure over 0.3 MPa. Therefore, the latter pressure value can be set as the reasonable operative condition, in order to lower the cost of the related fans. As the final choice of HTF, carbon dioxide achieves the best performance, while improving system safety in comparison to air, which may lead to safety issues due to its oxygen content.

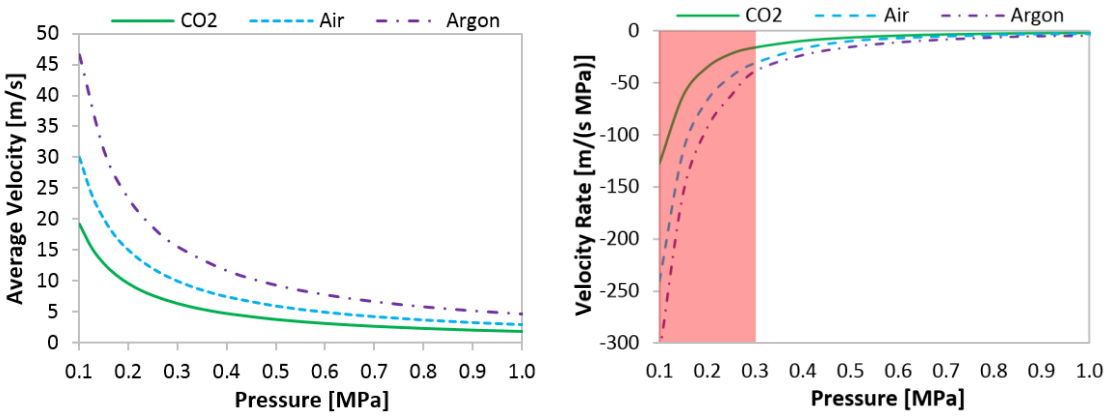

(a) (b)

Figure 3.49 a) Average velocity and b) rate by pressure of the analysed heat transfer fluids

3.6.4 Final system configuration and energy recovery results

The final configuration of the PCM smoothing device is based on the R40 configuration, with aluminium as phase change material and carbon dioxide as heat transfer fluid to control overheating.

The device consists of a sequence of modules, in which the PCM containers are installed (see Figure 3.50). Each module can be interchanged and independently extracted to improve system maintainability.

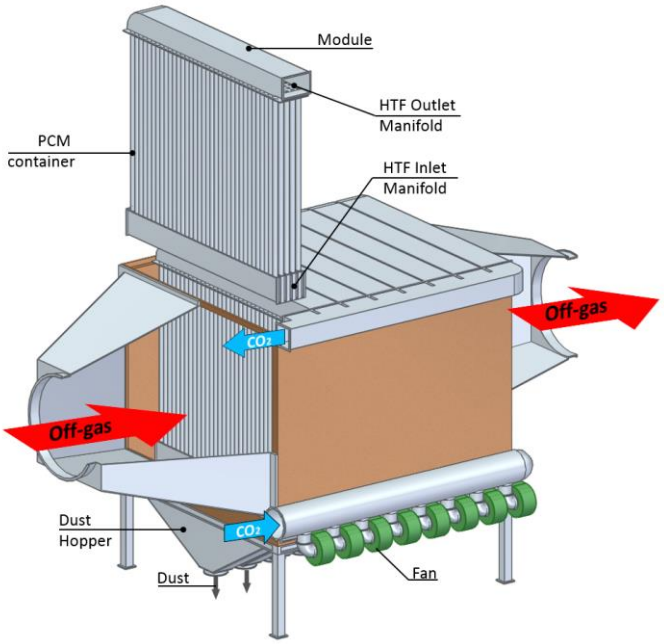

Figure 3.50 Final configuration of the PCM smoothing system

In order to avoid PCM overheating, in each module a control system makes use of a suitable thermocouple installed within a PCM container to manage the HTF rate flow by a dedicated fan. The HTF can then be used to reinforce steam production of the downstream energy recovery system based on a traditional Rankine cycle.

The installation of the proposed PCM device into the off-gas line allows to smooth off-gas temperature variability as shown by the profiles in Figure 3.51, calculated by means of the developed CFD model and imposing the actual values of the off-gas inlet temperatures of the reference cycle. Duration curves, showing the time-spans within a TTT cycle during which the off-gas presents different values of thermal power, are provided in Figure 3.52.

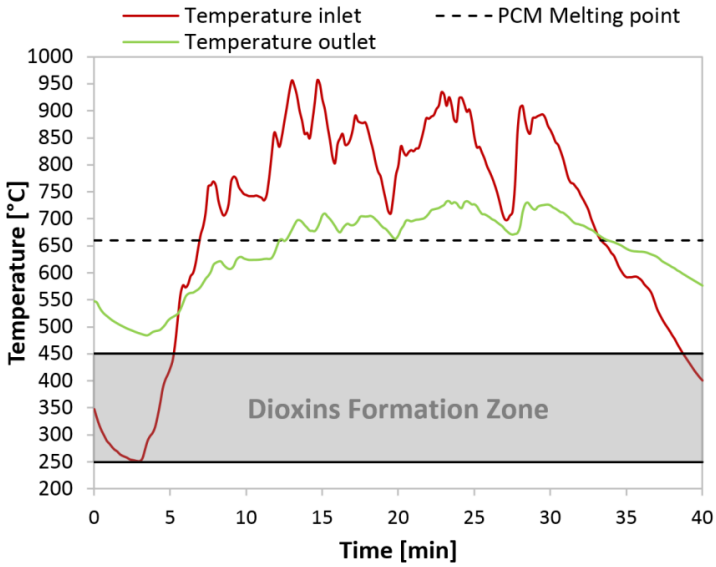

Figure 3.51 Off-gas temperature profiles of the reference cycle with the final PCM system configuration

While the traditional system with no PCM device (see the red lines in Figure 3.51 and Figure 3.52) has a maximum thermal power of 55.4 MW_t corresponding to a TTT temperature peak of 956°C, the new system is characterised by a maximum thermal power of 41.3 MW_t corresponding to a TTT temperature peak of 737 °C. This has a direct effect on the downstream steam-based recovery system size, which should be dimensioned on the maximum thermal power; in this case the reduction factor between the traditional and the PCM enhanced system is 25.4%.

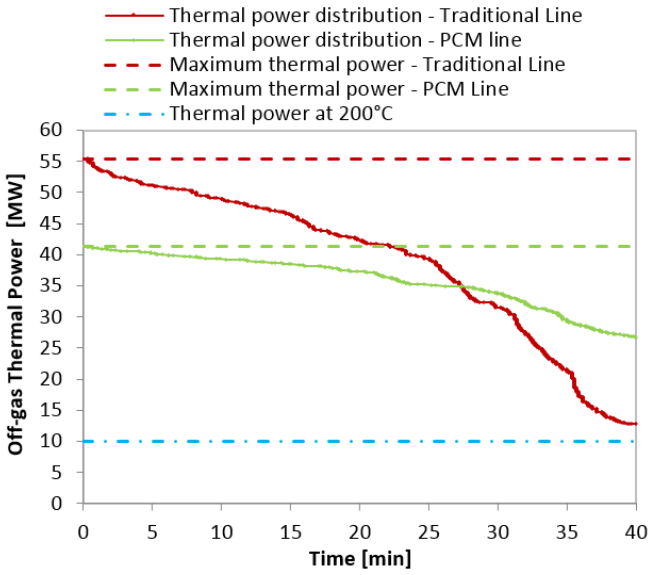

Figure 3.52 Off-gas thermal power duration curves for the final configuration

Therefore, in order to recovery the same amount of off-gas energy, smaller sizes of both the boiler and the steam turbine can be adopted; considering a 0.27 electrical efficiency of the turbine at nominal power conditions, a 8.45 MW_e can be installed instead of 12.25 MW_e for a traditional system, with significant investment cost saving.

The minimum off-gas temperature is increased from 252 °C of the traditional system to 501 °C of the PCM empowered system (see Figure 3.51), with related minimum thermal power moving from 12.8 MW_t (see red lines in Figure 3.52) to 26.7 MW_t (see green lines in Figure 3.52). This shifted and smoothed profile of the final duration curve leads to an expected load factor profile of the steam turbine as reported in Figure 3.53 (compare green lines to the red ones). The proposed system leads to a minimum load factor of 65% during the whole TTT cycle; on the contrary, the profile of the traditional system decreases down to 23%. Thus, with the insertion of the PCM device, boiler and turbine are allowed to work in non-critical ranges with benefits on the overall recovery performance. Considering the values reported in Figure 3.52, the turbine utilization factor, which affects electrical energy revenues, can be increased from 60% to 82% for the new system. Therefore, a final energy recovery of 51.3 kWh_e per steel tons can be estimated, which is significantly greater than the value of 27.8 kW_e/tons reported by [117] for energy recovery from EAF off-gas by ORC technologies in current EU plants.

Furthermore, the temperature profile of the off-gas exiting the PCM smoothing system is always above the range for dioxins generation by de novo synthesis from macromolecular carbon and organic or inorganic chlorine present in the fly ash matrix and for formation from organic precursors. These two processes are considered to cause about the 70% of the total dioxins generation [136]. According to [137] the maximum formation occurs at a temperature of about 300-325 °C, while small amounts are detected for temperature below 250 °C and over 450 °C. As reported in Figure 3.51, in a traditional system off-gas remains in the dioxins generation range for a 16.7% time of the TTT cycle, leading to those environmental issues that represent a main drawback of direct recovery systems, as underlined in section 0. The insertion of the PCM smoothing system downstream the scrap preheating section contributes to overcome such environmental issues, thus increasing the sustainability of the whole direct-indirect energy recovery.

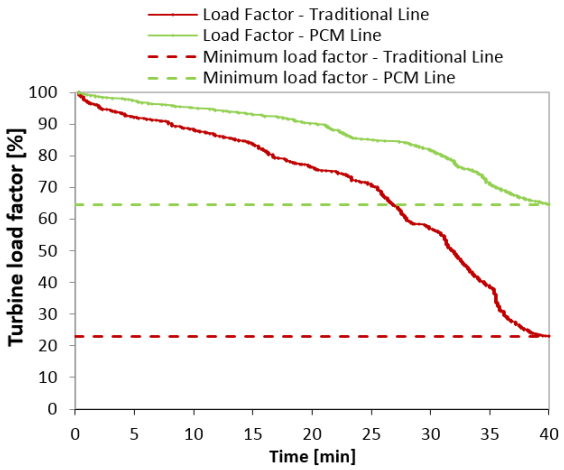

Figure 3.53 Duration curve of the Load Factor of the turbine

As concerns energy recovery economics, values reported in Table 3.17 have been estimated by interaction with local component suppliers. The smoothing device investment cost, comprising PCM modules, HTF piping and control system, can be set to 750,000 €. Taking into account system utilization, a yearly electrical energy generation of 48,500 MWh/year can be estimated, which leads to 2,425,000 €/year cost saving when an energy supply cost of 50 €/MWh_e, currently granted to the steel industry by the Italian energy system, is considered. Furthermore, energy efficiency certificates (EEC) can be ascribed to the proposed system; for an up-to-date Italian value of 115 €/TOE [138], increased by the durability factor of 3.36 introduced by the Italian white certificates scheme in order to account energy recovery from industrial processes over a 5-years period only [155], a positive cash flow of 3,000,000 € can be estimated for the first 5 years.

Table 3.17 Economics of the recovery system

	Costs		**Incomes**
	Investment [€]	*O&M[€/year]*	*[€/year]*
Smoothing device	800,000	90,000	-
Steam generator	8,800,000	450,000	-
Steam turbine	3,000,000	121,000	-
Other (design, safety, etc.)	975,000	135,000	-
Electric energy saving	-	-	2,425,000
Energy efficiency certificates	-	-	3,000,000

Therefore, a simple pay-back period of about 3 years can be derived, which underlines the profitability of the recovery system enabled by the adoption of the PCM smoothing device.

3.6.5 Conclusions

A conjoint direct-indirect recovery of off-gas thermal energy is proposed in order to maximize energy efficiency in EAFs with continuous charge. After preheating the scrap charge as in direct recovery, off-gas enters a PCM (aluminium) smoothing device which reduces its temperature variability, providing a more regular feeding of the downstream indirect recovery system by steam generation and power production. Thermo-fluid dynamic simulations allow identifying the best configuration in terms of PCM container size and layout, as well as the benefits of introducing a proper heat transfer fluid flowing through PCM containers in order to avoid overheating issues. An analytical model has been developed to guide the selection of the proper heat transfer fluid, leading to adopt carbon dioxide in a closed-loop circuit feeding PCM containers.

The resulting low cost device allows to increase energy efficiency of the whole recovery system. Maximum off-gas temperature is lowered and the resulting maximum thermal power is reduced by 25.4% with respect to a traditional plant with no smoothing device. This has a direct impact on the downstream energy recovery system based on consolidated Rankine cycle technologies: smaller sizes of both the boiler and the steam turbine can, in fact, be adopted to recover the same amount of waste heat, thus reducing investment cost significantly. Furthermore, the minimum off-gas temperature is increased due to the latent heat released to off-gas by the PCM smoothing device; the minimum load factor of the steam turbine can be enhanced from 23% in the traditional plant to 65% for the proposed system during the whole TTT cycle. The resulting turbine utilization factor, which affects electrical energy revenues, is increased from 60% to 82%.

The installation of the proposed PCM smoothing device allows also to overcome some of the environmental issues that have hindered energy recovery in the steel industry. The profile of off-gas temperature, in fact, is shifted above the range for dioxins generation by de novo synthesis and for formation from organic precursors. Since recovery of energy from EAF steelmaking processes has been identified as the greatest single opportunity for reducing energy use, the proposed system can be a feasible way of addressing the challenge.

3.7 Coupling PCM-based waste heat extraction with steam generation

To allow a better exergy exploitation than the current state-of-the-art waste heat to power solutions in the steel industry, a new type of energy recovery system based on Phase Change Materials is proposed. In particular, the use of high temperature PCMs evolves from simply smoothing off gas temperature (see Sections 3.4 and 3.6) to generating constant superheated steam able to feed the downstream turbine nearly at nominal load. This result is achieved by introducing an auxiliary section between the PCM Section and the steam generation one, which provides the auxiliary heat needed to level the thermal content of off gas. The auxiliary heat is extracted from the PCM units by a heat transfer fluid flowing across the inner tube of each PCM container.

Different models to properly size and simulate the operations of the proposed energy recovery system have been developed and integrated. Results show how the size of the steam generator and the turbine can be reduced of about 41% with respect to traditional solutions, while increasing electric power production by 22% thanks to the reduced fluctuation in steam parameters at the turbine inlet, which leads to a greater overall efficiency.

3.7.1 Introduction

Waste heat recovery in steel industry represents one of the greatest opportunity to reduce the consumption of primary energy while increasing the sustainability of the steelmaking process [18–21]. One of the most important and challenging source of waste heat is represented by the off gas emitted by the Electric Arc Furnace (EAF), which accounts for about 30% of the total energy provided to the process [23]. However, due to the dynamic of the EAF process, off gas temperature fluctuates intensively causing large variations in thermal power and an inefficient energy recovery, consequently [15,104]. Current available technologies can be classified depending on the final use of the recovered heat as performing a direct or an indirect recovery (refer to section 3.3 for a detailed review). In direct recovery, off gas thermal energy is recuperated and directly used to preheat the scrap before its charging into the furnace. In indirect recovery, instead, off gas thermal energy is carried out by a heat transfer fluid (HTF), mainly steam, and used for several applications such as district heating, vacuum degasser, and power production [156].

However, a thermal energy storage system (TESS) is generally required in the attempt of providing a constant supply of heat downstream [104].

Recently, innovative TESS based on the capacity of phase change materials (PCMs) to store and release latent heat have been proposed also for high temperature conditions such those encountered in the steel industry [15,140,157–159]. In particular, an innovative solution for indirect energy recovery in a discontinuous charge EAF process (section 3.4) and a conjoint direct–indirect recovery in a continuous charge one (section 3.6) have been developed in this thesis. The features of metal PCMs have been exploited not only for latent heat storage, but mainly to smooth the variability of off gas temperature and feed the downstream energy conversion technology more constantly at around 400 °C.

The aim of this technology is to further increase the efficiency of indirect energy recovery from EAF off gas by providing superheated steam with low thermal variability, but also with higher temperature to a steam turbine for power production. Therefore, in the following sub-section 3.7.2 the potential evolution of steam-based energy recovery in steel industry is depicted, departing from current technologies and moving to the novel energy recovery approach proposed in this study. In sub-section 3.7.3, the new PCM-coupled energy recovery system is described, while in sub-section 3.7.4 the models created for its development and performance analysis are reported. In sub-section 3.7.5 results are discussed, while in sub-section 3.7.6 conclusions are derived.

3.7.2 Managing the evolution of steam-based energy recovery from EAF

State-of-the-art solutions for EAF waste heat to power (WHTP) systems can be considered as composed by three main components:

1. a waste heat recovery boiler (WHRB);
2. a thermal energy storage system (TESS);
3. an energy conversion technology (ECT).

Concerning the waste heat recovery boiler, two technologies are commonly used: the saturated steam generator (Sat-SG) and the hot water boiler (HWB). The choice between saturated steam and hot water usually depends on their adoption also as a cooling medium

in off gas ducts. The use of thermal oil boilers is generally excluded by steel plant operators due to safety issues related to fire risk.

When a saturated steam generator is used, Ruth's steam accumulators (RSA) are employed as TESS, while two type of energy conversion technologies can be used: the saturated steam turbine (Sat-ST) [104] and the Organic Rankine Cycle (ORC) turbine [127]. When a hot water boiler is used as WHRB, instead, only a hot water tank (HWT) and an ORC turbine can be used as TESS and ECT, respectively [120].

The design of the whole waste heat to power system normally starts from the WHRB, followed by the TESS, and finally by the ECT (see the grey coloured portion in Figure 3.54a) in a sequential approach. Each system is sized individually and the output parameters are used as input parameters of the following component (i.e. maximum steam flow rate and temperature exiting TESS become the design parameters of the downstream ECT). As shown in Figure 3.54b, such state-of-the-art solutions are able to manage thermal power fluctuations, but the ECT feeding temperature is rather low.

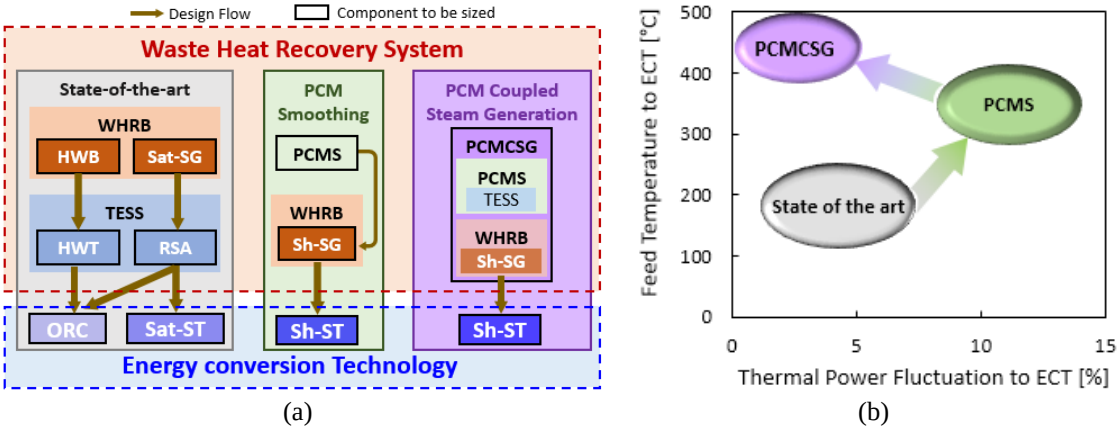

Figure 3.54 a) Comparison between the design approach of the state-of-the-art and the PCM-based WHR systems from EAF; b) performance evolution of the WHTP systems

Since the average temperatures of the off gas are usually around 600 °C, in order to reduce exergy losses a better solution could be the generation of superheated steam at higher temperature to directly feed a superheated steam turbine (Sh-ST). In [160], two solutions have been proposed: 1) applying a duct burner before the super heater and 2) providing a common WHRB by combining the off gas ducts of two EAFs. The former solution implies the use of additional fossil fuel, while the latter leads to manage a double production process. An innovative solution has been proposed in [119], where a heat

recovery boiler based on molten salt is coupled with superheated steam generation. In this case, molten salt acts both as a heat transfer fluid and as a thermal storage system, thus facing the same issues of solar plants, such as fast draining of the liquid and freezing prevention during EAF shutdown.

High temperature phase change materials (PCMs) can be employed to reduce the fluctuating thermal power entering the steam generator. Previous findings have shown that the introduction of a PCM-based smoothing (PCMS) device is capable to smooth off gas temperature profiles, significantly affecting the design of the whole waste heat to power system [161]. The PCMS has been further developed in [162], with the introduction of a heat transfer fluid (HTF) to overcome overheating issues in PCM containers. The change in the design approach is reported in Figure 3.54a (green coloured portion). TESS features are integrated into the PCMS, which becomes the first component of the waste heat to power system to be sized, followed by the WHRB. In this case, the WHRB is a superheated steam generator (Sh-SG) and its size depends on the performance of the upstream PCMS. Referring to Figure 3.54b, the PCMS allows to enhance the steam temperature, but the control of thermal fluctuations is less effective than current state-of-the art solutions.

In this section, the chance of actively managing the heat transfer fluid flowing through the PCM-based device to improve steam parameters (i.e. temperature and mass flow rate) is investigated. The basic idea is to make the whole waste heat to power system evolving towards the left upper side of Figure 3.54b, thus providing both higher steam temperature and near-zero thermal power fluctuations to the downstream energy recovery section.

To this end, a new type of heat recovery system called PCM-Coupled Steam Generator (PCMCSG) is developed by integrating the PCMS features (TESS and temperature smoothing) with the superheated steam generator (Sh-SG) ones, as described in the following sub-section 3.7.3. The effects of combining the off gas temperature smoothing and the latent heat extraction from PCM by a HTF are analysed with regards to steam parameters and the related performance of the downstream energy conversion system. Since the PCMCSG is the single component of the waste heat recovery section integrating different features (see the purple coloured part of Figure 3.54a), its sizing should rely on both PCMS and Sh-SG performances, thus further changing the design approach of waste

heat to power energy systems. Integrated models are needed to develop and analyse the performance of the novel PCMCSG, as described in sub-section 3.7.4.

3.7.3 The PCM-coupled steam generator

The proposed new PCM-coupled steam generator is composed by three sections: the PCM Section, the Steam Generation Section, and the Auxiliary Section (see Figure 3.55).

The PCM Section (red coloured in Figure 3.55) is composed by a set of Heat Exchange and Storage Units (HESUs), which exchange thermal energy with the off gas and the auxiliary heat transfer fluid (HTF) during charging or discharging phases of the PCM. When the off gas enters the PCM Section, in facts, its temperature can be increased or decreased by the action of the HESUs. When off gas temperature is lower than the PCM melting point, in particular, each HESU releases latent heat from the PCM to the off gas increasing its temperature. On the contrary, when the off gas temperature is higher than the PCM melting point, the HESU absorbs heat from the off gas decreasing its temperature, by storing latent heat in the PCM. The combination of these two effects leads to smooth the off gas temperature, which tends to stabilise at the PCM phase transition temperature.

After the PCM Section, the off gas enters the Steam Generation Section (blue coloured in Figure 3.55), where it exchanges heat with the superheater, the evaporator, and the economizer, thus generating superheated steam. The Steam Generation Section is sized taking into account the maximum thermal power of the off gas exiting the PCM Section.

The Auxiliary Section (purple coloured in Figure 3.55) connects the PCM Section and the Steam Generation Section by providing the additional heat supply required to achieve constant steam parameters at the turbine inlet. In order to obtain a constant mass flow rate of steam, an auxiliary evaporator located downstream the evaporator of the Steam Generation Section is employed. To achieve a constant temperature of the superheated steam, instead, an auxiliary superheater is installed downstream the superheater of the Steam Generation Section. Both the auxiliary evaporator and the auxiliary superheater are connected to the PCM Section by a closed loop circuit with the gaseous heat transfer fluid flowing through the HESUs.

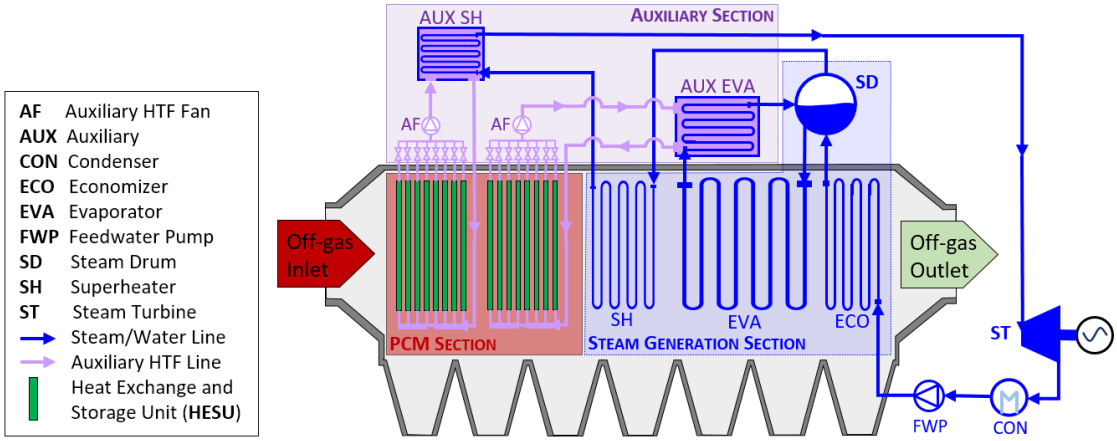

Figure 3.55 PCM-coupled steam generator for waste heat recovery

As reported in [10], several systems for containing PCM employ cylindrical pipes [75,76]. The use of cylindrical pipes allows increasing heat exchange surfaces thereby optimizing the process both from the point of view of recovery efficiency and of cost, as well as preventing breakage and crack formation [161]. Based on the previous considerations, the Heat Exchange and Storage Unit (HESU) is composed by two coaxial pipes; the gap between the inner pipe and the external one is filled with the PCM (Figure 3.56). The external pipe is in direct contact with the off gas, whereas the inner pipe contains the heat transfer fluid feeding the heat exchangers of the Auxiliary Section. At the bottom of each HESU insulation is provided in order to dampen the generation of a thermal bridge between the external wall and the bottom.

Since all the HESUs within a given row (see Figure 3.56b) undergo the same off gas thermal load, the same thermal power can be extracted from each of them by the HTF. Thus, HESUs within the same row are connected in parallel by using a single inlet and outlet manifold (see Figure 3.56a), so that the same HTF control parameters can be applied to all of them.

The design of the PCM Section has to take into account the very high concentration of dust in off gas (typically 20 g/Nm^3 [127]), therefore a vertical arrangement of the HESU should be chosen in order to reduce dust accumulation on external pipe surface. Since dust accumulation among HESUs can create a barrier to off gas flow, an aligned layout of the HESUs (Figure 3.56b) should be preferred to a staggered one, as analysed in [161].

Furthermore, an easy dust removal can be enabled by hanging the HESUs to the upper wall of the waste heat boiler, as can be seen in Figure 3.56a.

As underlined in [12] and [15], metals have greater potential as high temperature PCMs than molten salts, since they are generally characterised by higher thermal conductivity and smaller volume expansion. In particular, Al–Si alloys [13,87,96] represent the most promising high temperature PCMs for waste heat recovery from EAF, due to their suitable melting temperature, high latent heat of fusion and high thermal conductivity [73]. However, as pointed out by Fukahori et al. in [96,97], Al–Si alloys have highly corrosive nature to metals such as steel based-materials. They investigated the use of ceramics as shell materials for high-temperature metallic PCMs and they found out that Al_2O_3 is the most suitable ceramic to employ, even though ceramics are quite fragile and expensive for industrial application.

A suitable alternative could be coating the steel walls in contact with the PCM with a thin film of Al_2O_3, which can be obtained by means of an aluminizing and oxidation treatment [100].

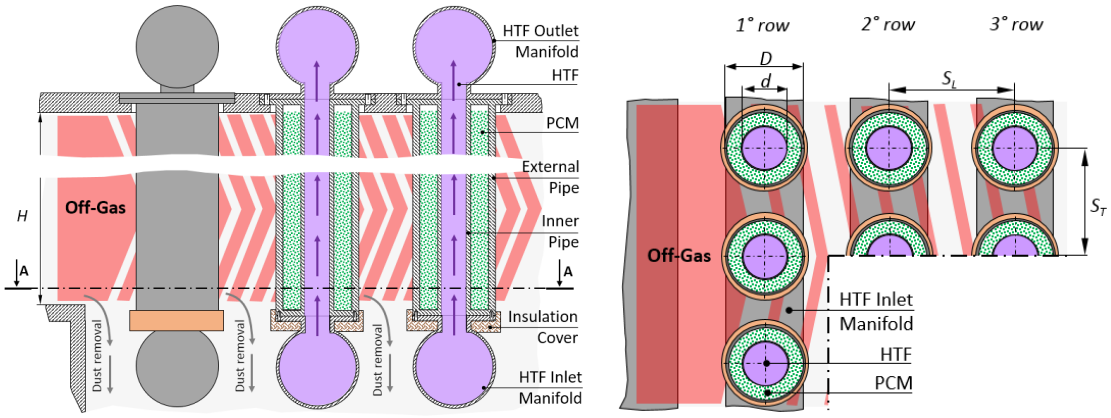

(a) (b)

Figure 3.56 Geometrical configuration of the HESU: a) lateral and b) A-A section view

In this section, alloy Al-12%Si (in mass %) has been chosen, because it presents one of the highest heat of fusion (560 kJ/kg) and thermal conductivity (160 W/m K) among Al-Si alloys; its temperature of fusion is about 576 °C, which is very close to the average temperature of the off gas emitted by an Electric Arc Furnace.

3.7.4 Integrated models for system analysis and optimisation

The optimisation of system configuration and management assuring the best performance of the novel PCM-coupled steam generation has required the development and integration of different models, which in turn rely on different software, as shown in Figure 3.57.

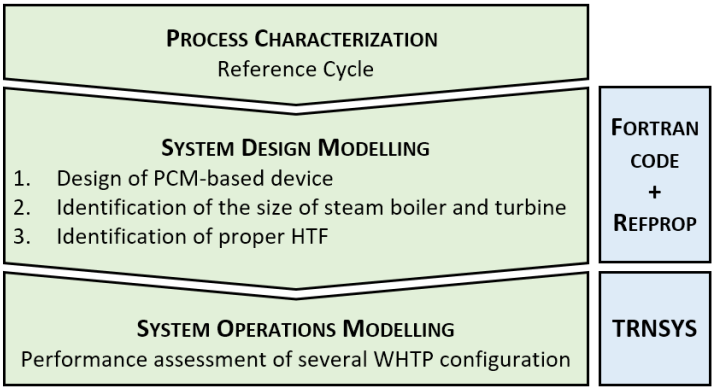

Figure 3.57 Flow diagram for the optimisation of system configuration and management

The first step to be faced is the process characterisation, which should generate a reference profile of the off gas temperature resembling the real behaviour in an electric arc furnace plant. In the second step, which leads to system sizing, the main components of the PCM-device are designed, the size of the steam boiler and the turbine are identified, and a proper HTF is selected. Once this stage is completed, system operations should be modelled and simulated in order to improve its performance. In the following, each modelling phase is analysed in more details.

3.7.4.1 Process characterisation

In order to fully exploit waste heat, the most energy intensive cycle occurring during an EAF process should be identified as the reference cycle for the design of the related energy recovery system. Then, a generalisation of the reference cycle should be performed to create an off gas temperature profile characterised by the same highest temperature, total energy, and critical temperature gradient of the original reference cycle, which can be easily processed by models. In this study, a generalized off gas temperature profile has been generated from analyses carried out on several EAF processes; the mass flow rate of the off gas is assumed to be constant. Figure 3.58 compares the reference cycle (solid black line) to the generalised cycle (red dotted line).

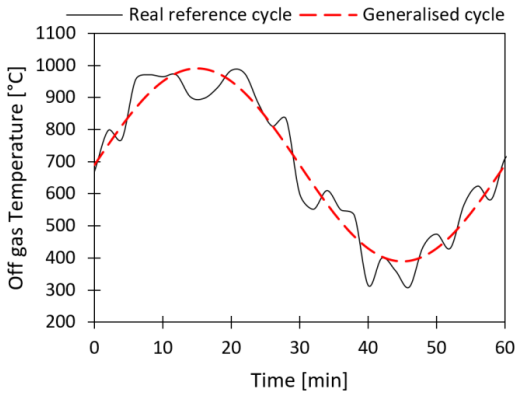

Figure 3.58 Generalization of the reference cycle

3.7.4.2 System modelling

The design of the whole PCMCSG involves a series of energy balances between the PCM Section and the Steam Generation Section, based on the temperature profile of the generalised cycle at the inlet of the PCM Section.

The PCM Section should be sized in order to guarantee that the thermal energy stored in the PCM is able to completely smooth thermal power fluctuations when feeding the steam turbine. The reduction of the maximum off gas temperature exiting the PCM Section (see the smoothed profile of the green solid line in Figure 3.59a) is linked to the decrease of the maximum off gas thermal power entering the downstream Steam Generation Section. Thus, as reported in Figure 3.59b, the design point thermal power q_{des} of the Steam Generation Section is calculated as the difference between the maximum off gas thermal power exiting the PCM Section and the thermal power at the Steam Generation Section outlet. The latter is usually assigned by considering the minimum off gas temperature admissible at the stack. The purple area in Figure 3.59b, represents the required auxiliary energy $E_{aux_{req}}$ to be provided by the Auxiliary Section to guarantee constant steam parameters at the turbine inlet. It can be calculated as shown in the following equation (3.29):

$$E_{aux_{req}} = \int_0^{TTT} q_{aux_{tot}}(t)\, dt \tag{3.29}$$

where the auxiliary thermal power $q_{aux_{tot}}(t)$ is the difference between the design point q_{des} and the off gas thermal power exiting the PCM Section at time *t*, to be accounted for

a whole tap-to-tap cycle (TTT). The auxiliary thermal power $q_{aux_{tot}}(t)$ provided to steam by the Auxiliary Section should be distributed among the auxiliary evaporator and the auxiliary superheater.

In first instance, heat exchange within the PCM Section can be characterized by considering the off gas temperature with respect to the PCM melting point. In particular, two important heat exchange phases can be identified: the hot phase, occurring when the off gas temperature is greater than the phase change temperature, and the cold phase, occurring when the off gas temperature is lower than the phase change one.

During the hot phase, a HESU absorbs and stores the thermal energy $E_{hot}(R)$ from the off gas, while during the cold phase it releases the thermal energy $E_{cold}(R)$ to the off gas. Both energies depend on the row *R* where each HESU is located, since the thermal load of the off gas decreases while moving from the first to the last rows of HESUs in the PCM Section.

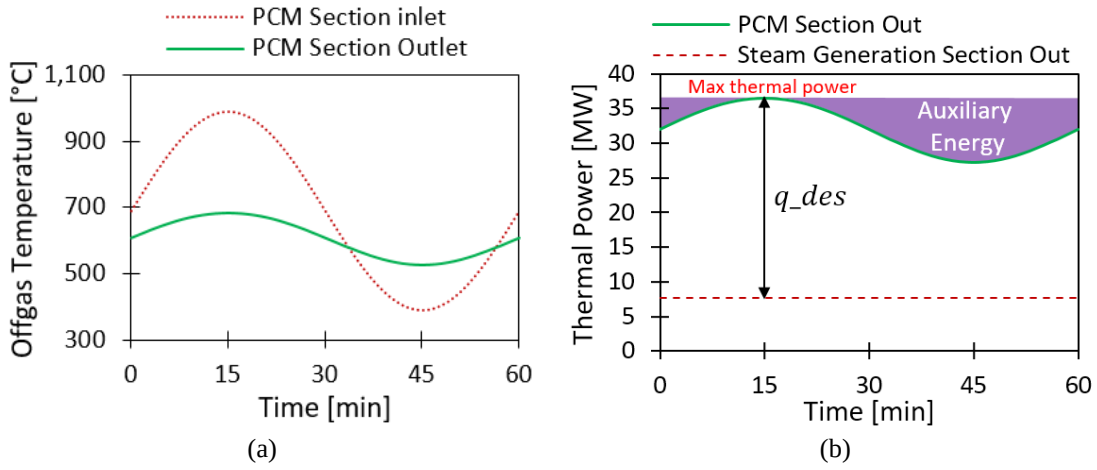

Figure 3.59 a) Temperature profile at inlet and outlet of the PCM Section and b) thermal power profile in the Steam Generation Section

Figure 3.60a reports the profile of the heat transfer rate between the off gas and a HESU; the red area represents the hot phase energy, while the light blue area represents the cold phase energy. The PCMSG design model involves the identification of the external diameter *D* for a HESU so that each HESU is able to store, in the form of the latent heat E_{sto}, the hot phase energy it can absorb during the generalised cycle. Moreover, the

number of HESU rows n_R should be chosen in order to enable the whole PCM Section to store all the required auxiliary energy $E_{aux_{req}}$.

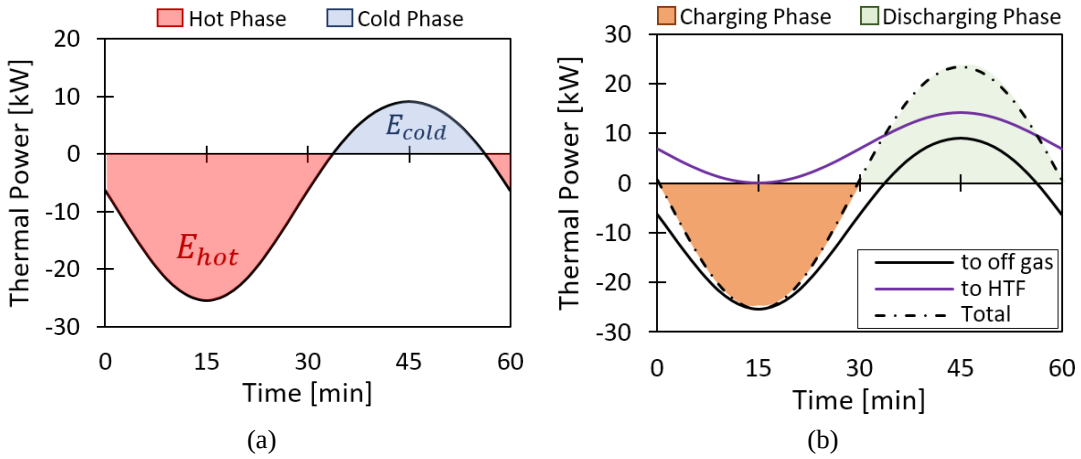

Figure 3.60 a) Hot and cold phases and b) charging and discharging phases in the HESU

For a given diameter, by increasing n_R, the available auxiliary energy $E_{aux_{av}}$ in the PCM Section increases, while the required auxiliary energy $E_{aux_{req}}$ decreases. When the external diameter and the total number of rows balancing required and available energies have been selected, the thermal power to be provided to the auxiliary evaporator $q_{aux_{EVA}}$ and to the auxiliary superheater $q_{aux_{SH}}$ can be identified. The total number of rows of the PCM Section can be further split into the auxiliary evaporator rows $n_{R_{EVA}}$ and the auxiliary superheater rows $n_{R_{SH}}$.

Figure 3.60b shows the total thermal power exchanged by the HESU (black dash-dot line), which is the sum of the thermal power exchanged with the off gas (black solid line) and the heat transfer fluid (purple solid line). The total thermal power identifies the charging (orange area) and discharging (green area) phases occurring within each HESU. During the charging phase, the stored thermal energy within the HESU increases, while during the discharging phase it is released. While the thermal power exchanged with the off gas depends on the geometrical configuration of the HESU and the off gas thermodynamic properties, the thermal power exchanged with the heat transfer fluid can be controlled by varying HTF thermodynamic parameters (inlet temperature, velocity and pressure). Thus, the profile of the thermal power exchanged with the auxiliary HTF should guarantee that the energy stored by the HESUs during the charging phase is equal

to the thermal energy to be released during the discharging one. The selection of the proper HTF involves managing the trade-off between minimising pressure drop and lowering circuit pressure.

Based on the above considerations, the overall PCM coupled steam generator design model has been developed. The flow chart in Figure 3.61 summarizes the related algorithm, which has been implemented in Fortran 90, using the open-source integrated development environment Force [163]. The workflow encompasses three main iterative loops representing the three main steps of the design process, which are: 1) the identification of the external pipe diameter *D* of the HESUs (green coloured portion in Figure 3.61), 2) the determination of the number of HESUs' rows n_R (orange coloured portion in Figure 3.61), and 3) the selection of the heat transfer fluid (grey coloured portion in Figure 3.61).

In the first step, starting from the input design parameters (off gas temperatures and flow rates), by means of a first guess of the diameter *D* of a HESU, the cross-flow area of the whole system is calculated by taking into account the maximum inlet velocity of the off gas. [164].

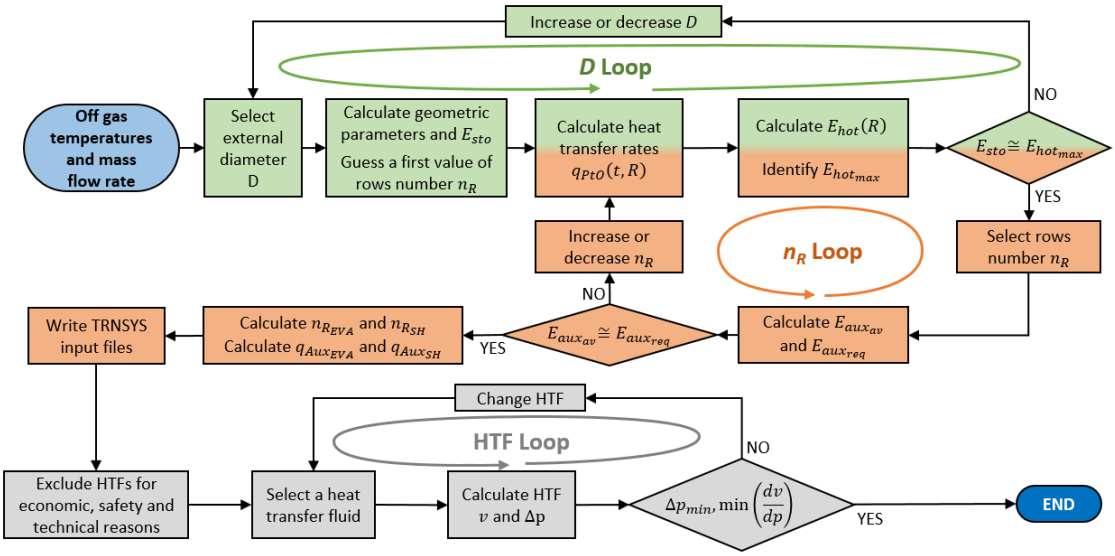

Figure 3.61 Flowchart of the PCM-coupled steam generator design model

A maximum inlet velocity of 12 m/s has been chosen in order to limit the erosion effect due to the high dust content in the off gas. The choice of the inner pipe diameter *d*, instead, relies on acceptable thermo-structural stresses generated by the difference between the

thermal linear expansion coefficients of PCM and tube material [165]. Given the geometric configuration and the PCM characteristics, the amount of energy storable E_{sto} as latent heat in each HESU can be easily calculated.

At the same time, the HESUs geometry deeply affects the heat transfer between off gas and PCM. Since during normal operating conditions the PCM is kept in phase change at its melting temperature, thus behaving as a body of infinite heat capacity, both the PCM and the cylindrical outer surface of the external tubes can be assumed as isothermal at the PCM melting temperature. Accordingly, the problem can be dealt with as an external forced convection analysis in a tube bundle with constant temperature on the outer surface of the tubes. The heat transfer rate $q_{PtO}(t, R)$ from PCM to off gas (positive or negative) at time *t* and for row *R* (with *R* ranging from 1 to a first guess value of n_R) can be evaluated as:

$$\mathrm{q}_{PtO}(t, R) = U_{PtO}\, A_{PtO}(\Delta T_{ml})_{PtO} \tag{3.30}$$

where U_{PtO} is the overall heat transfer coefficient (which basically corresponds to the convective heat transfer coefficient α_{PtO}), A_{PtO} is the heat exchange area, and $(\Delta T_{ml})_{PtO}$ is the log mean temperature difference between PCM and off gas. The value of α_{PtO} is calculated using the Grimson correlation for aligned tube bundles [166].

Off gas properties are estimated using an iterative procedure, where the outlet off gas temperature for each row is first guessed and then corrected using the heat balance for the off gas. The inlet temperature for a given row corresponds to the outlet temperature of the previous one. All the thermo-physical properties have been evaluated at the mean off gas temperature and operating pressure using the REFPROP 8.0 routines [167], conveniently interfaced with the Fortran code.

From $q_{PtO}(t, R)$ it is possible to calculate the hot phase thermal energy of the row which undergoes the maximum thermal load ($max[E_{hot}(R)]_R$); this energy, in turn, should be equal to the storable energy E_{sto}. When this condition is fulfilled, it is possible to move to the following second step of the design procedure.

At the beginning, the available auxiliary energy $E_{aux_{av}}$ is calculated as the integral over time of the heat transfer rates $q_{PtO}(t, R)$ for a first guess of the number of rows n_R.

$E_{aux_{av}}$represents the maximum amount of energy the off gas is able to exchange with the PCM and should be equal to the energy $E_{aux_{req}}$ (see equation (3.29)) required by the Auxiliary Section in order to ensure the desired constant steam parameters. If the available auxiliary energy is less than the required one, the number of rows should be increased and vice-versa. Once the number of rows which balances the required and available energies is identified, the thermal powers to be provided to the auxiliary evaporator $q_{aux_{EVA}}$ and the auxiliary superheater $q_{aux_{SH}}$ can be estimated. The thermal power distribution between the auxiliary evaporator and the auxiliary superheater is based on the enthalpy differences required by each heating phase of the steam cycle (i.e. feedwater heating, evaporation and superheating). Such enthalpies can be derived from feedwater temperature, circuit pressure and turbine inlet temperature. The total number of rows of the PCM Section can be split into the number of rows $n_{R_{EVA}}$and $n_{R_{SH}}$ devoted to the auxiliary evaporator and the superheater, respectively.

The third and final step of the overall model involves the selection of a proper gaseous HTF able to extract the desired amount of heat from the PCM at the right time with low pressure drops. For any suitable fluid, the velocities v at time *t* and for any row *R* can be inferred from the auxiliary thermal power $q_{aux}(t,R)$. The problem can be modelled as internal forced convection in a tube of inner diameter *d* with constant temperature equal to the PCM phase change temperature. Similarly, the heat transfer rate $q_{aux}(t,R)$ at the time *t* and for the row *R* can be expressed as:

$$q_{aux}(t,R) = U_{PtH}\, A_{PtH} (\Delta T_{ml})_{PtH} \tag{3.31}$$

where symbols have the same meaning as those in equation (3.30), but here they refer to the heat exchange between the PCM and the HTF.

Based on the value of q_{aux} and guessing the outlet temperature from the inner tube, the value of U_{PtH} , which essentially corresponds to the convective heat transfer coefficient α_{PtH}, can be easily calculated. From the value of α_{PtH}, using the Gnielinski formula [153], the HTF velocity v can be inferred through the Reynolds number. Iteratively, the heat balance for the duct is used to provide updated values of the tube outlet temperature. Pressure losses are finally calculated via the Petukhov correlation [154].

The thermo-physical properties of the HTF are evaluated at its mean temperature and operative pressure using the REFPROP software interfaced with the Fortran code. HTF velocities and their rates versus operative pressure dv/dp are analyzed together with pressure drops Δp in the row undergoing the maximum thermal load, in order to manage the trade-off between minimising pressure drop and lowering circuit pressure.

3.7.4.3 System Operations modelling

Two models for operations of waste heat to power systems based on steam generation have been developed in TRNSYS 17.0 [168]: the former refers to a traditional Sh-SG (see Figure 3.62), while the latter to the proposed PCMCSG (see Figure 3.63). The implemented models aim to evaluate and compare the electric power production of the two systems. The first model simulates a traditional Sh-SG with and without a PCM-based smoothing-only device (PCMS) installed upstream. Such condition is simulated applying two different off gas thermal power profiles to the Sh-SG: the reference profile and the smoothed profile due to PCMS insertion.

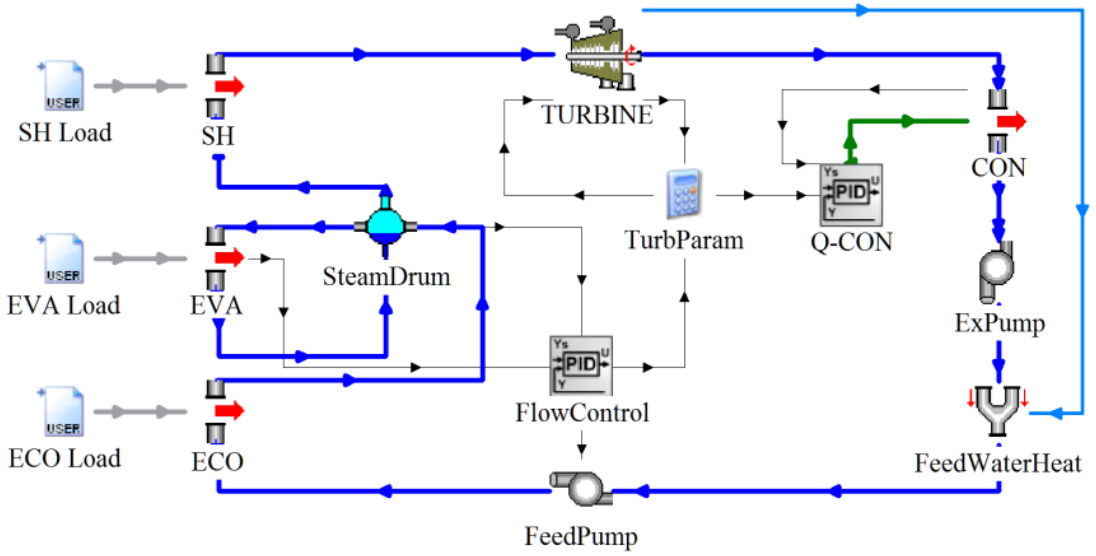

Figure 3.62 TRNSYS model of a traditional superheated steam generator for waste heat recovery and downstream energy conversion technology

The design of the PCMS refers to the technical solutions described in section 3.6, where a heat transfer fluid is used to control the PCM temperature in order to overcome overheating issues in PCM containers. The PCMS has been sized so that the same smoothing effect (i.e. same thermal power fluctuation) of the PCM Section of the novel

system is achieved. Therefore, the geometry and the layout of the PCMS are the same of the PCM Section of the PCM-coupled steam generator.

The output files generated by the Fortran code are used as input in the TRNSYS simulation. In the traditional Sh-SG model, a control loop is implemented in order to provide a constant steam temperature at the turbine inlet by varying the flow rate of the feed pump.

The flow rate of the feed pump in the PCMCSG is, instead, fixed at the design value; the control on the steam parameters is obtained by providing the auxiliary evaporator and the auxiliary superheater with the auxiliary thermal powers from the PCM Section. In both models, the performances of the turbine have been modelled by using an efficiency curve for partial loads, which has been created thanks to interactions with a local supplier (see Figure 3.64).

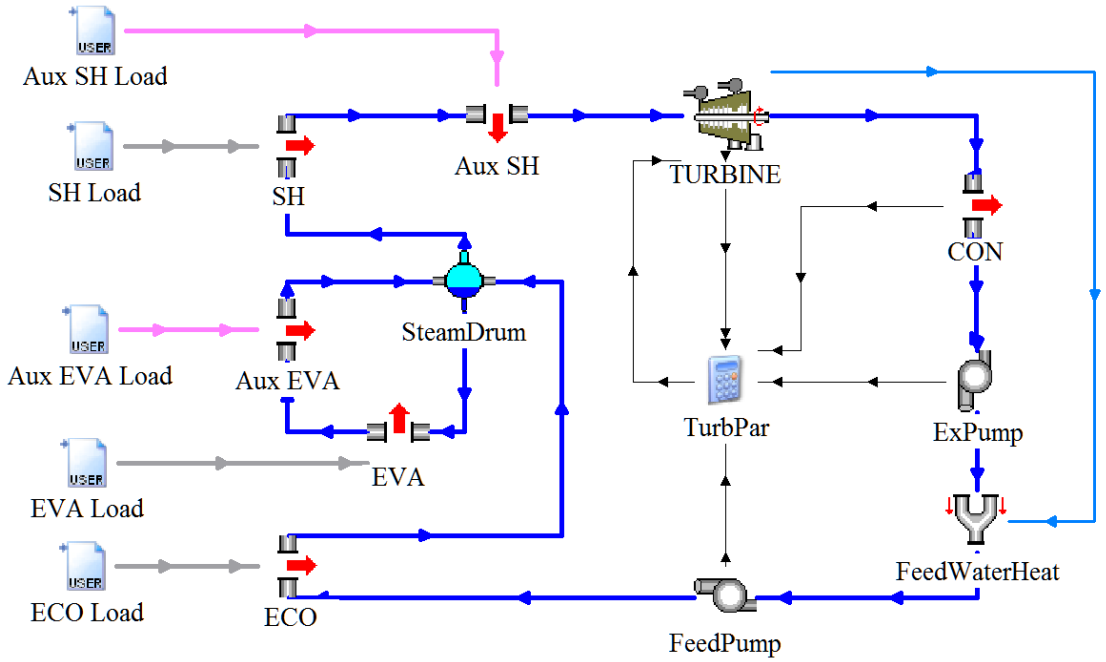

Figure 3.63 TRNSYS model of a traditional superheated steam generator for waste heat recovery and downstream energy conversion technology

The part-load efficiency curve represents the isentropic efficiency ratio $= \frac{\eta_{is,a}}{\eta_{is,d}}$ (where $\eta_{is,d}$ and $\eta_{is,a}$ are the design and actual isentropic efficiency, respectively) as a function

of the mass flow ratio $\chi = \frac{\dot{m}_a}{\dot{m}_d}$, where $\dot{m}_a$ and $\dot{m}_d$ are the actual and design mass flow rate of the steam, respectively.

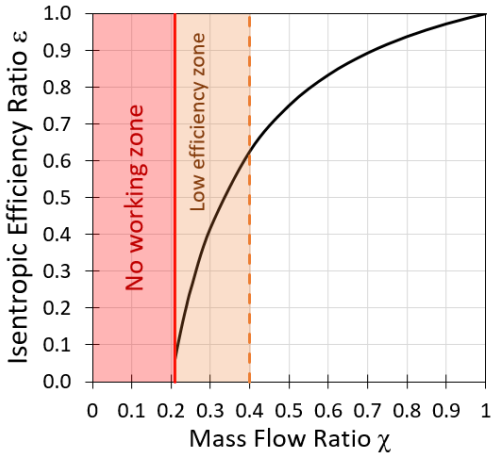

Figure 3.64 Part-load efficiency curve of the steam turbine

Typically, steam turbines are designed to work at mass flow ratios higher than 0.4, since lower values lead to a drastic reduction of the turbine performance and a significant increase of the maintenance costs. In this study, it has been assumed that the steam turbine can work also in the low efficiency zone in order to highlight the effects of thermal power fluctuations.

3.7.5 Results and discussion

The off gas temperature profile at the PCM inlet section adopted to optimise the proposed novel system is represented by the red dotted line in Figure 3.59a and has been derived by analysing several EAF plants. The flow rate is equal to 130,000 Nm^3/h. Al-12%Si has been used as PCM material, with a phase change temperature of about 576 °C.

Table 3.18 reports the optimal geometric configuration of the PCM Section, provided by the Fortran code; it consists of 41 rows of HESUs, with external *D* and inner *d* pipe diameters equal to 128 mm and 88 mm, respectively. In Figure 3.65a, the PCM state evolution over time is shown for three specific HESU rows: the first one, the reference one, namely the row undergoing the maximum thermal load, and the last one facing the minimum thermal load. It is worth noting how the reference row is not the first one, because in the first rows of a bank of tubes the turbulent flow is not completely developed.

In this section, the correlation for aligned tube bundles proposed by Grimson [166] has been used. As expected, the PCM state goes from completely liquid to completely solid only in the reference row, proving the effectiveness of the sizing procedure.

Table 3.18 Optimal geometric configuration of the PCM Section

HESU External Diameter, *D* (mm)	128
HESU Internal Diameter, *d* (mm)	88
PCM Section Height, *H* (m)	3
PCM Section Width, *W* (m)	4.6
PCM Section Length, *L* (m)	7.9
Transverse pitch, S_T (mm)	192
Longitudinal pitch, S_L (mm)	192
Number of rows	41
Number of columns	24
Number of rows Aux Eva	30
Number of rows Aux SH	11
Maximum speed (m/s)	12.1
Minimum speed (m/s)	6.3

Concerning HTF selection, three different fluids have been investigated: air, for its low cost and large availability, carbon dioxide, which is an inert gas with high specific thermal capacity, and argon, since it is commonly used in steel industry.

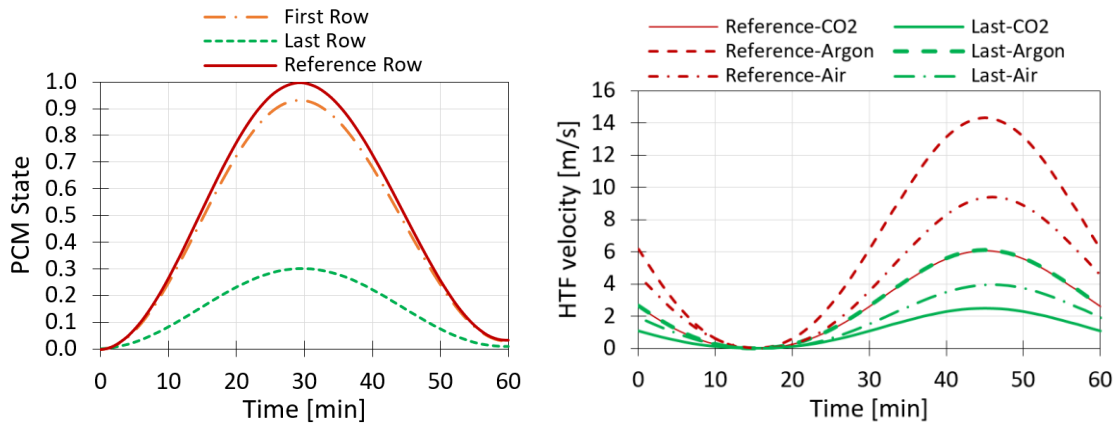

Figure 3.65 a) PCM state profile in the first, last and design reference row and b) velocity profile in the reference and last row for several HTFs

Different values of the operating pressure *p* in the range between 0.1 and 1 MPa have been analysed. Small variations of the HTF velocity, and of pressure drops consequently, are gained by increasing operative pressure over 0.4 MPa. Therefore, the latter has been set as the reasonable operating condition, in order to lower the cost of fans and their

energy consumption. As shown in Figure 3.65b, carbon dioxide achieves the best performance, while improving system safety in comparison to air, which may lead to safety issues due to its oxygen content.

In Table 3.19 the main performances of the PCM-Section are summarised. Thermal fluctuation decreases from 32.4 % to 12.7 %; the maximum thermal power of the off gas exiting the PCM Section is reduced by 34.4 %.

Table 3.19 Performance of the PCM-Section

	Inlet	**Outlet**
Max Temperature (°C)	990	681
Min Temperature (°C)	390	524
Max ΔT (K)	600	157
Standard deviation	212	55
Max Thermal Power (kW)	55,630	36,496
Min Thermal Power (kW)	19,624	27,201
Thermal Power Fluctuation (%)	32.4	12.7
Max Thermal Power Reduction (%)	-	34.4

Figure 3.66a reports the steam temperature profile at the outlet of the PCMSG components; a constant temperature of about 400°C is achieved at the outlet of the auxiliary superheater, while at the economizer and at the superheater outlet a temperature fluctuation still exists.

Figure 3.66b shows the profile of the electric power production for the three waste heat to power systems simulated in TRNSYS: the traditional steam generator with and without the PCMS, and the PCMCSG. It can be noted that the WHTP system employing a traditional Sh-SG without a PCMS has a huge fluctuation in electric power production (near-zero electric power production is reached), much larger than the fluctuation in the off gas thermal profile. This behaviour is due to the intrinsic limits of the turbine, whose performance drastically falls down when a too low steam flow rate is provided (see Figure 3.64).

Table 3.20 compares the performance of the three possible configurations of the WHTP system. The introduction of a PCM-based device reduces the size of the waste heat recovery components (steam generation boiler and turbine) of about 41%. However, when a PCM-based device is used for smoothing only, the production of electric energy

undergoes a slight reduction of about 2% with respect to the traditional configuration. This reduction can be ascribed to the working principle of the PCMS, which dissipates part of the recovered energy to control the temperature of the PCM and avoid overheating.

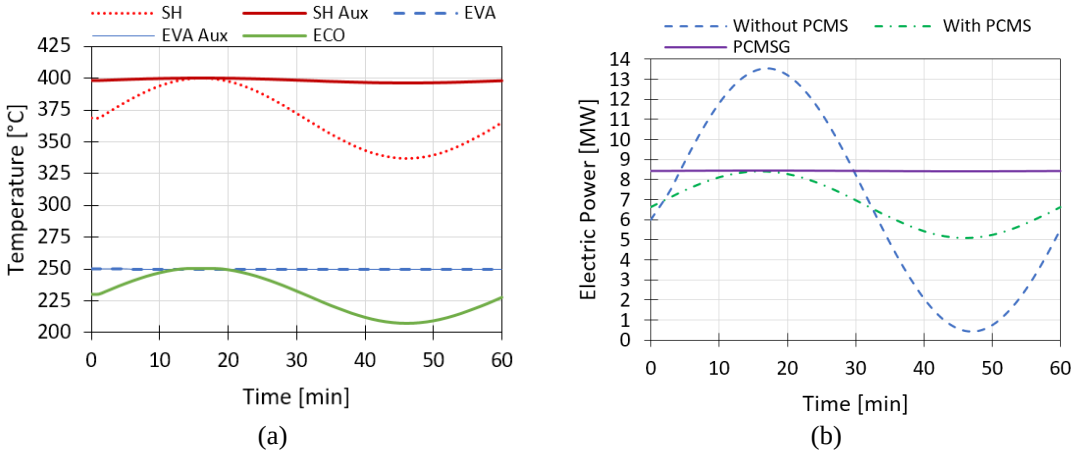

Figure 3.66 TRNSYS results: a) Temperature profile at heat exchangers outlet and b) Electric power generated by the traditional system with and without PCM-based smoothing and by the novel PCM-coupled steam generation

When the PCM-coupled steam generator is adopted, the electric production increases of 22% with respect to the traditional configuration. These results are achieved thanks to the reduced fluctuation in the steam parameters at the turbine inlet, which leads to a greater overall efficiency of the turbine.

Table 3.20 Comparison between traditional and innovative WHTP systems based on superheated steam generation

	Traditional	**Innovative**	
		PCMS	PCMCSG
Steam Generator size (kW_{th})	47,934	28,800	28,800
Max Mass Flow (kg/s)	18	11	11
Turbine size (kW_e)	14,380	8,640	8,640
Produced electricity (kWh)	7,036	6,897	8,563
Increased electric production (%)	n.a.	- 2	22

Table 3.21 reports the cost-benefit analysis of the PCM-coupled steam generator; capital expenditure (CAPEX) and operational expenditure (OPEX) have been estimated together with local suppliers. An electrical energy generation of 48,166 MWh/year can be estimated by assuming that the EAF operates 7500 h/year and the WHTP system availability is 75%. Considering an energy supply cost of 50 €/MWh_e, currently granted to the steel industry by the Italian energy market, a cost saving of about 2,408,290 €/year

can be achieved. Furthermore, a positive cash flow of 3,631,349 € can be estimated for the first 5 years taking into account an up-to-date value of 120 €/TOE [138] of the Italian energy efficiency certificates. Thus, a pay-back period of about 3 years can be expected, which underlines the profitability of the proposed novel WHTP system.

Table 3.21 Economics of the PCM-coupled steam generator: investment, operations and maintenance (O&M) costs, revenues

	Costs		**Incomes**
	CAPEX [€]	*OPEX [€/year]*	*[€/year]*
PCM Section	1,000,000	100,000	
Steam Generation Section	8,112,847	400,000	
Auxiliary Section	500,000	30,000	
Steam turbine	3,023,965	50,000	
Other (design, safety, etc.)	1,200,000	135,000	
Total	***13,836,812***	***715,000***	
Electric energy saving			2,408,290
Energy efficiency certificate			3,631,349

3.7.6 Conclusions

In this section, the evolution of current waste heat to power systems for the steel industry towards the production of high temperature superheated steam with limited variability is enabled by coupling PCM-based heat extraction with steam generation. In particular, the use of high temperature PCMs evolves from smoothing off gas temperature only, as studied in previous sections (3.4 and 3.6), to generating constant superheated steam able to feed the downstream turbine nearly at nominal load. This result is achieved by introducing an auxiliary section between the PCM Section and the Steam Generation one, which provides the auxiliary heat needed to further level the thermal content of the off gas. The auxiliary heat is extracted from the PCM units by a gaseous heat transfer fluid flowing across the inner tube of each PCM container. Different models to properly size the proposed energy recovery system and simulate its operations have been developed and integrated, adopting both commercial tools and ad hoc elaborated codes.

Results show how the new system is able to prevent the steam turbine from working at partial loads, thus drastically increasing its efficiency. Furthermore, the size of the steam generator and of the turbine, required to exploit the same amount of waste heat, can be significantly reduced in comparison to current solutions with benefits on related investments.

3.8 Conclusions

In this chapter, the energy recovery from electric arc furnace has been addressed. In particular, the limitations related to the large fluctuation of temperature have been faced. After evaluating the potential of energy recovery in Section 3.2, an overview on the current state-of-the-art of energy recovery from electric arc furnace has been given in Section 3.3. Pros and cons of the analysed energy recovery technologies have also been reported.

A series of systems exploiting aluminium and its alloys as high temperature phase change materials (PCMs) have been developed in Sections 3.4 (i.e. Passive PCM-based device for temperature smoothing), 3.6 (i.e. Active PCM-based device for temperature smoothing) and 3.7 (PCM-coupled steam generator) with the aim of reducing the temperature fluctuation of the off-gas and increasing the overall efficiency of the downstream energy conversion technology. Moreover, an analytical and numerical approach to evaluate thermal stress in the cylindrical PCM container has been developed in Section 3.5.

The PCM-based device developed in Section 3.4 has shown the capability to reduce the maximum temperature difference of the off-gas from about 723°C to 273°C, thus increasing the capacity factor of the steam-based energy recovery system from 0.55 to 0.81. A simple payback period slightly lower than 4 year has been estimated for the passive PCM-based device for temperature smoothing, thus demonstrating its economic viability. It has also been estimated that the adoption of the proposed system has a potential energy saving equal to 0.34% of the whole Italian electricity consumption. Nevertheless, the system proposed in Section 3.4 is limited by the uncontrolled PCM temperature that can lead to the overheating of the PCM container, thus affecting their structural resistance.

The thermal stress analyses of the PCM container carried out in Section 3.5 have shown that using a geometry based on concentric pipes allows the maximum stresses in the PCM container to be kept below the yielding point. The analyses identified diameter of inner pipe and thickness of the external pipe as the most relevant design parameters.

Furthermore, AISI 316 has been identified as the most suitable material for the PCM container among stainless steels.

In order to overcome the limitation due to PCM overheating, in Section 3.6 an improved configuration of the PCM-based device has been proposed (i.e. active PCM-based device); a heat transfer fluid flowing through PCM containers has been introduced in order to control the PCM temperature. The analyses carried out in Section 3.6 have shown that the improved configuration of the PCM-based device guarantees the same performance of the previous configuration (i.e. PCM-based device) while overcoming the overheating issue. In addition to this, the analyses revealed that the heat transfer fluid can also be used to reinforce steam production, thus enabling a further level of integration with the downstream energy recovery system.

The chance of actively managing the heat transfer fluid flowing through the PCM-based device to improve steam parameters has been investigated in Section 3.7. A new type of heat recovery system has been developed by integrating the features of the PCM-based device described in Section 3.6 with a superheated steam generator. Results have shown that the electric power production can be increased up to 22% with respect to traditional solutions, allowing a payback period lower than 3 years.

Concluding, in this chapter it has been demonstrated that the proposed PCM-based technologies can actually trigger effective waste heat recovery in such an energy intensive sector as the steel industry, thus fostering the evolution towards more sustainable industrial processes.

Chapter 4

ENERGY RECOVERY FROM BILLET REHEATING FURNACE

4.1 Introduction

There is a huge potential to exploit excess/low grade heat from industrial processes for power generation, a sizeable cause of energy inefficiencies is due to low grade heat generated particularly in large scale thermal energy systems that is not subsequently recovered. Estimations about the percentage of industrial primary energy consumption that is released as waste heat, provide figures of 20 to 50%. Sources of waste heat include primarily the release of hot flue gases into the atmosphere and heat losses due to hot equipment surfaces [169]. Table 4.1 summarizes some of the possible sources from waste heat and its potential uses.

The harnessing and reuse of waste heat is a potential alternative to high-priced imported fossil fuels or electricity [3]. There are several technologies currently being used in several industrial facilities and the main barrier for wider adoption is due to economic and technical barriers. These technologies include heat exchangers for high temperature (e.g. recuperators, regenerators, economizers, waste heat boilers) and for low temperature (e.g. deep economizers, indirect/direct contact condensation recovery, heat pump, etc.)

and load preheating (e.g. boiler feed water preheating). Typically, in waste heat recovery power applications, the heat is recuperated by means of a waste heat boiler that is then transferred to a working fluid generating mechanical energy in some kind of expander coupled to an electric generator. Apart from the common and well developed such power cycles that include the steam Rankine cycle, organic Rankine cycle and Kalina cycle; there are also innovative technologies directly generating electricity from heat (e.g. piezoelectric and thermo-electric generators) [3].

Table 4.1 Waste heat sources and uses [3]

WASTE HEAT SOURCES	USES FOR WASTE HEAT
Combustion Exhausts:	Combustion air reheating
Glass melting furnace	Boiler feedwater reheating
Cement kiln	Load reheating
Fume incinerator	Power generation
Aluminium reverberatory furnace boiler	Steam production for power generation
Process flue gases:	Space heating and cooling
Aluminium reverberatory furnace	Waster reheating
Steel electric arc furnace	Transfer to liquid or gaseous streams
Cooling water from:	
Furnaces	
Air compressors	
Internal combustion engines	
Conductive, convective and radiative losses from heated products	

However, there is a fundamental issue that needs further investigation: the mismatch between the fluctuating nature of the waste heat available and the recovery system. Typically, there is a fluctuation in terms of flow rate and/or temperature of the waste heat profile according to the variability of the upstream process. This poses a challenge on the downstream recovery systems since they do not account for this fluctuating nature and this leads to sub-optimal component selection and poor cycle performance at off-design conditions. Indeed, waste heat recovery systems are commonly designed for a single operating point (i.e. *design point*); due to time constraint, resource availability and lack of know-how, current design practice does not take into account the fluctuation of the waste heat source and some waste heat recovery systems adopt as design point either the upper boundary [5–7] or average values of the fluctuation range [8,9]. This means that the systems will operate for most of the time under part load (*off-design*) thus severely reducing the efficiency of energy recovery.

One of the most established technologies for waste heat recovery is Organic Rankine Cycle (ORCs) which is extensively being investigated over the years. However, many of the current studies [170–174] on ORC-based waste heat recovery systems focus on optimization or parametric investigation of the working fluids and system components mainly considering the design point [175]. Meanwhile, on the other hand, there is limited activity in trying to understand the dynamic behaviour of the ORC systems and/or mitigate the effects of the waste heat fluctuation. One possible solution to this is that of using an upstream thermal energy storage system to smooth the thermal power fluctuation of the flue gases entering the ORC system, thus allowing operating near the design-point.

Different thermal energy storage (TES) systems have been studied in the past [176]. Apart from traditional sensible heat storage systems [177], novel storage systems based on the latent heat of Phase Change Materials (PCMs) have gained attention in recent years [10]. The advantage of using PCMs over sensible heat storage is that they hold higher capacity of storage per unit volume, provide most of the heat energy at constant temperature and hold small temperature difference between charging and discharging [162].

In the case of PCM for high temperature applications, limited research has been done so far. A chemical recuperator based on PCMs has been proposed in [157]; the proposed system stores in a PCM the waste heat released by an electric arc furnace, and then supplies constant heat to an endothermic reaction (i.e. methane-steam reforming MSR). . A novel technology using aluminium encapsulated in cylindrical containers as phase change material (PCM-based technology) has been proposed in [161]to smooth the fluctuations of the waste heat from an electric arc furnace. . The proposed PCM-based technology has been further developed in [162], with the introduction of a heat transfer fluid (HTF) to overcome overheating issues in PCM containers.

In this chapter, it is investigated the performance impact of retrofitting the PCM-based technology to a steel billet reheating furnace already installing an ORC system as main waste heat recovery system; the performance analysis of the ORC system with and without the PCM-based technology will be assessed in detail. The analysis of the performance of the ORC system with the proposed modifications is done by means of a plant-level dynamic model developed in the Modelica language and simulated in the simulation environment Dymola [178].

The chapter is structured as follows: in Section 4.2 a general overview on the issues related with the thermal power fluctuations as well as the description of the existing waste heat recovery system layout and operations is provided; in Section 4.3 a modification of the plant is proposed by using the PCM-based technology to reduce the thermal power variability of the flue gas and recirculate some of its non-exploited thermal energy; Section 4.4 details the modelling methodology used while Section 4.5 presents the results of the simulations; finally the conclusion are given in Section 4.6.

4.2 Thermal power fluctuations in waste heat to power plants

4.2.1 General overview

The benefit of waste heat to power generation is that the outcome is a high exergy product that can be easily transported and used in other processes [179]. From the various possible technologies for waste heat to power (e.g. Stirling Engine, Thermo-electric, Inverted Brayton Cycle) the ORCs stand out as the technology with the best performance in the temperature range of 200°C ÷ 400°C [180].

Even though there is huge potential for waste heat to power applications, waste heat is often not fully exploited due to techno-economic challenges - such as low performance, long payback period, large investments costs, etc. One of the technical challenges directly affecting the low performance of ORC systems comes from the fluctuating, irregular or intermittent nature of waste heat sources; this variability is due to the fluctuation of the thermal power proper conveyed by the off-gases mass flow, and/or due to temperature fluctuation of the heat. Furthermore, in addition to the poor performance at off-design conditions, in case of ORC systems, the operating range is constrained by the risk of chemical decomposition of the organic fluid at high temperatures as well as restrictions for the operation of the expander with wet vapour.

4.2.2 Case study: billet preheating furnace

The steel industry is one of the most energy intensive industries and one of the major responsible of CO2 emissions (in 2012 it consumed about 5 % of all primary energy produced worldwide contributing to 7 % of all global CO2 emissions [16]). However, this sector has the potential to further reduce of 20% both energy consumption and greenhouse gas emission. In this context, waste heat recovery in steel industry represents one of the

greatest opportunity to reduce the consumption of primary energy [18–21]. Moreover, of all the processes that produce waste heat in the steel production, billet reheating furnaces consumes 15÷20% of the total energy consumption and 70% the energy consumption of the rolling process [24], releasing as waste heat about 16% of the total energy input [25].

Billet reheating furnaces are needed to heat steel slabs to a pre-defined temperature needed for the subsequent hot rolling process. They can be of the pusher type or walking beam or hearth type [181]. In all these furnaces the steel billets are heated in four different zones (pre-heating, 1st and 2nd heating zones, and soaking zones), according to a specific temperature curve [182]. The heating is made by top and/or bottom fired burners. Because of the strict temperature control required to meet the quality of the billets properties, the temperature variability within the reheating furnace is minimal; this is not the case for the flow rate of the flue gas which is affected by the different batches and production rates.

In order to show the benefits of the PCM-based technology as a smoothing and recuperating device, a case study of an existing steel plant is presented; an ORC system with nominal power output of 555 kW is installed downstream of the reheating furnace.

In Figure 4.1 it is shown the layout of the existing waste heat recovery system, which is composed by an air pre heater and an ORC system, from billet reheating furnace; the flue gases exit the furnace at temperatures of around 850 °C (T1); after this, a vent-valve injects some fresh air in the flue gas stream in order to avoid thermal damage for the downstream heat exchangers. The flue gases then enter the first heat exchanger (Air preheater) where some thermal energy is transferred in order to preheat the air that is being used in the furnace combustion. After the air pre-heater, the flue gas at temperatures of around 400 °C (T3) enters the waste heat recovery boiler of the ORC system where the flue gas transfers some of its thermal energy to the working fluid flowing within the ORC system.

The flue gases leaving the ORC waste heat recovery boiler (4) - usually at temperature no lower than 150 °C - are rejected to the atmosphere through a chimney; a by-pass valve is installed upstream of the waste heat boiler for the cases in which the ORC system is off due to either a too low thermal power available in the flue gas or scheduled maintenance, service and so on.

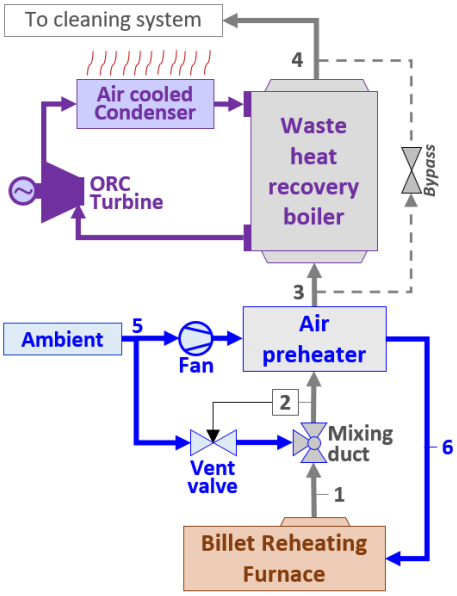

Figure 4.1 Layout of the current waste heat recovery system from billet reheating furnace

4.3 Integrating a PCM-based device with current energy recovery system

This chapter proposes the introduction of a latent heat storage system based on high temperature phase change materials (i.e. PCM-based technology) in an existing waste heat recovery system, composed by an air preheater and an ORC system, in order to increase the energy efficiency and capacity factor of the ORC system. The existing system recovers the waste heat of a billet reheating furnace through a waste heat boiler and converts the thermal energy into electric power by means of an ORC turbine.

The PCM-based technology employs the eutectic alloy Al-12%Si (in mass %) as high temperature PCM. The proposed technology stores and releases thermal energy on demand acting as a sort of "thermal flywheel" allowing the ORC system to operate closer to the design-point.

The idea of using a PCM-based technology for smoothing the thermal power fluctuations in waste heat recovery systems has already been proposed in Chapter 3. Nevertheless, these solutions only aimed at smoothing the temperature fluctuation of the flue gas, since the considered waste heat source (i.e. flue gas from electric arc furnace) was characterised

by a near-constant mass flow rate and large temperature fluctuations. In this chapter, the considered waste heat source is a billet reheating furnace, which is characterised by a near-constant temperature and a large fluctuation in the mass flow rate. In addition to this, it should be considered that the PCM-based technology proposed in Chapter 3 was developed considering an ex novo waste heat to power system, while in this chapter the proposed device is integrated in an existing waste heat recovery system; hence the design of the PCM-based technology should be rearranged according to the new requirements.

The expected impact of the PCM-based technology on the performance of the waste heat recovery system is that of:

- reducing the thermal load fluctuation entering the ORC system and therefore reducing the lower efficiency operating points by effectively levelling-up the thermal load closer to the design-point;
- increasing the power output from the waste heat by means of the recirculation of a fraction the thermal energy present in the flue gas that exits the waste heat recovery boiler.

The next sub-sections describe in detail the PCM-based technology and how it is integrated in the existing waste heat recovery system.

4.3.1 The PCM-based technology

The PCM-based technology (see Figure 4.2) consists of a set of Heat Exchange and Storage Units (HESUs), in which the heat is absorbed from the flue gases and released to a heat transfer fluid; the thermal energy is stored and released at constant temperature thanks to the contained high temperature PCM.

As reported in [10], several systems for containing PCM employ cylindrical pipes [75,76]. In particular, the use of cylindrical pipes allows the area of heat exchange to be increased thus optimizing the heat recovery efficiency, cost reduction as well as preventing crack formation and breakage [161]. The proposed HESU is composed by two coaxial pipes filled by the PCM (see Figure 4.2a); a heat transfer fluid flows through the inner pipe in order to transfer the heat from the PCM to the thermal user (e.g. ORC boiler), while the flue gases release heat to the PCM through the external pipe.

In Section 3.4, an assessment of the pipes layout was carried out; the aligned layout was preferred over the staggered one because of the reduced pressure drop through the device. In addition to this, the aligned layout allows reducing dust accumulation on the external pipe surface, which can have an adverse effect on both the heat transfer rate and flow of the flue gases across the device; the vertical arrangement allows an easy dust removal, while facilitating maintenance. Based on these considerations and the dusty nature of the flue gases from the billet reheating furnace, the aligned and vertical layout for the HESUs was chosen (see Figure 4.2a).

An insulation is installed at the bottom of each HESU in order to dampen the generation of a thermal bridge between the external wall and the bottom, which may generate a non-symmetric melting and thus a point of thermal stress concentration.

Since metals and metal alloys have higher thermal conductivity, larger latent heat per volume and smaller volume expansion than molten salts, they have greater potential as high temperature PCMs than molten salts [12]. In particular, Al-Si alloys have been considered as one of the most promising choices for PCM in the high temperature range [87,13] due to their suitable melting temperature, high latent heat of fusion and high thermal conductivity [73]. In this work, the material selected as high temperature PCM is the eutectic alloy Al-12%Si (in mass %), which has one of the highest thermal conductivity (160 W/m K) and latent heat of fusion (560 kJ/kg); its melting temperature is about 576 °C.

However, such an alloy can exhibit a very corrosive behaviour while in contact with steel [96], which is the most practical material for the pipe enclosure of the PCM. Thus, the use of ceramics as shell materials for high-temperature metallic PCMs have been recently investigated in [96], in which the corrosion resistance of several commercial ceramics was tested. The corrosion tests revealed that Al_2O_3, AlN and Si_3N_4 have high corrosion resistance to the molten Al-Si alloys. In a further work [97], a cylindrical-type ceramic container for the macro-encapsulation of Al-Si alloys as phase change materials was tested and it was found that it has excellent cyclic durability. Nevertheless, the proposed PCM container was meant for latent heat storage systems based on packed bed heat exchanger type, which is not suitable for the device developed in this work. An alternative solution could be to protect the HESU surfaces in contact with the PCM by means of a

thin film of Al_2O_3, which can be obtained by means of an aluminizing and oxidation treatment [100].

Since all the HESUs within a given row (see Figure 4.2b) undergo the same off gas thermal load, the same thermal power can be extracted from each of them by the heat transfer fluid. Thus, the HESUs within the same row are connected in parallel (see Figure 4.2b) by using a single inlet and outlet manifold (see Figure 4.2a), so that the same control parameters of the heat transfer fluid (i.e. mass flow rate) can be applied to all of them. In particular, a throttling valve can be used to control the HTF mass flow rate entering each row.

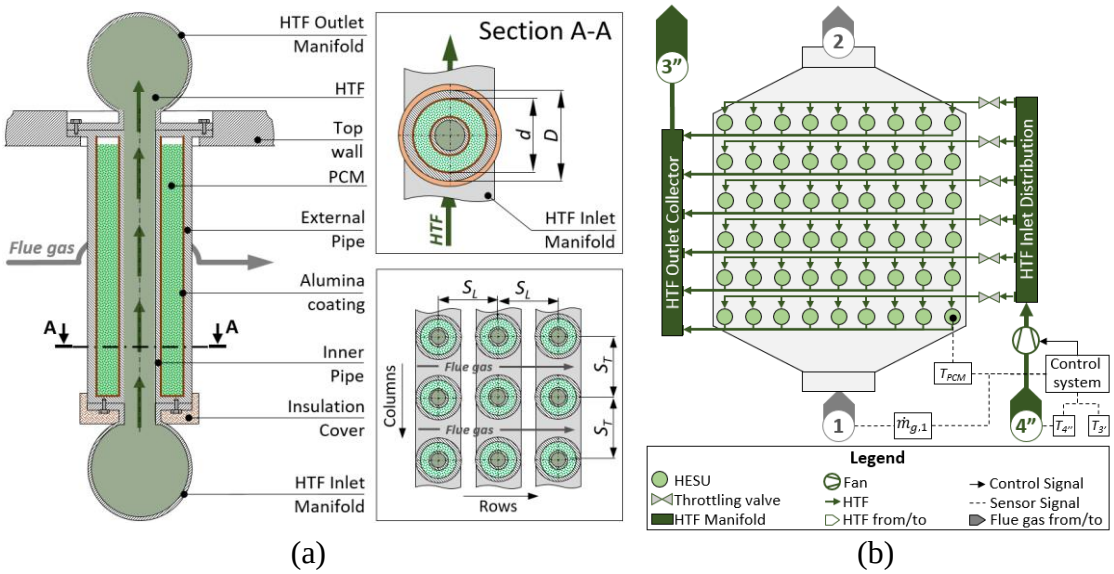

Figure 4.2 a) Geometrical configuration and layout of the HESU and b) Layout of the PCM-based technology

A fan is used to deliver the required mass flow rate of the heat transfer fluid (i.e. cold flue gas) $\dot{m}_{HTF}$ to the whole device. The amount of mass flow rate to be provided is managed by a dedicated control system, whose set point parameters are the maximum PCM temperature $T_{PCM_{max}}$ and the minimum thermal power $\dot{Q}_{min}$ entering the ORC. Referring to Figure 4.2b, the control system employs the PCM temperature T_{PCM} of a HESU in the first row, the mass flow rate at point (1), the temperatures at point (4") and (3') as controlled variables. In the following section, more details will be given on the logics of the control system.

4.3.2 Integration of the PCM-based device into the waste heat recovery system

Figure 4.3 shows the integration of the novel PCM-based technology in the existing waste heat recovery system, in which the PCM-based technology replaces the previous cooling system (see Figure 4.1), which was using fresh air to cool down the flue gas. In the proposed layout, the PCM-based technology recirculates these cooled flue gases leaving the waste heat recovery boiler to extract the stored thermal energy from the PCM and to supply the mass flow rate required by the ORC system to operate in the high efficiency zone.

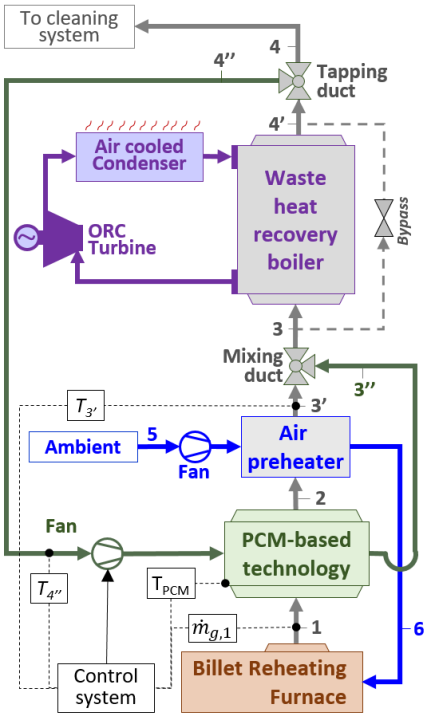

Figure 4.3 Integration of the PCM-based technology in the current waste heat recovery system

The hot flue gases from the furnace enter the PCM-based technology (1) releasing their thermal energy to the PCM. Then, the flue gases leave the PCM-based technology (2) and enter the downstream air preheater, where their temperature is further decreased down to about 400°C (3'); the temperature of the flue gases leaving the PCM-based technology is comparable to that entering the air preheater in the initial configuration of the waste heat recovery system (i.e. no PCM-based technology). In this new layout, a mixing duct is installed between the air preheater and the waste heat recovery boiler in order to combine the flue gases from the air preheater and the PCM-based technology.

After the mixing duct (3), the flue gas enters the waste heat recovery boiler of the ORC system releasing part of its thermal energy to the working fluid of the ORC system. Downstream the waste heat recovery boiler (4'), a tapping duct (i.e. plenum) is installed to allow the cooled flue gas to be recirculated within the PCM-based technology. Finally, the flue gases enter a cleaning system (4) before being discharged to the atmosphere through a chimney. Likewise the initial configuration, a by-pass valve is installed upstream the ORC waste heat boiler to decouple the entire ORC system in case of low thermal power of the flue gases, scheduled maintenance, etc.

The introduction of the PCM-based technology allows then the heat loss due to air dilution (i.e. the heat absorbed by the dilution air and not recovered by the waste heat recovery system) to be completely avoided and the heat loss at the stack to be reduced.

4.4 Methodology and System modelling

In order to analyse the performances of the proposed enhancements of the energy recovery system and to compare them to those of the current waste heat recovery system, the methodology shown in Figure 4.4 has been adopted. The methodology consists of four main stages: 1) Data analysis, 2) Design and Modelling, 3) Simulation and 4) Results analysis and comparison.

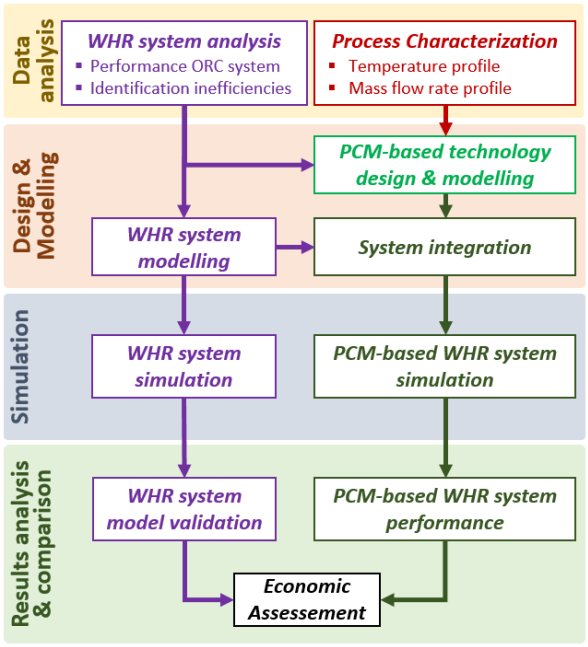

Figure 4.4 Flow diagram of the adopted methodology

In the first step, real data output from the existing waste heat recovery system is analysed to identify the thermal inefficiencies; specific focus is in the performance of the ORC system, which is analysed in detail in order to extrapolate the part-load curve. Furthermore, the process is characterised in terms of temperature and mass flow rate of the flue gas with the aim of identifying a representative series of duty cycles.

In the second step the design of the PCM-based technology is carried out; the design criteria are based on the analysis made in the previous step. The design of the PCM-based technology consists in the selection of the geometry and layout of the HESUs, which in turn define the thermal energy that can be stored in form of latent heat (i.e. amount of PCM). Furthermore, the main control parameters (e.g. minimum thermal power entering the ORC system, maximum PCM temperature) are identified at this stage. Once this stage is completed, the components of the current waste heat recovery system and the PCM-based technology are modelled in the *Modelica* coding language. Two models of the waste heat recovery system are then developed and used to evaluate the current system and that integrated with the PCM-based technology. In the last step, the performances of the two systems are analysed and compared. Finally, an economic assessment of the introduction of the PCM-based technology is carried out.

4.4.1 Analysis of the waste heat recovery system and process characterization

Measurements carried out in the existing energy recovery plant have been used for the analysis of the performance of the ORC system and for the process characterisation[1]. The main parameters of the ORC system system are listed in Table 4.2.

Table 4.2 ORC system main operating parameters

Nominal Thermal Power (kW)	3,000
Nominal Electric Power (kW)	555
Nominal efficiency (%)	18.5
Evaporator Pressure (bar)	4 – 7
Condenser Pressure (bar)	0.15 – 0.25
Fluid Mass Flow (kg/s)	3.5 – 6.5
Working Fluid	Hexamethyl-disiloxane

[1] The sampling rate of the measurements is one minute

Figure 4.5a shows the mass flow rate of the flue gas at point (1) and (2) - before and after the vented duct - as well as the mass flow rate of the dilution air entering the vented duct (i.e. point (5)); the flue gas temperature at inlet (1) and outlet (2) of the vented duct are reported in Figure 4.5b.

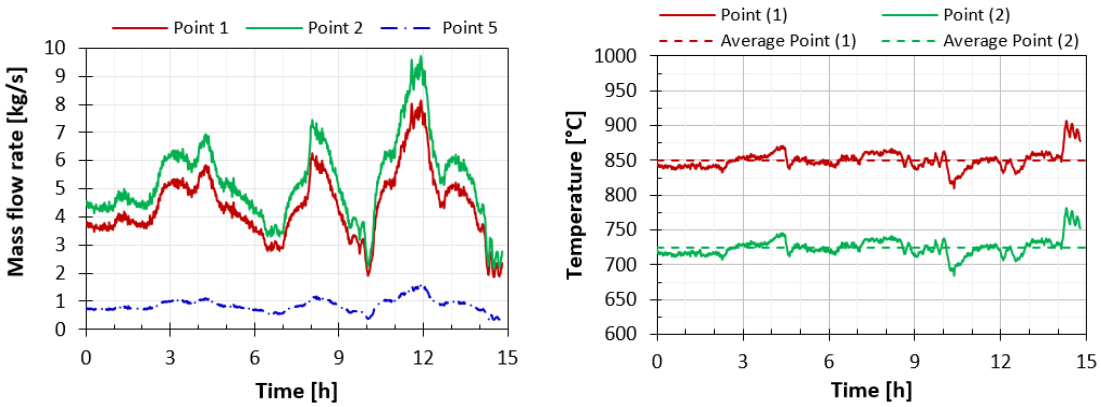

(a) (b)

Figure 4.5 a) Mass flow rates at the vented duct and b) flue gas temperature at the vented duct inlet and outlet

In the current waste heat recovery system, it is possible to identify the main heat losses: the heat loss due to air dilution, $\dot{Q}_{dil}$ and the stack loss, $\dot{Q}_{st}$. The heat loss due to air dilution can be calculated as:

$$\dot{Q}_{dil} = \dot{m}_{dil}(h_4 - h_{amb}) \tag{4.1}$$

where $\dot{m}_{dil}$ is the mass flow rate of the dilution air at point (5), h_4 and h_{amb} are the enthalpies at point (4) and at ambient temperature respectively. The measured data reveals that the heat losses due to air dilution vary from 38 to 237 kW, with an average value of 114 kW; this heat loss is completely avoided by the introduction of the PCM-based technology because it replaces the vented duct thus avoiding the dilution of fresh air.

The stack loss $\dot{Q}_{st}$, which is expressed in Equation (4.2), cannot be avoided but can be reduced by recirculating part of the mass flow rate $\dot{m}_{g,4}$ - at point (4) - into the waste heat recovery, thus reducing the total mass flow leaving the stack.

$$\dot{Q}_{st} = \dot{m}_{g,4} \cdot (h_4 - h_{amb}) \tag{4.2}$$

In the current system, the stack loss varies from a minimum value of 249 kW to a maximum value of 1464 kW, with an average value of 702 kW.

Among the measured quantities, the most useful for the performance analysis of the ORC system are the gross electric power $\dot{W}_e$, the temperatures of the flue gas at the inlet (3) and outlet (4) of the waste heat recovery boiler (refer to Figure 4.1) and the mass flow rate of the flue gases. Based on the available measurements, the thermal power entering the ORC system, $\dot{Q}_{ORC}$ can be calculated as:

$$\dot{Q}_{ORC} = \dot{m}_{g,2}(h_3 - h_4) \tag{4.3}$$

where $\dot{m}_{g,2}$ is the mass flow rate of the flue gas at point (2), h_3 and h_4 are the enthalpies of the flue gas points (3) and (4) respectively. The thermal efficiency is then derived accordingly to Equation (4.4).

$$\eta_{th} = \frac{\dot{W}_e}{\dot{Q}_{ORC}} \tag{4.4}$$

In this chapter, the part-load efficiency curve of the ORC system represents the thermal efficiency η_{th} as a function of the load factor of the ORC boiler, which is defined as:

$$\chi = \frac{\dot{Q}_{ORC}}{\dot{Q}_{ORC,d}} \tag{4.5}$$

where $\dot{Q}_{ORC,d}$ is the design thermal power and $\dot{Q}_{ORC}$ is the actual thermal power recovered by the boiler. The trend line shown in Figure 4.6a represents the part-load efficiency curve extrapolated from the actual thermal efficiencies (grey dots in Figure 4.6a) calculated based on the real data measured in the ORC system. It is worth remarking that the large distribution in the actual thermal efficiencies is due to measurement noise and high transients; based on the trend line reported in Figure 4.6a, the part-load efficiency curve can be expressed a logarithmic function. From Figure 4.6a it is possible to observe that no data are recorded for load factor lower than 0.2, meaning that the below such a value the ORC system is bypassed.

In this chapter, two working zones of the ORC system have been identified based on the efficiency ratio ε, which is defined as follows:

$$\epsilon = \frac{\eta_{th}}{\eta_{th,d}} \tag{4.6}$$

where η_{th} is the actual thermal efficiency and $\eta_{th,d}$ is the design thermal efficiency. When ε > 0.85, the ORC system is considered to be operating in the high efficiency zone ($\chi >$ 0.5 - green area in Figure 4.6b), whereas ε ≤ 0.85 the ORC system operates in the low efficiency zone ($\chi <$ 0.5 - orange area in Figure 4.6b).

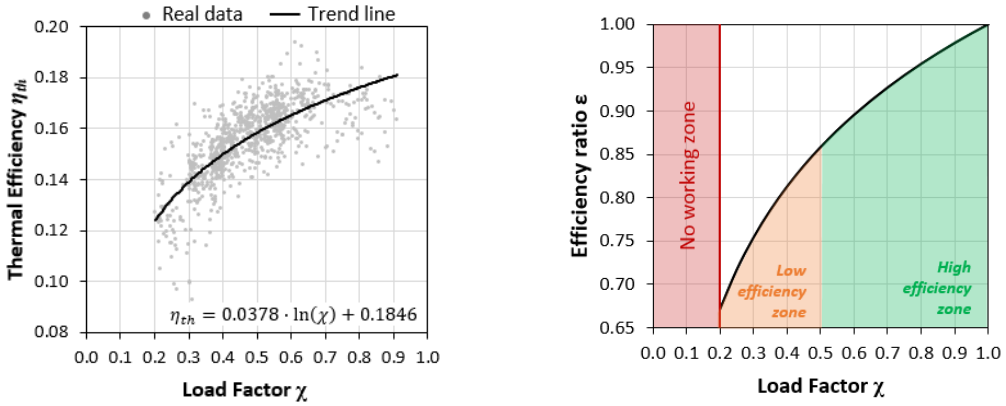

(a) (b)

Figure 4.6 a) Part load curve derived from real data and b) identification efficiency zone of the turbine

Hence, there is a need to reduce the times in which the ORC system operates in the low-efficiency zone; this can be achieved by means the PCM-based technology. A typical profile of the mass flow and temperature variation of the flue gases at the inlet and outlet of the ORC waste heat recovery boiler during a day of operation of the billet reheating furnace is shown in Figure 4.7a; the data is for approximately 15 hours of continuous operation of the ORC system. It is worth noting that, unlike Electric Arc Furnace which is characterized by a large fluctuation in temperature and minimum variation in flow rate of the flue gas, in the billet reheating furnace the flue gas is characterized by minimum variation in temperature and large fluctuation in the flow rate. It can also be observed that the ORC system is optimized to recover most of the thermal energy available on the flue gases above 150 °C, whereas all the thermal energy below this temperature is discarded.

Figure 4.7b reports the duration curve of the load factor calculated from the measured data of the ORC system; from the figure it is apparent that the ORC system never reaches its design point , but it works always under off-design conditions. The load factor varies from a minimum value of 0.19 up to a maximum value of 0.84; the ORC system then operates with an average load factor of 0.46, which leads to an average thermal efficiency of 15.5%.

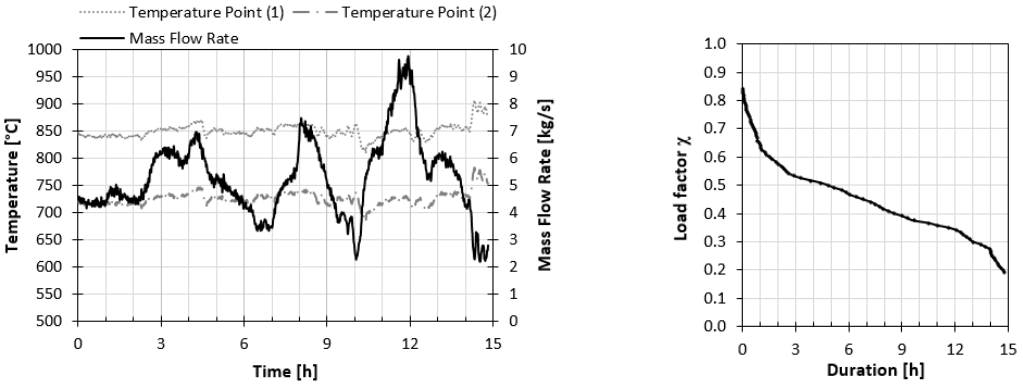

(a) (b)

Figure 4.7 a) Profile of the flue gas mass flow rate and temperature measured at the inlet and outlet of the waste heat recovery boiler; b) duration curve of the recorded load factor

The capacity factor of the analysed ORC system, which is defined as the ratio of the actual electric energy produced over the energy produced from continuous operation at nominal power, has been estimated to be about 38%.

4.4.2 Current WHR system modelling

In this sub-section the model of the current plant developed in the Modelica language is described. In order to avoid excessive computational burden and because this study is intended as a system-level performance estimation, and focused on the PCM-based technology performance, the model avoids dynamic treatment of the components.

The input to the model is the experimental data of the mass flow and temperature of the flue gas leaving the furnace at point (1) and the mass flow rate of the fresh air entering the vented duct at point (5); since the exact composition of the flue gas is unknown, properties of standard air are taken as reference.

The air pre-heater component is modelled as a simple counter-current heat exchanger, in which the heat transfer coefficient U expressed as:

$$U = U_{ref} \cdot \left(\frac{\dot{m}_{g,2}}{\dot{m}_{ref}}\right)^{0.4} \cdot \left(\frac{\dot{m}_a}{\dot{m}_{ref}}\right)^{0.4} \tag{4.7}$$

where U_{ref} is the reference heat transfer coefficient, $\dot{m}_{ref}$ is the reference mass flow rate, $\dot{m}_{g,2}$ and $\dot{m}_a$ are the mass flow rates of flue gas and of the ambient air entering the air preheater respectively; the reference coefficients U_{ref} and $\dot{m}_{ref}$ have been tuned to fit the experimental data.

According to the NTU-effectiveness method, the heat flow exchanged in the pre-heater $\dot{Q}_{APH}$ between the air and the flue gas can be estimated as:

$$\dot{Q}_{APH} = \varepsilon \cdot C_{min}(T_{g,2} - T_{a,6}) \tag{4.8}$$

where C_{min} is the minimum heat capacity, $T_{g,2}$ is the flue gas temperature at point (2) and $T_{a,6}$ is the air temperature at point (6); ε is the effectiveness of a simple counter-current heat exchanger and it is calculated as:

$$\varepsilon = \frac{1 - exp[-NTU(1 - C_{min}/C_{max})]}{1 - (C_{min}/C_{max})exp[-NTU(1 - C_{min}/C_{max})]} \tag{4.9}$$

where C_{max} is the maximum heat capacity and NTU is the number of transfer units for a given heat transfer area A_{ht}, which can be expressed as:

$$NTU = \frac{A_{ht} \cdot U}{C_{min}} \tag{4.10}$$

the ORC system is modelled as a "black-box" in which the flue gas temperature T_4 at the outlet of the ORC system is expressed as a function of the mass flow rate, $\dot{m}_{g,3}$ and the temperature at the inlet of the ORC system, T_3; the temperature function $T_4(\dot{m}_{g,3}, T_3)$ has been extrapolated by means of a regression analysis of the experimental data. The thermal power entering ORC system $\dot{Q}_{ORC}$ is calculated as:

$$\dot{Q}_{ORC} = \dot{m}_{g,3} \cdot (h_3 - h_4) \tag{4.11}$$

where h_3 and h_4 are the enthalpies of the flue gas at point (3) and (4) assuming the properties of standard atmospheric air.

The gross electric power generated by the ORC system, $\dot{W}_{el}$ is then estimated by means of the part load curve of the thermal efficiency, η_{th} which has been extrapolated from experimental data and expressed as a function of the load factor χ (see Figure 4.6a).

$$\dot{W}_{el} = \dot{Q}_{ORC} \cdot \eta_{th}(\chi) \tag{4.12}$$

4.4.3 PCM-based device design and modelling

Since the introduction of the PCM-based technology is a retrofitting intervention, its design is aimed to minimize plant modification of the waste heat recovery system while maximizing its performance. In addition to this, the furnace operation should be as less as possible affected by the installation of the proposed technology. In order to guarantee such a requirement, the average temperature at the inlet of the air preheater (i.e. outlet temperature of the PCM-based technology) should be kept as close as possible to that in the existing plant (i.e. 725°C). Thus, the flue gas temperature at the outlet of the PCM-based technology becomes one of the design criteria of the proposed technology. In addition to this, the temperature of the heat transfer fluid leaving the PCM-based technology should be as close as possible to the average temperature entering the ORC system (i.e. 397°C).

Since this chapter aims to evaluate the impact of the introduction of a PCM-based technology on the performance of an existing waste heat recovery system, the HESUs have been modelled as lump elements.

As shown in Figure 4.8, the model of the HESU consists of three main blocks: the flue gas heat transfer, the HTF heat transfer and the PCM blocks. The flue gas and the HTF heat transfer blocks calculate the heat flow exchanged with the PCM by means of the heat flows of the flue gas, $\dot{Q}_g$ and of the HTF, $\dot{Q}_h$ respectively. Both the heat transfer blocks are interfaced with the external environment by means of an inlet and an outlet, which inform the HESU about the temperature, mass flow and pressure. The heat flows - $\dot{Q}_g$ and $\dot{Q}_h$ - are used by the PCM block to calculate the PCM temperature, T_{PCM} and the thermal energy stored, E_{PCM} (i.e. the internal energy of the PCM); an iterative procedure is used

to calculate the heat flows exchanged within the PCM (explained in more details later in this section).

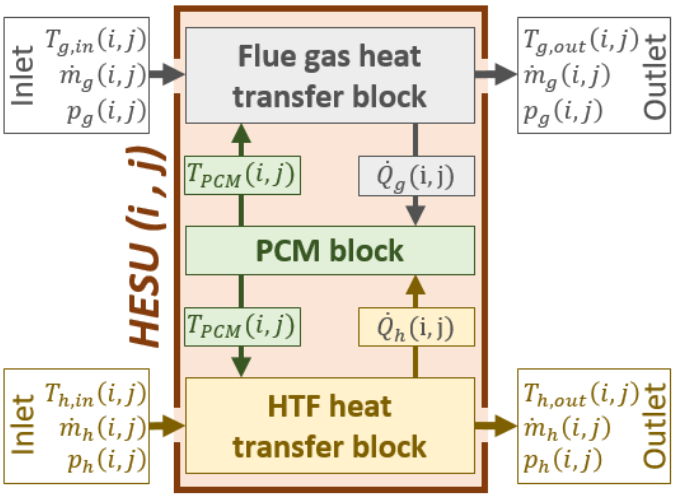

Figure 4.8 Scheme of the HESU model

In [183], three methods have been proposed to calculate the enthalpy of a PCM in the Modelica language: the linear interpolation method, the arc tangent function method and the error function method; in this chapter, the linear interpolation method is used.

The linear interpolation method uses conditional statements to define the enthalpy of the PCM, h_{PCM} as a function of the PCM temperature, T_{PCM}. According to this method, the enthalpy of the PCM can be expressed as in Equation (4.13), where $c_{p,s}$ and $c_{p,l}$ are the specific heat capacity of the PCM in the solid and liquid phase respectively.

$$h_{PCM}(T_{PCM}) = \begin{cases} c_{p,s} \cdot T_{PCM}, & T_{PCM} \leq T_s \\ c_{p,s} \cdot T_s + \dfrac{H}{T_l - T_s}(T_l - T_{PCM}), & T_s < T_{PCM} < T_l \\ c_{p,s} \cdot T_s + H + c_{p,l} \cdot T_l, & T_{PCM} \geq T_l \end{cases} \quad (4.13)$$

The terms T_s and T_l represent the solidus and liquidus temperature of the PCM, while H is the latent heat of fusion of the PCM. This formulation is valid when a temperature difference exists between the melting temperature and the solidus-liquidus temperatures. In this chapter, since the selected PCM is a eutectic alloy (i.e. theoretically constant melting temperature), solidus and liquidus temperatures are assumed to be very close to

the melting point of the PCM; in such a way, a phase transition at near-constant temperature can be reproduced.

The internal energy of the PCM, E_{PCM} is calculated as:

$$E_{PCM}(T_{PCM}) = h_{PCM}(T_{PCM}) \cdot m_{PCM} \tag{4.14}$$

where m_{PCM} is the mass of PCM contained in the HESU, which depends on the geometrical parameters of the HESU. The thermo-physical properties employed in the modelling and simulation of the selected PCM are reported in Table 4.3.

Table 4.3 Thermo-physical properties of the selected PCM

Melting temperature, T_{melt} (°C)	576
Difference Solidus-Liquidus (K)	1
Latent heat of fusion, H (kJ/kg)	560
Density, ρ (kg/m^3)	2,700
Specific heat capacity at solid state, $c_{p,s}$ (J/kgK)	1,038
Specific heat capacity at liquid state, $c_{p,l}$ (J/kgK)	1,741

The inputs of the flue gas heat transfer block are the inlet temperature $T_{g,in}$, the static pressure p_g, the mass flow rate $\dot{m}_g$, geometry (i.e. external diameter D and length L) and layout (i.e. transversal pitch ratio A and longitudinal pitch ratio B) parameters of the HESU. The pressure drop across the pipe is assumed to be negligible. The iterative procedure implemented in the flue gas heat transfer block consists of the following steps[2]:

1. A first guess value of the outlet temperature, $T_{g,out}$ is assumed to calculate the average thermo-physical properties of the flue gas (i.e. density $\rho_{g,a}$, thermal conductivity $\lambda_{g,a}$, viscosity $\mu_{g,a}$ and specific heat capacity $c_{g,a}$) and the average speed $v_{g,a}$;
2. Two correction factors are then calculated to take into account the effects of the layout of the HESUs (i.e. the void fraction ψ and the arrangement factor f_a) :

$$\psi = \begin{cases} 1 - \dfrac{\pi}{4 \cdot A} & B \geq 1 \\ 1 - \dfrac{\pi}{4 \cdot A \cdot B} & B < 1 \end{cases} \tag{4.15}$$

[2] In steps 2÷4, the correlations for aligned tube bundles proposed in [147] have been used.

$$f_a = 1 + \frac{0.7}{\psi^{1.5}} \cdot - \frac{\frac{B}{A} - 0.3}{\left(\frac{B}{A} + 0.7\right)^2} \tag{4.16}$$

3. The Reynolds and Prandtl numbers are calculated using the thermo-physical properties calculated in step (1) and the correction factors calculated in step (2):

$$Re_g = \frac{\rho_{g,a} \cdot v_{g,a} \cdot D}{\psi \cdot \mu_{g,a}} \tag{4.17}$$

$$Pr_{\mathrm{g}} = \frac{\mu_{g,a} \cdot c_{g,a}}{\lambda_{g,a}} \tag{4.18}$$

4. Once the Reynolds and Prandtl numbers are calculated, the Nusselt number is estimated according the following correlations:

$$Nu_g = f_A \cdot \ Nu_{l,0} \tag{4.19}$$

$$Nu_{l,0} = 0.3 + \sqrt{Nu_{l,lam}^2 + Nu_{l,turb}^2} \tag{4.20}$$

$$Nu_{l,lam} = 0.664 \sqrt{Re}_g \sqrt[3]{Pr_g} \tag{4.21}$$

$$Nu_{l,turb} = \frac{0.037 \cdot \ Re_g^{0.8} \cdot \ Pr_g}{1 + 2.443 \cdot \ Re_g^{-0.1} \cdot (Pr_g^{2/3} - 1)} \tag{4.22}$$

Then, the convection heat transfer coefficient α can be derived by the following expression:

$$\alpha_g = \frac{Nu \cdot \lambda_{g,a}}{D} \tag{4.23}$$

5. The log-mean temperature ΔT_{lm} and the heat flow $\dot{Q}_g$ are calculated as:

$$\Delta T_{lm} = \frac{\left(T_{g,in} - T_{PCM}\right) - \left(T_{g,out} - T_{PCM}\right)}{\ln \frac{T_{g,in} - T_{PCM}}{T_{g,out} - T_{PCM}}} \tag{4.24}$$

$$\dot{Q}_g = \alpha_g \cdot (\pi \cdot D \cdot L) \cdot \Delta T_{lm} \tag{4.25}$$

6. Finally, the heat balance reported in Equation (4.26) is used to provide an updated value of the outlet temperature $T_{g,out}$.

$$\alpha_g = \frac{Nu \cdot \lambda_{g,a}}{D} \tag{4.26}$$

The iterative procedure implemented in the heat transfer block of the HTF is similar to that adopted in the flue gas heat transfer block; the main difference is that in the former, the input parameters are the inlet temperature $T_{h,in}$, the static pressure p_h, the mass flow rate $\dot{m}_h$, the inner diameter d and length L of the HESU. One difference between the iterative procedure used in the two heat transfer blocks regards the correction factors (i.e. the void fraction ψ and the arrangement factor f_a) , which in the case of the HTF heat transfer block are not calculated. The other difference regards the correlation used for calculating the Nusselt number; in the HTF case the well-known Dittus–Boelter equation for turbulent flow in smooth circular tube for heating condition has been used [144]:

$$Nu_h = 0.023 \cdot Re_h^{\frac{4}{5}} \cdot Pr_h^{0.4} \tag{4.27}$$

The control system of the PCM-based technology aims to supply a minimum thermal power $\dot{Q}_{min}$ to the ORC system while maintaining the maximum temperature of the PCM below a given value (i.e. limit on maximum PCM temperature) by managing the mass flow rate $\dot{m}_h$ of the HTF. The first action of the control system, whose flow diagram is reported in Figure 4.9, is to acquire the mass flow rate of the flue gas $\dot{m}_g$, the PCM temperature T_{PCM} in the first row of HESUs and the flue gas temperature at the point (1), (2), (3'), (3") and (4). Then, the control system calculates the thermal power leaving the preheater $\dot{Q}_{3'}$ and the thermal power entering the PCM-based technology $\dot{Q}_{1-2}$ according to Equations (4.28) and (4.29).

$$\dot{Q}_{3'} = \dot{m}_g \cdot (h_{3'} - h_4) \tag{4.28}$$

$$\dot{Q}_{1-2} = \dot{m}_g \cdot (h_1 - h_2) \tag{4.29}$$

where $h_1, h_2, h_{3'}$ and h_4, are the enthalpies at point (1), (2), (3'), and (4), respectively.

From Figure 4.9, it is possible to observe that the control logic has been divided in three main operative modes: *discharging mode*, *charging mode* and *balance mode.* For each operative mode, a specific mass flow rate is calculated: discharging mass flow rate $\dot{m}_{dis}$, charging mass flow rate $\dot{m}_{cha}$ and balance mass flow rate $\dot{m}_{bal}$; the definition of these mass flow rates is reported in Table 4.4.

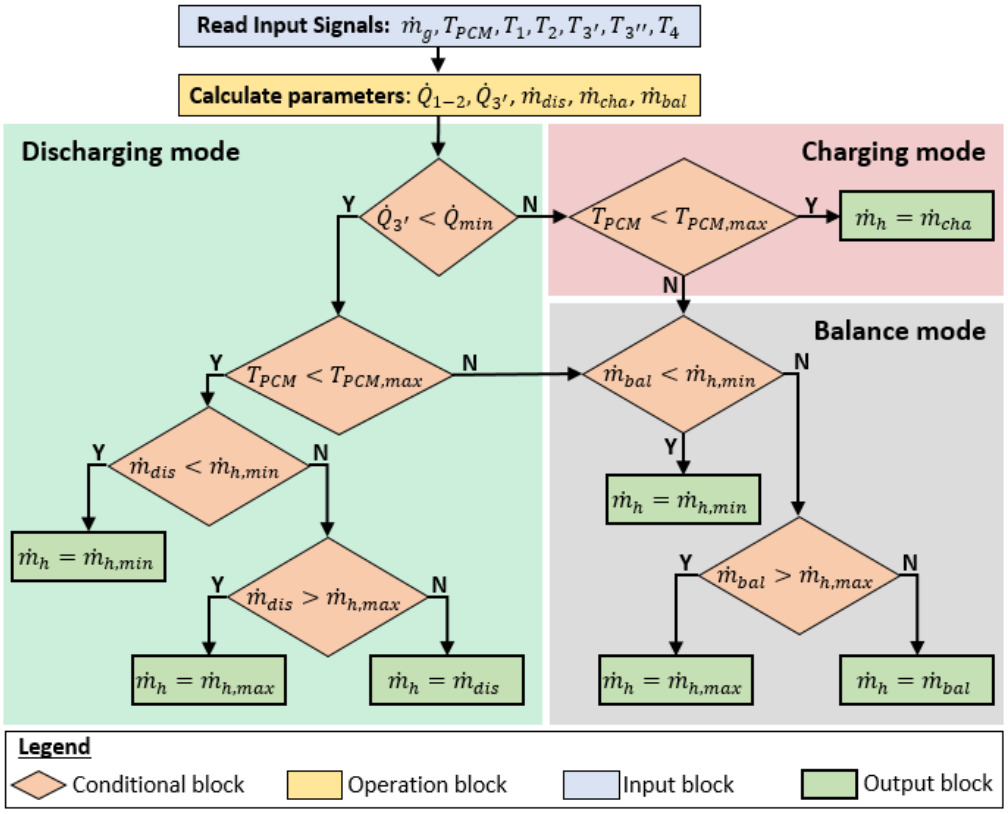

Figure 4.9 Flow diagram of the control system of the PCM-based technology

When the thermal power $\dot{Q}_{3'}$ is lower than the minimum thermal power $\dot{Q}_{min}$ and the PCM temperature T_{PCM} is lower than its upper limit (i.e. $T_{PCM,max}$), the *discharging mode* is activated and the HTF mass flow rate $\dot{m}_h$ is set equal to the *discharging mass flow rate* $\dot{m}_{dis}$. When the thermal power $\dot{Q}_{3'}$ is higher than the minimum thermal power $\dot{Q}_{min}$ and the PCM temperature T_{PCM} is lower than its upper limit, the *charging mode* is activated and the HTF mass flow rate $\dot{m}_h$ is set equal to the charging mass flow rate $\dot{m}_{cha}$. The balance mode is instead activated when the PCM temperature T_{PCM} overcomes its upper limit; in that case, the HTF mass flow rate $\dot{m}_h$ is set equal to the balance mass flow rate $\dot{m}_{bal}$.

Table 4.4 Mass flow rates characterising the three operative modes

Operative mode	Calculated mass flow rate
Discharging mode	$\dot{m}_{dis} = \frac{\dot{Q}_{min} - \dot{Q}_{3'}}{h_{3''} - h_4{''}}$
Charging mode	$\dot{m}_{cha} = \dot{m}_{h,min}$
Balance mode	$\dot{m}_{bal} = \frac{\dot{Q}_{1-2}}{h_{3''} - h_4{''}}$

The minimum and maximum values of the HTF mass flow rate $\dot{m}_h$ can be limited by means of the control parameters $\dot{m}_{h,min}$ and $\dot{m}_{h,max}$. In this paper, the minimum and maximum mass flow rates - $\dot{m}_{h,min}$ and $\dot{m}_{h,max}$- of the HTF have been set to 1.5 and 5 kg/s, respectively.

4.5 Results and discussion

4.5.1 Validation of the existing waste heat recovery system

The model of the current waste heat recovery system was validated against the available measured plant data. The comparison of the thermal power entering ORC system between the measured data and those calculated by the model is shown in Figure 4.10a, while the comparison of the gross electric power between measured data and the model is reported in Figure 4.10b.

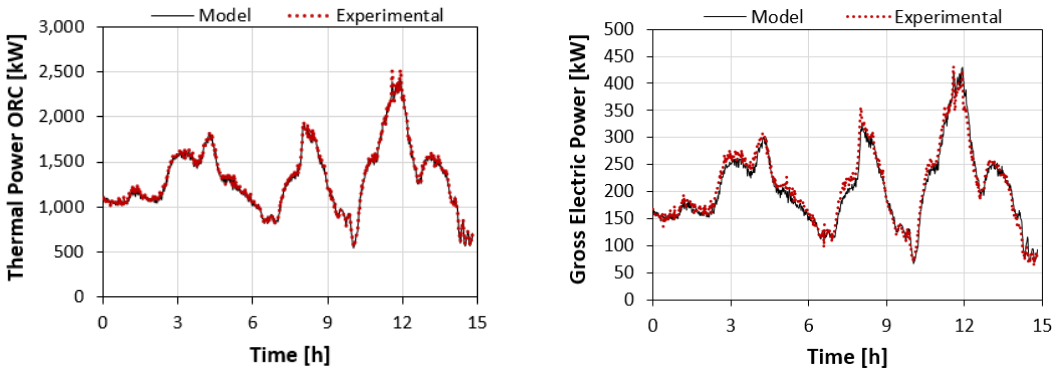

Figure 4.10 Comparison of experimental and model data: a) Thermal power entering ORC system and b) gross electric power generated

Figure 4.11a reports the comparison of the flue gas temperature after the preheater between the experimental data and those calculated by the model, while the flue gas

temperature after the ORC system obtained from the measurements and the model calculation are compared in Figure 4.11b.

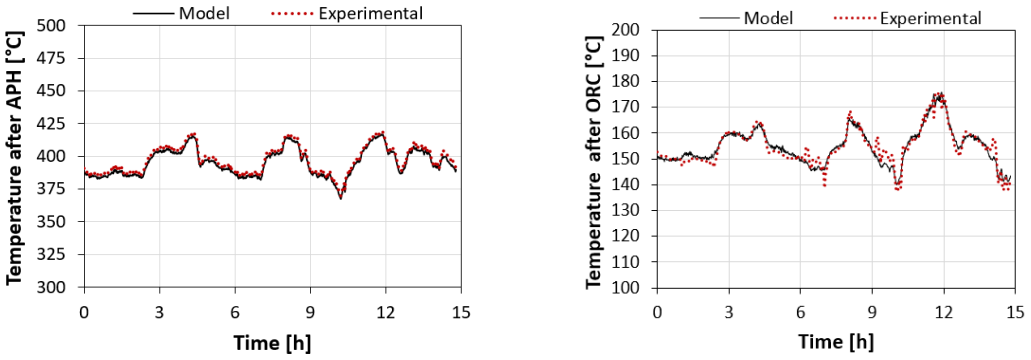

Figure 4.11 Comparison of flue gas temperature between experimental and model data: a) after pre-heater and b) after ORC system

From Figure 4.10 and Figure 4.11 it is apparent that model replicates the measured plant data with good accuracy: there is an almost perfect match with the thermal power input in the ORC system as well as with the temperature of the flue gases after the air-preheater; there is also a good agreement of temperature of the flue gas after the ORC system and with a maximum absolute error of around 5% and an average absolute error of 1%; for the gross electric power generated there is an average absolute deviation from the experimental data of about 5%. These minor discrepancies can be attributed to differences on the properties due to air being taken as that of the real flue gas as well as of the non-perfect fitting of the regressions based on the data and measurement inaccuracies of the instrumentation in the plant.

4.5.2 Performance of the PCM-based WHR system

The geometric and layout parameters as well as the control parameters of the PCM-based technology are reported in Table 4.5. The temperature profile of the flue gas and the heat transfer fluid entering and leaving the PCM-based technology are shown in Figure 4.12a; in addition to this, the temperature profile of the PCM in the first and last row of HESU are reported. The PCM temperatures (green solid and dotted lines) are nearly constant around the melting temperature (576°C), meaning that the PCM-based technology is for the most of the time using the latent heat of the PCM. From Figure 4.12a it is possible to observe some small temperature peak occurring in the temperature of the first row of HESU (green solid line), which occurs when the HESU is fully charged and the control

system activate the balance mode (i.e. maintaining the maximum allowable PCM temperature).

Table 4.5 Geometric, layout and control parameters of the PCM-based technology

Geometry parameters	
HESU External diameter, D (mm)	98
HESU Internal diameter, d (mm)	50
HESU Length, L (mm)	2,400
PCM mass per HESU, m_{PCM} (kg)	36.5
Layout parameters	
Longitudinal pitch, P_L	1.82
Transverse pitch, P_T	1.82
Number of rows, n_R	10
Number of column, n_C	8
System Longitudinal size, S_L (m)	1.78
System Transverse size, S_T (m)	1.43
System Vertical size, S_V (m)	2.4
Total PCM mass, $m_{PCM,tot}$ (kg)	2,916
Control parameters	
Minimum thermal power, $\dot{Q}_{min}$ (kW)	1,500
Minimum HTF flow rate, $\dot{m}_{min}$ (kg/s)	1.5
Maximum HTF flow rate, $\dot{m}_{max}$ (kg/s)	5.0
Maximum PCM temperature, $T_{PCM,max}$ (°C)	580

In Figure 4.12b it is reported the mass flow rates of the flue gas (red dashed line) and of the HTF (green solid line) entering the mixing duct; the total mass flow exiting the mixing duct is also reported (black solid line). In addition to these mass flow rates, the minimum (dash-dot black line) and maximum (dashed black line) value of the HTF mass flow rate are shown.

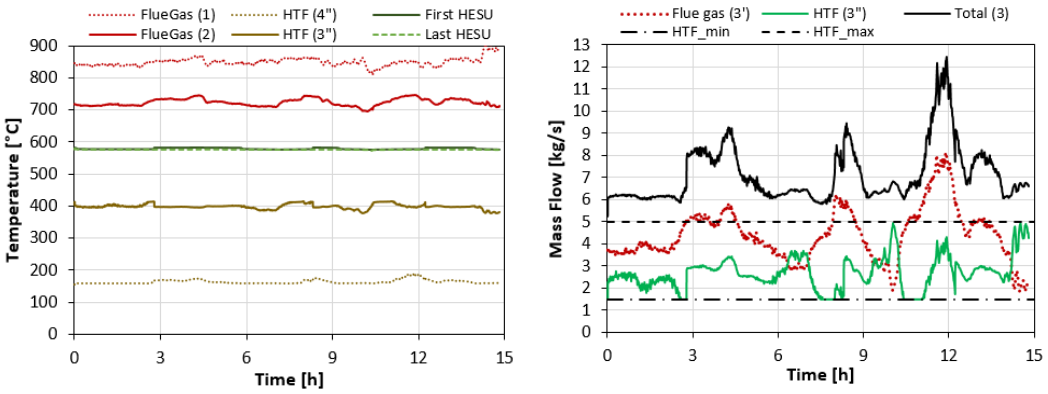

(a) (b)

Figure 4.12 a) Temperature profiles within the PCM-based technology; b) mass flow rates at the mixing duct

The performance parameters of the PCM-based technology are summarised in Table 4.6. It can be observed that the average temperature of the flue gas temperature at point (2) and that of the heat transfer fluid at point (3'') fulfil the design requirements detailed in sub-section 4.4.3, which are 725°C and 397°C respectively.

Table 4.6 Performance parameters of the PCM-based technology

Parameter	Item	Location	Min	Max	Average
Temperature (°C)	Flue gas	Point (1)	809	907	850
		Point (2)	725	748	696
	HTF	Point (3'')	155	188	163
		Point (4'')	376	414	397
	HESU	First row	575	581	578
		Last row	573	579	576
Mass flow rate (kg/s)	Flue gas	Point (3')	1.8	8.2	4.4
	HTF	Point (3'')	1.5	4.9	2.7
	Total	Point (3)	5.2	12.5	7.1

Observing Figure 4.12b and Table 4.6, it can be seen that the HTF mass flow rate ranges between the minimum and maximum values set in the control system, meaning that the control system operates adequately. The effect of the introduction of the PCM-based technology can be seen in Figure 4.13a, where the profile of the thermal power entering the ORC system is reported together with the minimum allowable thermal power $\dot{Q}_{min}$. The resulting duration curve of the load factor is reported in Figure 4.13b.

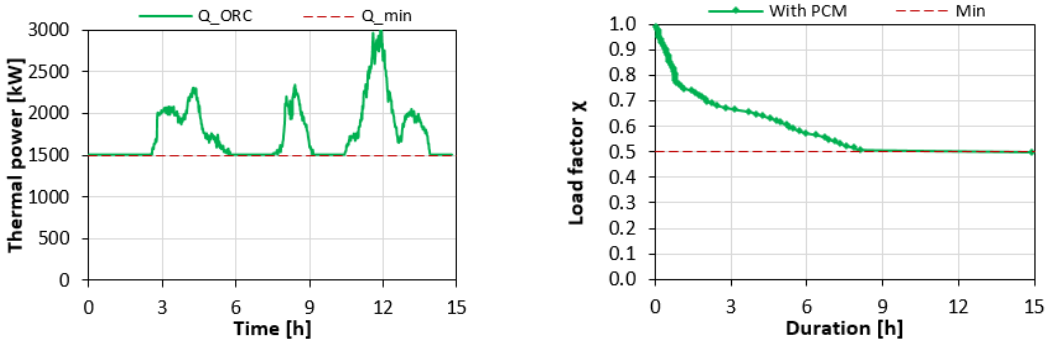

(a) (b)

Figure 4.13 a) Thermal power profile entering the ORC system; b) load factor duration curve

Figure 4.14a shows the profile of the heat flows $\dot{Q}_g$ and $\dot{Q}_h$ for a generic HESU; the heat flow is assumed to be positive when entering the HESU (i.e. the HESU absorbs heat) and negative when leaving the HESU (i.e. the HESU releases heat). The heat profile shown in Figure 4.14b represents the sum of $\dot{Q}_g$ and $\dot{Q}_h$, which identifies the charging (red area),

discharging (green area) and balance (i.e. sum equal to zero) phases occurring within each HESU.

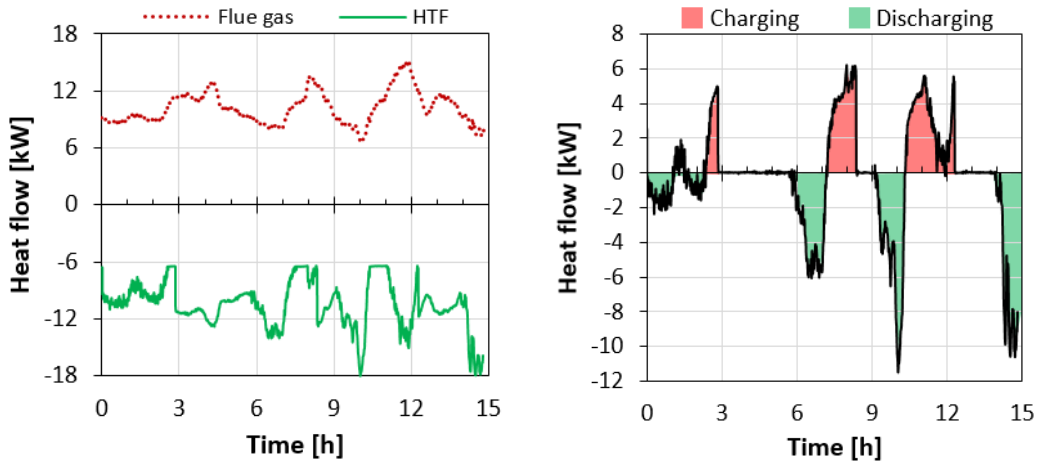

(a) (b)

Figure 4.14 a) Heat flows exchanged by the HESU; b) charging-discharging of the HESU

4.5.3 Comparison of the performance and economics

Figure 4.15a compares the thermal power entering the ORC system in the current waste heat recovery system (black solid line) with that of the waste heat recovery system integrated with the PCM-based technology (green solid line). It can be observed that the PCM-based technology allows the ORC system to operate above the minimum thermal power (red dotted line) for all the time, while in the current waste heat recovery system the ORC system operates for the most of the time below the minimum thermal power.

This difference in performance can be better observed in Figure 4.15b, where the duration curves of the load factor of the ORC system in the current waste heat recovery system (black solid line) and in the waste heat recovery system integrated with the PCM-based technology (green solid line) are reported. When the PCM-based technology is introduced, the ORC system operates always in its high efficiency zone (i.e. load factor $\chi \geq 0.5$), while in the current waste heat recovery system the ORC system operates for more than 67% of the total working time in the low efficiency zone.

The introduction of the PCM-based technology allows the capacity factor of the ORC system to be increased from 38% to 52%; the average thermal efficiency is increased from 15.5% to 16.4%.

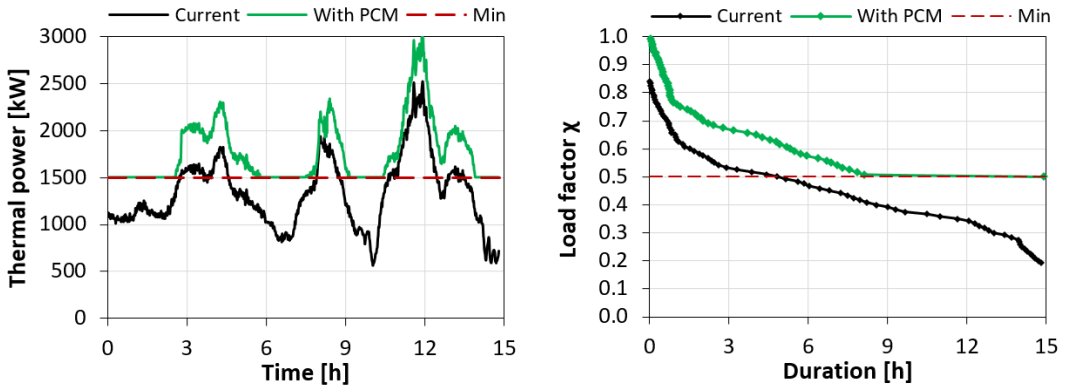

(a) (b)

Figure 4.15 Comparison between current waste heat recovery system and with the PCM-based technology: a) Thermal power profiles entering the ORC system and b) duration curves of the load factor

Table 4.7 provides a comparison of the main performance parameters of the ORC system between the current waste heat recovery system and that integrated with the PCM-based technology. Considering the increased capacity factor of 52% and assuming that the ORC system operates 7,500 hours per year, an additional electric energy production of 583 MWh per year can be estimated.

Table 4.7 Comparison of the main performance parameters of the ORC system between current and proposed waste heat recovery system

		Current	With PCM
Thermal Power (kW)	Max	2,483	3,000
	Min	614	1,500
	Average	1,331	1,756
Electric Power (kW)	Max	402	555
	Min	76	238
	Average	210	290
Thermal efficiency	Max	0.169	0.185
	Min	0.123	0.158
	Average	0.155	0.164
Load Factor	Max	0.83	1.00
	Min	0.20	0.50
	Average	0.44	0.59
Capacity factor	-	38%	52%

The capital expenditure (CAPEX) and operational expenditure (OPEX) of the PCM-based technology reported in Table 4.8 have been calculated based on estimations carried out in Chapter 3. The revenues generated by the PCM-based technology depend on the selling price of the electric energy and the additional electric energy production. While

the additional electric energy production depends only on the performance of the ORC system, the selling price of the electric energy depends on many external factors which cannot be controlled. Thus, a sensitivity analysis on the selling price of the electric energy has been carried out to identify which selling price allows to obtain a payback period between 3 and 5 years.

Table 4.8 Capital and operative expenditure of the PCM-based technology

CAPEX [€]	
PCM-based technology	85,000
Auxiliary facilities (Fan, piping, etc.)	25,000
Other costs (design, safety, etc.)	50,000
OPEX [€/year]	
Maintenance cost	9,500
Personnel cost	5,000

The results of the analysis showed that a selling price of 120 €/MWh and 83 €/MWh should be guaranteed to obtain a payback of 3 and 5 years, respectively. Considering that the average electricity prices for industrial consumers in Europe is about 119 €/MWh [184], the proposed PCM-based technology can be considered an affordable solution for improving the efficiency of existing waste heat recovery systems.

4.6 Conclusion

The current chapter describes the outcomes of a numerical research on a novel PCM-based technology to be retrofitted in an existing waste heat recovery system, composed by an air preheater and an ORC system, installed downstream of a steel billet reheating furnace. The proposed PCM-based technology consists of a set of Heat Exchange and Storage Units (HESUs), in which the heat is absorbed from the flue gases and released to a heat transfer fluid; the thermal energy is stored and released at constant temperature thanks to the contained high temperature PCM. The aim of this work is that of assessing the impact of the PCM-based technology on the efficiency and capacitance factor of the ORC system subjected to variable input thermal power fluctuation of the waste heat source. Firstly, the measurements carried out in an existing energy recovery plant were used for the analysis of the performance of the ORC system and for the process characterisation. The former was assessed by means of the gross electric power output, thermal power input and efficiency, load factor and efficiency ratio whereas the latter by

calculating the heat losses associated with the stack and air dilution. Secondly the design of the PCM-based technology was carried out. The design of the PCM-based technology consists in the selection of the geometry and layout of the HESUs, which in turn define the thermal energy that can be stored in form of latent heat. The main control parameters for the PCM-based technology were then identified and implemented. The control strategy is twofold: serving as a thermal buffer to mitigate the thermal power fluctuations of the waste heat and conditioning the thermal power entering the ORC system identified (e.g. minimum thermal power entering the ORC system, maximum PCM temperature). The components of the current waste heat recovery system and the PCM-based technology were then modelled in the *Modelica* coding language. Finally, a comparison between the ORC system efficiency and capacity factor with and without the PCM-based technology was then performed together with an economic assessment of the introduction of the PCM-based technology is carried out. Results showed that the introduction of the PCM-based technology allows the capacity factor of the ORC system to be increased from 38% to 52% and the average thermal efficiency to be increased from 15.5% to 16.4%. The cost-benefit analysis showed that a selling price of the electric energy between 120 and 83 €/MWh can guarantee a payback period between 3 and 5 years.

Chapter 5

ENERGY RECOVERY FROM WASTE INCINERATION

5.1 Introduction

In the last decades, the design of Waste-to-Energy (WtE) plants was focused on lowering the discharge rate of pollutants, while maximizing the waste throughput and minimizing the maintenances costs. This goal has been achieved by using costly flue gas treatment units, which has led to the increase of the capital cost of whole WtE plant. Nowadays, to counterbalance this cost increase, the research is focused on improving the overall efficiency of the WtE plants. Steam boiler operating with higher steam parameters (temperature and pressure) is one of the main technical solutions that can be adopted to achieve this aim. Nevertheless, higher steam parameters increase the corrosion risk and the associated cost for plant downtime and repair.

Some WtE plants (Stuttgart-Germany and Naples-Italy) have achieved higher steam temperature (up to 500 °C) by using monolithic SiC concrete to protect the superheaters operating at temperature higher than 400 °C. The disadvantage of this solution is the lower availability due to higher inspection and maintenance requirements. An alternative solution has been tested in the WtE plant in Rosenheim (Germany), where rear-ventilated

tiles has been used to protect radiant superheaters located in the upper furnace area. In this case, the limits regard the maximum steam temperature achieved (i.e. 480 °C) and the increased plant complexity, which requires additional skills and competence for plant design, process control and operation. In addition to this, it has to be considered that closer to the hottest zone of the plant the radiant superheater is, more difficult the control of the superheated steam temperature. In fact, the inhomogeneous nature of Municipal Solid Waste (and hence the variation in the calorific value associated with it) causes disturbances during the combustion process which lead to significant fluctuations in the thermal power of the flue gas. As a consequence of this variability, the risk of failure of the superheater tubes due to excessive overheating is increased.

In this chapter, an innovative refractory brick technology based on phase change material (PCM) for corrosion protection of the radiant superheaters is proposed. PCM-based technologies exploit the phase change phenomenon of pure material or eutectic compounds, in which the latent heat of phase transition is absorbed or released at constant temperature. Exploiting this working principle, the PCM-based refractory brick is capable to store the fluctuating thermal power generated by the waste combustion and to release the stored thermal energy on demand as a steady heat flux. Thus, the proposed technology could enable the installation of radiant superheater in the hottest zone of the WtE plants, which then allows the steam to be heated up to 600°C.

The proposed technology considers aluminium and its eutectic alloys as PCMs since they offer good thermal properties (i.e. high thermal conductivity, high latent heat of fusion and high melting temperature) amongst high temperature PCMs. Several commercial ceramics are instead considered as containment material since they offer high resistance to high temperature corrosion.

The design challenge is given by the remarkable difference in the coefficient of thermal expansion between the selected PCMs and ceramics. Thus, a detailed thermomechanical analysis is assessed in the chapter in order to demonstrate the technological feasibility of the proposed technology. Finally, a computational fluid dynamic (CFD) simulation is carried out in order to compare the performance of the traditional refractory brick technology with that proposed in this chapter.

5.1.1 Problem statement

In current Waste-to-Energy plants, heat recovery of thermal power generated during combustion process is completely carried out by traditional steam generation boilers, which is usually composed by water-walls (i.e. radiant evaporators), evaporators, economizers and superheaters (see Figure 5.1).

Although being well established, this configuration of WtE plants is subjected to some technical limitations such as:

a. The limits on the maximum steam temperature, due to corrosion occurring at high metal surface temperature (i.e. superheater tube surface);
b. The fluctuation in steam production, due to non-homogeneous composition of waste.

These technical limitations affect the maximum electrical efficiency achievable and the proposed PCM-based technology intends to offer a novel solution to solve them.

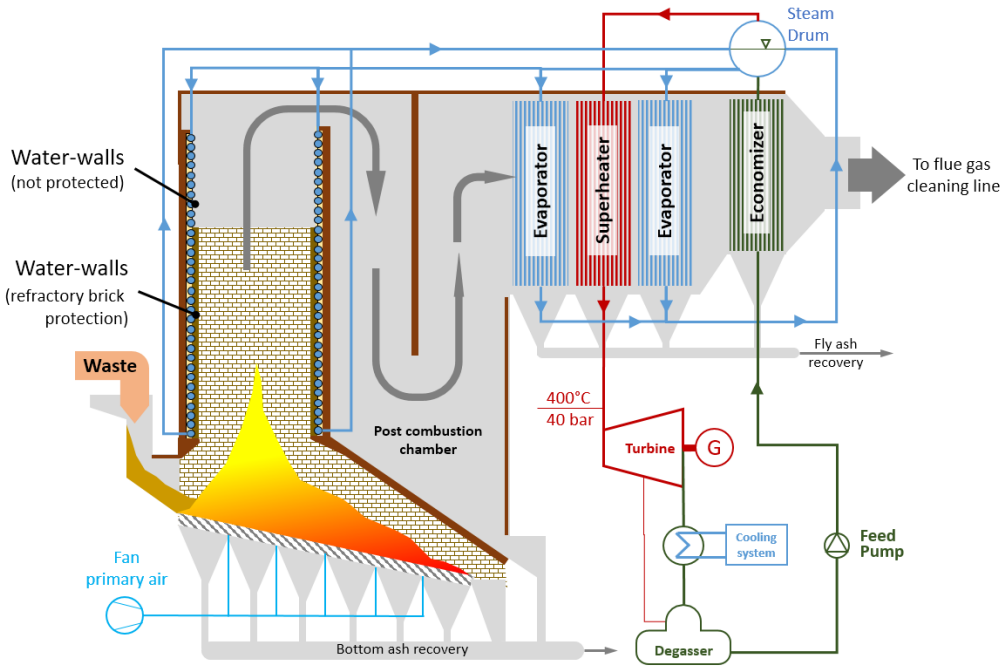

Figure 5.1 Typical configuration of heat recovery by steam generation in WtE plants

5.1.1.1 Corrosion at high metal surface temperature

High temperature of metal surface of the heat exchangers results in the melting of deposits and acceleration of the corrosion rate. Figure 5.2 shows typical charts of the corrosion

risk on boiler tubes as function of flue gas temperature [185] when using steel pipes (Figure 5.2a) and Inconel alloy pipes (Figure 5.2b). The green area represents the conditions in which the corrosion risk is very low and the WtE plant can operate without particular limitations. Most of the newer generation WtE plants (net electrical efficiencies around 23%) operate in the green area, with typical steam temperature values of 400°C at 40 bar [186].

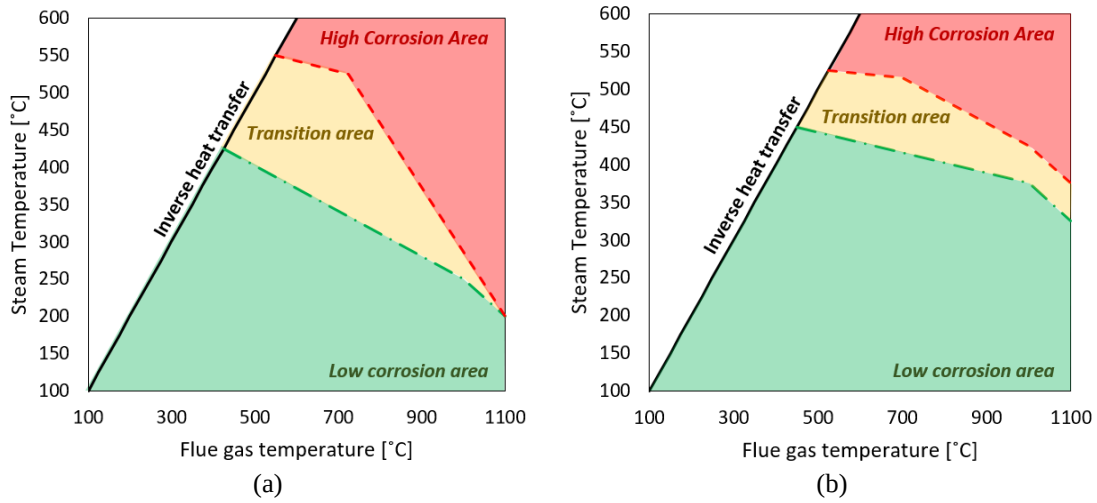

Figure 5.2 Corrosion diagram of a) steel and b) Inconel alloy [185]

When the operating conditions of heat exchangers move in the yellow area (transition area), the corrosion risk is no longer negligible and the lifetime of heat exchangers begins to reduce thus increasing the cost for preventive maintenance; in this area anti-corrosion coating is recommended. The red area represents the conditions in which heat exchangers are subjected to high corrosion rate. Uncoated heat exchangers have a short lifetime (5,000÷8,000 working hours for steam temperature of 500°C). Long lifetime of superheaters can be achieved by using monolithic SiC concrete, but under the precondition of ensuring regular inspections and direct repair of cracks before the tube itself shows corrosion attacks [187]. The monolithic SiC concrete is currently employed in those WtE plants which adopt high steam parameters to increase gross electric efficiency up to 30%, such as the WtE plants in Stuttgart (Germany) and in Naples (Italy). An alternative solution has been tested in the WtE plant in Rosenheim (Germany), where rear-ventilated tiles have been used to protect radiant superheaters located in the upper furnace area [188]. In this case, the limitations are on the maximum steam temperature

achieved (i.e. 480 °C) and the increased plant complexity, which requires additional skills and competence for plant design, process control and operation.

In addition to this, it has to be considered that the closer to the hottest zone of the plant the radiant superheater is, the more difficult the control of the superheated steam temperature will be. In fact, the inhomogeneous nature of Municipal Solid Waste (and hence the variation in the calorific value associated with it) causes disturbances during the combustion process which lead to significant fluctuations in the thermal power of the flue gas. As a consequence of this variability, the risk of failure of the superheater tubes due to excessive overheating is increased.

5.1.1.2 Process stability: fluctuating temperature and steam production

Good stability of the steam produced by the boiler (and hence of the combustion process) is required to maximise the annual waste throughput and the energy production. However, maintaining the process stability for combustion of household waste is a significant challenge. The inhomogeneous nature of Municipal Solid Waste (and hence the variation in the calorific value associated with it) causes disturbances during the combustion process which lead to significant fluctuations in the thermal power of the flue gas.

Because of this variability, the steam production in WtE boilers exhibits a fluctuating pattern; in Figure 5.3a is reported the fluctuation of the steam production (blue line) in a real WtE plant. In addition to this, likewise in any other large industrial system or process, the thermal inertia of a boiler gives rise to intrinsic over/undershoots of the steam curve. This delaying behaviour of the boiler is commonly tackled by means of conventional PID controllers whereas the waste-induced effects are usually stabilised by controlling the combustion process. However, these two techniques (PID controllers & combustion process control) only succeed in a partial mitigation of the fluctuation in steam production thus forcing the WtE plants' operators to limit the output from the steam turbine by reducing the waste throughput (hence reducing the energy output). On this issue, in WtE plants with no PID controllers, the fluctuation in steam production typically ranges between ±5% with respect to the baseline whereas, in plants using PID controllers, the fluctuation can be reduced to ±3%. Nevertheless, fluctuation in steam production cannot be completely avoided even if the best control systems are applied [189]. In addition to

this, it has to be pointed out that temperature fluctuations are always present in the combustion chamber (see Figure 5.3b) even when optimized control systems are used. In particular, from Figure 5.3b, it is possible to observe that two types of temperature fluctuations exist: the fast and slow fluctuations which occur within few minutes and few hours respectively.

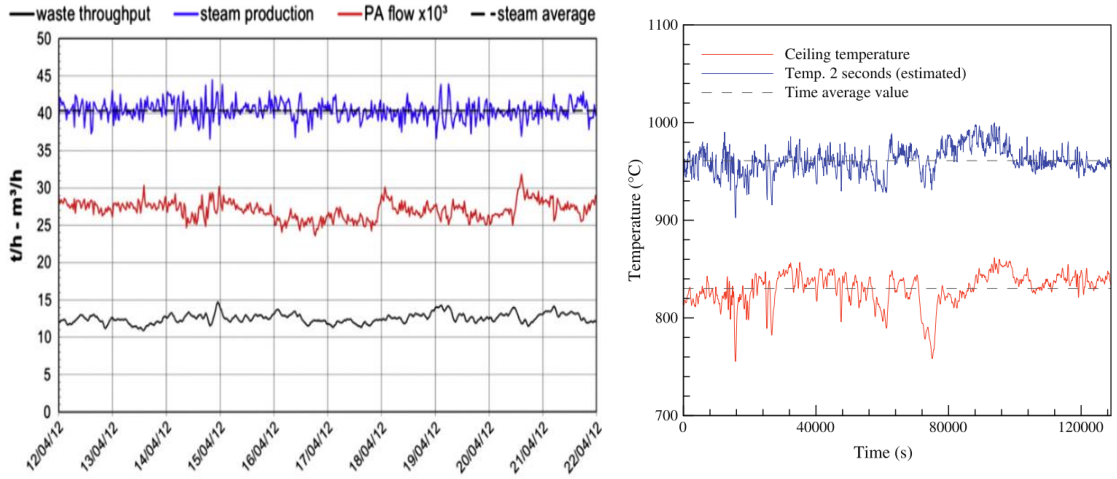

(a) (b)

Figure 5.3 a) Fluctuation in steam production in a WtE plant with PID control [189]**; b) Temperature fluctuation in the combustion chamber of a WtE plant** [190]

The slow temperature fluctuations can be controlled and mitigated by means of the combustion control system, whereas the fast temperature fluctuations cannot be avoided since the control system cannot react fast enough; in order to achieve a rapid response and an optimum control system for the combustion process, high costs are required for both the measurement instrumentation and the plant modifications needed for its installation [190].

For these reasons, fast temperature fluctuations are the most dangerous type of temperature fluctuations in WtE plants and they represent the main risk of tube failure for superheaters installed in the combustion chamber. The PCM-based brick is then aimed to solve this issue by absorbing the fast temperature fluctuation in the form of latent heat at constant temperature, so that the superheater tubes will not be subjected to the risk of failure due to uncontrolled temperature increase.

5.2 Proposed solution: PCM-based refractory brick

The proposed solution consists in replacing the typical refractory brick installed into the combustion chamber with a PCM-based refractory brick capable to store a variable heat flux coming from a high temperature heat source (i.e. incineration chamber) and to release it on demand as a steady heat flux. By introducing the PCM-based refractory brick, an extra degree of freedom in the heat recovery/management which did not exist before in combustion processes is introduced. In fact, the steady heat flux will be used to avoid steam production fluctuation and to increase temperature of superheated steam over current corrosion limits (450 °C) without using coated superheaters.

5.2.1 Working principle and component description

The proposed PCM-based refractory brick exploits the working principle of thermal energy storage based on latent heat. This type of heat storage system stores or releases latent heat when a phase change material, which can be a pure material (e.g. aluminium) or a eutectic compound (e.g. Al-12%Si), undergoes the phase transition from solid to liquid, or vice versa. The storage and release of heat occurs at the phase transition temperature of the PCM, which can be considered to be constant. This technique for heat storage allows designing thermal energy storage systems with a high energy density capable to store heat at high temperature (>300°C). The PCM-based technology presented in this section employs aluminium and its eutectic alloys because they offer the best thermal properties amongst high temperature PCMs [12]:

- High thermal conductivity (solid state > 200 W/mK – liquid state > 90 W/mK);
- High latent heat of fusion (280÷560 kJ/kg)
- High melting temperature (470÷660 °C)

Although aluminium and its alloys own the best thermal properties, their usage as PCM is limited by the high Coefficient of linear Thermal Expansion (CTE) and the high reactivity when in liquid phase. As reported in [96], the limit of the high reactivity (i.e. high corrosivity) of the molten aluminium (pure or alloyed) can be overcome by using high density ceramics (such as Al_2O_3, AlN and Si_3N_4) to contain the PCM. Furthermore, the use of ceramics to contain the PCM allows the PCM-based technology to operate at

very high temperature and in extremely corrosive environment, such as the combustion chamber of a WtE plant.

Since aluminium and its alloys have one of the highest CTE ($23 \cdot 10^{-6}$/K) amongst the various engineering materials, it is very likely that the material used for containment will have a lower CTE. The mismatch between the CTE of the PCM (i.e. aluminium or its alloys) and that of the container material leads to non-negligible thermal stresses, which can affect the structural integrity of the PCM container. Thus, the PCM should be encapsulated within the ceramic material by adopting cylindrical holes with round bottom edges, see Figure 5.4 (a) and (b). In addition to this, an empty space is left at the top of the brick in such a way that the PCM is free to expand along the vertical direction (both in solid and liquid state). In this way, the thermal stresses within the ceramic container can be controlled by setting the diameter of the holes and the interaxis between them.

In order to facilitate the installation of the PCM-based refractory brick, its shape and size should be similar to the ones of traditional bricks. Figure 5.4c shows an example of installation by using mortar of the PCM-based refractory brick. However, depending on the requirements of WtE plant operator, the PCM-based refractory brick can also be installed without mortar.

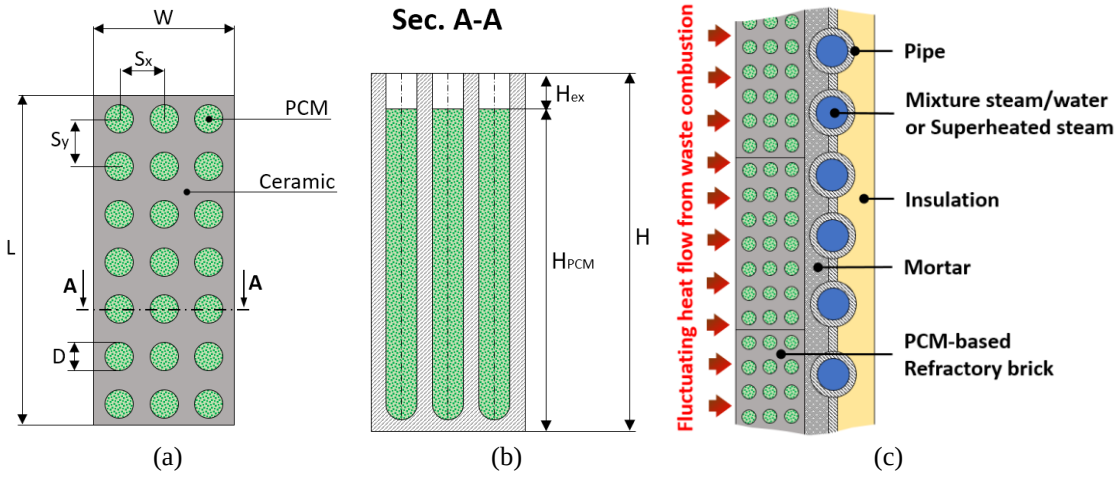

Figure 5.4 a) Top view and b) Section A-A of the PCM-based refractory brick; c) Water-wall or radiant superheater protected by PCM-based refractory brick

5.2.2 System layout

Figure 5.5 shows an example of the layout of a WtE plant where the PCM-based refractory brick is employed to avoid the fluctuation in steam production and to increase the temperature of the superheated steam. Comparing Figure 5.1 to Figure 5.5, it can be observed that the PCM-based refractory bricks simply replace the traditional refractory bricks in the protection of the water-walls, while an additional radiant superheater is installed in the lower bottom part of the furnace.

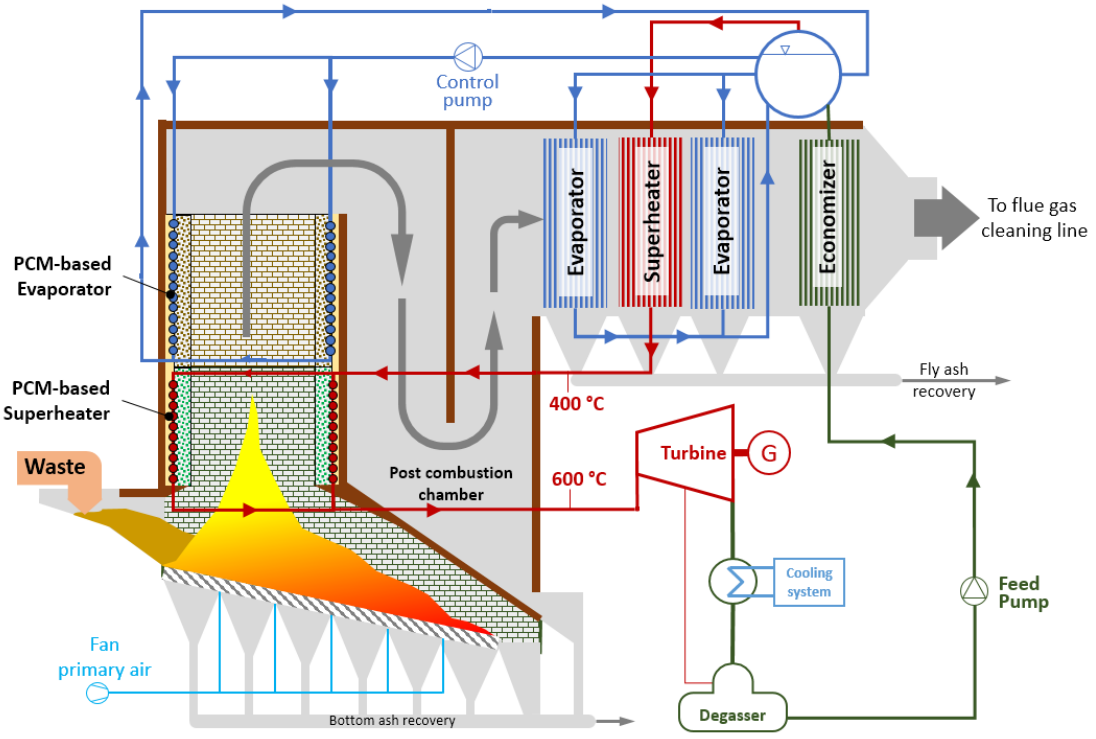

Figure 5.5 Integration between the PCM-based technology and heat recovery boiler based on steam generation in a WtE plant

Depending on the employed PCM, two different components can be identified: the PCM-based Evaporator and the PCM-based Superheater. The PCM-based refractory brick stores a part of the fluctuating thermal power generated by the waste combustion process. The stored thermal energy is then steadily transferred to the PCM-Superheater for steam temperature increase and to the PCM-evaporator for steam production control. Steam generation into the PCM-evaporator can easily be managed by varying the mass flow rate of the steam control pump which connects the steam drum to the PCM-evaporator; the generated steam is then used to completely avoid fluctuation in steam production.

For what concerns the PCM-based superheater, aluminium is the most suitable PCM to employ because of its high melting temperature (660°C). The use of aluminium as high temperature PCM allows heating the superheated steam up to 550-600°C, thus leading to a significant increase in efficiency of the WtE plant. In the PCM-based Evaporator instead, the eutectic alloy Al-12%Si (in mass %) is more suitable because of its higher latent heat of fusion (560 KJ/kg) and lower melting point (576 °C); it is worth noting that aluminium and Al-12%Si are both commercially available and do not require developing new/special alloy for this specific application.

Table 5.1 reports the comparison of the efficiencies which can be achieved in a WtE plant adopting the proposed PCM-based superheater and some of the existing techniques available in the market.

Table 5.1 Comparison between expected efficiency in a WtE plant using PCM-based superheater and some of the current techniques to improve WtE plant efficiency

		Baseline	High steam parameters	Steam reheating	PCM superheater
Max Steam Temperature	°C	400	500	420	600
Steam pressure	Bar	40	90	90	90
Flue Gas Temp. at Boiler Outlet	°C	190	190	190	190
Excess Air	%	60	60	60	60
Gross electrical efficiency	%	26.4	30.2	29.9	34.6

The comparison is based on the methodology described in [187] and it considers as baseline the typical WtE plant configuration (400 °C at 40 bar). From Table 5.1, it can be seen that WtE plants adopting the PCM-based superheater can potentially achieve a steam temperature up to 600 °C leading to a dramatic increase in gross electrical efficiency up to 34.6%.

5.3 Methodology and tools

In order to demonstrate the technological feasibility of the proposed technology, a detailed thermo-mechanical analysis has been carried out together with a CFD simulation aimed at comparing the performance of the traditional refractory brick technology with that proposed in this chapter. The thermo-mechanical analysis is carried out by means of a commercial software (ANSYS Mechanical APDL) employing the Finite Element Method (FEM), while for the CFD simulation ANSYS Fluent has been used.

5.3.1 Thermo-mechanical analysis

The typical duty cycle of the PCM-based refractory brick follows the usual operative phases of WtE plants: start-up phase, running phase and shut-down phase. According to [191] the start-up phase follows the steps listed below:

a. Temperature is raised using the auxiliary burner (gas temperature inside the combustion chamber: from ambient to 400 °C in 2 h).
b. The gas temperature is kept at 400 °C (2 h).
c. The gas temperature is further raised by the auxiliary burner from 400 to 600 °C in 2 h, from 600 to 900 °C in 2 h.
d. When the gas temperature at the baghouse inlet exceeds 160 °C, the gas flow begins.
e. When the gas temperature at the de-NOx catalytic reactor inlet exceeds 180 °C, the gas begins to flow through the reactor.
f. When the combustion gas exceeds 750 °C, the refuse feeding is started.
g. When the steam generation rate reaches target, the start-up phase is completed.

Operations (d) to (f) are carried out simultaneously with the raising of the temperature under step (c). The shutdown phase is simpler, since it follows the following steps:

a. The refuse hopper is closed. The gas temperature falls from 850 to 400 °C in 2 h.
b. When the gas temperature inside the combustion chamber falls below 450 °C, the forced draft fan is turned off.
c. When the gas temperature at the baghouse inlet falls below 125 °C, the baghouse is by-passed, the induced draft fan is turned off and the shutdown phase is completed.

During the start-up phase, the PCM-based refractory brick is heated from room temperature up to the melting point of the contained PCM. Once melting point is reached, the control system will maintain the PCM-refractory brick in that operating condition as long as the shutdown phase begins.

When the PCM is subjected to phase change, the coexistence of both liquid and solid states leads to a drastic reduction of the mechanical properties of the PCM (see Table 5.2). Therefore, the mechanical stresses in the PCM-based brick are very small, as they are only due to the metallostatic pressure. On the other hand, when the PCM is at solid

state and CTE of the containment material is lower than that of the PCM, the maximum stresses in the PCM-based refractory brick will be generated. Thus, the following thermo-mechanical analysis considers only the thermal conditions during which the PCM is at solid state, which is the condition encountered during the start-up and shut-down phases of the WtE plant.

Thermo-mechanical analyses available in literature usually study expansion of PCM in liquid phase [140–142]. To the author's knowledge, only [165] have analysed thermo-mechanical stresses generated by the expansion of PCM (aluminium) in solid phase. In particular, that study developed a simplified methodology to identify the most relevant design parameters for subsequent experimental validation.

Table 5.2 Thermo-physical properties of the aluminium [149]

Thermal conductivity (Solid State), λ_a (W/mK)	211
Melting temperature, T_m (°C)	660
Latent heat of fusion, H_{mass} (kJ/kg)	396
Volumetric latent heat of fusion, H_{vol} (MJ/m^3)	1089
Density, ρ_a (kg/m^3)	2750
Coefficient of thermal expansion, CTE (10^{-6}/K)	23
Poisson modulus, v	0.34

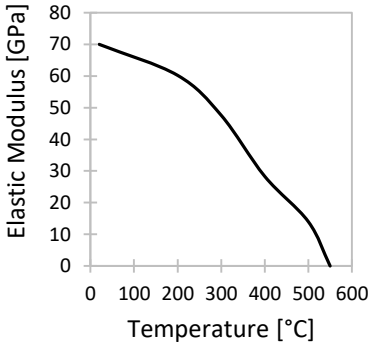

In this chapter, the FEM is used to analyse the thermo-mechanical behaviour of the PCM-based refractory brick. In particular, a simple bidimensional FEM model (see Figure 5.6a) has been preferred over a complex three dimensional FEM model because the use of complex model tends to hinder the understanding of the basic mechanisms that govern the thermo-mechanical response, as well as the identification of the relevant design parameters.

According to Appendix B, the plane stress hypothesis (i.e. axial stress $\sigma_z = 0$) is a reasonable assumption also for the bidimensional FEM model of the PCM-based refractory brick. The symmetry of the component allows the computational domain to be reduced to a small part, as shown in Figure 5.6b. The FEM model shown in Figure 5.6b, adopts 8-nodes isoparametric linear elements to discretise both the PCM and the ceramic parts; a mapped mesh is used for the whole domain. The thermal analysis is firstly carried

out to compute the temperature in each node; then the calculated nodal temperatures are used as thermal loads input in the mechanical analysis.

The start-up and shut-down phases previously described suggest that the thermal response of the PCM-based brick should be studied by a transient analysis with phase change. In addition to this, the flue gas side should be modelled with a radiation-convection model, while the steam side should be modelled with a convection model (see Figure 5.6c); the bulk temperature on both sides (i.e. flue gas and steam sides) should represent the start-up and shut-down phases.

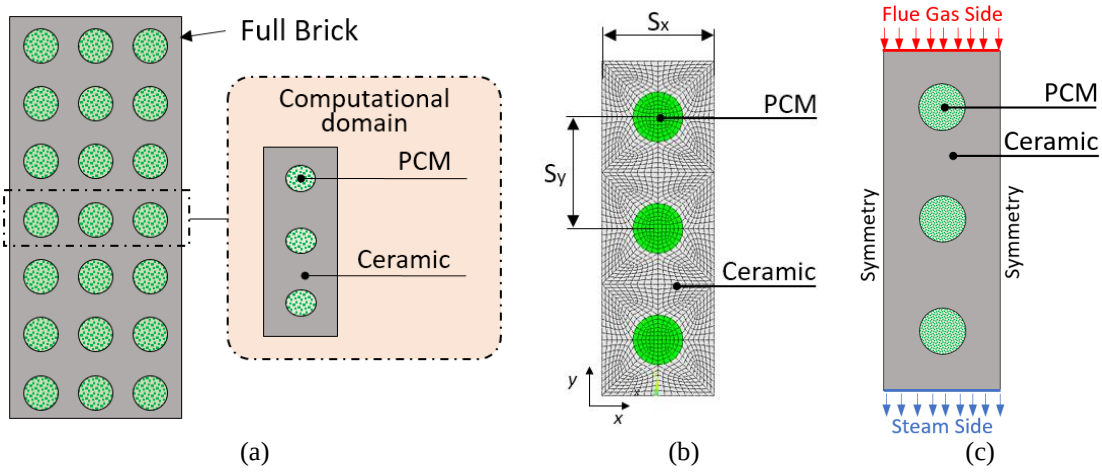

Figure 5.6 a) Computational domain, b) FEM model and c) Complex thermal model

The long duration of both start-up and shut-down phases and the high thermal conductivity of the PCMs suggest that it is reasonable to assume the whole system domain to have uniform temperature at any time instant (quasi-steady assumption). To justify this assumption, two different thermal models have been developed and compared:

a. *Complex model*: it considers radiation and convection heat transfer models on the flue gas side and a temperature ramp (representing the start-up of the steam loop) on the steam side. Bulk temperatures on both flue gas and steam sides are time dependent and they are derived from the temperature profiles reported in [191]; both start-up and shut-down phases are modelled.
b. *Simplified model*: it considers the whole domain to be at uniform temperature at any instant in time.

The ceramic with the lowest thermal conductivity (i.e. mullite) has been used as reference material for the model comparison, while the maximum principal stress has been used as comparison criteria.

A numerical uncertainty analysis has initially been performed to assess the approximation errors of the finite element solution. In particular, a sensitivity analysis on the mesh size has been carried out to identify at which element size the solution of the finite model becomes grid independent.

The results of the simulations have shown that the maximum difference in the maximum principal stress between the complex and the simplified models is less than 2%; this validates the assumption of uniform temperature; the analysis also showed that the complex model is roughly 6 times slower to converge than the simplified one.

The assumption of uniform temperature allows simulating the thermo-mechanic behaviour of the component by a sequence of steady state analyses. Thus, the applied thermal load is simply uniform temperature on the whole finite element model.

Six commercial high density ceramics (i.e. no porosity) have been considered as containment material for the PCM-based refractory brick: aluminium nitride (AlN), aluminium oxide at 96% purity level (Al_2O_3), mullite, sialon, silicon carbide (SiC) and silicon nitride (Si_3N_4). The thermo-mechanical properties reported in Table 5.3 have been obtained by comparing the data reported in the online database Matweb, which are provided by ceramic suppliers. Since the maximum considered temperature for the thermo-mechanical analysis is 660°C (i.e. PCM melting temperature), the ceramic properties can reasonably assumed to be constant.

Table 5.3 Thermo-mechanical properties of the considered ceramics

Ceramic	Young's modulus E (GPa)	Coeff. thermal expansion CTE (10^{-6}/K)	Thermal conductivity k (W/m·K)	Flexural strength MOR (MPa)
AlN	330	4.5	160	320
Al_2O_3 (96% purity)	300	8.2	25	345
Mullite	151	5.4	6	180
Sialon	288	3.0	17.5	760
SiC	410	4.0	120	550
Si_3N_4 (Sintered)	310	3.3	29	689

Since ceramics are brittle materials and their strength properties vary with the applied load (i.e. tensile strength is much lower than compressive strength), the equivalent stress along the first principal direction σ_{S1} has to be used to evaluate the material failure. More in particular, the maximum first principal stress $\sigma_{S1,max}$ must be lower than the modulus of rupture of the evaluated ceramic.

The main performance parameter of the PCM-based refractory brick is the energy density E_ρ, which represents the amount of energy that can be stored in the form of latent heat per unit of volume. Energy density is strictly related with the geometric parameters of the PCM-based refractory brick; in particular, referring to the bidimensional model, the ratio between the PCM area and the total area, which represents the PCM filling ratio, relates the energy density to the geometry of the PCM-based refractory brick.

5.3.2 Thermo-fluid dynamic analysis

A CFD analysis is carried out to compare the performance of a traditional refractory brick technology with that of the PCM-based refractory brick, when they are used to protect superheaters installed in the combustion chamber. In particular, the total heat flux entering the steam has been used as comparison criteria.

Two different bidimensional CFD models have been developed: the baseline model (see Figure 5.7a) and the PCM-brick model (see Figure 5.7b). In the baseline model, thermal properties of traditional alumina refractory brick have been used; in particular, a value of 3.5 W/mK has been used for the thermal conductivity. In the PCM-brick model, the considered PCM is the aluminium (see thermal properties in Table 5.2), while the adopted ceramic is the high density Al_2O_3 (96% purity), which properties are reported in Table 5.3. Both models share same material for steam pipe (i.e. carbon steel) and the mortar, which is a SiC-based mortar.

The same boundary conditions are applied in both models: radiation-convection heat transfer on the flue gas side (red line in Figure 5.7) and convection heat transfer on the steam side (green line in Figure 5.7). On the flue gas side, a sinusoidal temperature profile (average temperature 950 °C, amplitude 75 °C and period 600 s) is applied by means of a user-defined function (UDF); the emissivity of the flue gas and the refractory brick are

assumed to be 0.5 and 0.8, respectively. On the steam side, a constant temperature of 450 °C and a convection heat transfer coefficient of 250 W/m^{2}K have been applied.

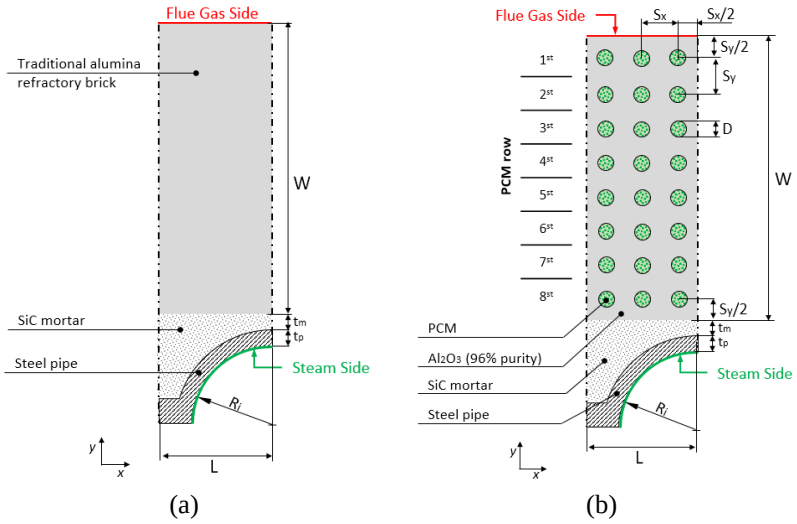

Figure 5.7 Geometry and materials of the CFD models of the a) baseline and b) PCM-based brick

The geometric parameters of both models are reported in Figure 5.7; it has to be pointed out that width W has been selected in such a way that the temperature fluctuation applied on the flue gas side is absorbed by the traditional refractory brick (i.e. negligible temperature fluctuations are present in the steel pipe).

Table 5.4 Geometric parameters of the CFD models

Width, W (mm)	72
Length, L (mm)	36
PCM hole diameter, D (mm)	4
PCM hole x interaxis, S_x (mm)	9
PCM hole y interaxis, S_y (mm)	9
Steam pipe inner radius, R_i (mm)	20
Steam pipe thickness, t_p (mm)	4
Mortar thickness, t_m (mm)	5

5.4 Results and discussion

In order to demonstrate the technological feasibility and the performance of the PCM-based technology, thermo-mechanical and thermo-fluid dynamic analyses have been carried out.

Figure 5.8a shows an example of the distribution of the first principal stress around the PCM (grey area); it can be observed the maximum stresses are concentrated at the

interface between the PCM and the ceramic. Figure 5.8b reports the typical distribution of the maximum first principal stress as a function of temperature for the considered ceramics; the reported stress distributions refer to the same geometric parameters (i.e. same hole diameter and interaxis). It can be observed that ceramics with low CTE and high young's modulus (i.e. AlN, SiC, Si_3N_4 and Sialon) generate the highest thermal stresses, while ceramics with low CTE and low Young's modulus (i.e. mullite) or with high CTE and high Young's modulus (i.e. Al_2O_3) generates the lowest thermal stresses.

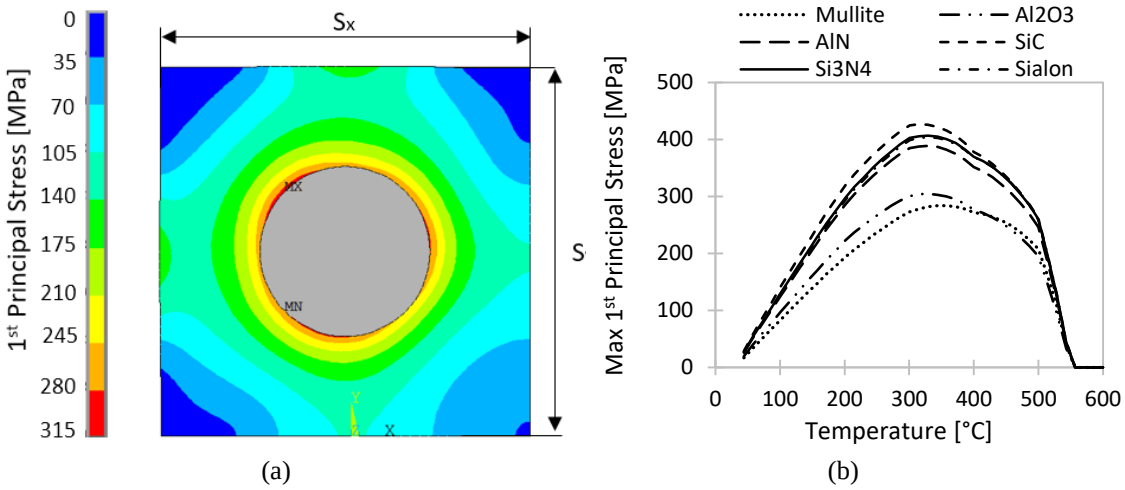

Figure 5.8 a) Distribution of σ_{S1} around the PCM and b) comparison of $\sigma_{S1,max}$ distribution as a function of temperature for the considered ceramics

As explained in the section 5.3.1, the main performance parameter of the PCM-based refractory brick is represented by the energy density E_ρ, calculated according to equation (5.1), is directly proportional to the PCM filling ratio χ and the latent heat of the PCM H.

$$E_\rho = \chi \cdot H \tag{5.1}$$

The PCM filling ratio χ is defined as:

$$\chi = \frac{A_{PCM}}{A_{tot}} \tag{5.2}$$

where A_{PCM} is the area occupied by the PCM and A_{tot} is the total area of the FEM domain.

Table 5.5 reports the PCM filling ratio of the PCM-based refractory brick when the considered ceramics are used; the reported PCM filling ratios and energy densities have

been calculated when the maximum first principal stress $\sigma_{S1,max}$ is equal to the 90% of the modulus of rupture.

Table 5.5 Performances of the PCM-based refractory brick for the considered ceramics

	PCM Filling Ratio, χ [-]	**Energy density,** E_ρ[MJ/m^3]
Mullite	1%	8.55
AlN	6%	69.82
Al_2O_3 (96% purity)	16%	168.95
SiC	21%	224.93
Si_3N_4 (Sintered)	33%	356.00
Sialon	39%	421.20

To control the maximum first principal stress, the diameter of the PCM holes has been maintained constant while the interaxis S_x and S_y, which are assumed to be equal, have been varied. It can be observed that mullite has the lowest performance; this is due to the combination of a low CTE and a low modulus of rupture. The best material results to be the sialon, followed by silicon nitride Si_3N_4 and silicon carbide SiC. Nevertheless, all these ceramics are usually quite expensive. Alumina-based ceramics are usually cheaper, so the alumina Al_2O_3 at 96% of purity probably represents the best trade-off between performance and cost.

Figure 5.9a shows the temperature of the PCM in different rows along the y axis, from the steam side (y=0) to the flue gas side (y=72 mm); the melting point temperature of aluminium is also illustrated with the dashed line. As it can be seen, all the rows of PCM pipes successfully experience phase change during the temperature fluctuation. The closer the PCM row to the steam pipe is, the less fluctuation of temperature they experience. Figure 5.9b reports the temperature distributions across the refractory bricks along the y direction from the steam pipe to the radiation wall. Contrary to the baseline case, which experiences over 500 °C of high temperature difference across the refractory material, the PCM case reveals much less temperature difference of less than 200 °C. The result indicates that the proposed PCM-based technology helps to reduce more than half of the thermal gradient, thus mitigating the thermal stress exposed to the highly brittle refractory materials.

The time-averaged value of the total surface flux for PCM case is 22139 W/m2, which is almost twice the value of the baseline case. This significant increasing of surface total heat flux demonstrates better heat transfer performance by using the PCM-based refractory brick.

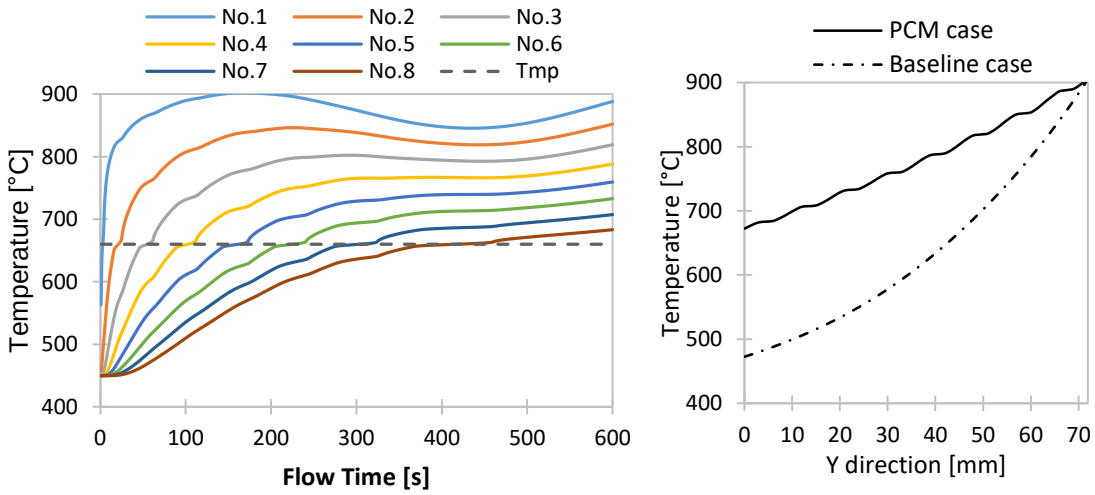

(a) (b)

Figure 5.9 a) Temperature of the PCM in different rows and b) comparison of the temperature gradient of the traditional technology and the PCM-based refractory brick

The CFD and FEM simulation demonstrate high feasibility of this technology in terms of buffering heat flow, reducing thermal gradient within ceramics, and delivering much higher heat flux to the steam flow.

5.5 Conclusions

In this chapter, an innovative refractory brick technology based on phase change materials for corrosion protection of the radiant superheaters has been proposed. The proposed technology could enable the installation of radiant superheater in the hottest zone of the WtE plants, which then allows the steam to be heated up to 600°C and the efficiency to be increased up to 34%. Aluminium has been considered as high temperature PCM, while several commercial ceramics (e.g. Al_2O_3, AlN and Si_3N_4) have been evaluated as containment material due to their high resistance to corrosion. A detailed thermomechanical analysis has demonstrated the technological feasibility of the proposed technology and it has identified Al_2O_3 has the most suitable ceramic for containing aluminium.

A computational fluid dynamic (CFD) simulation have been carried out to compare the performance of the traditional refractory brick technology with that proposed in this chapter. The results showed that the PCM-based refractory brick can almost double the heat flux to the steam flow, while reducing thermal power fluctuations entering the steam.

The results of the present chapter contribute to the establishment of high temperature phase change material thermal energy storage to improve energy efficiency of waste-to-energy plants.

REFERENCES

[1] IEA. Energy efficiency market report 2016. 2016.

[2] Wachsmuth J, Duscha V, Reuter M, Reinaldo B, Souza C, Canili RF. How energy efficiency cuts costs for a 2-degree future. Karlsruhe (DE): n.d.

[3] US Department of Energy. Waste Heat Recovery: Technology and Opportunities in U.S. Industry. 2010.

[4] Lu H, Price L, Zhang Q. Capturing the invisible resource: Analysis of waste heat potential in Chinese industry. Applied Energy 2016. doi:10.1016/j.apenergy.2015.10.060.

[5] Kim TS. Comparative analysis on the part load performance of combined cycle plants considering design performance and power control strategy. Energy 2004;29:71–85. doi:10.1016/S0360-5442(03)00157-9.

[6] Poullikkas A. Parametric study for the penetration of combined cycle technologies into Cyprus power system. Applied Thermal Engineering 2004;24:1697–707. doi:10.1016/j.applthermaleng.2003.10.033.

[7] Rovira A, Sánchez C, Muñoz M, Valdés M, Durán MD. Thermoeconomic optimisation of heat recovery steam generators of combined cycle gas turbine power plants considering off-design operation. Energy Conversion and Management 2011;52:1840–9. doi:10.1016/j.enconman.2010.11.016.

[8] Wang J, Dai Y, Gao L. Exergy analyses and parametric optimizations for different cogeneration power plants in cement industry. Applied Energy 2009;86:941–8. doi:10.1016/j.apenergy.2008.09.001.

[9] Pulat E, Etemoglu AB, Can M. Waste-heat recovery potential in Turkish textile industry: Case study for city of Bursa. Renewable and Sustainable Energy Reviews

2009;13:663–72. doi:10.1016/j.rser.2007.10.002.

[10] Agyenim F, Hewitt N, Eames P, Smyth M. A review of materials, heat transfer and phase change problem formulation for latent heat thermal energy storage systems (LHTESS). Renewable and Sustainable Energy Reviews 2010;14:615–28. doi:10.1016/j.rser.2009.10.015.

[11] Farid MM, Khudhair AM, Ali Razack SK, Al-Hallaj S. A review on phase change energy storage: materials and applications. Energy Conversion and Management 2004;45:1597–615. doi:10.1016/j.enconman.2003.09.015.

[12] Kenisarin MM. High-temperature phase change materials for thermal energy storage. Renewable & Sustainable Energy Reviews 2010;14:955–70. doi:10.1016/j.rser.2009.11.011.

[13] Wang Z, Wang H, Li X, Wang D, Zhang Q, Chen G, et al. Aluminum and silicon based phase change materials for high capacity thermal energy storage. Applied Thermal Engineering 2015;89:204–8. doi:10.1016/j.applthermaleng.2015.05.037.

[14] Zhang P, Xiao X, Ma ZW. A review of the composite phase change materials: Fabrication, characterization, mathematical modeling and application to performance enhancement. Applied Energy 2016;165:472–510. doi:10.1016/j.apenergy.2015.12.043.

[15] Nomura T, Okinaka N, Akiyama T. Technology of latent heat storage for high temperature application: a review. ISIJ International 2010;50:1229–39.

[16] Laplace-Conseil. Impacts of energy market developments on the steel industry. 74th Session of the OECD Steel Committee, 2013.

[17] Crude steel production 2015-2016. Word Steel Association 2016. http://www.worldsteel.org/statistics/crude-steel-production0.html (accessed August 8, 2016).

[18] Pardo N, Moya JA. Prospective scenarios on energy efficiency and CO2 emissions in the European Iron & Steel industry. Energy 2013;54:113–28. doi:10.1016/j.energy.2013.03.015.

[19] Arens M, Worrell E. Diffusion of energy efficient technologies in the German steel

industry and their impact on energy consumption. Energy 2014;73:968–77. doi:10.1016/j.energy.2014.06.112.

[20] Zhang S, Worrell E, Crijns-Graus W, Wagner F, Cofala J. Co-benefits of energy efficiency improvement and air pollution abatement in the Chinese iron and steel industry. Energy 2014;78:333–45. doi:10.1016/j.energy.2014.10.018.

[21] Johansson MT, Söderström M. Options for the Swedish steel industry – Energy efficiency measures and fuel conversion. Energy 2011;36:191–8. doi:10.1016/j.energy.2010.10.053.

[22] Rizwan Janjua. Energy use in steel industry. 2014.

[23] Kirschen M, Risonarta V, Pfeifer H. Energy efficiency and the influence of gas burners to the energy related carbon dioxide emissions of electric arc furnaces in steel industry. Energy 2009;34:1065–72. doi:10.1016/j.energy.2009.04.015.

[24] Lu B, Chen D, Chen G, Yu W. An energy apportionment model for a reheating furnace in a hot rolling mill – A case study. Applied Thermal Engineering 2017;112:174–83. doi:10.1016/j.applthermaleng.2016.10.080.

[25] Si M, Thompson S, Calder K. Energy efficiency assessment by process heating assessment and survey tool (PHAST) and feasibility analysis of waste heat recovery in the reheat furnace at a steel company. Renewable and Sustainable Energy Reviews 2011;15:2904–8. doi:10.1016/j.rser.2011.02.035.

[26] Themelis NJ. Waste-to-Energy: Renewable Energy Instead of Greenhouse Gas Emissions. Waste-to-Energy Research and Technology Council, 2007.

[27] Zalba B, Marín JM, Cabeza LF, Mehling H. Review on thermal energy storage with phase change: materials, heat transfer analysis and applications. Applied Thermal Engineering 2003;23:251–83. doi:10.1016/S1359-4311(02)00192-8.

[28] Hasnain SM. Review on sustainable thermal energy storage technologies, Part I: heat storage materials and techniques. Energy Conversion and Management 1998;39:1127–38. doi:10.1016/S0196-8904(98)00025-9.

[29] Nomura T, Akiyama T. High-temperature latent heat storage technology to utilize exergy of solar heat and industrial exhaust heat. International Journal of Energy

Research 2016;31:135–47. doi:10.1002/er.3611.

[30] Nomura T, Tsubota M, Oya T, Okinaka N, Akiyama T. Heat storage in direct-contact heat exchanger with phase change material. Applied Thermal Engineering 2013;50:26–34. doi:10.1016/j.applthermaleng.2012.04.062.

[31] Nkwetta D, Haghighat F. Thermal energy storage with phase change material—A state-of-the art review. Sustainable Cities and Society 2014;10:87–100. doi:10.1016/j.scs.2013.05.007.

[32] Sun Y, Wang S, Xiao F, Gao D. Peak load shifting control using different cold thermal energy storage facilities in commercial buildings: A review. Energy Conversion and Management 2013;71:101–14. doi:10.1016/j.enconman.2013.03.026.

[33] Jaworski M. Thermal performance of heat spreader for electronics cooling with incorporated phase change material. Applied Thermal Engineering 2012;35:212–9. doi:10.1016/j.applthermaleng.2011.10.036.

[34] Quader MA, Ahmed S, Ghazilla RAR, Ahmed S, Dahari M. A comprehensive review on energy efficient CO2 breakthrough technologies for sustainable green iron and steel manufacturing. Renewable and Sustainable Energy Reviews 2015;50:594–614. doi:10.1016/j.rser.2015.05.026.

[35] Yogev R, Kribus A. Operation strategies and performance of solar thermal power plants operating from PCM storage. Solar Energy 2013;95:170–80. doi:10.1016/j.solener.2013.06.012.

[36] Mahfuz MH, Kamyar A, Afshar O, Sarraf M, Anisur MR, Kibria MA, et al. Exergetic analysis of a solar thermal power system with PCM storage. Energy Conversion and Management 2014;78:486–92. doi:10.1016/j.enconman.2013.11.016.

[37] Broberg Viklund S, Johansson MT. Technologies for utilization of industrial excess heat: Potentials for energy recovery and CO2 emission reduction. Energy Conversion and Management 2014;77:369–79. doi:10.1016/j.enconman.2013.09.052.

[38] Johansson MT, Söderström M. Electricity generation from low-temperature

industrial excess heat—an opportunity for the steel industry n.d. doi:10.1007/s12053-013-9218-6.

[39] Zhang L, Akiyama T. How to recuperate industrial waste heat beyond time and space. International Journal of Exergy 2009;6:214. doi:10.1504/IJEX.2009.023999.

[40] Gil A, Medrano M, Martorell I, Lázaro A, Dolado P, Zalba B, et al. State of the art on high temperature thermal energy storage for power generation. Part 1—Concepts, materials and modellization. Renewable and Sustainable Energy Reviews 2010;14:31–55. doi:10.1016/j.rser.2009.07.035.

[41] Cárdenas B, León N. High temperature latent heat thermal energy storage: Phase change materials, design considerations and performance enhancement techniques. Renewable and Sustainable Energy Reviews 2013;27:724–37. doi:10.1016/j.rser.2013.07.028.

[42] Guillot S, Faik A, Rakhmatullin A, Lambert J, Veron E, Echegut P, et al. Corrosion effects between molten salts and thermal storage material for concentrated solar power plants. Applied Energy 2012;94:174–81. doi:10.1016/j.apenergy.2011.12.057.

[43] Sharma A, Tyagi VV, Chen CR, Buddhi D. Review on thermal energy storage with phase change materials and applications. Renewable and Sustainable Energy Reviews 2009;13:318–45. doi:10.1016/j.rser.2007.10.005.

[44] Lamberg P. Approximate analytical model for two-phase solidification problem in a finned phase-change material storage. Applied Energy 2004;77:131–52. doi:10.1016/S0306-2619(03)00106-5.

[45] Nomura T, Akiyama T. Latent heat storage technology using PCM and its applications. Highly-Efficient Utilization of Thermal Energy and Energy Conservation Technology 2015:125–36.

[46] Tamme R, Bauer T, Buschle J, Laing D, Müller-Steinhagen H, Steinmann W-D. Latent heat storage above 120°C for applications in the industrial process heat sector and solar power generation. International Journal of Energy Research 2008;32:264–71. doi:10.1002/er.1346.

[47] Yamagishi Y, Takeuchi H, Pyatenko AT, Kayukawa N. Characteristics of microencapsulated PCM slurry as a heat-transfer fluid. AIChE Journal 1999;45:696–707. doi:10.1002/aic.690450405.

[48] Pitié F, Zhao CY, Baeyens J, Degrève J, Zhang HL. Circulating fluidized bed heat recovery/storage and its potential to use coated phase-change-material (PCM) particles. Applied Energy 2013;109:505–13. doi:10.1016/j.apenergy.2012.12.048.

[49] Izquierdo-Barrientos MA, Sobrino C, Almendros-Ibáñez JA. Thermal energy storage in a fluidized bed of PCM. Chemical Engineering Journal 2013;230:573–83. doi:10.1016/j.cej.2013.06.112.

[50] Nomura T, Tsubota M, Oya T, Okinaka N, Akiyama T. Heat release performance of direct-contact heat exchanger with erythritol as phase change material. Applied Thermal Engineering 2013;61:28–35. doi:10.1016/j.applthermaleng.2013.07.024.

[51] Nomura T, Tsubota M, Sagara A, Okinaka N, Akiyama T. Performance analysis of heat storage of direct-contact heat exchanger with phase-change material. Applied Thermal Engineering 2013;58:108–13. doi:10.1016/j.applthermaleng.2013.03.041.

[52] Kaizawa A, Kamano H, Kawai A, Jozuka T, Senda T, Maruoka N, et al. Thermal and flow behaviors in heat transportation container using phase change material. Energy Conversion and Management 2008;49:698–706. doi:10.1016/j.enconman.2007.07.022.

[53] Nomura T, Tsubota M, Okinaka N, Akiyama T. Improvement on Heat Release Performance of Direct-contact Heat Exchanger Using Phase Change Material for Recovery of Low Temperature Exhaust Heat. ISIJ International 2015;55:441–7. doi:10.2355/isijinternational.55.441.

[54] Guo S, Li H, Zhao J, Li X, Yan J. Numerical simulation study on optimizing charging process of the direct contact mobilized thermal energy storage. Applied Energy 2013;112:1416–23. doi:10.1016/j.apenergy.2013.01.020.

[55] Prieto C, Cooper P, Fernández AI, Cabeza LF. Review of technology: Thermochemical energy storage for concentrated solar power plants. Renewable and Sustainable Energy Reviews 2016;60:909–29. doi:10.1016/j.rser.2015.12.364.

[56] Dincer I. On thermal energy storage systems and applications in buildings. Energy and Buildings 2002;34:377–88. doi:10.1016/S0378-7788(01)00126-8.

[57] Schröder J, Gawron K. Latent heat storage. International Journal of Energy Research 1981;5:103–9. doi:10.1002/er.4440050202.

[58] Abhat A. Low temperature latent heat thermal energy storage: Heat storage materials. Solar Energy 1983;30:313–32. doi:10.1016/0038-092X(83)90186-X.

[59] Tyagi VV, Buddhi D. PCM thermal storage in buildings: A state of art. Renewable and Sustainable Energy Reviews 2007;11:1146–66. doi:10.1016/j.rser.2005.10.002.

[60] Regin AF, Solanki SC, Saini JS. Heat transfer characteristics of thermal energy storage system using PCM capsules: A review. Renewable and Sustainable Energy Reviews 2008;12:2438–58. doi:10.1016/j.rser.2007.06.009.

[61] Sharma A, Chen CR, Murty VVS, Shukla A. Solar cooker with latent heat storage systems: A review. Renewable and Sustainable Energy Reviews 2009;13:1599–605. doi:10.1016/j.rser.2008.09.020.

[62] Liu M, Saman W, Bruno F. Review on storage materials and thermal performance enhancement techniques for high temperature phase change thermal storage systems. Renewable and Sustainable Energy Reviews 2012;16:2118–32. doi:10.1016/j.rser.2012.01.020.

[63] Bradshaw RW, Cordaro JG, Siegel NP. Molten Nitrate Salt Development for Thermal Energy Storage in Parabolic Trough Solar Power Systems. ASME 2009 3rd International Conference on Energy Sustainability, Volume 2, ASME; 2009, p. 615–24. doi:10.1115/ES2009-90140.

[64] Sabharwall P, Patterson M, Utgikar V, Gunnerson F. NGNP Process Heat Utilization: Liquid Metal Phase Change Heat Exchanger. Fourth International Topical Meeting on High Temperature Reactor Technology, Volume 1, ASME; 2008, p. 725–32. doi:10.1115/HTR2008-58197.

[65] Adinberg R, Zvegilsky D, Epstein M. Heat transfer efficient thermal energy storage for steam generation. Energy Conversion and Management 2010;51:9–15. doi:10.1016/j.enconman.2009.08.006.

[66] Hoshi A, Mills DR, Bittar A, Saitoh TS. Screening of high melting point phase change materials (PCM) in solar thermal concentrating technology based on CLFR. Solar Energy 2005;79:332–9. doi:10.1016/j.solener.2004.04.023.

[67] Birchenall CE, Riechman AF. Heat storage in eutectic alloys. Metallurgical Transactions A 1980;11:1415–20. doi:10.1007/BF02653497.

[68] C. Ernest Birchenall SIG, Diana Farkas MBL, Nikhil Nagaswami BP. Heat Storage in Alloy Transformation 1981. http://ntrs.nasa.gov/archive/nasa/casi.ntrs.nasa.gov/19810019065.pdf (accessed December 19, 2014).

[69] Wang X, Liu J, Zhang Y, Di H, Jiang Y. Experimental research on a kind of novel high temperature phase change storage heater. Energy Conversion and Management 2006;47:2211–22. doi:10.1016/j.enconman.2005.12.004.

[70] Sun JQ, Zhang RY, Liu ZP, Lu GH. Thermal reliability test of Al-34%Mg-6%Zn alloy as latent heat storage material and corrosion of metal with respect to thermal cycling. Energy Conversion and Management 2007;48:619–24. doi:10.1016/j.enconman.2006.05.017.

[71] Kenisarin MM, Mahkamov K. Solar energy storage using phase change materials. Renewable and Sustainable Energy Reviews 2007;11:1913–65. doi:10.1016/j.rser.2006.05.005.

[72] Kotzé JP, von Backström TW, Erens PJ. High Temperature Thermal Energy Storage Utilizing Metallic Phase Change Materials and Metallic Heat Transfer Fluids. Journal of Solar Energy Engineering 2013;135:35001. doi:10.1115/1.4023485.

[73] Khare S, Dell'Amico M, Knight C, McGarry S. Selection of materials for high temperature latent heat energy storage. Solar Energy Materials and Solar Cells 2012;107:20–7. doi:10.1016/j.solmat.2012.07.020.

[74] Horbaniuc B, Dumitrascu G, Popescu A. Mathematical models for the study of solidification within a longitudinally finned heat pipe latent heat thermal storage system. Energy Conversion and Management 1999;40:1765–74. doi:10.1016/S0196-8904(99)00069-2.

[75] Agyenim F, Eames P, Smyth M. A comparison of heat transfer enhancement in a medium temperature thermal energy storage heat exchanger using fins. Solar Energy 2009;83:1509–20. doi:10.1016/j.solener.2009.04.007.

[76] Papanicolaou E, Belessiotis V. Transient natural convection in a cylindrical enclosure at high Rayleigh numbers. International Journal of Heat and Mass Transfer 2002;45:1425–44. doi:10.1016/S0017-9310(01)00258-7.

[77] Silva PD, Gonçalves L., Pires L. Transient behaviour of a latent-heat thermal-energy store: numerical and experimental studies. Applied Energy 2002;73:83–98. doi:10.1016/S0306-2619(02)00060-0.

[78] Zivkovic B, Fujii I. An analysis of isothermal phase change of phase change material within rectangular and cylindrical containers. Solar Energy 2001;70:51–61. doi:10.1016/S0038-092X(00)00112-2.

[79] Ghoneim AA. Comparison of theoretical models of phase-change and sensible heat storage for air and water-based solar heating systems. Solar Energy 1989;42:209–20. doi:10.1016/0038-092X(89)90013-3.

[80] Lacroix M. Numerical simulation of a shell-and-tube latent heat thermal energy storage unit. Solar Energy 1993;50:357–67. doi:10.1016/0038-092X(93)90029-N.

[81] Bansal NK, Buddhi D. An analytical study of a latent heat storage system in a cylinder. Energy Conversion and Management 1992;33:235–42. doi:10.1016/0196-8904(92)90113-B.

[82] Esen M, Durmuş A, Durmuş A. Geometric design of solar-aided latent heat store depending on various parameters and phase change materials. Solar Energy 1998;62:19–28. doi:10.1016/S0038-092X(97)00104-7.

[83] Agyenim F, Eames P, Smyth M. Heat transfer enhancement in medium temperature thermal energy storage system using a multitube heat transfer array. Renewable Energy 2010;35:198–207. doi:10.1016/j.renene.2009.03.010.

[84] Zanganeh G, Khanna R, Walser C, Pedretti A, Haselbacher A, Steinfeld A. Experimental and numerical investigation of combined sensible–latent heat for thermal energy storage at 575°C and above. Solar Energy 2015;114:77–90. doi:10.1016/j.solener.2015.01.022.

[85] Khudhair AM, Farid MM. A review on energy conservation in building applications with thermal storage by latent heat using phase change materials. Energy Conversion and Management 2004;45:263–75. doi:10.1016/S0196-8904(03)00131-6.

[86] Hawlader MNA, Uddin MS, Khin MM. Microencapsulated PCM thermal-energy storage system. Applied Energy 2003;74:195–202. doi:10.1016/S0306-2619(02)00146-0.

[87] Nomura T, Zhu C, Sheng N, Saito G, Akiyama T. Microencapsulation of Metal-based Phase Change Material for High-temperature Thermal Energy Storage. Scientific Reports 2015;5:9117. doi:10.1038/srep09117.

[88] Cabeza LF, Castellón C, Nogués M, Medrano M, Leppers R, Zubillaga O. Use of microencapsulated PCM in concrete walls for energy savings. Energy and Buildings 2007;39:113–9. doi:10.1016/j.enbuild.2006.03.030.

[89] Sarı A, Alkan C, Karaipekli A, Uzun O. Microencapsulated n-octacosane as phase change material for thermal energy storage. Solar Energy 2009;83:1757–63. doi:10.1016/j.solener.2009.05.008.

[90] Mehling H, Cabeza LF. Heat and cold storage with PCM. Berlin, Heidelberg: Springer Berlin Heidelberg; 2008. doi:10.1007/978-3-540-68557-9.

[91] Ryu HW, Woo SW, Shin BC, Kim SD. Prevention of supercooling and stabilization of inorganic salt hydrates as latent heat storage materials. Solar Energy Materials and Solar Cells 1992;27:161–72. doi:10.1016/0927-0248(92)90117-8.

[92] Fang Y, Kuang S, Gao X, Zhang Z. Preparation and characterization of novel nanoencapsulated phase change materials. Energy Conversion and Management 2008;49:3704–7. doi:10.1016/j.enconman.2008.06.027.

[93] Fang G, Li H, Yang F, Liu X, Wu S. Preparation and characterization of nano-encapsulated n-tetradecane as phase change material for thermal energy storage. Chemical Engineering Journal 2009;153:217–21. doi:10.1016/j.cej.2009.06.019.

[94] Khodadadi JM, Hosseinizadeh SF. Nanoparticle-enhanced phase change materials (NEPCM) with great potential for improved thermal energy storage. International

Communications in Heat and Mass Transfer 2007;34:534–43. doi:10.1016/j.icheatmasstransfer.2007.02.005.

[95] Jacob R, Bruno F. Review on shell materials used in the encapsulation of phase change materials for high temperature thermal energy storage. Renewable and Sustainable Energy Reviews 2015;48:79–87. doi:10.1016/j.rser.2015.03.038.

[96] Fukahori R, Nomura T, Zhu C, Sheng N, Okinaka N, Akiyama T. Thermal analysis of Al–Si alloys as high-temperature phase-change material and their corrosion properties with ceramic materials. Applied Energy 2016;163:1–8. doi:10.1016/j.apenergy.2015.10.164.

[97] Fukahori R, Nomura T, Zhu C, Sheng N, Okinaka N, Akiyama T. Macro-encapsulation of metallic phase change material using cylindrical-type ceramic containers for high-temperature thermal energy storage. Applied Energy 2016;170:324–8. doi:10.1016/j.apenergy.2016.02.106.

[98] Sugo H, Kisi E, Cuskelly D. Miscibility gap alloys with inverse microstructures and high thermal conductivity for high energy density thermal storage applications. Applied Thermal Engineering 2013;51:1345–50. doi:10.1016/j.applthermaleng.2012.11.029.

[99] Zhang G, Li J, Chen Y, Xiang H, Ma B, Xu Z, et al. Encapsulation of copper-based phase change materials for high temperature thermal energy storage. Solar Energy Materials and Solar Cells 2014;128:131–7. doi:10.1016/j.solmat.2014.05.012.

[100] Wang D, Shi Z. Aluminizing and oxidation treatment of 1Cr18Ni9 stainless steel. Applied Surface Science 2004;227:255–60. doi:10.1016/j.apsusc.2003.11.076.

[101] Remus R, Roudier S, Aguado Monsonet MA, Sancho LD. Best Available Techniques (BAT) Reference Document for Iron and Steel Production. European Commission Joint Research Centre; 2013. doi:10.2791/97469.

[102] Born C, Granderath R. Benchmark for heat recovery from the offgas duct of electric arc furnaces. MPT International 2013;1:32–5.

[103] JP Steel P. Waste Heat Recovery for EAF. Japanese Smart Energy Products & Technologies. 2014th ed., Japanese Business Alliance for Smart Energy Worldwide; 2014.

[104] Steinparzer T, Haider M, Fleischanderl a, Hampel a, Enickl G, Zauner F. Heat exchangers and thermal energy storage concepts for the off-gas heat of steelmaking devices. Journal of Physics: Conference Series 2012;395:12158. doi:10.1088/1742-6596/395/1/012158.

[105] Fruehan R, Fortini O, Paxton H. Theoretical minimum energies to produce steel for selected conditions. US Department of Energy Office of Industrial Technologies 2000.

[106] Santangelo N, Tomadin L, Bertolissio A. Toward zero-energy fumes treatment plant. Proceedings of European Steel Technology and Application Days, Dusseldorf (Germany): 2015.

[107] Çamdali Ü, Tunç M. Exergy analysis and efficiency in an industrial AC electric ARC furnace. Applied Thermal Engineering 2003;23:2255–67. doi:10.1016/S1359-4311(03)00192-3.

[108] Hasanbeigi A, Price LK, McKane AT. The State–of-the-Art Clean Technologies (SOACT) for Steelmaking Handbook (2nd Edition). 2010.

[109] The benefits of Consteel Evolution. Tenova News 2011:5–7.

[110] Schmidt R, Goodwill J. Electric arc furnace scrap preheating. 1997.

[111] Available and Emerging Technologies for Reducing Greenhouse Gas Emissions from the Iron and Steel Industry 2012.

[112] Memoli F, Bianchi Ferri M. New track record for Consteel due to new environment-friendly features. MPT International 2007;5:58–65.

[113] Giavani C, Malfa E, Memoli F. Consteel evolution – the second generation of consteel technology. Industrial Heating 2012;80.

[114] Yamaguchi R, Mizukami H, Maki T, Ao N. ECOARC technology. Proceedings of the 58th electric furnace conference, 2000, p. 325–38.

[115] Rummler K, Tunaboylu A, Ertas D. New generation in preheating technology for electric arc furnace steelmaking. Iron and Steel Technology 2013;10:90–8.

[116] Ester H. Energy recovery technology for EAFs. International convention on clean, green and sustainable technologies in iron and steel making, Bhubaneswar (India):

2009.

[117] Campana F, Bianchi M, Branchini L, De Pascale a., Peretto a., Baresi M, et al. ORC waste heat recovery in European energy intensive industries: Energy and GHG savings. Energy Conversion and Management 2013;76:244–52. doi:10.1016/j.enconman.2013.07.041.

[118] Baresi M. Layman report: H-REII Project 2012. http://ec.europa.eu/environment/life/project/Projects/index.cfm?fuseaction=home.showFile&rep=file&fil=LIFE08_ENV_IT_000422_LAYMAN.pdf (accessed May 15, 2014).

[119] Steinparzer T, Haider M, Zauner F, Enickl G, Michele-Naussed M, Horn AC. Electric Arc Furnace Off-Gas Heat Recovery and Experience with a Testing Plant. Steel Research International 2014;85:519–26. doi:10.1002/srin.201300228.

[120] Santangelo N, Bertolissio A, Tomadin L. Clean Heat Recovery From EAF Hot Fumes Into Electric Energy, With Consequent Fuel Saving and Reduction of Greenhouse Gas Emission. AISTECH, 2015.

[121] Pardo N, Moya J, Vatopoulos K. Prospective Scenarios on Energy Efficiency and CO2 Emissions in the EU Iron & Steel Industry. 2012. doi:10.2790/64264.

[122] Toulouevski YN, Zinurov IY. Implementation of New Technology. Electric Arc Furnace with Flat Bath, 2015, p. 25–43. doi:10.1007/978-3-319-15886-0_2.

[123] Fuchs G, Rummler K, Hassig M. New energy saving electric arc furnace designs. Proceedings of AISTech Conference, Pittsburgh (Pennsylvania): 2008.

[124] Rummler K, Müller H. Operating experience at a 170t EAF with EPC scrap preheating system. Proceedings of SEASI Conference, Dusit Thani Pattaya (Thailand): 2013.

[125] Forni D, Rossetti N, Baresi M, Di Santo D. Heat recovery for electricity generation in Industry. Proceedings of the European Council for an Energy Efficient Economy (Industrial Summer study), 2012.

[126] Schliephake H, Born C, Memoli F, Simmons. Heat Recovery for the EAF of Georgsmarienhütte. Proceedings of AISTech Conference, 2010.

[127] Bause T, Campana F, Filippini L, Foresti A, Monti N, Pelz T. Cogeneration with ORC at Elbe-Stahlwerke Feralpi EAF Shop. AISTECH, 2014.

[128] HREII DEMO Observatory. ORC Waste Heat Recovery for a more Competitive and Sustainable Steel Industry Policy paper. 2013.

[129] Forni D, Santo D Di, Campana F. Innovative system for electricity generation from waste heat recovery. Proceedings of the European Council for an Energy Efficient Economy (Industrial Summer study), 2014, p. 393–403.

[130] Nardin G, Dal Magro F. Innovative devices for smoothing thermal power fluctuations of waste gas. Consultancy Report 2012.

[131] Energy_Strategy_Group. Energy Efficiency Report. Politecnico Di Milano 2012.

[132] VDEh Plantfact database 2012.

[133] Nardin G. Apparatus and method to transfre heat energy by means of phase change materials - WO 2014/064508 A1, 2014.

[134] Nyssen P, Colin R, Knoops S, Junque J. On-line EAF control with a dynamic metallurgical model. Proceedings of the 7th European electric steelmaking conference, Venice: 2002, p. 293–304.

[135] Takasuga T, Makino T, Tsubota K, Takeda N. Formation of dioxins (PCDDs/PCDFs) by dioxin-free fly ash as a catalyst and relation with several chlorine-sources. Chemosphere 2000;40:1003–7. doi:10.1016/S0045-6535(99)00345-8.

[136] Altarawneh M, Dlugogorski BZ, Kennedy EM, Mackie JC. Mechanisms for formation, chlorination, dechlorination and destruction of polychlorinated dibenzo-p-dioxins and dibenzofurans (PCDD/Fs). Progress in Energy and Combustion Science 2009;35:245–74. doi:10.1016/j.pecs.2008.12.001.

[137] Huang H, Buekens A. De novo synthesis of polychlorinated dibenzo-p-dioxins and dibenzofurans Proposal of a mechanistic scheme. Science of The Total Environment 1996;193:121–41. doi:10.1016/S0048-9697(96)05330-2.

[138] GME. Energy efficiency certificates market 2016. www.mercatoelettrico.org (accessed April 1, 2016).

[139] Federacciai. Italian Steel Industry Report 2012. http://www.federacciai.it/ (accessed October 1, 2013).

[140] Maruoka N, Akiyama T. Thermal stress analysis of PCM encapsulation for heat recovery of high temperature waste heat. Journal of Chemical Engineering of Japan 2003;36:794–8. doi:10.1252/jcej.36.794.

[141] Parrado C, Cáceres G, Bize F, Bubnovich V, Baeyens J, Degrève J, et al. Thermo-mechanical analysis of copper-encapsulated NaNO3–KNO3. Chemical Engineering Research and Design 2015;93:224–31. doi:10.1016/j.cherd.2014.07.007.

[142] Blaney JJ, Neti S, Misiolek WZ, Oztekin A. Containment capsule stresses for encapsulated phase change materials. Applied Thermal Engineering 2013;50:555–61. doi:10.1016/j.applthermaleng.2012.07.014.

[143] UNI. EN 1993-1-2 “Eurocode 3: Design of steel structures - Part 1-2: General rules - Structural fire design” 2005.

[144] Incropera FP, DeWitt DP, Bergman TL, Lavine AS. Fundamentals of Heat and Mass Transfer. vol. 40. John Wiley & Sons; 2007. doi:10.1073/pnas.0703993104.

[145] Bertelli F, Brito C, Meza ES, Cheung N, Garcia A. Inward and outward solidification of cylindrical castings: The role of the metal/mold heat transfer coefficient. Materials Chemistry and Physics 2012;136:545–54. doi:10.1016/j.matchemphys.2012.07.024.

[146] Kirschen M, Velikodorov V, Pfeifer H. Mathematical modelling of heat transfer in dedusting plants and comparison to off-gas measurements at electric arc furnaces. Energy 2006;31:2926–39. doi:10.1016/j.energy.2005.12.006.

[147] VDI Heat Atlas. Berlin, Heidelberg: Springer Berlin Heidelberg; 2010. doi:10.1007/978-3-540-77877-6.

[148] Timoshenko s., Goodier JN. Thermal Stress - Chap. 14. Theory Of Elasticity, McGraw-Hill; 1951, p. 399–437.

[149] UNI. Eurocode 9 : Design of aluminium structures Đ Part 1-2 : General rules Structural fire 2000.

[150] Manson SS. Thermal stress and low-cycle fatigue. McGraw-Hill; 1966.

[151] Jiemin T, Ferri MB, Argenta P. EAF technology evolution by continuous charging. Ironmaking & Steelmaking 2005;32:191–4. doi:10.1179/174328105X38080.

[152] Iten M, Liu S. A work procedure of utilising PCMs as thermal storage systems based on air-TES systems. Energy Conversion and Management 2014;77:608–27. doi:10.1016/j.enconman.2013.10.012.

[153] Gnielinski V. New equation for heat and mass transfer in turbulent pipe and channel flow. Int Chem Eng 1976;16:359–67.

[154] Petukhov B, Irvine T, Hartnett J. Advances in heat transfer. New York: Academic Press 1970;6.

[155] Italian Regulatory Authority for Electricity Gas and Water. EEN 9/11 Decree n.d. http://www.autorita.energia.it/allegati/docs/11/009-11eenall.pdf (accessed November 1, 2014).

[156] Trunner P, Steinparzer T. Integrated energy recovery and utilization of waste heat for integrated plants and EAF route. METEC 2015, Düsseldorf: 2015.

[157] Maruoka N, Mizuochi T, Purwanto H, Akiyama T. Feasibility Study for Recovering Waste Heat in the Steelmaking Industry Using a Chemical Recuperator. ISIJ International 2004;44:257–62. doi:10.2355/isijinternational.44.257.

[158] Maruoka N, Akiyama T. Development of PCM Reactor for Methane Steam Reforming. ISIJ International 2010;50:1305–10.

[159] Nomura T, Okinaka N, Akiyama T. Waste heat transportation system, using phase change material (PCM) from steelworks to chemical plant. Resources, Conservation and Recycling 2010;54:1000–6. doi:10.1016/j.resconrec.2010.02.007.

[160] Yamazaki M, Sato Y, Seki R. Hybrid Way Eaf Off Gas Heat Recovery. Proceedings of South East Asia Iron&Steel Institute, Singapore: 2011, p. 1–10.

[161] Nardin G, Meneghetti A, Dal Magro F, Benedetti N. PCM-based energy recovery from electric arc furnaces. Applied Energy 2014;136:947–55.

doi:10.1016/j.apenergy.2014.07.052.

[162] Dal Magro F, Meneghetti A, Nardin G, Savino S. Enhancing energy recovery in the steel industry: Matching continuous charge with off-gas variability smoothing. Energy Conversion and Management 2015;104:78–89. doi:10.1016/j.enconman.2015.05.012.

[163] FORCE. Version 2.0.9p n.d.

[164] Brandt C, Schüler N, Gaderer M, Kuckelkorn JM. Development of a thermal oil operated waste heat exchanger within the off-gas of an electric arc furnace at steel mills. Applied Thermal Engineering 2014;66:335–45. doi:10.1016/j.applthermaleng.2014.02.003.

[165] Dal Magro F, Benasciutti D, Nardin G. Thermal stress analysis of PCM containers for temperature smoothing of waste gas. Applied Thermal Engineering 2016;106:1010–22. doi:10.1016/j.applthermaleng.2016.06.074.

[166] Becker M. Heat Transfer - A Modern Approach. Boston, MA: Springer US; 1986.

[167] NIST-REFPROP. Version 8.0 2007.

[168] TRNSYS. Simulation Studio - Version 17.02 2012.

[169] Infiniti_Research_Limited. Global Waste Heat Recovery Market 2015-2019. 2015.

[170] Casarosa C. Thermoeconomic optimization of heat recovery steam generators operating parameters for combined plants. Energy 2004;29:389–414. doi:10.1016/S0360-5442(02)00078-6.

[171] Valdés M, Rapún JL. Optimization of heat recovery steam generators for combined cycle gas turbine power plants. Applied Thermal Engineering 2001;21:1149–59. doi:10.1016/S1359-4311(00)00110-1.

[172] Guo J, Xu M, Cheng L. Thermodynamic analysis of waste heat power generation system. Energy 2010;35:2824–35. doi:10.1016/j.energy.2010.03.012.

[173] Roy JP, Mishra MK, Misra A. Parametric optimization and performance analysis of a waste heat recovery system using Organic Rankine Cycle. Energy 2010;35:5049–62. doi:10.1016/j.energy.2010.08.013.

[174] Roy JP, Mishra MK, Misra A. Performance analysis of an Organic Rankine Cycle with superheating under different heat source temperature conditions. Applied Energy 2011;88:2995–3004. doi:10.1016/j.apenergy.2011.02.042.

[175] Sun Z, Gao L, Wang J, Dai Y. Dynamic optimal design of a power generation system utilizing industrial waste heat considering parameter fluctuations of exhaust gas. Energy 2012;44:1035–43. doi:10.1016/j.energy.2012.04.043.

[176] Haider M, Werner A. An overview of state of the art and research in the fields of sensible, latent and thermo-chemical thermal energy storage. E & I Elektrotechnik Und Informationstechnik 2013;130:153–60. doi:10.1007/s00502-013-0151-3.

[177] Li G. Sensible heat thermal storage energy and exergy performance evaluations. Renewable and Sustainable Energy Reviews 2016;53:897–923. doi:10.1016/j.rser.2015.09.006.

[178] Dassault Systèmes. Dymola n.d.

[179] Lu H, Price L, Zhang Q. Capturing the invisible resource: Analysis of waste heat potential in Chinese industry. Applied Energy 2016;161:497–511. doi:10.1016/j.apenergy.2015.10.060.

[180] Tian H, Shu GQ. Organic Rankine Cycle systems for large-scale waste heat recovery to produce electricity. Organic Rankine Cycle (ORC) Power Systems, Elsevier; 2017, p. 613–36. doi:10.1016/B978-0-08-100510-1.00017-X.

[181] SMS-Group. Reheat furnaces and heat treatment technology 2016. https://www.sms-group.com (accessed December 1, 2016).

[182] Wang J-G, Shen T, Zhao J-H, Ma S-W, Wang X-F, Yao Y, et al. ARTICLE IN PRESS Soft-sensing method for optimizing combustion efficiency of reheating furnaces. Journal of the Taiwan Institute of Chemical Engineers 2016;8:0–1. doi:10.1016/j.jtice.2016.09.037.

[183] Buschle J, Steinmann WD, Tamme R. The Modelica Association Analysis of steam storage systems using Modelica 2006.

[184] Eurostat. Energy price statistics 2016.

[185] Bogale W, Viganò F. A Preliminary Comparative Performance Evaluation of

Highly Efficient Waste-to-Energy Plants. Energy Procedia 2014;45:1315–24. doi:10.1016/j.egypro.2014.01.137.

[186] Lee SH, Themelis NJ, Castaldi MJ. High-temperature corrosion in waste-to-energy boilers. Journal of Thermal Spray Technology 2007;16:104–10. doi:10.1007/s11666-006-9005-4.

[187] Main A, Maghon T. Concepts and experiences for higher plant efficiency with modern advanced boiler and inciniration technology. Proceedings of the 18Th Annual North American Waste-to-Energy Conference - NAWTEC18, Orlando, Florida, USA: 2010, p. 1–8.

[188] Martin JJE, Koralewska R, Wohlleben A. Advanced solutions in combustion-based WtE technologies. Waste Management 2015;37:147–56. doi:10.1016/j.wasman.2014.08.026.

[189] De Greef J, Villani K, Goethals J, Van Belle H, Van Caneghem J, Vandecasteele C. Optimising energy recovery and use of chemicals, resources and materials in modern waste-to-energy plants. Waste Management 2013;33:2416–24. doi:10.1016/j.wasman.2013.05.026.

[190] Costa M, Dell'Isola M, Massarotti N. Temperature and residence time of the combustion products in a waste-to-energy plant. Fuel 2012;102:92–105. doi:10.1016/j.fuel.2012.06.043.

[191] Tejima H, Nishigaki M, Fujita Y, Matsumoto A, Takeda N, Takaoka M. Characteristics of dioxin emissions at startup and shutdown of MSW incinerators. Chemosphere 2007;66:1123–30. doi:10.1016/j.chemosphere.2006.06.015.

APPENDIX A

TRANSIENT THERMO-MECHANICAL SIMULATION OF PCM SYSTEM RESPONSE

This Appendix presents the distribution of temperature and thermal stresses calculated by a transient thermo-mechanical simulation, which also includes the phase change (melting) of the PCM. The purpose of this simulation is to confirm how the hypothesis of steady state analysis and uniform temperature distribution in the PCM system is a very good approximation of transient analysis. Secondly, the simulation results will also show how the modelling of phase change of PCM is actually not necessary in the computation of thermal stresses, as the highest stress occurs only at the start-up phase when the PCM is solid, whereas much lower stresses occur when the PCM is liquid, or even when it is still solid at temperatures far below the melting point.

The transient thermo-mechanical simulation adopts the same mesh distribution used in the one quarter finite element plane model of Figure 3.33a, although 8-nodes elements are preferred here to improve solution accuracy. The model is under 'plane stress' condition (i.e. zero axial stress), which is also justified in Appendix B. In transient simulations, thermal analysis is carried out first to compute the time-varying temperature in each node, which is next applied as a load thermal input in the mechanical analysis.

In thermal analysis, to replicate as close as possible the operating condition in the settling chamber (see Figure 3.29a), the PCM system is subjected to a convection boundary condition, with a film coefficient h_{ext} = 126 W/m^{2}K and a waste gas temperature (bulk temperature) that increases linearly from 200 °C to 950 °C over a time interval of 20 min, then back to 200 °C over the next 20 min, and then kept constant over the final 20 min.

The phase change (melting) of the PCM (aluminium) is simulated by defining an enthalpy vs. temperature curve, which increases by the latent heat H_a=396 kJ/kg (see Table 3.12) at the melting temperature.

In mechanical simulation, an elastic material model is used, with temperature-dependent mechanical properties as per Table 3.13; note how the elastic modulus of the PCM (aluminium) rapidly goes to zero for temperatures approaching 660 °C (for example, from 20 °C to 400 °C the elastic modulus is halved). In simulations, the AISI 316 steel is used for the container, but similar conclusions would be obtained by using AISI 410S as well.

In transient simulation, a Newmark time integration scheme is adopted, with a very small integration time step to assure numerical convergence.

Figure A.1 shows the temperature and stress over time, monitored at four different locations in the PCM system: i) outer surface of steel container (labelled 'surface'), ii) inner surface of steel container, at the PCM/steel interface (labelled 'interface'), iii) at a point in PCM part, 4 mm underneath the PCM/steel interface (labelled 'sub-interface'), iv) at the centre of PCM.

Figure A.1a shows that the temperature distribution within the PCM systems is almost uniform at any time instant (the four lines in the graph are overlapped). Melting of PCM starts after about 20 minutes and lasts for about 18 minutes; the temperature of PCM system then decreases as the bulk temperature goes down to 250 °C. It can be concluded that the hypothesis of uniform temperature distribution within the PCM system is fully justified by the results of transient thermal analysis shown in Figure A.1a.

Figure A.1b shows the change over time of radial and tangential (hoop) thermal stresses at some locations in the PCM system. The radial stress at 'surface' is always zero, as expected. For more clarity, the graph does not show the lines of radial σ_r and hoop σ_θ stresses at 'centre' and 'sub-interface' locations, because they are practically overlapped to the radial stress σ_r at 'interface', which is compressive in the time intervals 0÷15 min and 38÷60 min (while it is almost zero elsewhere). In the same time intervals where σ_r is compressive, tensile hoop stresses are observed at 'surface' and 'interface' locations. Finally, the graphs in Figure A.1b also shows the change over time of Von Mises stress at 'interface' locations, as calculated by equation (3.21).

The results of Figure A.1b show the following important findings. The Von Mises stress has a maximum after about 11 min, when the PCM system is at 400 °C and the PCM is

still in solid phase, see Figure A.1a (melting only starts after 20 min). The maximum Von Mises stress is slightly higher than 250 MPa, which is a value in close agreement to the estimation in Figure 3.34b given by the analytical model of section 3.5.4.

For time values larger than 11 min, the Von Mises stress (as all other stress components) rapidly decrease; they become almost zero at about 15 min (i.e. when the PCM is still in solid phase). This sharp decrease of stress is explained by the drop in elastic properties of PCM material, which at temperatures above 400 °C actually has a very low value of its elastic modulus (see Table 3.13). Negligible stresses are then maintained up to 18 min (when melting of PCM starts) and later on, up to 38 min (when the PCM comes back to solid state). The results in Figure A.1b then show that melting of PCM actually does not contribute in an increase in calculated stresses, as compared to the values estimated by the analytical model in section 3.5.4.

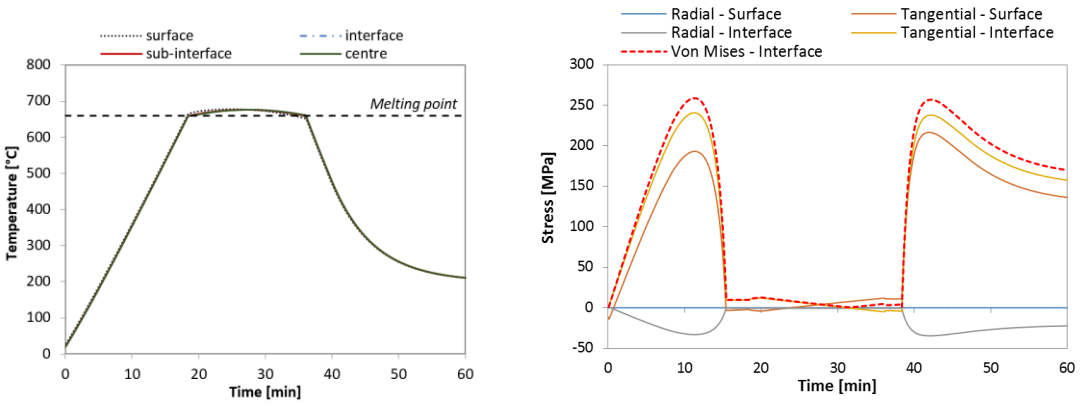

(a) (b)

Figure A.1 Results of transient numerical analysis with melting of PCM, monitored at four different locations in the PCM system: a) temperature evolution and b) stresses.

APPENDIX B

NUMERICAL STUDY WITH A PLANE AXISYMMETRIC MODEL

A small longitudinal portion of the PCM system in Figure 3.29b is analysed by a plane axisymmetric finite element model. Both aluminium and steel regions are discretised by 4-nodes elements with axisymmetric option, arranged in a mapped mesh over the whole domain. Contact elements are also placed at the interface between aluminium and steel container, to simulate the separation and then to allow a relative sliding between the two materials. Two values of the friction coefficient μ were used to simulate two limiting situations: μ=0 for perfect sliding (i.e. no constraint to aluminium thermal expansion), μ=0.65 (a typical value for aluminium/steel coupling) to simulate a constrain to thermal expansion of aluminium. Both aluminium and steel materials are assumed to be linear elastic, with mechanical properties listed in Table 3.13.

The whole model is subjected to a uniform temperature increase (to simulate the start-up phase described in section 3.5.2), which induces a thermal expansion of the contained aluminium. Figure B.1 shows the distribution of stresses (radial σ_r , hoop σ_θ , axial σ_z and shear τ_{rz}) resulting from the analyses with the two values of friction coefficient. The figures also compare the equivalent Von Mises stress:

$$\sigma_{vm} = \sqrt{\sigma_r^2 + \sigma_\theta^2 + \sigma_z^2 - \sigma_r\sigma_\theta - \sigma_r\sigma_z - \sigma_\theta\sigma_z + 3\tau_{rz}^2} \qquad \text{(B.1)}$$

to the von Mises stress calculated by equation (3.21) under the plane stress hypothesis (σ_z=τ_{rz}=0).

With no friction at the interface (μ=0), there is no constraint to thermal expansion and only radial σ_r and hoop σ_θ stresses develop, while, as expected, the axial and shear stresses are zero (σ_z=τ_{rz}=0). Instead, with a high friction coefficient (μ=0.65) the free thermal expansion of aluminium is prevented and both axial σ_z and shear stress τ_{rz} appear, along with radial σ_r and hoop σ_θ stresses.

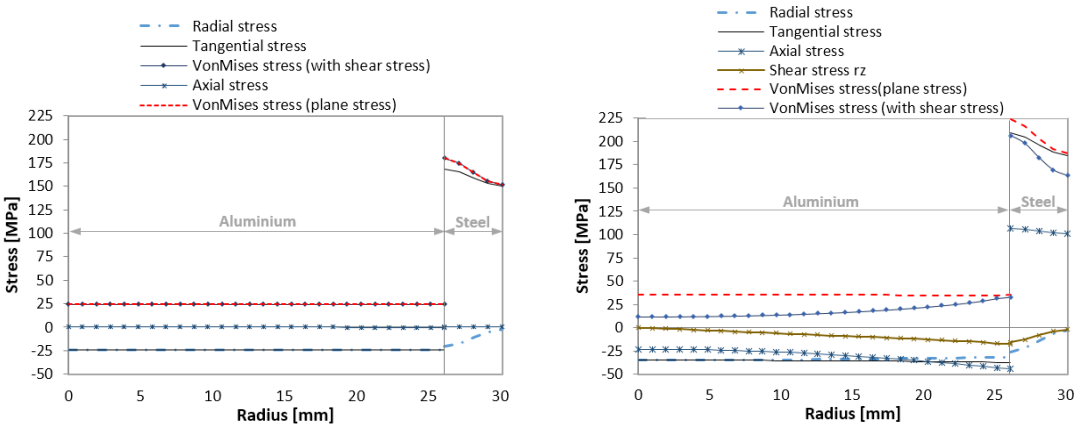

Figure B.1 Stress distribution as a function of radial coordinate for two values of friction coefficient at the aluminium/steel interface: a) zero friction (μ=0) and b) μ=0.65.

In aluminium the axial stress is compressive, while it is discontinuous at the interface and then tensile in the steel. The figures show that the axial stress has a small influence on the von Mises stress in the steel container. At the inner radius, the equivalent von Mises stress under plane stress, see equation (3.21), is about 14% higher than the von Mises stress of equation (B.1), which considers instead all stress components. Remarkably, the plane stress model is then over-conservative. As known from the theory of strength of materials, there would actually be no difference in equivalent stresses, if they were calculated by using the Guest-Tresca criterion (i.e. maximum shear stress), which computes the equivalent stress $\sigma_{gtr}=|\sigma_\theta-\sigma_r|$ as the difference of maximum principal stresses.

These results allow one to conclude that the plane stress hypothesis is a reasonable assumption for the analytical model of the PCM system.

APPENDIX C

SIMPLE TWO-BARS MECHANICAL MODEL

The two-bars model in Figure 3.30b exemplifies two elementary elements at the aluminium/steel interface in the PCM system. The two elements are attached at two rigid plates at both ends. One end plate is fixed, while the plate at the opposite side can translate. No rotations are allowed and the bars can only deform along the longitudinal direction (i.e. this is a one-dimensional model).

The two bars, which represent aluminium and steel, have, respectively, areas A_a and A_s, elastic modulus E_a and E_s, and coefficient of thermal expansion α_a, α_s. Both bars are subjected to a temperature increment $\Delta T = T\text{-}T_{ref}$, with respect to a reference temperature T_{ref}.

The thermal expansion of the system is partially constrained by the different longitudinal elongation of the two bars, which are then subjected to thermal stresses. The value of thermal stresses can be computed analytically by the expressions. The total strain in each bar is the sum of thermal strain and mechanical strain:

$$\varepsilon_{tot} = \varepsilon_{th} + \varepsilon_{mec} \tag{C.1}$$

Thermal strain is caused by the temperature increase, $\varepsilon_{th}=\alpha\Delta T$, while the mechanical strain ε_{mec} gives the thermal stress $\sigma=E\varepsilon_{mec}$. The response of the two-bar model in Figure 2b is governed by the following equations (equilibrium and compatibility):

$$\begin{cases} \varepsilon_{tot,a} = \varepsilon_{tot,s} \\ \sigma_a A_a + \sigma_s A_s = 0 \end{cases} \tag{C.2}$$

The first equation states that the elongations of both bars must be equal, because the bars are attached to the same rigid end plate; the second equation specifies the equilibrium of forces transmitted by the two bars to the top rigid plate. By using equation (C.1), the first of previous equations can be rewritten as:

$$\alpha_{\mathrm{a}}\Delta T + \frac{\sigma_{\mathrm{a}}}{E_{\mathrm{a}}} = \alpha_{\mathrm{s}}\Delta T + \frac{\sigma_{\mathrm{s}}}{E_{\mathrm{s}}} \tag{C.3}$$

After rearranging, and by using the second equation in (B.2), the stress in the steel bar is obtained as:

$$\sigma_{\mathrm{s}} = \frac{(\alpha_{\mathrm{a}} - \alpha_{\mathrm{s}})E_{\mathrm{s}}\Delta T}{1 + \frac{E_{\mathrm{s}}A_{\mathrm{s}}}{E_{\mathrm{a}}A_{\mathrm{a}}}} \tag{C.4}$$

while the stress in the aluminium bar is:

$$\sigma_{\mathrm{a}} = -\frac{(\alpha_{\mathrm{a}} - \alpha_{\mathrm{s}})E_{\mathrm{a}}\Delta T}{1 + \frac{E_{\mathrm{a}}A_{\mathrm{a}}}{E_{\mathrm{s}}A_{\mathrm{s}}}} \tag{C.5}$$

Equations (C.4) and (C.5) show that thermal stresses are directly proportional to the temperature change and, of course, no stress would develop without a temperature variation ($\Delta T = 0$). No stress is also generated (even with a temperature change $\Delta T \neq 0$) if both materials have identical thermal expansion coefficients ($\alpha_a = \alpha_s$), because the two bars elongate with identical thermal expansions. For the aluminium/steel system (where $\alpha_a > \alpha_s$), the equations (C.4)-(C.5) correctly predict a tensile stress in the steel bar and a compressive stress in the aluminium bar, as also shown by the results in Figure 3.31.

Equations (C.4) and (C.5) also show that thermal stress is controlled by the stiffness values of aluminium and steel elements (summarised by the elastic moduli E_a, E_s), other than by the relative ratio of stiffness (summarised by the ratios E_a/E_s and E_s/E_a).